CRANFIELD INSTITUTE OF TECHNOLOGY

SCHOOL OF MECHANICAL ENGINEERING

M.Phil. THESIS

ACADEMIC YEAR 1984-88

SATEEAM ARITHOPPAH

THEORY AND PRACTICE OF A HORIZONTAL-AXIS FLEXIBLE SAIL TYPE WIND-TURBINE BEHAVIOUR

SUPERVISOR PROF.S.D.PROBERT

TO MY MUM.

ABSTRACT

A sail of 0.3m x 0.28m, with 1% slack, was placed in the test section of a wind tunnel. Both surface visualization and pressure distribution tests were undertaken with the sail at various angles of attack, α, relative to the wind, for a constant wind speed of 5 m/s. As the angle of incidence was increased from 2.5°, it was found that the flow round the sail behaved in a smooth manner until α reached 15°. Beyond 15°, flow separation became dominant and for higher angles of attack (i.e. $\alpha > 25^{\circ}$) the sail flapped violently. It was also found that the lift increased linearly with α and the sail stalled at an angle of incidence of $\alpha = 15^{\circ}$. At zero angle of attack the lift was found to be negative.

The performance of a fully-augmented flexible sail-type wind turbine has been investigated. The augmentation devices (i.e. centre-body and tip-fins) used resulted in an increase of about 60% over the unaugmented wind turbine. Tests were carried out so as to determine the pumping characteristics of the wind turbine when it was coupled to a commercially-available peristaltic pump.

Aerodynamic characteristics of the interacting sails, together with the effectivenesses of the above mentioned augmenting devices, were investigated using a flow-visualization technique and this was done at the optimal operating wind-speed of 5 m/s.

Tests on the wind-turbine/pump combination show that the cut-in and cut-out wind speeds for the pump to function were 3.71 and 11 m/s respectively.

ACKNOLEDGEMENTS

I would like to extend my thanks to several people who helped me with their kind assistance in carrying out this project. My thanks go first to Professor S.D.PROBERT, my supervisor, whose patience, criticism and advice were of great help to me. I would also like to thank Charlie Knight for his helpful comments and guidance throughout my practical work. I am indebted to the workshop staff, especially Norman, without whose help this project would never have finished. Finally, I would like to express my gratitude to Jayne, my wife, for being very patient and understanding.

CONTENTS

Figures | Page Number

Graphs | Page Number

Graphs | Page Number

Graphs | Page Number

APPENDICES

NOMENCLATURE

Symbols	Description	Units
A	area	m^2
A.R	aspect ratio = (height^2 / area)	-
a'	axial interference factor	-
a	tangential interference factor.	-
B	number of blades.	-
b	span of sail.	m
c	chord of sail.	m
C	camber of sail.	m
C_d	drag coefficient.	-
C_L	lift coefficient.	-
C_P	power coefficient.	-
C_t	torque coefficient.	-
d	angle of yaw (rotor axis - wind direction)	deg
d	diameter	m
E	energy	J
E_v	energy per volume.	J/m^3
g	gravity	m/s^2
h	height	m
L	length	m
L	lift force.	N
m	mass	Kg
M	dynamometer mass reading.	Kg

N	rotor revolutions.	rpm
P	power	watts
P(hyd)	hydraulic power.	watts
P(mech)	mechanical power.	watts
p	force	N
p	pressure	N/m^2
q	flowrate	m^3/s
r	local radius.	m
r_1	fixed pulley radius	m
r_2	rope radius.	m
R	rotor radius.	m
Re	Reynolds number.	-
T	torque	Nm
T	thrust force	N
U	speed	m/s
V	wind speed.	m/s
V_∞	undisturbed wind speed.	m/s
V	wind velocity far behind the rotor.	m/s
W	relative wind velocity.	m/s
w	induced tangential angular wind velocity.	m/s
α	angle of incidence.	deg
β	blade setting angle.	deg
η	efficiency	-
λ	tip speed ratio	-
λ_r	local tip speed ratio	-
μ	dynamic viscosity	Ns/m^2
ν	kinematic viscosity	m^2/s

ρ	density	Kg/m^3
ρ_a	air density.	Kg/m^3
ρ_w	water density.	Kg/m^3
σ	solidity ratio.	-
Ω	angular velocity of rotor.	l/s
ϕ_v	volume flow.	m^3/s

CHAPTER ONE

WIND POWER

OBJECT OF THE PRESENT INVESTIGATION

There has been much interest in the theory of aerodynamic surfaces formed of flexible membranes. While sails are the historical example of such surfaces, other examples such as parawings, rotor blades, and even glider wings utilizing flexible lifting surfaces have recently been investigated. The aerodynamics of flexible aerofoils present a facinating problem in theoretical aerodynamics, in that the shapes of such surfaces depend on their load distribution and vice versa.

It is proposed to investigate experimentally the behaviour of a flexible sail as its angle of incidence is varied. Tests were also carried out in order to determine the pressure distribution over and under the sail surfaces. These tests should help determine:-

1. the optimal angle of attack for that particular sail;
2. the air-flow behaviour (i.e. whether laminar, turbulent or mixed) as it passes over and under the sail;
3. the angle of attack, α , at which the lift is zero and the lift force when $\alpha = 0$ degree.

Also investigated were the power characteristics of a fully-augmented wind rotor in order to determine the

optimal shape of the augmentation devices (i.e. Centre-bodies and Tip-fins) which will result in achieving the highest performance.

Finally, the overall objective was to develop a cheap power-augmented sail-type wind-turbine, capable of driving a self-regulating peristaltic pump for water pumping purposes. The design should be easy to construct and maintain by unskilled workers using indigenous materials.

THE SAIL TYPE WIND TURBINE

This type of wind turbine is commonly found on the Aegean Islands. Its origin is obscure, but it probably evolved because of the local knowledge and experience of handling sailing ships. The recent resurgence of interest in the sail wind rotor has occurred because of its cheapness, design simplicity and ease of construction and repair using indigenous materials by local semi-skilled labour. Its other major advantage is its ability to produce worthwhile power outputs harnessed from relatively low-speed (<5m/s) winds.

The sail wind-turbine is unique in that the wind shapes the sail profile. This enables horizontal axis rotors to have varying profiles dependent upon wind strength. Sail-type wind-turbines are self-starting, and when used with elastic sail-attachments, self-regulating in high winds, although the sails should be furled during (infrequent) gales.

Third World

These countries are inhabited by approximately two-thirds of the people of the Earth. Rapid population growth there is putting pressure on food supplies and economic resources, and per capita income is decreasing. Between 70 and 80% of the population lives in rural areas. There is high unemployment and under-employment. This encourages migration to the cities, which creates new problems because it destroys traditional self sustaining societies and also creates urban slums in the form of shanty towns. The exports from these countries are usually raw materials and cash crops such as coffee, rice and tea. Manufactured goods are imported, but it is considered (e.g., in the Brandt report (1)) that the trade system is unfairly balanced in favour of the richer countries. For this reason Third-World countries have balance-of-payments difficulties, which have been made worse by the rise of unit oil prices.

Many developing countries depend upon hydro-electric power generation in order to meet their electricity requirements, over half of which are for irrigation purposes (2). In India, poor farmers are faced with a dilemma: either to invest in electric pumps which are "capital-intensive" or to rely on animal power, a "labour-intensive" task, as a means of raising water from underground. The gap between the two technologies employed is so enormous that a transition from the one to the other will only occur very slowly. If effective help is to be

brought to these farmers more rapidly, a more easily acceptable technology is required. Such an intermediate technology (3) would need to be cheaper than the sophisticated, highly capital-intensive technology of the western world. At such a level of capitalisation, very large numbers of workplaces could be created within a fairly short time; and the creation of such workplaces would be "within reach" for the more enterprising minority within each Third World community, not only in financial terms but also in terms of their education, aptitude, and managerial skills.

The intermediate technology would also fit much more smoothly into the relatively unsophisticated environment in which it is to be utilised. The equipment would be simple and therefore easily understandable, so suitable for maintenance and repair "on the spot". Such vernacular equipment is normally far less dependent on raw materials of great purity or exact specifications and much more adaptable to market fluctuations than highly sophisticated equipment. Men are more easily trained; supervision, control and organisation are simpler and there is far less vulnerability to unforeseen difficulties.

The real task of the intermediate technology employed may be formulated in four propositions:-

Firstly, the workplaces have to be created in these areas where people are living now and not primarily in metropolitan areas into which they tend to migrate.

Secondly, these workplaces must be, on average,

cheap enough so that they can be created in large numbers without this requiring an unattainable level of capital investment and imports.

Thirdly, the production methods employed must be relatively simple, so that the demands for high skills are minimised, not only in the production process itself but also in matters of organisation, raw material supply, financing and so forth.

Fourthly, the production should be mainly from indigenous materials and mainly for local use.

These four requirements can be met by the Cretan-type windwheel which is of simple design. Such turbine could be constructed using local materials so avoiding the need for importation. In contrast to complex machinery, the windwheel may be constructed using simple hand tools. Workplaces in villages could be used to construct Cretan-type windwheels. This would enable the wind-turbines to be produced at a price farmers could afford. Another advantage is that the money spent would probably remain within the community.

One of the oldest uses of wind energy is water pumping. Mainly due to a lack of irrigation, only a fraction of the cultivated area of india is sown more than once annually. However, if sufficient water becomes available, i.e by employing a Cretan-type windwheel, crops can be grown throughout the year. For example, three crops of rice can be raised (4). The necessity for increased food production can

be realised by the fact that at least one person out of every nine in the world suffers from severe malnourishment (5).

Cretan windpumps can also be used to raise drinking water. Over half of the inhabitants of the Third World do not have access to safe drinking-water, and three-quarters have no sanitary facilities (6).

Wind-turbines will become more economical if their design can be optimised. Tewari (7) concludes that there is a considerable need for research into ways of improving the design of low-cost wind-turbines, which can be made locally.

PREVIOUS STUDIES ON TWO-DIMENSIONAL SAILS

During the 1920's, Warner and Ober (8) carried out experimental tests on a full sized yacht. They observed the air flows and pressure distributions over the sail, and the interference to the air flows produced by the mast and jib. Measurements were taken under a variety of sailing conditions, e.g in the sail's angle of attack to the wind, so the data obtained could not be compared meaningfully with each other.

In the 1930's, Cissoti (9) produced a mathematical model describing the air flows over a two dimensional non-porous sail. This was a free-stream tube model, in which the flow seperated at the trailing edge of the sail, thereby forming a quiescent wake.

In the Voelz model (10), with the exception of the boundary-layer conditions, the sail was replaced by a linear

distribution of vortices (as in the aerofoil theory). He chose the sail shape and obtained a first eigen-value solution of the linear integral equation for the strength of the vortex sheet. However, it was Bugler (11) who undertook the first major theoretical analysis using the assumptions of thin-aerofoil theory. His findings broadly agreed with those of Thwaites (12) and Nielsen (13). However, the latter showed the existence of higher eigen-values. Thwaites used linearised thin-aerofoil theory to relate the sail shape to the loadings imposed upon it. He obtained an integro differential equation (i.e the sail equation), which he first converted into matrix form at a number of chord wise points, and then solved numerically.

Also during the 1960's, Nielsen (13) carried out theoretical and experimental investigations into the two dimensional aerodynamic characteristics of flexible, infinitesimally-thin aerofoils. He formulated the theoretical problem in terms of differential equations for the camber and aerodynamic loading of the sail: these were based upon Fourier series and numerical matrix techniques, rather than upon integral equations as used by Thwaites. Nielsen concluded that the behaviour of a flexible sail is strongly dependent upon the tension it experiences, as shown in Fig.1.

Later in the 1960's, Chambers (14) demonstrated that variational methods could be applied to solve the Thwaites sail equation. Barakat (15) studied the influence

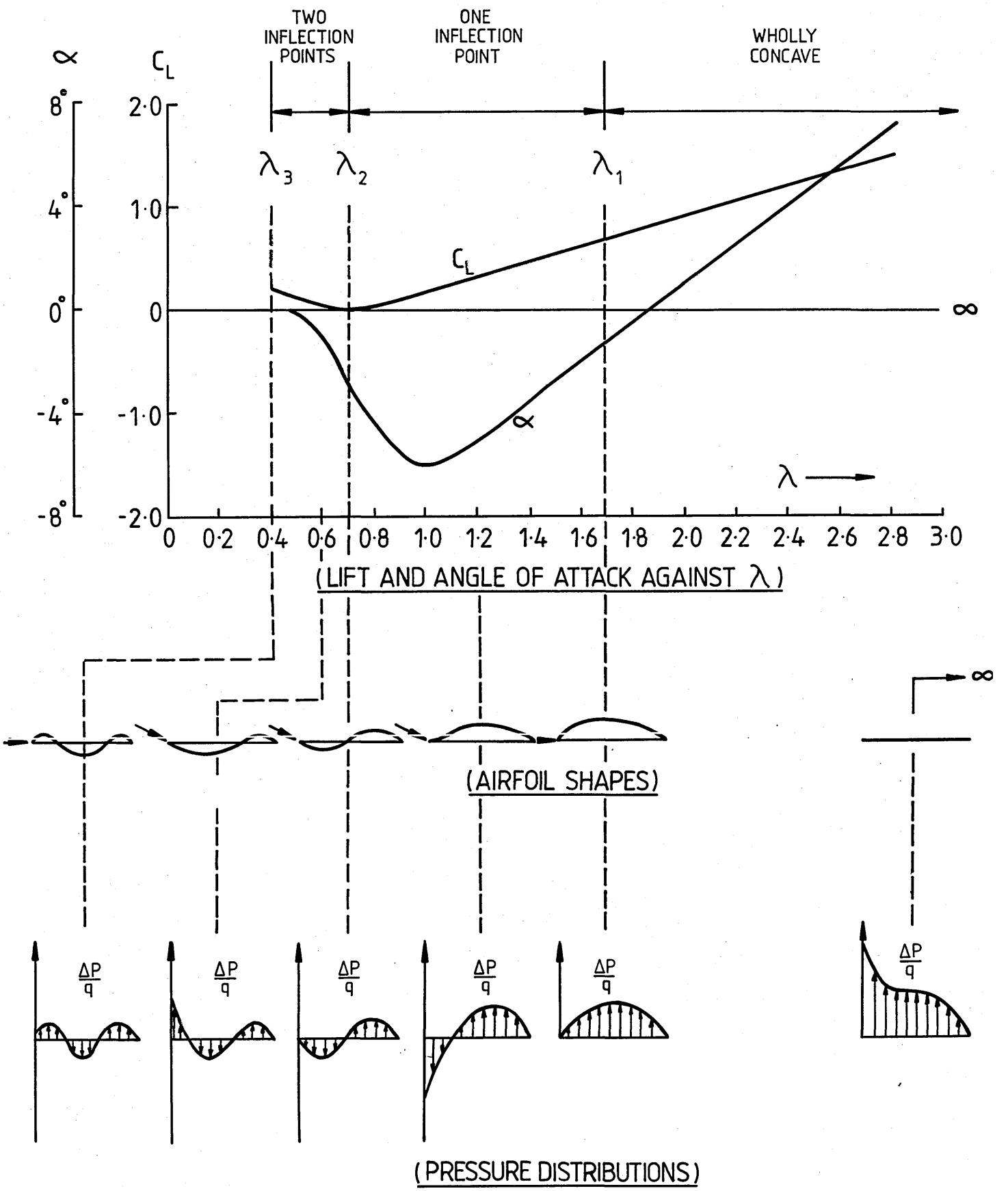

FIG. 1 LIFT COEFFICIENT AND ANGLE OF ATTACK FOR AIRFOILS OF 1% SLACK, CHAMBER-LINE SHAPES AND PRESSURE DISTRIBUTIONS.

of the porosity of a sail, using the Thwaites analysis. The major effect was to influence the vorticity equation linking the strength of the vortex sheet to the camber of the aerofoil. For a non-porous sail, this equation is of singular integral form of the second kind. Barakat also extended the theory to a two-lobed sail.

Dugan (16) used the behavioural model that was first developed by Cissoti in the 1930's. He solved the equations numerically in order to obtain the sail profiles and the free streamlines as well as the drag, lift and moment experienced by the sails. He also used the free streamline model to describe the aerodynamics of a two dimensional flexible sail. His model extended the aerofoil model, because of the different ranges of validity, with respect to the angle of attack that applied. For small angles of attack, where each model can lead to the prediction of sensible solutions, Cissoti's model should be a better representation of reality because, in practice, the stream would begin to separate from the back of the sail.

During the late 1960's, Myall and Berger (17) concluded that, for positive angles of attack, large fluctuations in the pressure distribution are possible. These affect, and are influenced by, the local curvature of the sail, but the variations are usually too small to be detected by the naked eye.

More recently, Vanden Broeck (18) investigated the deformation of a two-dimensional sail in a steady potential

flow of an incompressible inviscid fluid. The theory thereby developed follows from that of Thwaites and Nielsen and enables one to solve the fully non-linear problem numerically.

THE SAIL

The two-dimensional sail is considered to be an infinitesimally thin, inextensible, perfectly flexible aerofoil, with leading and trailing edges held a firm distance, c, apart (see Fig.2). The sail is attached to these two long rigid parallel masts, which are assumed to be so thin as to not disturb the air flow appreciably. Thus, there is a slack (l-c) in the sail.

If a uniform wind blows onto the sail, at an angle of attack, α , to the plane of the two masts, it causes the sail to fill and so become taut. It thus takes a shape determined by the wind's magnitude and direction as well as by the flexibility of the material.

BENEFITS OF A FLEXIBLE SAIL OVER A RIGID BLADE

The sail wind-turbine is unique in that the wind shapes the sail profile. This enables the sail to have varying profiles dependent upon the wind strength. Sail-type wind-turbines are self-starting and, when used with elastic sail attachments, self-regulating in high speed winds, although the sails should be furled during (the infrequently occurring) excessively high-speed winds. They are inherently slow running (with optimal tip-to-wind speed ratios of

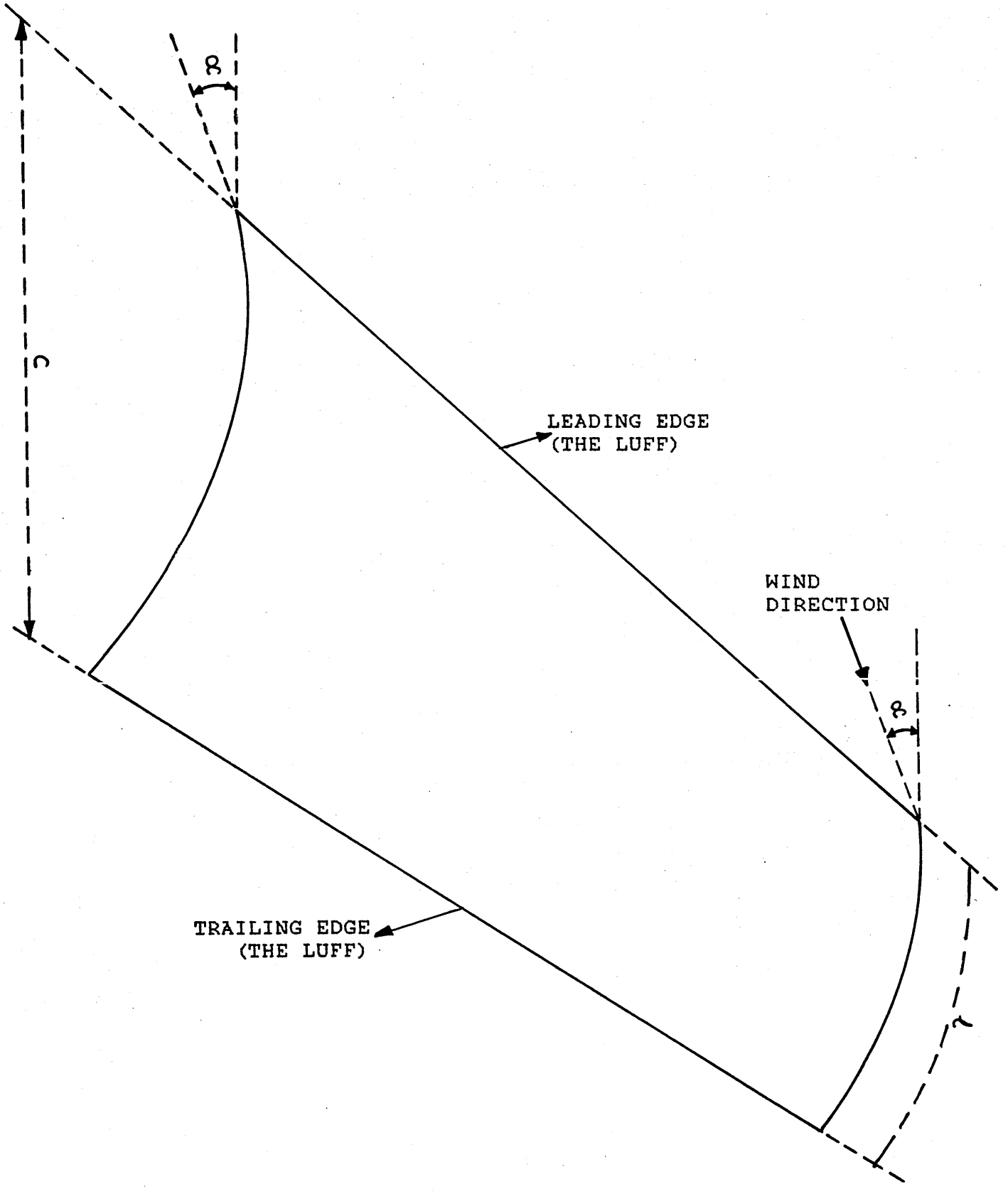

Fig.2 Two-dimensional sail at an angle of incidence, α.

approximately unity) and have large solidity ratios and high starting torques, so readily overcoming the relatively large torques required to start the majority of irrigation pumps.

Flexible sails are employed because of the following attributes:

a) self-starting capabilities: a relatively high torque is produced at low rotational speeds;

b) useful power is harnessed even from low-speed winds;

c) the sails provide a degree of self regulation, when used with elastic sail attachments, they "spill the wind" at high speeds, so only needing to be furled during the infrequent, excessively high winds; and

d) the sail profile is determined by the strength and direction of the wind , so it does not possess a constant sail-profile, as with the more conventional rigid-blade wind-turbines.

The greater the number of sails or blades, the lower the tip-to-wind speed ratios and the higher the developed torques. A wind turbine with few blades attains higher rotational speeds (and hence tip-to-wind speed ratios), but generates a smaller starting torque than a correspondingly-sized high-solidity wind-turbine. Slow-speed sail-type and multi-vane type wind-turbines are thus suitable for driving water-pumps and high-speed propeller-type rotors for generating electricity. For low tip-to-wind speed ratio wind-turbines, the large number of sails (or blades) compensates for the reduction in the power

harnessed due to drag.

Sail-type wind-turbines could be used to raise water from considerable depths. The main criterion is that the wind turbines can be manufactured locally in developing countries, using relatively unskilled lobour. Often these people, who would benefit most from harnessing wind energy, are those least able to afford to do so. But by constructing the turbines locally, the major portion of the wealth so spent would help the local community and the manufacturing costs would be kept relatively low.

CHAPTER TWO

YACHT SAIL ANALOGY

POWER HARNESSING BY THE SAIL

If we consider a sail profile and the effect of the wind of velocity U in providing the lift and drag forces (see Fig.2a), we see that the power extracted by the sail from the wind is given by:

$$P = Fu.U \qquad (1)$$

where Fu is the force in the U-direction. This force is composed of contributions by the lift L and drag D.

$$Fu = L \sin \phi - D \cos \phi \qquad (2)$$

From Fig.2a, the lift and drag are given by:

$$L = 1/2\ C_L\ c\ b\ p\ W^2 \qquad (3)$$

$$D = 1/2\ C_d\ c\ b\ p\ W^2 \qquad (4)$$

where c is the chord of the sail, b the span of the sail and p is the force, and the relative velocity W can be expressed in terms of U and V by

$$W^2 = V^2 + U^2 - 2UV\sin\delta \qquad (5)$$

Where ϕ and δ are related as follows:

$$\sin \phi = V \cos\delta / W, \text{ and}$$

$$\cos \phi = (U - V \sin\delta) / W$$

Introducing the tip-speed ratio $\lambda = (U/V)$, the power becomes:

$$P=1/2cbpV^3\ \lambda\left[(1+\lambda^2 - 2\lambda\sin\delta)\ (C_L\cos\delta - C_d\ (\lambda - \sin\delta)\right] \qquad (6)$$

From the above relationship, the two cases of lift and drag can be distinguished, as is outlined below.

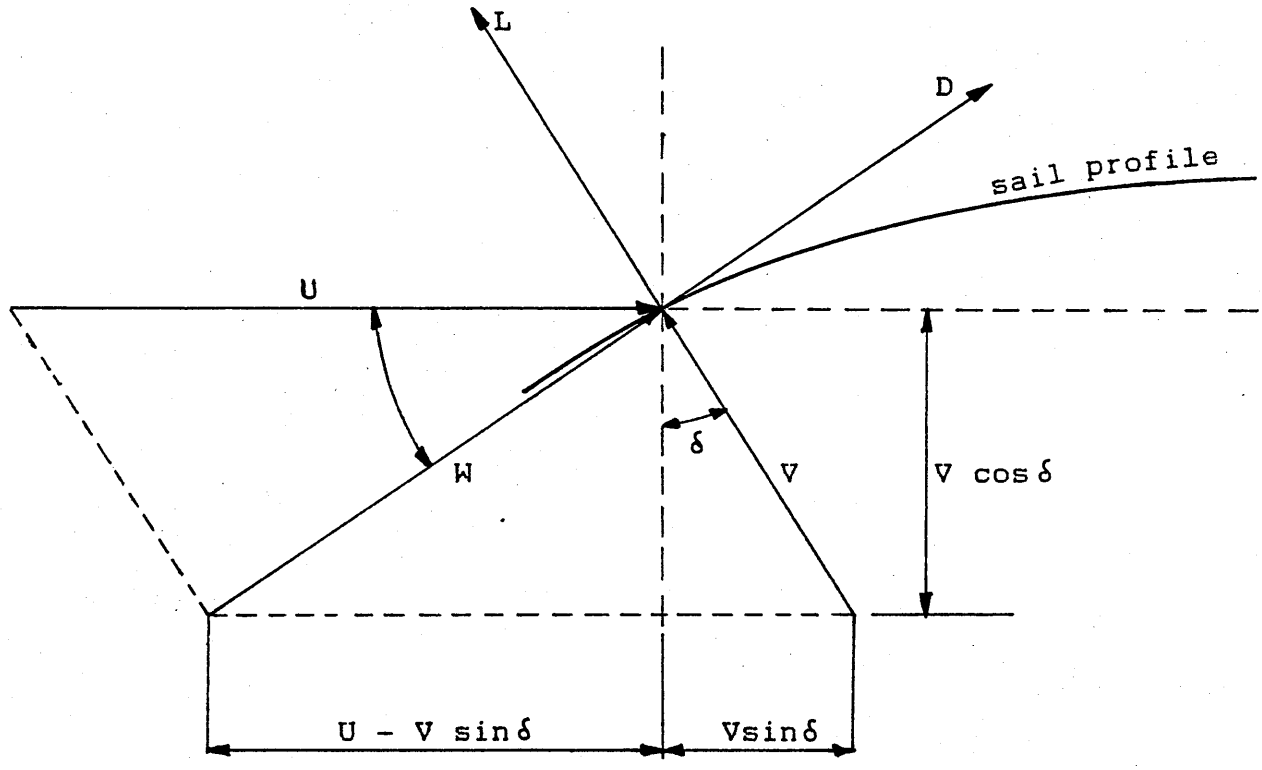

FIG.2a. POWER FROM THE SAIL.

DRAG PROPULSION occurs when the lift coefficient (C_L) is assumed to be zero.

From equation (6), the highest power available is when $\sin\delta = 1$ or $\delta = 90^\circ$. Hence

$$P = 1/2\ c\ b\ p\ V^3 \lambda \left[(1 + \lambda^2 - 2\lambda)\ (-C_d(\lambda - 1))\right] \quad (7)$$

$$= 1/2\ c\ b\ p\ V^3 \left[(\lambda - 3\lambda^2 + 3\lambda^3 - \lambda^4)\ (-C_d)\right] \quad (8)$$

Differentiating the expression for P in terms of λ yields a value of λ for P(max).

$$dP/d\lambda = (-C_d)\ 1/2\ cbpV^3(1 - 6\lambda + 9\lambda^2 - 4\lambda^3) \quad (9)$$

At a turning point $dP/d\lambda = 0$, i.e

$$1 - 6\lambda + 9\lambda^2 + 4\lambda^3 = 0 \qquad (10)$$

$d^2P/d\lambda^2$ is negative (i.e indicating a maximum value of P) when $\lambda = 1/3$. Hence,

$$P(max) = 4/27.1/2\ C_d\, c\ b\ p\ V^3 \qquad (11)$$

Therefore it can be seen from equation (11) that even with the highest value of $C_d = 2$ (i.e for a half cylinder), the maximum power is only 8/27 (= 30%) of the power in the wind reaching the swept area of the sail.

In the LIFT PROPULSION case, the highest power attained occurs when $\delta = 0$, i.e when the wind is perpendicular to the direction of the movement of the wind turbine. By substituting $\delta = 0$ into equation (6), we get:

$$P = 1/2\ c\ b\ p\ V^3\lambda \left[(1 + \lambda^2 - 2\lambda(0))\,(C_L(1) - C_d(\lambda - 0)\right]$$

$$= 1/2\ c\ b\ p\ V^3\lambda \left[(1 + \lambda^2)\,(C_L - \lambda C_d)\right] \qquad (12)$$

and $(1 + \lambda^2)$ is approximately equal to λ (within 2% for $\lambda >$ 5). Hence,

$$P = 1/2\ c\ b\ p\ V^3\lambda^2\ (C_L - \lambda C_d) \qquad (13)$$

$d^2P/d\lambda^2$ is negative (i.e max) when:

$$\lambda = (2/3)\,(C_L/\ C_d) \qquad (14)$$

Substituting from (14) into (13) we get:

$$P = 1/2\ c\ b\ p\ V^3(4/9)\,(C_L/\ C_d)^2\ (C_L - 2/3\ C_L)$$

$$P(max) = 1/2\ c\ b\ p\ V^3(4/27)\ C_L\ (C_L/\ C_d)^2 \qquad (15)$$

Equation (15) shows the importance of lift in relation to the wind turbine design, as outputs can be reached that are about 50 times higher than that of the power (eq.11) with drag propulsion.

AERODYNAMIC RESISTANCE OF SAILS

The rotor of a wind turbine consists of a number of blades whose cross section take several forms. In our case, the "sail with pole" configuration is considered as the aerofoil.

An aerofoil is a surface over which air flows and this flow results in two forces, namely LIFT and DRAG. Lift

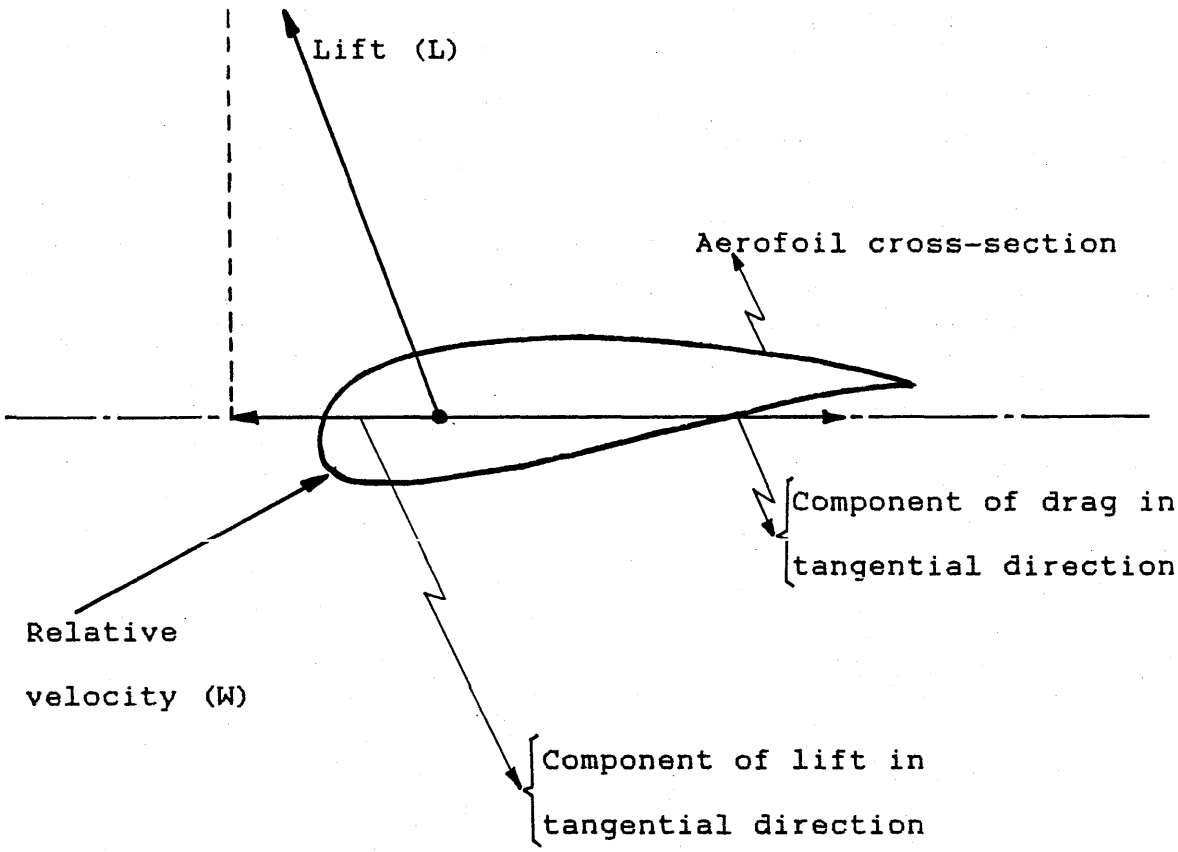

FIG. (3) Forces acting on the sail.

is the force measured perpendicular to the air flow and drag is measured parallel to the flow.

The amount of lift and drag that is produced depends on the angle of attack of the sail. From Fig. (3) above, it can be seen that in order to achieve a high

driving force, a greater lifting force and a small drag is required.

Theory and experiment show that the resultant drag D, is made up of three components, viz:-

a) Induced drag;

b) Friction drag; and

c) Form drag

Their individual contributions to the total drag D, depend on the shape of the sail, it's surface and the speed of the wind.

INDUCED DRAG ON A SAIL

The induced drag is that portion of the total drag which is inseperably connected with the formation of the cross wind force L. This force arises from the difference in pressure on the two sides of the sail. The air on the windward side, being generally at a higher pressure than that on the leaward side, round the boom and at the head of the sail. As a result of this flow of air round the "ends" of the sail, the pressure-difference between the two sides is reduced, and vortices are formed in the air flow.

The magnitude of the induced drag is not constant, but depends to a large extent on the magnitude of the cross wind force, L, and the aspect ratio, A.R., of the sail. The pressure difference experienced by the sail depends almost entirely on L, and depends on the amount of flow around the top and bottom of the sail and hence on the induced drag.

FRICTIONAL DRAG ON A SAIL

When a stream of air flows past a sail, the particles immediately adjacent to the fabric are inhibited by viscous forces. These particles then do not travel along the sail with the main stream velocity, but instead move more slowly, relative to the sail. The region between the sail and the main stream, in which the particle velocities are less than the main stream velocity, is termed the boundary layer.

As the air particles in the boundary layer are slowed down, from the main stream speed, they lose kinetic energy. This loss in energy results from friction forces acting throughout its boundary layer, until finally it is communicated to the sail as friction forces, acting parallel to the surface of the sail.

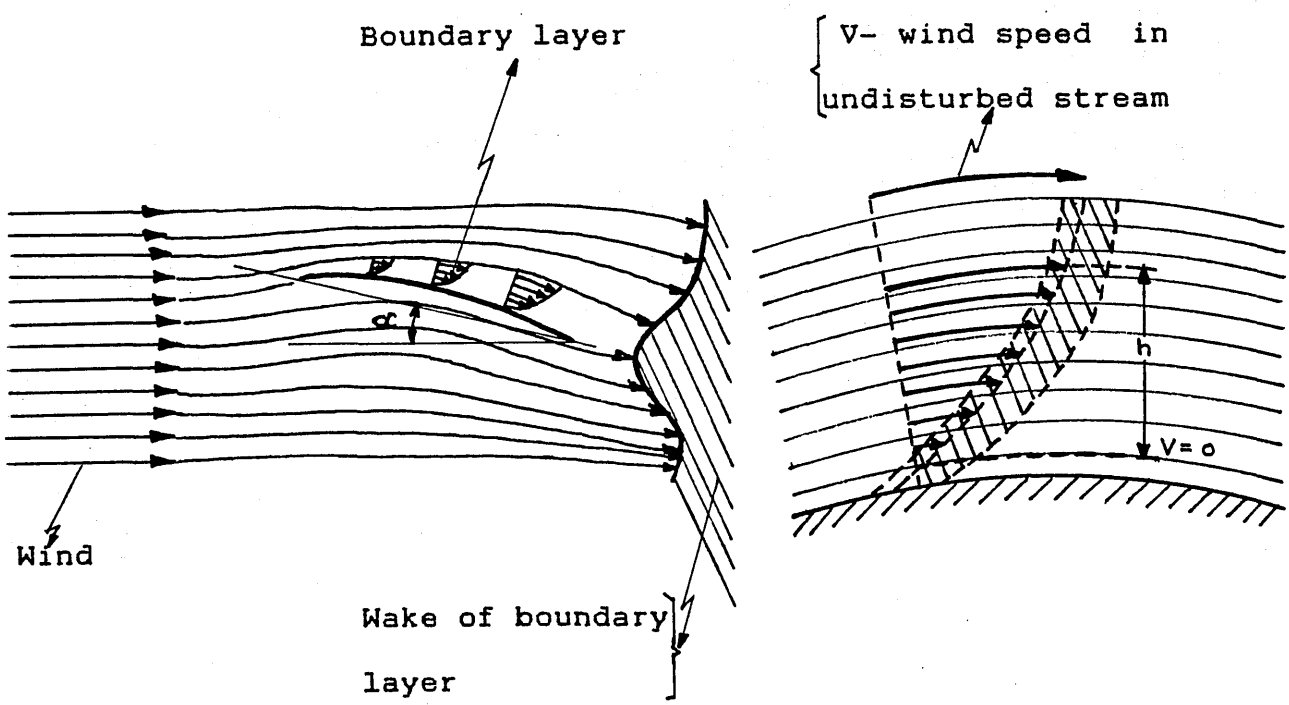

FIG.(4) Boundary layer formation on sail surfaces.

Experiments carried out by Osborne Reynolds (19), have shown that the characteristics of the flow within the boundary layer, and the associated friction forces depebnd on a quantity known as Reynolds Number,

i.e $Re = Vl/\nu$.

For a low Reynolds number (i.e a low wind speed) and not too long a body, the flow is essentially laminar. The thickness of the boundary layer is relatively small, reaching a maximum of about 5% of the sail chord, and the corresponding coefficient of frictional resistance is low.

When the Reynolds number reaches a critical value, transition of turbulent flow occurs, and the growth of the boundary layer increases (to a thickness equivalent approximately to 2% of the sail chord) giving higher coefficients of frictional resistance.

The coefficient of friction, Cf, thus not only depends on the Reynolds number but also on the smoothness of the surface and its shape.

Surface roughness (K) is given by (15):

$$K = 1200\,\nu/V$$

Where ,

k = mean height of surface roughness (m)

ν = coeff. of fluid's viscosity

V = air-flow velocity (m/s)

This roughness height will be covered by the laminar film underneath the turbulent layer.

Commercially-available sail materials have an effective roughness exceeding 0.0024cm.

FORM DRAG ON THE SAILS

Form drag arises from the turbulent flow which always exists over some part of a body placed in an air stream. This turbulence is on a larger scale than the turbulent boundary layer. It is called form drag because it is largely a consequence of the shape of the body.

The more highly curved the contour, particularly over the rear portions of the considered body, the more readily does the air flow cease to follow the contour, and so separates from it. So for a low form drag, the body should streamlined and present the smallest possible frontal area to flow.

The form drag of a sail at small angles of incidence is not great, as the predominant components then are the induced drag and the frictional drag. Fig.(5a) shows that at a small angle of incidence, the airflow is streamlined over the sail.

Fig.(5)a Fig.(5)b Fig.(5)c

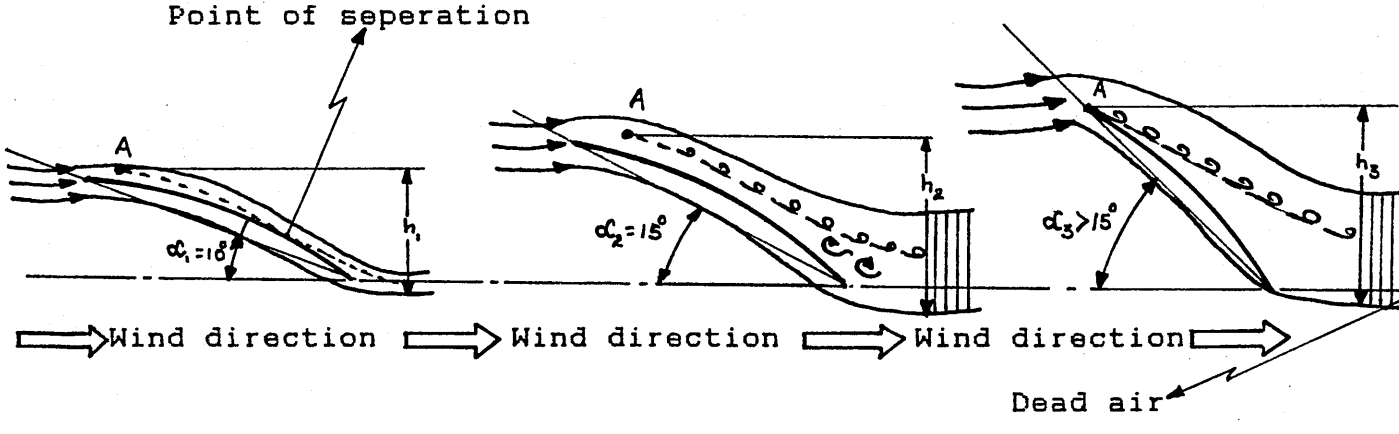

As the angle of incidence is increased, flow separation occurs and transition to turbulence ensues over part of the sail, see Fig.(5b). At higher angles of incidence, the point of separation moves forward, so increasing the form drag and hence reducing the lift force, as shown in Fig.(5c).

The condition of the flow on the leeward side of the sail is of great practical significance in this investigation, because a separated flow reduces the effective driving force and hence the speed of rotation of the wind turbine.

IMPORTANCE OF SAIL SHAPE : BASIC SAIL SHAPE ANALYSIS

To predict the performance of a sail-type wind turbine, it is necessary to know the total aerodynamic force developed on a well-designed set of sails.

The sail problem is primarily a problem in aerodynamics, similar to the problem of designing a rigid aerofoil or a turbine blade. However, it is more complex; a rigid aerofoil can be shaped and the airflow will adapt itself to that shape. The shape assumed by a flexible sail is a compromise reached between the air pressures and the sail tension and some factors have to be found that decide this shape.

In determining the shape of the sail under loaded conditons, a simple analysis is presented here by assuming that the sail is made up of long flexible strips (20).

If such a strip of length, L, and unit width is

held at it's ends and subjected to a uniform pressure, p, it will assume the shape of a circular arc of camber, C, and the tension in the strip will be pL/8C (20). To set the strip with a small camber, a big tension is required and no matter how large a tension is applied the strip cannot be pulled quite flat, see Fig.(6a).

If the camber is small, any calculations which have to be made are simplified without introducing any great error by assuming that the pressure acts normal to the chord rather than to the surface of the strip and that the shape is parabolic, Fig.(6b).

If the pressure varies linearly along the strip (48) as shown in Fig.(6c) then the position of maximum camber moves to 0.42L and the tension is 0.5pL/7.8C, the total load on the strip now being 0.5pL. With a peaky or parabolic pressure distribution as shown in Fig.(6d), the maximum camber is 0.37L and the tension is: total load / 8.5C.

It is possible by measuring the shape of the strip to decide the distribution of the load on it. The answer is unlikely to be accurate, but general inferences can be made. A fair approximation of the tension in the strip is (20):

Tension = total load / 8C

With an originally flat sail square rigged as shown in Fig.(6e), whatever the pressure distribution may be along the sections parallel to the spars, each strip of sail running from spar to spar will carry an approximately uniform load. The sail will form a cylindrical surface with

straight aerofoil sections. This phenomenon has been confirmed by Marchaj (19, 21). Solutions for the shape of a sail of this type of infinite span have been obtained by Thwaites (12), and it was shown that it sets in the shape shown in Fig.(6f), with the maximum camber towards the trailing edge.

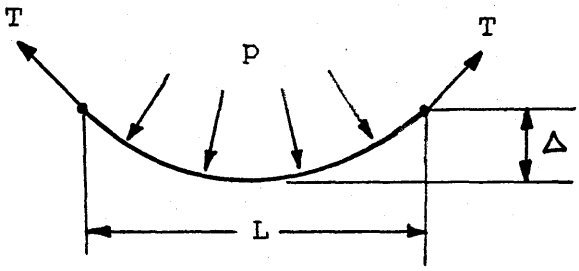

Fig.6a.

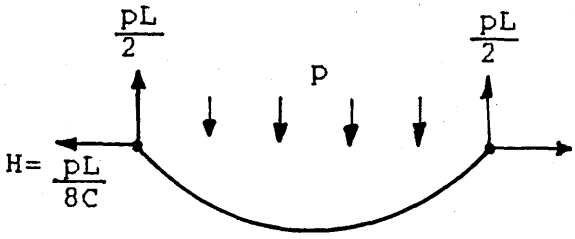

Fig.6b.

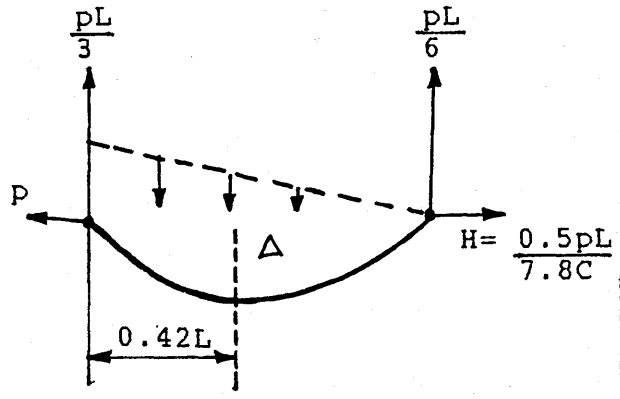

Fig.6c.

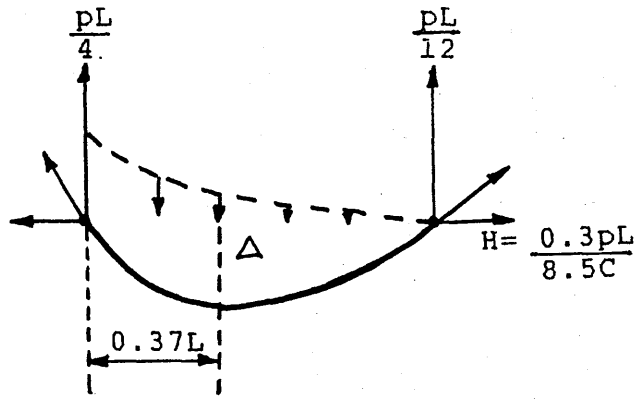

Fig.6d.

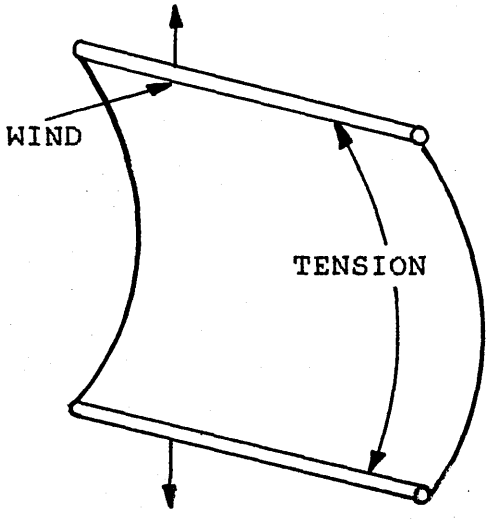

Fig.6e.

Fig.6f.

Fig.6a-6f Basic sail shape analysis.

SAIL FORCES ANALYSIS

For simplicity a uniform pressure p is assumed to be acting on the sail. If the sail is originally flat, flow or camber will be developed in the sail.

It can be seen from simple geometry (Fig.7) of the sail that this kind of action will impart equal camber C to each leech wise strip. From Fig.7, the load on a typical strip of length L and unit width equals pL and the tension along the strip is pL/8c.

These strip forces acting on the spar have been resolved along and at right angles to it as shown.

The air loading is approximately normal to the plane of the sail and is made up of the:

1) total sail force =P,

2) reaction forces on the mast and boom =P/2.

A major detailed analysis will modify the results obtained in two ways:

a) the actual pressure being high at the luff and zero at the leech which will cause the centre of force to shift towards the luff (the original assumption being that the pressure distribution was uniform).

b) flow built into the sail to reduce the camber at the leech will shift the forces towards the leech.

The effects of the modifications tend to cancel one another out and the above approximation is not altered.

A calculation can be made using a pressure pattern which is more realistic, i.e. greatest value p_o at the tack

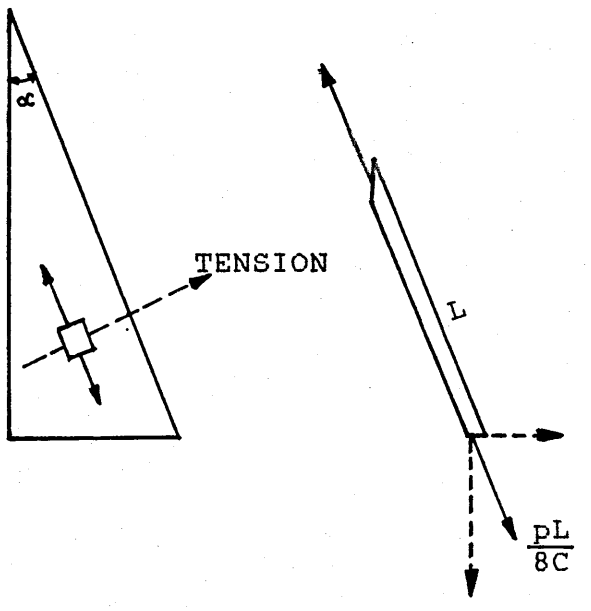

Fig.7a.

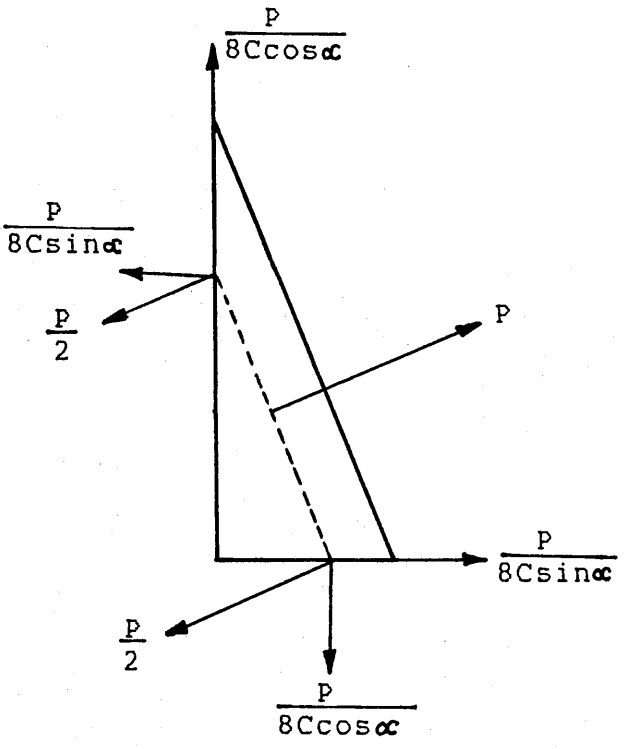

Fig.7b.

Fig.7c.

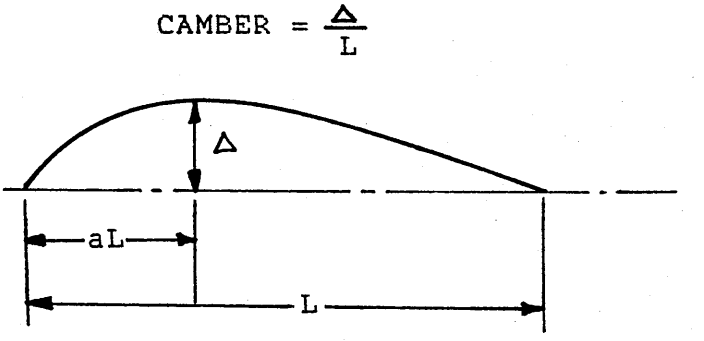

Fig.7d.

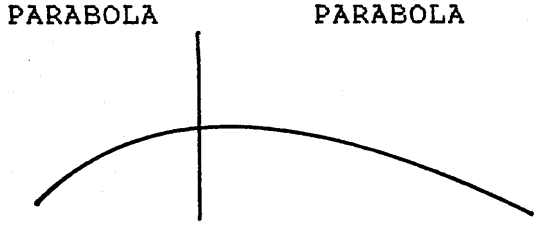

Fig.7e.

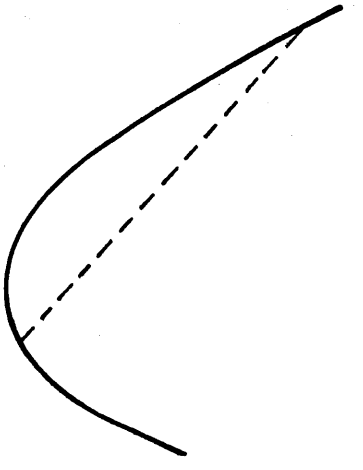

Fig.7f.

Fig.7a-7f Sail forces analysis.

falling to zero at the head (front) and the clew (corner), i.e the pressure distribution (20) is given by,

$$p(x) = p_o \left(1 - \frac{X}{B} - \frac{Y}{4}\right)$$

THE IMPORTANCE OF CAMBER

There are two requirements (20):

a) the curve must have good aerodynamic characteristics _ the desirable characteristic is a high LIFT to DRAG ratio, which ensures that the maximum camber occurs well forward on the sail.

b) the sail must set in the curve chosen and it will probably set more readily if the maximum camber is well back.

The main variables defining a camber line are the maximum camber Δ/L, and the point along the chord at which it occurs, aL from the luff. A smooth curve is required for the line itself as shown in Fig.8 below.

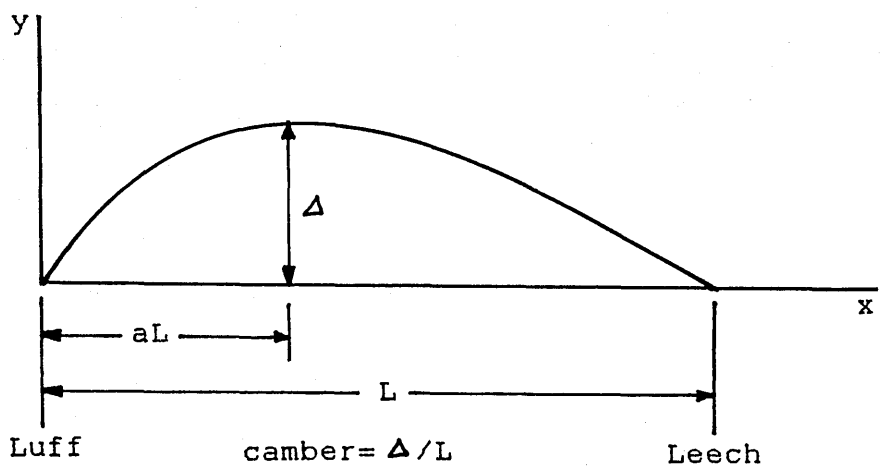

FIG.8

A compromise must be made between the above two requirements, and a=0.33 is reasonable, with a camber of 10% (21).

An equation for the camber line (22) is

$$y = \frac{x(L-x)}{L\,a^2 L + (1-2a)\,x}$$

If a=0.5, this degenerates into a parabola. Values of a between 0.3 and 0.4 which occur in practice give curves close to parabolic arcs. At the extremes, a=0 and a=1 the curve becomes triangular.

PRESSURE DISTRIBUTION AROUND A SAIL

If we consider the air flow round a sail (see Fig.9a), then the air stream divides into two parts, that traversing the leeward side and that on the weather side. From Fig.9a, the flow on the lee side is constricted from a section S to the section Sa. The wind speed V_L, in this region must therefore be greater than the free stream wind speed V. According to Bernouilli's equation, an increase in speed must therefore have a corresponding decrease in the static pressure P_L on the lee side. The greatest changes in speed, and hence suction, occur near the luff of the sail. By a similar analysis for the weather side, the local wind speed V_W falls, and the static pressure P_W, rises as the kinetic energy of the air is converted.

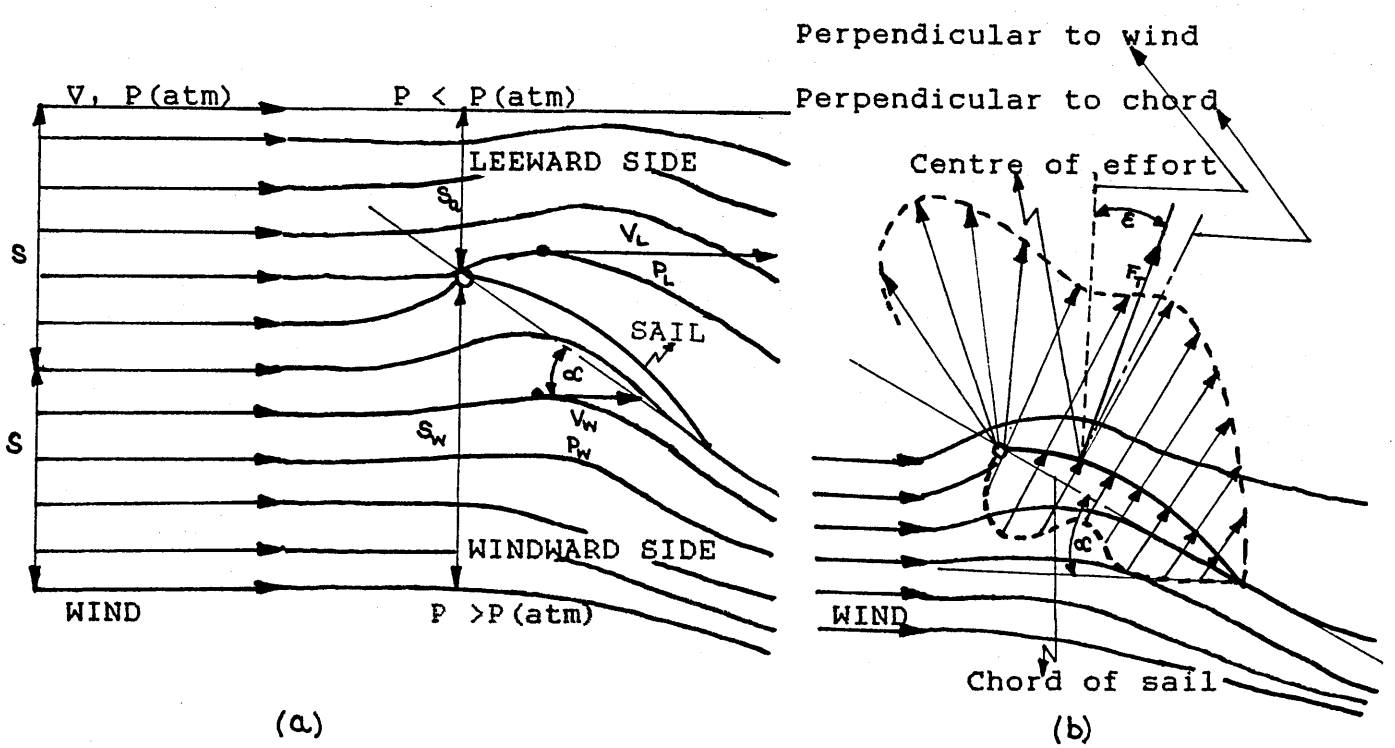

Fig.(9) Pressure distribution on sail.

Thus, on the windward side, the pressure is greater than the atmospheric, and on the lee side it is less than atmospheric. This gives rise to a single resultant force F_t acting at right angles to the sail, passing through the centre of effort of the sail.

The efficiency with which a sail produces a driving force depends to a large extent on two factors:
1) the sail profile, which is largely determined by its cut,
2) the possition of the sail relative to the wind direction (i.e. sail angle).

Certain features of the pressure distribution on a sail are noteworthy and provide some explanation of lift and drag characteristics. Thus, if leeward side pressures, as given by curve A (Fig.10b), are concentrated far aft, they will tend to give large drag.

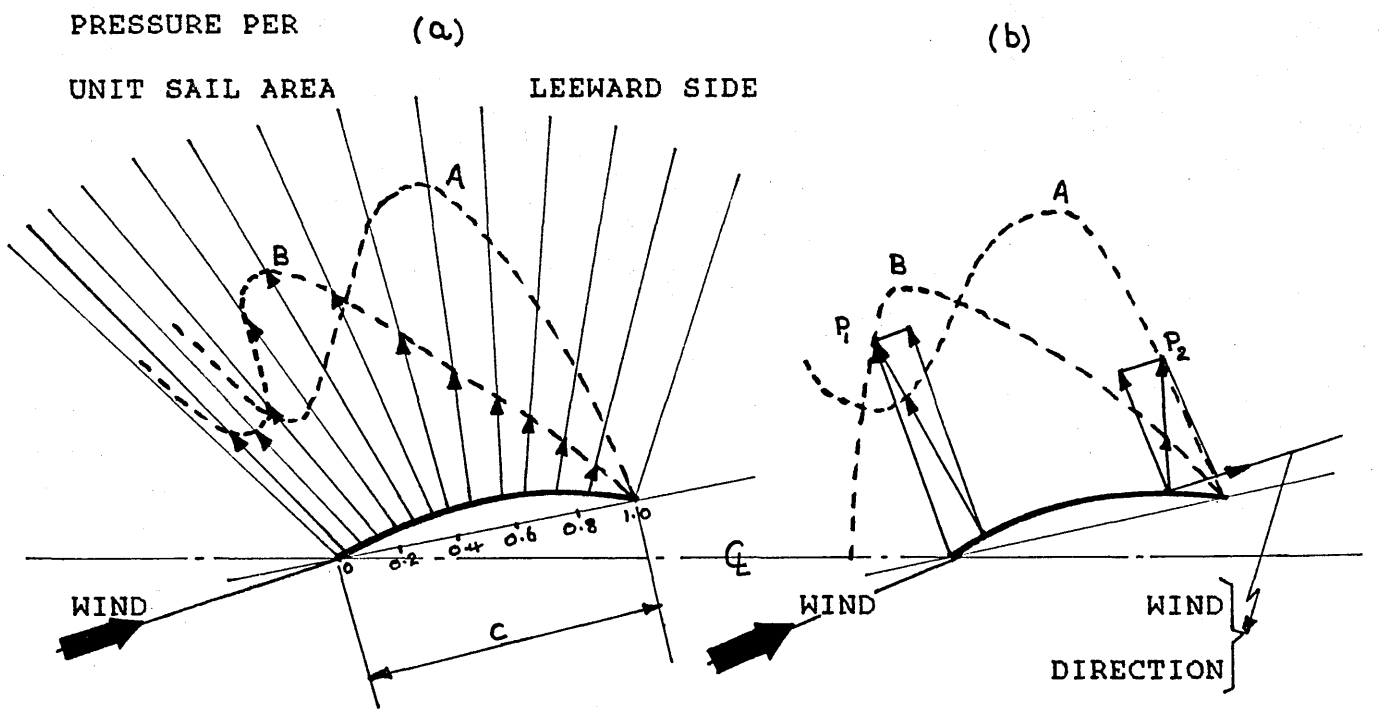

Fig.(10) Effect of pressure distribution on resulting sail forces.

The two pressure force vectors P_1 , and P_2 , acting normal to the sail curvatures, illustrate the point. These vectors resolved into two components along and across the wind direction, show that the greatest contribution to the driving force comes from the forepart of the sail by virtue of both the magnitude and direction of the pressure force P_1 . The high pressure P_2 near the leech gives no driving force component but mostly drag. The same reasoning applies to pressure developed on the windward side.

So far as the interaction between the forces, pressure and the shape of the sail is concerned, a greater understanding is required of the flow pattern, particularly close to the leading edge, and how the shape of a sail adopts at various wind strengths. For both experimental and theoretical considerations it may infer that by its very nature, the flexible sail adjusts to some extent its shape so as to maintain an attached flow at its leading edge.

To obtain a complete picture of the pressure distribution over the whole sail Fig.11 shows the pressure distribution on a Bermudian sail (Ref.23). The results are plotted in the form of contours, lines joining points of equal pressure.The contour lines follow a regular pattern in the middle of the sail, but near the head and the boom they have certain irregularities indicating flow changes at the extremes of the sail.By comparing the pressure and suction fields from the two cases, it can be seen that the resultant force on sail "a" will be greater than that on "b".

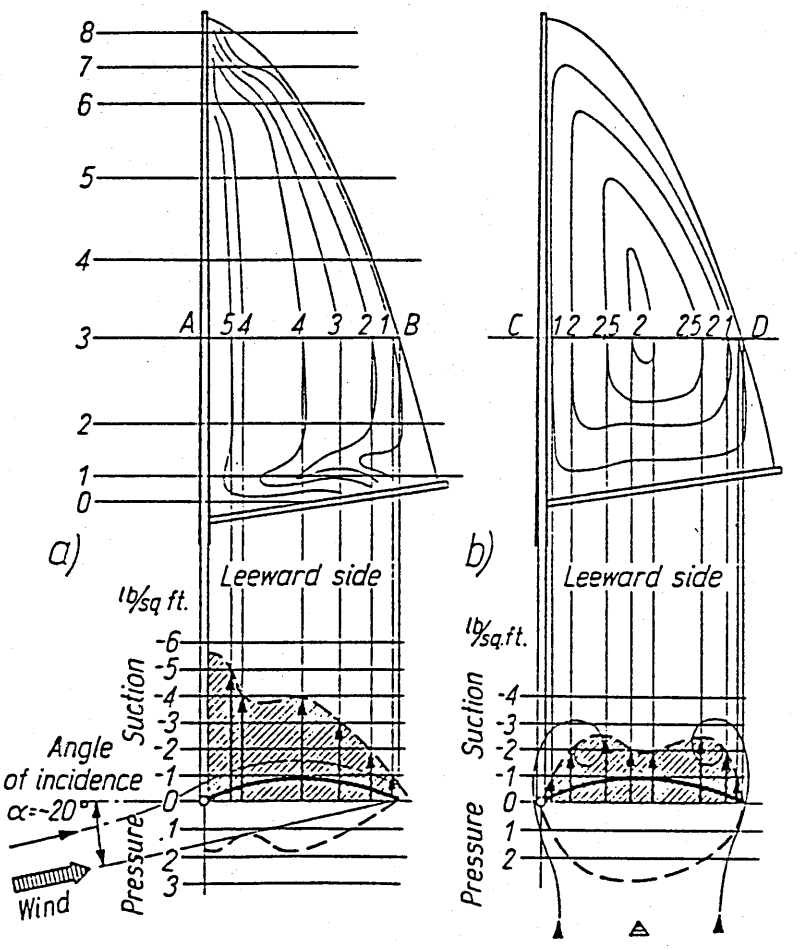

Fig.11 Pressure distribution on a Bermudian sail.
(contour representation, Ref.23)

CHAPTER THREE

WIND-POWER THEORY

WIND ENERGY

Wind is air set in motion by the uneven heating of the Earth by the Sun. The air mass is of low density, and when this mass has velocity, the wind has kinetic energy. The wind's kinetic energy per unit volume of air, flowing at velocity U, may be expressed by the formula:

$$K.E = 1/2\, \varrho\, U^2 \qquad (16)$$

WIND POWER

If we consider a cylinder of cross sectional area A (see Fig.12) through which air flows perpendicularly with a volumetric flow rate $\dot{V}$, then the steady state power developed is the product of kinetic energy, area and volumetric flow rate, i.e.

$$P = 1/2\, \varrho\, U^2 A\, \dot{V} \qquad (17)$$

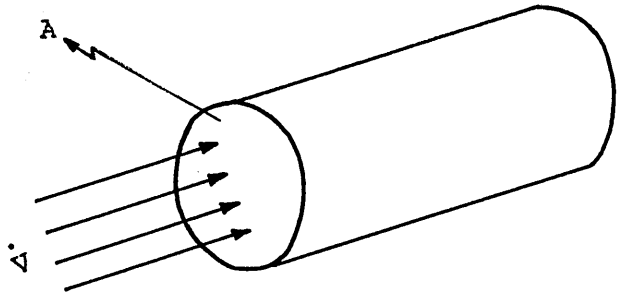

Fig.12 Flow rate through a cylinder of cross-sectional area A.

Substituting the values $A = \pi R^2$ and $\dot{V} = U A$ into equation (17), we get:

$$P = 1/2 \, \rho U^3 \pi R^2 \qquad (18)$$

The power transfered by the windwheel is given by:

$$P = T\omega \qquad (19)$$

where T is the torque and ω the angular velocity.

From equation (18), we can deduce that:

1. The wind power increases as the cube of the wind speed (i.e the power increases eightfold if the wind speed doubles).

2. The power is proportional to the area $A = \pi R^2$ (i.e. the area swept by the blades and thus to R^2).

3. The power is proportional to the density ρ of the air (this factor cannot be influenced and varies slightly with the height and temperature). For 15°C at sea level, $\rho = 1.225$ Kg/m^3.

AXIAL-MOMENTUM THEORY

The first description of the axial momentum theory was given by Rankine in 1865 and was improved later by Froude. The theory provides a relationship between the forces acting on a rotor and the resulting fluid velocities and predicts the ideal efficiency of a rotor. Later Betz included rotational wake effects in his theory. Recently Wilson, Lissaman and Walker (24) have further studied the aerodynamic performances of wind turbines, based on the analysis of Glauert (22).

The assumptions underlying the axial momentum theory are:

1. incompressible medium,
2. no frictional drag.
3. infinite number of blades,
4. homogeneous flow,
5. uniform thrust over the rotor area,
6. non-rotating wake,
7. static pressure far below and far behind the rotor is equal to the undisturbed ambient static press.

In Fig.13, the conservation dictates that

$$\rho A_1 V_1 = \rho A\ V(\text{axial}) = \rho A_2 V_2 \qquad (20)$$

The thrust force T on the rotor is given by the change in the momentum of the incoming flow compared with the outgoing flow.

$$T = \rho A_1 V_1^2 - \rho A_2 V_2^2 \qquad (21)$$

with eq.20 this becomes:

$$T = \rho A\ V(\text{axial})\ (V_1 - V_2) \qquad (22)$$

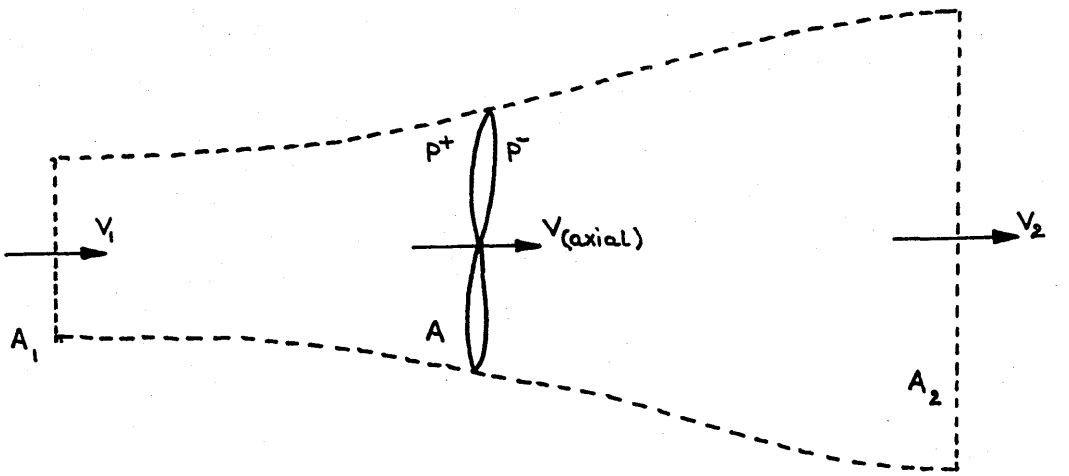

Fig.13 Schematic representation of stream-tube model.

The thrust on the rotor expressed as a result of the pressure difference over the rotor area is,

$$T = (P^+ + P^-)\ A \tag{23}$$

The pressures, using Bernouilli's equation are,

before the rotor:

$$P + 1/2\,\rho\,V_1^2 = P^+ + 1/2\,\rho\,V(\text{axial})^2$$

behind the rotor: (24)

$$P^- + 1/2\,\rho\,V(\text{axial})^2 = P + 1/2\,\rho\,V_2^2$$

This then yields:

$$P^+ - P^- = 1/2\,\rho\ (V_1^2 - V_2^2) \tag{25}$$

and the thrust becomes:

$$T = 1/2\,\rho\,A\ (V_1^2 - V_2^2) \tag{26}$$

Equating eq.26 and eq.22, we get

$$V(\text{axial}) = 1/2\ (V_1 + V_2) \tag{27}$$

Now introducing the axial interference factor a, gives:

$$V(\text{axial}) = V_1 \ (1 - a) \tag{28}$$

substituting into eq.27 gives:

$$V_2 = V_1 \ (1 - 2a) \tag{29}$$

The power given to the rotor is equal to the change in kinetic power of the mass flowing through the rotor area.

$$P = 1/2 \, \rho \, A \, V(\text{axial}) \ (V_1^2 - V_2^2) \tag{30}$$

with eq.28 and eq.29, the expression for power becomes:

$$P = 4a \ (1 - a)^2 \ 1/2 \, \rho \, A \, V_1^3 \tag{31}$$

The maximum value of P is reached when $dP/da = 0$, and this occurs when $a = 1/3$.

Substituting $a = 1/3$ into eq.31, gives:

$$P = \frac{16}{27} \cdot \frac{1}{2} \, \rho \, A \, V_1^3 \tag{32}$$

The factor 16/27 is often called the Betz coefficient (1926) and represents the maximum fraction with which an ideal rotor, under given conditions, can extract energy from the air flow. This fraction is related to the power of an undisturbed flow through area $A_1 = A \ (1 - a)$.

EFFECT OF WAKE ROTATION

The ideal model of a completely axial flow before and behind the rotor has to be modified when realising that a rotating rotor implies the generation of angular momentum (torque). Slow-running wind-rotors (with a low tip-to-wind speed ratio and a low torque) experience more wake rotation losses than the high tip speed machines with low torque (25).

This is analysed by assuming the angular stream model of Fig.14 with a ring of radius r and a thickness dr, the cross-sectional area of the annular tube becomes $2\pi r dr$. Now the relative angular-velocity increases from Ω to $\Omega + \omega$, while the axial components of the velocity remains unchanged.

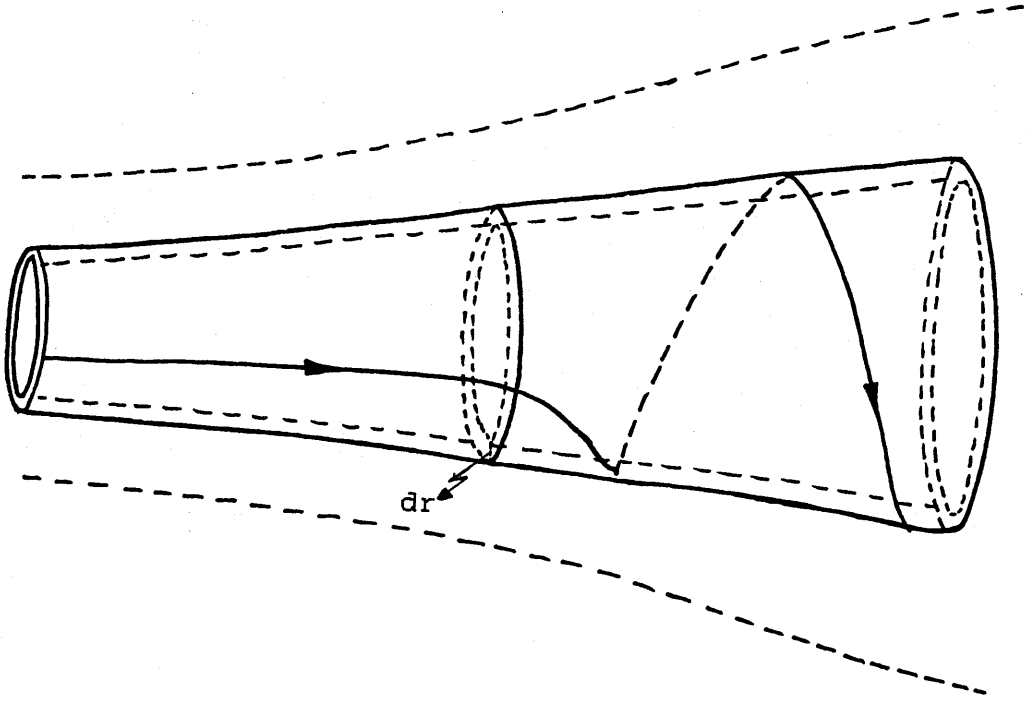

Fig.14 The stream-tube model, illustrating the rotation of the wake.

Hence, applying Bernouilli's equation across the blades, we get:

$$p^+ - p^- = \frac{1}{2}\rho\,(\Omega + \omega_1)^2\, r^2 - \frac{1}{2}\rho\,\Omega^2\, r^2$$

or

$$p^+ - p^- = \rho\,(\Omega + \frac{1}{2}\omega_1)\,\omega_1\, r^2 \qquad (33)$$

The resulting thrust on the annular element of the rotor is:

$$dT = \rho\,(\Omega + \frac{1}{2}\omega_1)\,\omega_1 r^2\; 2\pi r dr \qquad (34)$$

By introducing the tangential interference factor a', where a' is:

$$a' = (\frac{1}{2}\omega_1)/\Omega \qquad (35)$$

hence eq.34 becomes:

$$dT = 4a'\,(1 - a')\,\frac{1}{2}\rho\,\Omega^2\; 2\pi r dr\; r^2 \qquad (36)$$

Now in eq.26, introducing a' and looking at an annular cross section, where $A = 2\pi r dr$ and $V_1 = V$, then

$$dT = 4a\,(1 - a)\,\frac{1}{2}\rho\, V^2\; 2\pi r dr \qquad (37)$$

Equating (36) and (37) we get:

$$\frac{a\,(1 - a)}{a'\,(1 + a')} = \frac{\Omega^2 r^2}{V^2} = \lambda_r^2 \qquad (38)$$

Now the torque exerted is:

$$dQ = \rho\, V(\text{axial})\; 2\pi r dr \;.\; \omega r \;.\; r \qquad (39)$$

The term $V(\text{axial})\; 2\pi r dr$ is the mass flow. Introducing the axial and tangential interference factors into eq.39, we get:

$$dQ = 4a'\,(1 - a)\,\frac{1}{2}\,\rho\, V\,\Omega\, r \;.\; r\; 2\pi r dr \qquad (40)$$

The power generated is $dP = \Omega\, dQ$, so the total power is equal to,

$$P = \int_0^R \Omega\, dQ$$

Introducing the local speed ratio

$$\lambda_r = \frac{\Omega\ r}{V} \tag{41}$$

The power becomes,

$$P = \frac{1}{2} A V^3 \cdot \frac{8}{\lambda^2} \int_0^\lambda a' (1 - a) \lambda_r^3\, d\lambda_r \tag{42}$$

or the power coefficient Cp is equal to

$$Cp = \frac{8}{\lambda^2} \int_0^\lambda a' (1 - a) \lambda_r^3\, d\lambda_r \tag{43}$$

The maximum value of $a'(1 - a)$ can be found by using relation (38) to express a' in terms of a (22), i.e.

$$a' = -\frac{1}{2} + \frac{1}{2} \sqrt{(1 + 4a (1 - a))} \tag{44}$$

Substituting this expression in $a'(1 - a)$ and putting the first derivative equal to zero yields

$$\lambda_r^2 = \frac{(1 - a)\ (4a - 1)}{(1 - 3a)} \tag{45}$$

and

$$a' = \frac{(1 - 3a)}{(4a - 1)} \tag{46}$$

Via numerical integration, values of maximum power coefficient Cp as a function of λ using eq.43 can be calculated. The results are shown below of the maximum power coefficient to be extracted by Ideal Wind Rotor at a given tip speed ratio.

λ	0	0.5	1.0	1.5	2.0	2.5	5.0	7.5	10.0	∞
Cp max	0	0.3	0.42	0.48	0.5	0.57	0.58	0.582	0.585	$\frac{16}{27}$

BLADE-ELEMENT THEORY

The momentum theory described in this section does not on its own provide the necessary information concerning

1. blade chords and angles,
2. influence of friction,
3. influence of number of blades.

However the blade-element theory combined with the momentum theory does provide this information.

The assumptions underlying the blade-element theory are

1. there is no interference between the airflows over adjacent blade elements along each blade; and
2. the forces acting on a blade element are solely due to the lift and drag characteristics of the sectional profile of a blade element.

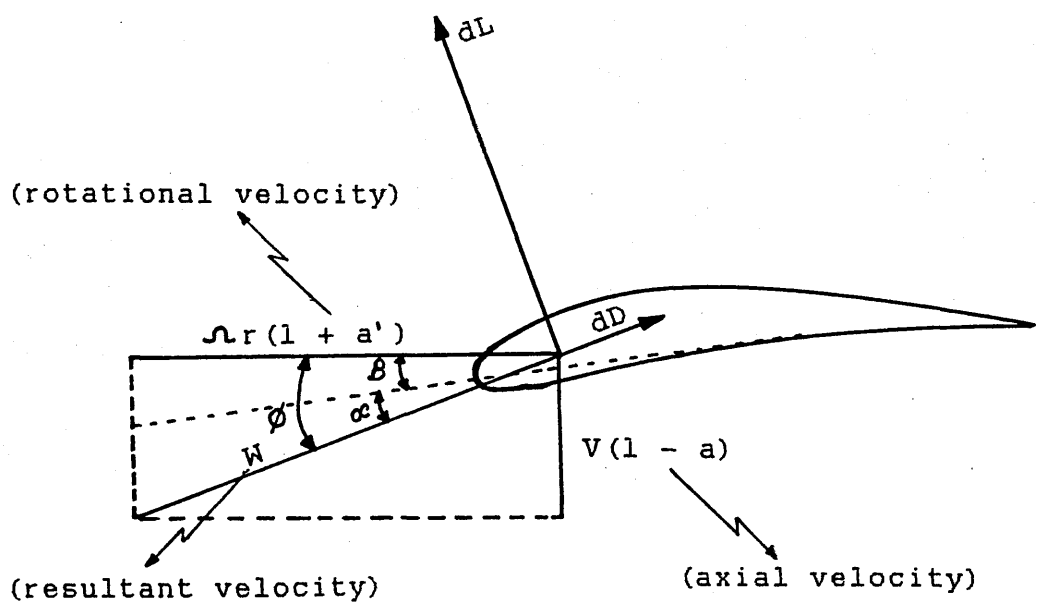

Fig.15 Forces on a blade element.

If we consider a blade element of a horizontal axis rotor, see Fig.15, then the sectional lift and drag are:

$$\left.\begin{aligned} dL &= \frac{1}{2}\,\rho\, C_L\, c\, w^2\, dr \\ dD &= \frac{1}{2}\,\rho\, C_d\, c\, w^2\, dr \end{aligned}\right\} \qquad (47)$$

where c and w are chord of the sail and the relative wind speed respectively.

The thrust and torque experienced by the blade element are

$$dT = dL \cos \phi + dD \sin \phi \qquad (48)$$

$$dQ = (dL \sin \phi - dD \cos \phi).r \qquad (49)$$

Substituting from (47) into (48) and (49), and assuming that the rotor has B number of blades, then:

$$dT = \frac{1}{2}\, B\, \rho\, w^2 (C_L \cos \phi + C_d \sin \phi)\, c\, dr \qquad (50)$$

$$dQ = \frac{1}{2}\, B\, \rho\, w^2 (C_L \sin \phi - C_d \cos \phi)\, c\, r\, dr \qquad (51)$$

COMBINATION OF MOMENTUM THEORY AND BLADE ELEMENT THEORY

From the momentum theory (22), the expression for torque and thrust are,

$$dT = 4a\ (1 - a)\ \frac{1}{2}\ \rho V^2\ 2\pi r dr \qquad (37)$$

$$dT = 4a'\ (1 + a')\ \frac{1}{2}\ \rho \Omega^2 r^2\ 2\pi r dr \qquad (36)$$

$$dQ = 4a'\ (1 - a)\ \frac{1}{2}\ \rho V \Omega r\ 2\pi r dr \qquad (40)$$

and from the blade element theory, the expression for torque and thrust are given by equations (50) and (51).

Now from the velocity diagram below, Fig.16,

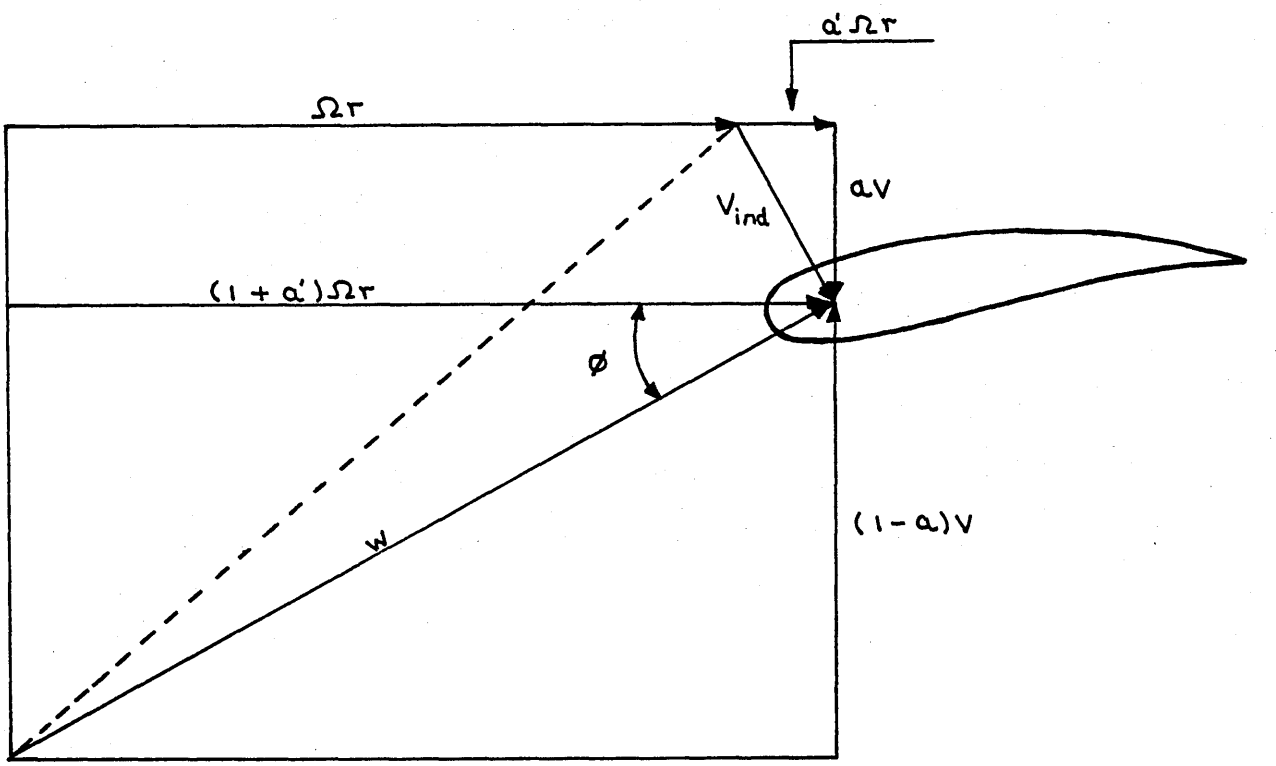

Fig.16 Velocity diagram.

$$W = \frac{(1 - a)V}{\sin \phi} = \frac{(1 + a')\Omega r}{\cos \phi} \tag{52}$$

and

$$\tan \phi = \frac{(1 - a)V}{(1 + a')\Omega r} = \frac{(1 - a)}{(1 + a')} \cdot \frac{1}{\lambda} \tag{53}$$

Introducing the local solidity ratio:

$$\sigma = Bc / 2\pi r \tag{54}$$

Then the results of the blade-element theory transforms into:

$$dT = (1 - a)^2 \frac{C_L \cos\phi}{\sin\phi} \left(1 + \frac{C_d \tan\phi}{C_L}\right) \frac{1}{2} \rho V^2 2\pi r dr \tag{55}$$

$$dQ = (1 + a')^2 \frac{\sigma C_L \sin\phi}{\cos\phi} \left(1 - \frac{C_d}{C_L} \cdot \frac{1}{\tan\phi}\right) \frac{1}{2} \rho \Omega^2 r^2 r \, 2\pi r dr \tag{56}$$

Combining equations (55) and (36) gives:

$$\frac{4a}{(1 - a)} = \sigma \frac{C_L \cos\phi}{\sin^2 \phi} \left(1 + \frac{C_d \tan\phi}{C_L}\right) \tag{57}$$

whereas (56), (40) and (53) gives:

$$\frac{4a'}{(1 + a')} = \sigma \frac{C_L}{\cos\phi} \left(1 - \frac{C_d}{C_L \tan\phi}\right) \tag{58}$$

It is argued by some authors (26, 27, 28) that the drag terms should be omitted from equations (57) and (58) because the profile drag does not induce velocities at the blade itself within the approximations of small blade chords. Using this argument, then equations (57) and (58) become:

$$\frac{4a}{(1 - a)} = \sigma \frac{C_L \cos\phi}{\sin^2 \phi} \tag{59}$$

$$\frac{4a'}{(1 + a')} = \sigma \frac{C_L}{\cos\phi} \tag{60}$$

These two relationships and the two expressions for dT and dQ, (55) and (56) determine the behaviour of the wind rotor.

TIP LOSSES

This theory has been developed by assuming that the wind turbine has a finite number of blades. In such a case then, the lift is generated by the pressure distribution around the blade due to the two-dimensional flow of air. On the upper side, the pressure is below the ambient static pressure and on the lower side it is above the ambient static pressure. At the tip, however, this pressure difference leads to secondary flow around the tip and hence the flow becomes three-dimensional, thus reducing the lift. This effect is more pronounced as one approaches the tip. It results in a reduction of the torque on the rotor and so reduces the power output.

The Prandtl model (26) is presented here, although other theories do exist. To calculate the tip losses, Prandtl explained that the velocities in the rotor plane, as seen by the blade are altered by the distributed flow near the tip.

A tip-loss factor F was developed by Prandtl, as given by:

$$F = \frac{2}{\pi} \arccos \left\{ \exp \frac{(-1B(R - r))}{(2\ (r \sin\phi))} \right\} \qquad (61)$$

The effect of the tip-loss factor is that it modifies the axial and tangential velocities in the rotor plane. It is assumed that these corrections only involve the momentum formulae.

Equation (37) becomes:

$$dT = 4aF\ (1 - aF)\ \frac{1}{2} \rho V^2 \pi r dr \qquad (62)$$

and equation (40) becomes:

$$dQ = 4a' F (1 - aF) \frac{1}{2} \rho V \Omega r \; r \; 2\pi r dr \tag{63}$$

The results of the blade-element theory remain unchanged and hence by substituting equation (53) into (55) and (56), we get:

$$dT = (1 - a)^2 \frac{\sigma C_L \cos\phi}{\sin^2\phi} (1 + \frac{C_d}{C_L} \tan\phi) \frac{1}{2} \rho V^2 2\pi r dr \tag{64}$$

$$dQ = (1 - a)^2 \frac{\sigma C_L}{\sin\phi} (1 - \frac{C_d}{C_L} \cdot \frac{1}{\tan\phi}) \frac{1}{2} \rho V^2 r \; 2\pi r dr \tag{65}$$

Hence equating (65) and (56), we get:

$$4a' F (1 - aF) = (1 - a)^2 \frac{\sigma C_L}{\sin\phi} (1 - \frac{C_d}{C_L} \cdot \frac{1}{\tan\phi}) \tag{66}$$

and equating (64) and (55), we get:

$$4aF (1 - aF) = (1 - a)^2 \frac{\sigma C_L \cos\phi}{\sin^2\phi} (1 + \frac{C_d}{C_L} \tan\phi) \tag{67}$$

Equating (66) and (67) together with

$$\tan\phi = \frac{(1 - a)}{(1 + a')} \cdot \frac{1}{\lambda_r} \tag{68}$$

and $$\alpha = \phi - \beta \tag{69}$$

and equation (61) describe the behaviour of the rotor.

Assuming that the following data are available for the rotor,

1. radius, R
2. setting angle, $\beta(r)$
3. chords, $c(r) \longrightarrow \sigma(r)$
4. tip-speed ratio, λ
5. number of blades, B
6. profile characteristics, $C_L(\alpha)$ and $C_d(\alpha)$.

Then the procedure to solve the equations are,

a) choose a value for r from $\lambda_r = r\frac{\lambda}{R}$

b) estimate a and a' (e.g a = 1/3 and a' = 0 for starting values)

c) calculate ϕ (via equation 69)

d) calculate $C_L(\alpha)$ and $C_d(\alpha)$ from graph or table of aerofoil profile.

e) calculate a (via equation 67)

f) calculate a' (via equation 66)

g) compare values of a and a' from (b) and iterate until the desired accuracy is attained.

h) calculate the values of C_d, dQ/dr and dT/dr or directly the values of dC_q/dr and dC_t/dr.

This then enables us to find the values of Ct (thrust coefficient) , Cq (torque coefficient) and hence Cp (power coefficient) for a number of positions r along the blade. The total values are found by numerical integration procedures.

THIN AEROFOIL THEORY

Velocity and pressure perturbations

If the local velocity vector at a point in the flow differs from the velocity U at ∞ by u in the x-direction, and v in the y-direction (see Fig.17), then u and v are the velocity perturbations in the x and y-directions respectively. If the local static-pressure differs from the static pressure p at ∞ by Δp, then Δp is the pressure perturbation.

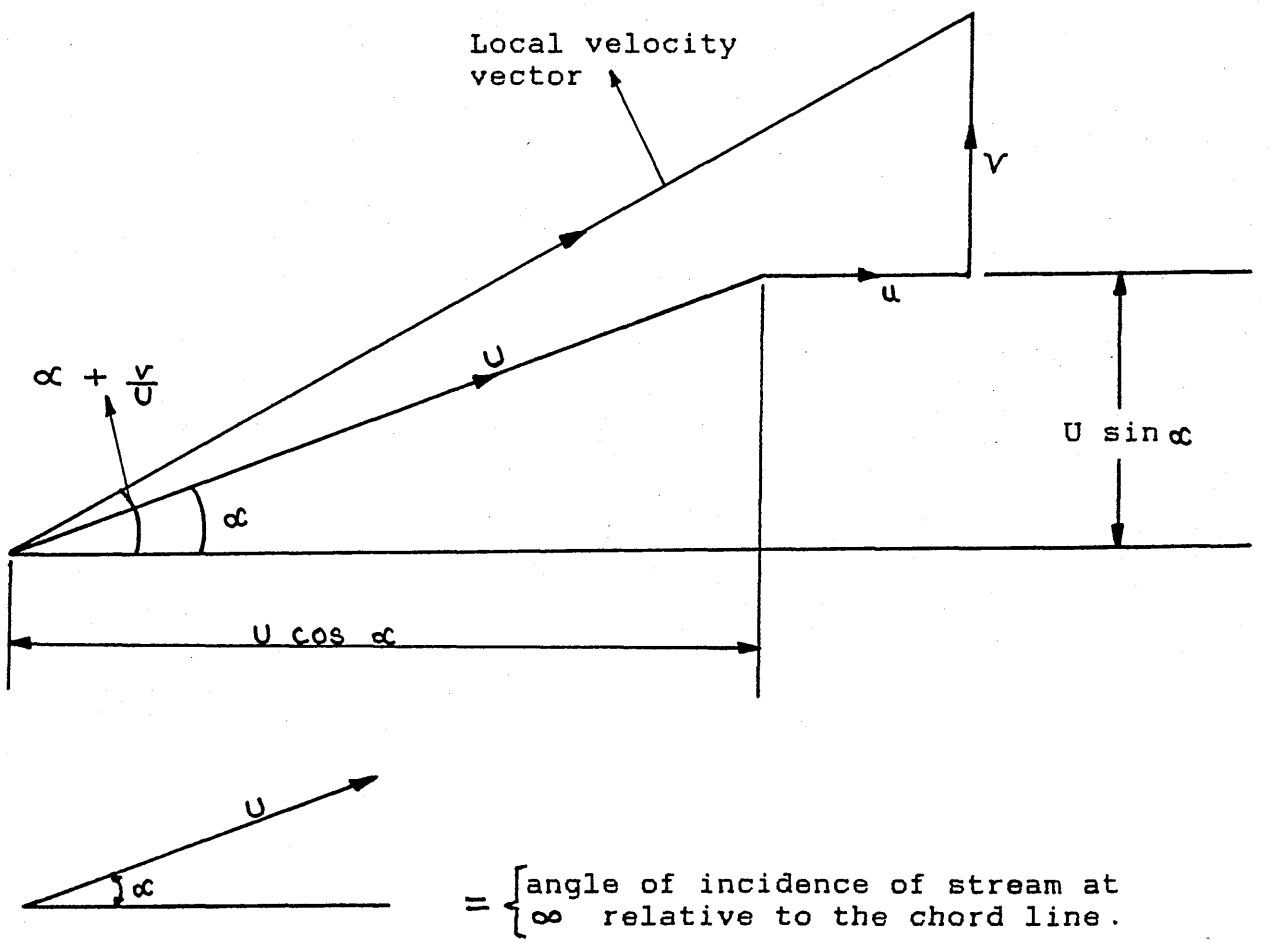

Fig.17 Velocity representation.

If the angle of incidence and the camber are both assumed to be small, then u/U and v/U << 1, and also the inclination of the local velocity vector to U can be taken to be v/U nearly enough; then a corresponding approximation to Δp is obtained from Bernouilli s equation:

$$p + \frac{1}{2}\rho U^2 \approx (p + \Delta p) + \frac{1}{2}\rho\left(\overline{U\cos\alpha + u^2} + \overline{U\sin\alpha + v^2}\right)$$

$$0 \approx \Delta p + \frac{1}{2}\rho(2Uu\cos\alpha + u^2 + 2Uv\sin\alpha + v^2)$$

$$\Delta p \approx -\rho Uu \qquad (70)$$

The pressure coefficient Cp at any point, defined as $\frac{\Delta p}{1/2\,\rho U^2}$, is

$$Cp \approx -\frac{2u}{U} \qquad (71)$$

Representation of incidence and camber

Because the thickness of an aerofoil plays an insignificant part in the generation of lift (29), its shape may be simplified by reducing its thickness to zero so that it is represented simply by its camber line. The leading edge and trailing edge can be taken to be on the x-axis at x=0 and x=1 respectively (see Fig.18).

A vortex sheet with strength $\gamma = f(x)$, $0<x<1$ is located theoretically along the chord line (with $\gamma \longrightarrow 0$ at the trailing edge, so that the Kutta-Joukowski condition (22) can be satisfied).

The aim is to determine the distribution $\gamma(x)$ by requiring that the angle $(\alpha + \frac{v}{U})$ at y=0, $0<x<1$ (see Fig.17), between the flow direction and the chord line, be everywhere equal to the inclination of the camber line to the chord line.

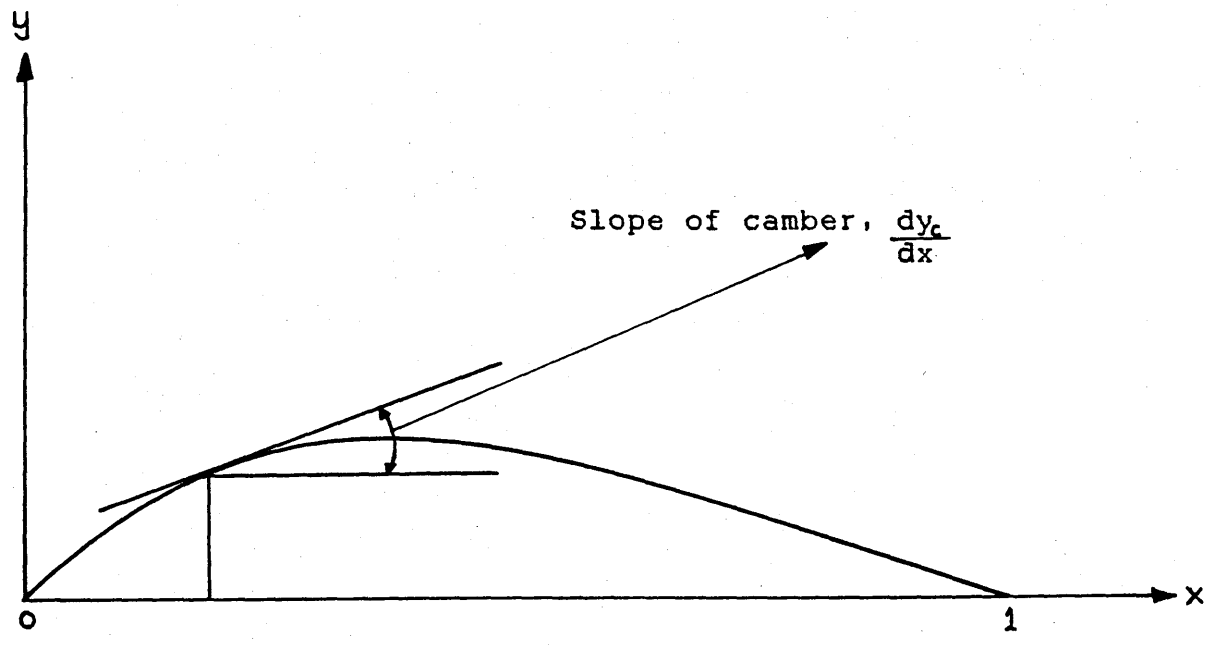

Fig.18 Aerofoil of zero thickness represented here by its camberline.

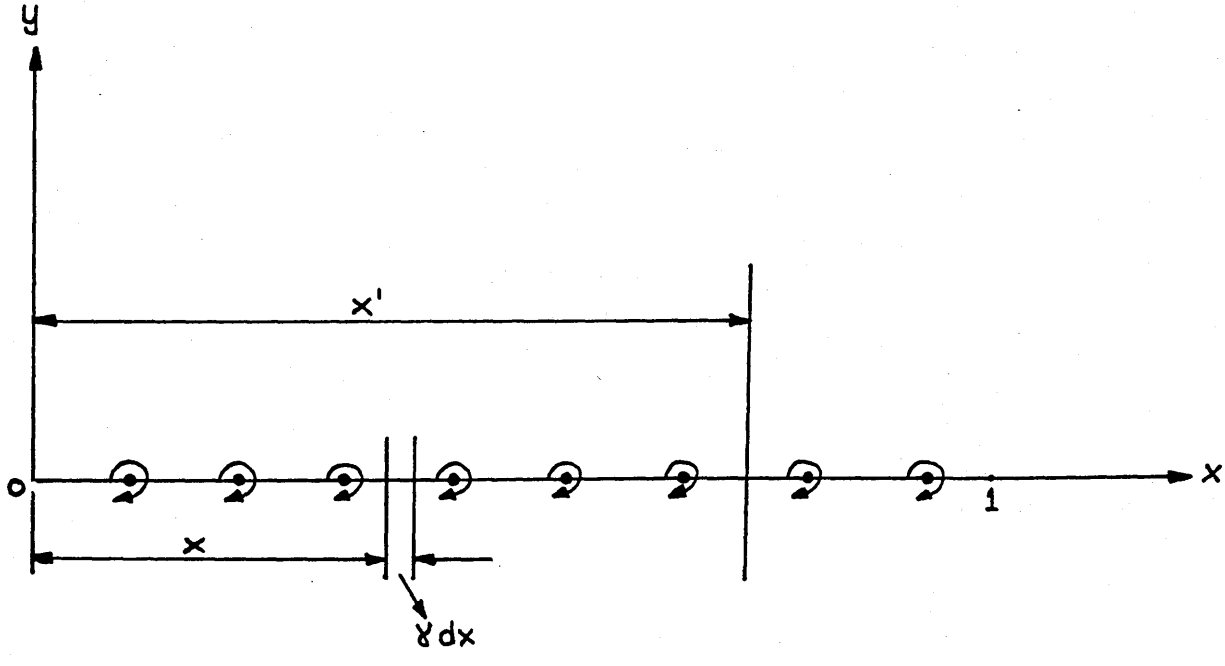

Fig.19 Representation of vortex sheet along the chord line.

From Fig.19, dv at x' due to γdx at x is:

$$dv = -\frac{\gamma\, dx}{2\pi(x' - x)} \tag{72}$$

Total v at x' due to the whole vortex sheet,

$$v = -\int_0^1 \frac{\gamma\, dx}{2\pi(x' - x)} \tag{73}$$

From the above statement we therefore require:

$$\frac{dy_c}{dx} = \alpha + \frac{v}{U} \tag{74}$$

$$= \alpha - \int_0^1 \frac{\gamma\, dx}{2\pi U(x' - x)} \tag{75}$$

Introducing new variables θ and θ' such that

$$\left.\begin{aligned} x &= \frac{1}{2}(1 - \cos\theta) \\ x &= \frac{1}{2}(1 - \cos\theta') \end{aligned}\right\} \tag{76}$$

(θ and θ' vary from zero to π, as x and x' vary from zero to unity).

Substituting for x and x' from (76) into (75) gives:

$$\left(\frac{dy_c}{dx}\right)_{x'} - \alpha = \int_0^{\pi} \frac{\gamma \sin\theta\, d\theta}{2\pi U(\cos\theta' - \cos\theta)} \tag{77}$$

with $\frac{dy_c}{dx}$ and γ now functions of θ' and θ.

For a flat plate at an angle of incidence α, $\left(\frac{dy_c}{dx}\right)_{x'} = 0$ for all values of x' between zero and unity corresponding to $0 < \theta' < \pi$ equation (77) then simplifies to

$$\gamma = 2U\alpha\left(\frac{1 + \cos\theta}{\sin\theta}\right) = 2U\alpha \cot\frac{\theta}{2} \tag{78}$$

When incidence and camber are combined, then the variation

of γ along the chord is represented by a Fourier sine series in θ plus a term similar to equation (78).

$$\gamma = 2U \left\{ A_0 \frac{1 + \cos\theta}{\sin\theta} + \sum_1^\infty A_n \sin n\theta \right\} \tag{79}$$

Substituting for γ, from equation (79), into equation (77) gives:

$$\frac{dy_c}{dx} - \alpha = - A_0 + \frac{1}{2\pi i} \int_0^\pi \sum A_n \frac{\sin n\theta \sin\theta}{\cos\theta' - \cos\theta} \, d\theta$$

$$= - A_0 + \frac{1}{2\pi i} \int_0^\pi \sum A_n \frac{\cos \overline{n-1}\,\theta - \cos \overline{n+1}\,\theta}{\cos\theta' - \cos\theta} \, d\theta$$

Using Glauert's definite integral (22), then

$$\alpha - \frac{dy_c}{dx} = A_0 - \sum_1^\infty A_n \cos n\theta'$$

or

$$\frac{dy_c}{dx} = (\alpha - A_0) + \sum_1^\infty A_n \cos n\theta' \tag{80}$$

From which, when dy_c/dx is given as a function of x' and therefore of θ', $(\alpha - A_0)$ and A_1, A_2 etc can be obtained by standard Fourier analysis methods, i.e.

$$\left.\begin{aligned} \alpha - A_0 &= \frac{1}{\pi} \int_0^\pi \left(\frac{dy_c}{dx}\right) d\theta' \\ A_n &= \frac{2}{\pi} \int_0^\pi \left(\frac{dy_c}{dx}\right) \cos n\theta' \, d\theta' \end{aligned}\right\} \tag{81}$$

Hence the required distribution of $\gamma(x)$ as a function of θ and so of x can be determined.

Determination of Lift (per unit span).

$$L = \int_0^{\pi} \rho U \gamma \, dx \tag{82}$$

Substituting for γ from equation (79) into (82) gives:

$$L = \int_0^{\pi} \rho U . 2U \left(A_0 \frac{1 + \cos\theta}{\sin\theta} + \sum A_n \sin n\theta \right) \frac{1}{2} \sin\theta \, d\theta$$

$$= \rho U^2 \int_0^{\pi} \left[A_0 (1 + \cos\theta) + \sum A_n \sin n\theta \sin\theta \right] d\theta$$

$$= \rho U^2 \left(A_0 \pi + \frac{1}{2} A_1 \pi \right)$$

$$= \rho U^2 \pi \left(A_0 + \frac{1}{2} A_1 \right) \tag{83}$$

The lift coefficient C_L is then:

$$C_L = \frac{L}{1/2 \, \rho U^2} = \pi \, (2A_0 + A_1) \tag{84}$$

and from the A_0 term:

$$\frac{dC_L}{d\alpha} = 2\pi \tag{85}$$

Equation (85) is independent of the exact shape of the camber.

Pressure distribution

The pressure on lower surface exceeds pressure at ∞ by ρUu. Pressure on upper surface is less than pressure at ∞ by ρUu.

now $u = \pm \gamma/2$

$$p_L - p_u = \rho U \gamma \tag{86}$$

$$Cp_L - Cp_u = \frac{\rho U \gamma}{1/2 \, \rho U^2} = 2 \frac{\gamma}{U} \tag{87}$$

We note that the pressure difference becomes infinite at the leading edge where $\theta = 0$.

INCOMPRESSIBLE TWO-DIMENSIONAL FLEXIBLE SAIL THEORY

All the usual assumptions of linearized aerofoil theory are made, viz:- that the camber of the sail and angle of attack, α, are small. In the (x,z) plane the leading edge L (or luff) of the sail is taken at the origin, and the trailing edge T (or leach) at (c,0). The uniform stream has speed U and is inclined at the angle α to the x-axis. $\Psi(x)$ is the slope of the sail and $\gamma(x)$ the strength, per unit length, of the vortex sheet in z=0, $0 \leqslant x \leqslant c$, which according to linearized theory, represents the sail. ξ is used as an x-variable of integration. The notation is illustrated in Fig.20.

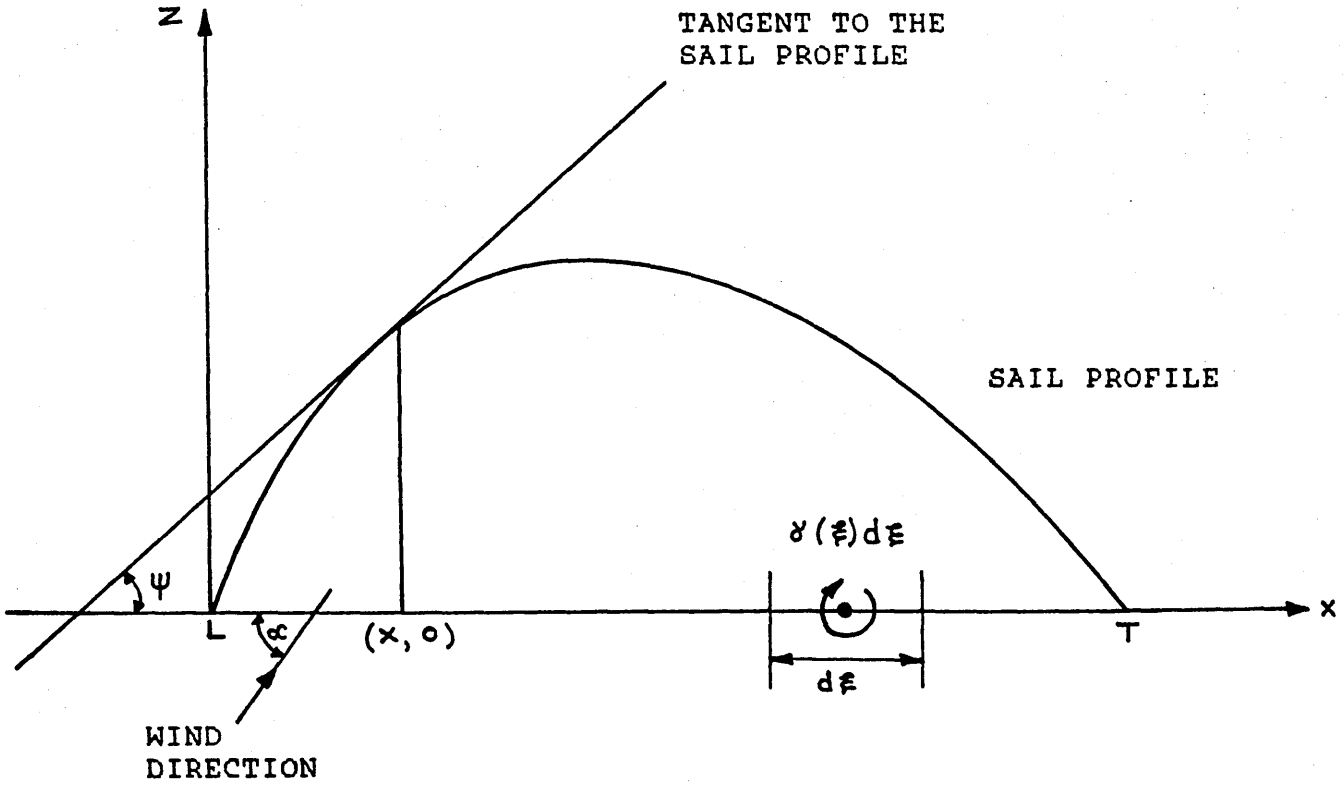

Fig.20 Sail co-ordinate system and notation.

If the density of the stream is ρ, the lift on the element dx is $\rho U \gamma(x) dx$ and so the pressure difference, Δp, between the lower and upper surfaces of the sail is related to the vortex strength by:

$$\Delta p = \rho U \gamma(x) \tag{88}$$

The through-flow due to the porosity of the sail may be taken to be proportional to Δp, and hence to $\gamma(x)$, and so the coefficient of porosity $\sigma(x)$ is defined in such a manner that the through-flow speed in the z-direction is $\sigma(x)\gamma(x)$. The inclination to the x-axis of the velocity at the sail is therefore $(\psi + \sigma\gamma/U)$ and this must equal the inclination induced by the combined stream and vortex sheet, namely:

$$\alpha + \frac{1}{2\pi i U} \int_0^c \frac{\gamma(\xi)\, d(\xi)}{\xi - x}$$

$$\therefore \quad \psi + \frac{\sigma(x)\gamma(x)}{U} = \alpha + \frac{1}{2\pi i U} \int_0^c \frac{\gamma(\xi)\, d(\xi)}{\xi - x}$$

Rearranging the above, we get:

$$-\frac{1}{\pi i} \int_0^c \frac{\gamma(\xi)\, d(\xi)}{\xi - x} = 2\left\{ U\alpha - U\psi(x) - \sigma(x)\gamma(x) \right\} \tag{89}$$

which is the aerodynamic equation connecting the shape of the sail and the distribution on it.

From Fig.21, we deduce the equations of static equilibrium. The tangential condition of equilibrium reduces, with neglect of viscous shearing forces, to $dT=0$, or

$$T = \text{constant} \tag{90}$$

T being the tension in the sail, while the normal condition

gives:

$$\Delta p \, dx = - T \, d\Psi$$

or from equation (88)

$$\rho U \gamma(x) = - T \frac{d\Psi}{dx} \tag{91}$$

Substituting from equation (91) into equation (89) gives:

$$\frac{1}{2\pi i} \cdot \frac{T}{\rho U^2} \int_0^c \frac{d\Psi/d\xi}{\xi - x} \, d\xi = \alpha + \Psi + \left[\frac{\sigma(x) T}{\rho U^2} \right] \frac{d\Psi}{dx} \tag{92}$$

This is the basic equation for a two-dimensional porous sail.

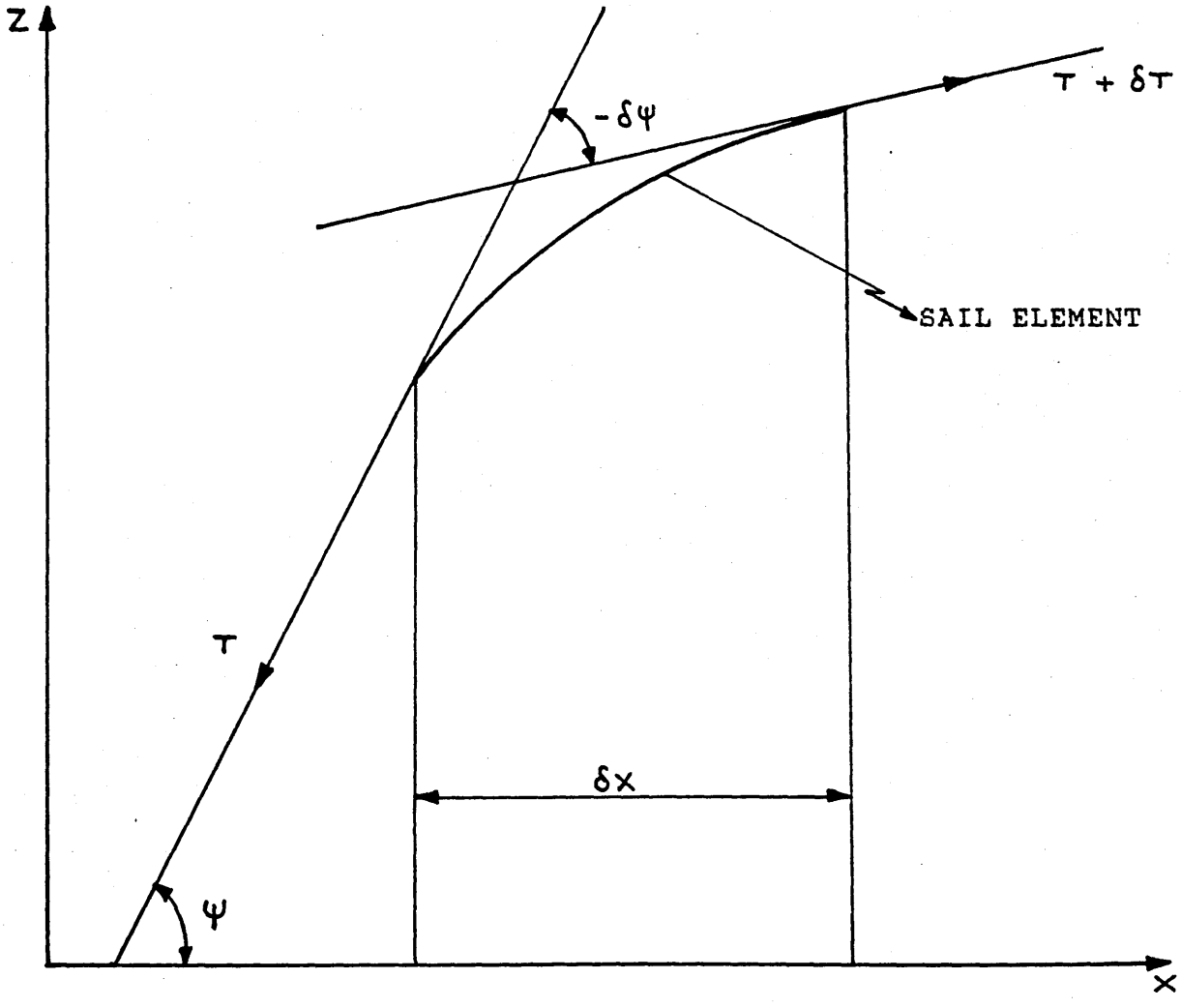

Fig.21 The tension distribution experienced by a sail element.

In order to avoid an infinite velocity at the trailing edge Joukowski (5) suggests that the circulation should be chosen so that the point (c,0), Fig.20, is a stagnation point. The flow past the aerofoil is then such that it leaves the trailing edge smoothly. For this to be true, then

$$\gamma(c) = 0 \tag{93}$$

The slope Ψ is also conditioned by the fact that L and T lie on the x-axis; thus

$$\int_0^c \Psi(x)\, dx = 0 \tag{94}$$

The problem of the two-dimensional sail then reduces to the solution of equation (92) subject to conditions (93) and (94). It is convenient to make the following transformations:

$$x = \frac{1}{2} c\ (1 - \cos\theta) \tag{95}$$

$$(0 \leqslant \theta,\ \phi \leqslant \pi)$$

$$= \frac{1}{2} c\ (1 - \cos\phi) \tag{96}$$

$$\gamma(x) = 4U\alpha\Delta(\theta)\ \mathrm{cosec}\theta \tag{97}$$

$$\Psi(x) = \alpha\mathcal{Y}(x) \tag{98}$$

$$\text{and}\quad 2\rho U^2 c/T = \lambda \tag{99}$$

Equation (92) then becomes:

$$-\frac{1}{\lambda}\frac{d\mathcal{Y}}{d\theta} = \left[1 - \frac{1}{\pi}\int_0^\pi \mathcal{Y}(\theta)\, d\theta\right] \cos^2\frac{1}{2}\theta - \frac{\sin^2\theta}{2\pi}\int_0^\pi \frac{\mathcal{Y}(\phi)\, d\phi}{\cos\theta - \cos\phi} \tag{100}$$

while the condition (94) is

$$\int_0^\pi \mathcal{Y}(\theta)\ \sin\theta\ d\theta = 0 \tag{101}$$

An integration of (100), with the constant chosen to satisfy (101), leads to

$$\psi(\theta)+\lambda\left\{-\frac{1}{2\pi i}\int_0^{\theta}\sin^2\theta\int_0^{\pi}\frac{\psi(\phi)\,d\phi}{\cos\theta-\cos\phi}\,d\theta+\frac{1}{4\pi i}\int_0^{\pi}\sin\theta\int_0^{\theta}\sin^2\theta\int_0^{\pi}\frac{\psi(\phi)\,d\phi}{\cos\theta-\cos\phi}\,d\theta d\theta\right\}$$

$$+\lambda\left(\frac{3\pi i}{8}-\frac{1}{2}\theta-\frac{1}{2}\sin\theta\right)\left[\frac{1}{\pi i}\int_0^{\pi}\psi(\theta)\,d\theta\right]=\lambda\left(\frac{3\pi i}{8}-\frac{1}{2}\theta-\frac{1}{2}\sin\theta\right) \qquad (102)$$

Equation (102) is called the sail equation.

When $\lambda=0$, i.e for a sail of infinitely large tension, equation (102) becomes $\psi(\theta)=0$ which gives a completely flat sail as is to be expected. From equation (99) as the tension T decreases, λ increases. Fig.1 (page 9) shows a complete variation of λ with lift coefficient C_L and angle of attack α.

Sail characteristics.

If the total length of the sail is $(c+\ell)$, then

$$c+\ell=\int_0^{c}\left[1+\left(\frac{dz}{dx}\right)^2\right]^{\frac{1}{2}}dx$$

which reduces, under the assumptions of linearized theory, to

$$c+\ell=\int_0^{c}\left[1+\frac{1}{2}\left(\psi(x)\right)^2\right]dx$$

or from (95) and (98), to

$$\frac{\ell}{c\alpha^2}=\frac{1}{4}\int_0^{\pi}\psi^2(\theta)\sin\theta\,d\theta \qquad (103)$$

The total lift L is given by:

$$L = \int_0^c \rho U \gamma(x)\, dx$$

Thus the lift coefficient defined as $C_L = \frac{L}{1/2\rho U^2 c}$ is found from equation (95), (97) and (99) as:

$$C_L = (4\alpha / \lambda)\left[\Psi(0) - \Psi(\Pi)\right] \tag{104}$$

From equations (88), (97), (98) and (99), for the pressure coefficient $C_p(x)$, defined by $C_p(x) = \frac{\Delta p}{1/2\rho U^2}$, it is found that:

$$\left(\frac{\lambda}{\alpha}\right) C_p(\theta) = -8 \operatorname{cosec}\theta \frac{d\Psi}{d\theta} \tag{105}$$

The fluid speeds on the two surfaces of the sail are $u = U \pm \frac{1}{2}\gamma(x)$, thus:

$$\frac{u}{U} = 1 \pm 2\left(\frac{\alpha}{\lambda}\right) \operatorname{cosec}\theta \frac{d\Psi}{d\theta} \tag{106}$$

while the ordinates of the sail are given by:

$$z = \int_0^x \Psi(x)\, dx$$

or

$$\frac{z}{c\alpha} = \frac{1}{2} \int_0^\theta \Psi(\theta) \sin\theta\, d\theta \tag{107}$$

APPLICATION OF THIS THEORY TO A FLEXIBLE-SAIL WIND-TURBINE

The theories described in this chapter raise some doubts about their direct application to wind turbines with flexible aerofoils. The axial momentum theory, for instance, makes a fundamental assumption that the aerofoil is rigid and that its shape is invariant with respect to the wind speed and the rotation of the wind turbine.

The behaviour of flexible sails are much more complicated to describe exactly, because each sail's shape will vary with the wind load imposed on it. The sails attached to the prototype wind turbine are considered to be infinitesimally-thin, inextensible and possibly porous. The sails are held rigidly at the leading edges, a distance c apart (i.e the chord). The edges are held by two finite length, rigid masts, which are assumed to be so thin as not to affect the air flow appreciably.

When a uniform wind blows onto the sail, at a particular angle of attack, to the plane of the masts, it causes the sail to fill up and so become taut. It thus takes up a shape determined by the wind's magnitude and direction, as well as by the flexibility of the material used. Hence at a specific sail loading, the wind turbine's sail shape is invariant with respect to time. The sail then behaves as a rigid aerofoil at that moment in time and so the theory outlined in this chapter is applicable to the system.

However, in order to evaluate the theory for rigid bladed aerofoil wind-turbines, the shape of the aerofoil and its lift and drag properties (with respect to the angle of

attack) need to be known for a given wind load. Thus there are two basic inter-related problems when this theory is applied to flexible aerofoil wind turbines, namely:

1) sail shape prediction at a particular time for a given wind speed; and

2) determination of the lift experienced by that shape of sail and hence the torque exerted upon the rotor at that instant of time.

The lift and drag characteristics of flexible sails vary tremendously with different sails, and Jansen and Smulder (26), have outlined some values of lift and drag coefficients applicable to flexible-aerofoil wind-turbines, (see Fig.22).

At present a generalised theory applicable to sail type wind-turbines is still in its infancy and no established theory applicable exactly to this type of system is available to predict the wind turbine's performance.

airfoil name	geometrical description	$(C_d/C_l)_{min}$	α°	C_l
sail and pole	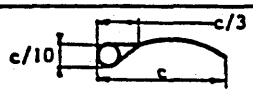	0.1	5	0.8
flat steel plate		0.1	4	0.4
arched steel plate				
	f/c=0.07	0.02	4	0.9
	f/c=0.1	0.02	3	1.25
arched steel plate with tube on concave side				
	f/c=0.07	0.05	5	0.9
	f/c=0.1	0.05	4	1.1
arched steel plate with tube on convex side	 f/c=0.1	0.2	14	1.25
sail wing	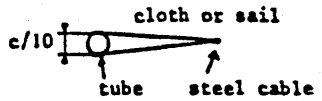	0.05	2	1.0
sail trouser f/c=0.1 d_{tube}=0.6f		0.1	4	1.0
NACA 4412	see appendix II	0.01	4	0.8
NACA 23015	see Lit(1) in appendix I	0.01	4	0.8

Fig.22 Design values for some flexible aerofoils (ref.73).

CHAPTER FOUR

THE PROTOTYPE WIND TURBINE

SAIL DESIGN

The sail configuration usually associated with horizontal-axis wind-rotors, run radially from hub to circumference. In order to provide maximum torque, the sails in this study were designed with emphasis on maximum sail area towards the periphery of the wheel. The sail material used was Melinex sheet, of thickness 0.2 mm, which is airtight, strong, lightweight and flexible.

The sails, nine in all, were attached to the pole of the rotor in such a way that they overlapped each other, (Fig.23).

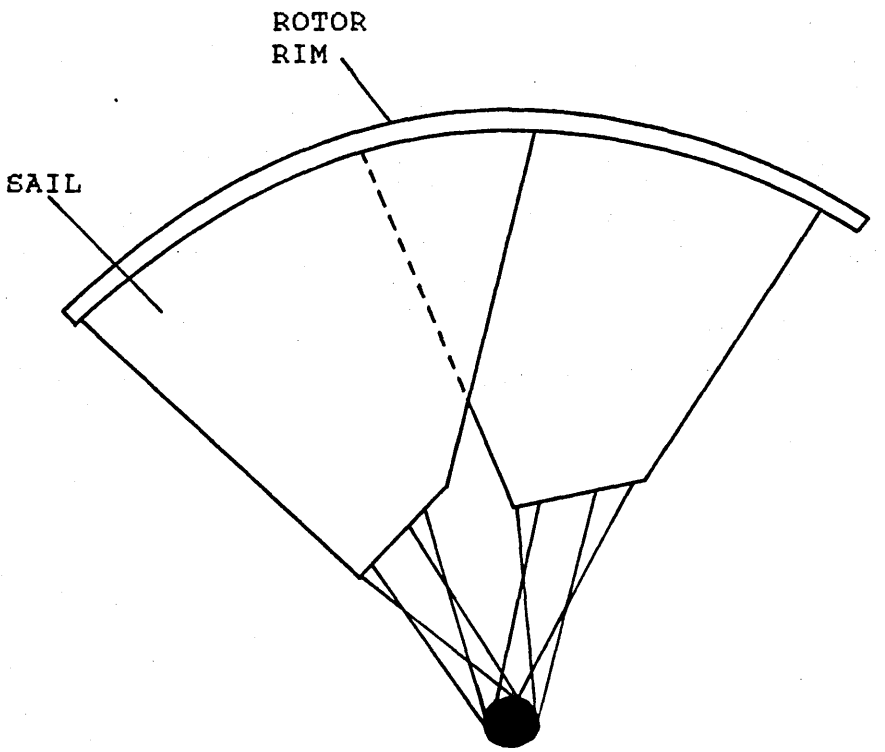

Fig.23 Interacting sail design.

This interaction in sail design was considered for two reasons, viz:-

1) it reduces the form drag,

2) it increases the suction and hence the magnitude of the aerodynamic force on the sail.

Marchaj (48) explained one of the many theories describing the air flow through two aerofoils (sails) set in tandem with a small overlap (see Fig.24). The forward foil A (Fig.24), set at an angle of incidence α, has a pressure distribution represented by the continuous line "a" on the left of the diagram. When the other foil B, set at the same incidence α and which by itself would have had approximately the same pressure distribution as foil A, is

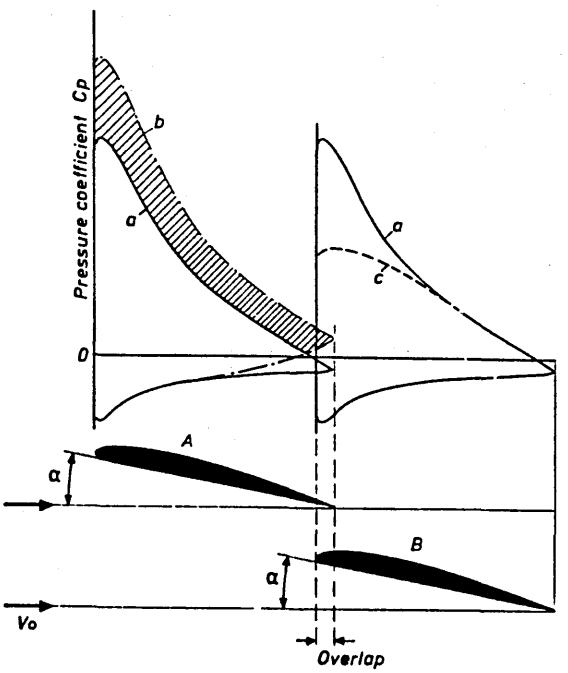

Fig.24 Effect of mutual interference between two foils, set in tandem with small overlap, on pressure distribution on separate foils and while interacting.

brought near to the first one, the trailing edge of the forward foil A will be in the region of greater velocity and correspondingly lower pressure produced by the rear foil B. This will have the effect of modifying the pressure distribution curve "a" of the front foil. Since its trailing edge is immersed in a region of flow velocity appreciably higher than that of free stream, the velocity at all points along the foil surface is increased, thus alleviating separation problems or permitting increased lift. In consequence of this alteration in flow conditions the negative pressure or suction over the front foil is more favourable, as indicated by the broken line "b" in Fig.24. Apparently the lift, which is represented by the area enclosed by curve "b", has been considerably increased in comparison with that enclosed by curve "a".

Exatly corresponding phenomena occur with the rear foil B. The front foil produces a diminution of velocity in the region of overlap and hence a reduction of suction at the nose of the rear foil. Consequently, the suction peak is much lower and the resulting pressure distribution is given by the broken curve "c" in Fig.24. On the whole, the two foils, interacting in the manner described, produce a greater maximum lift than if they were separated; and this increase is to be found entirely at the front foil.

In about the year 1920 Handley-Page and Lachman (19) demonstrated that an aerofoil incorporating a slot in front can, as a system, develop considerably greater maximum

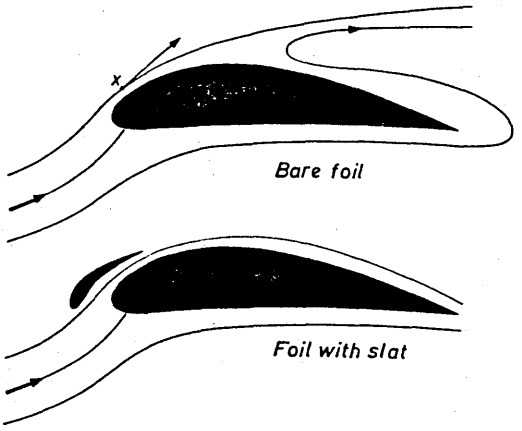

Fig.25 Prandtl's slotted foil: flow separation on the foil behind the slat is delayed or avoided by the jet of "fresh" air that flows through the slot.

lift than a single aerofoil (sail) of the conventional form. Prandtl (30), was the first fluid dynamicist to explain this, by saying that the air coming out of the slot blows into the boundary layer on top of the interacting foil and imparts fresh momentum to the particles in it, which have been slowed down by the action of viscosity.

Basically there are two interpretations (48) of the interacting effects between the two sails, namely:

1) the circulation effect,

2) upwash-downwash effect.

The Circulation Effect

To explain the interaction between the front and rear sails, it may be said that the circulation round the front sail is increased to the same extent as the circulation round the rear sail is decreased. From Fig.26 in

order to satisfy the Kutta-Joukowski condition (ref.30), the strength of the circulation developed by the front sail will automatically be adjusted on account of the higher flow velocity at its trailing edge.

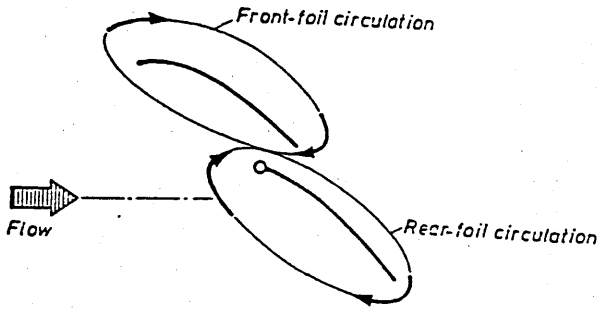

Fig.26 The Circulation Effect.

Upwash-Downwash Effect

Alternatively, the effectiveness of the two interacting sails may be accounted for by the upwash and downwash effects shown in Fig.27. The forward sail is

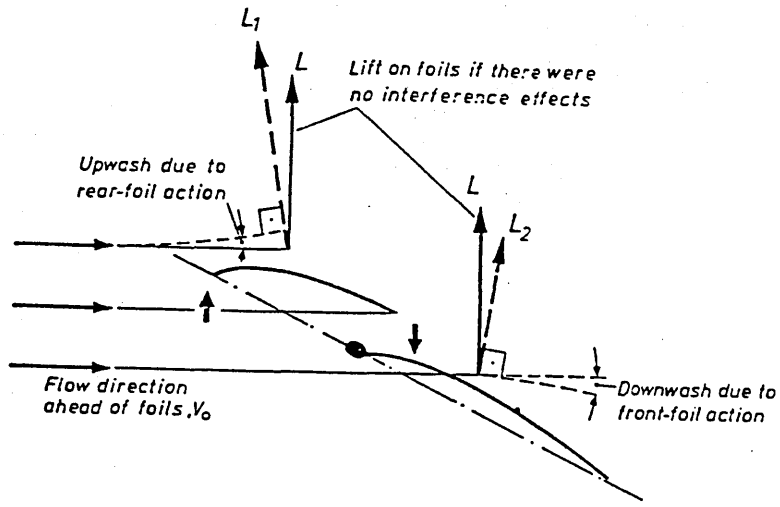

Fig.27 The Upwash - Downwash Effect.

situated in the upwash of the rear and as a result the incidence angle at which the flow meets the front foil is greater than the angle α. The air flow can be traced over the front sail and continued on over the rear foil, where it is found that the angle made by the air flow meeting the main sail is less than the incidence angle α. That is to say, the rear sail is in the region of downwash from the front sail, and the air, having been deflected downwards to some extent already, finds less difficulty in adhering to the surface instead of seperating as it otherwise would.

The net gain of such an effect is that the lift L_1, generated on the front sail is higher and more favourably inclined when compared with the lift L on the foil without interference effect. Conversely the lift L_2 developed by the rear sail is comparatively smaller, and is unfavourably inclined backwards (i.e the leading sail carries a heavier load than the rear sail).

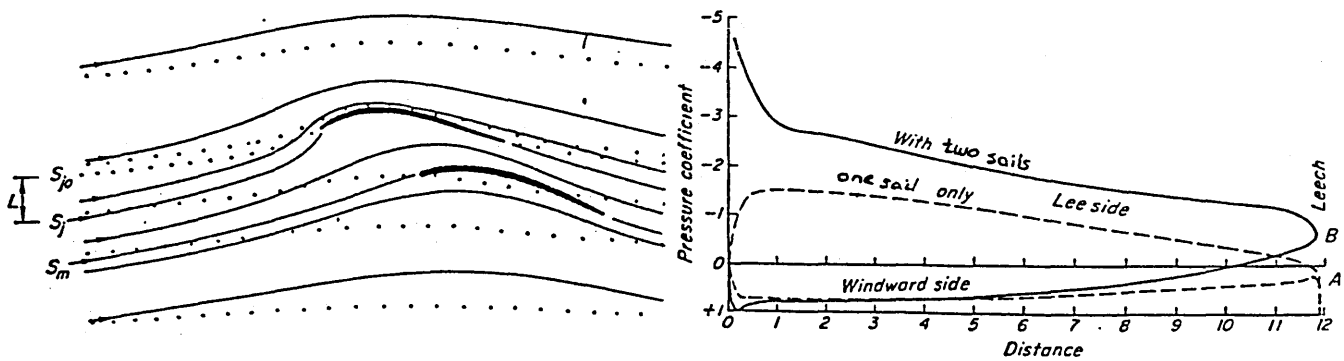

Fig.28 Flow pattern around sail system and the corresponding pressure distribution.

On the whole, the two sails, interacting in the manner described, produce a greater maximum lift than if they were separated and this increase is to be found entirely on the front sail. This theory has been verified by Gentry (21), who illustrated the flow pattern round the sail interactions and also the corresponding pressure distribution (see Fig.28).

POWER AUGMENTATION DEVICES

For wind-turbines to be adopted in everyday life for converting energy into usable electrical energy or other purposes, they have to be competitive economically in that the design must be as simple as possible and able to produce maximum power at least cost.

Two proposed schemes for inexpensively improving the horizontal-axis wind-turbine are the incorporation of a centre-body and tip-fins.

The Centre-body

The centre body, shown in Fig.29 consist of a hub-fairing and an after-body. The hub-fairing generally rotates (with the rotor), whereas the streamlined after-body is normally stationary and encloses the "power take-off" equipment.

The centre-body concept proposes that a streamlined body at the centre of an axial flow wind rotor will favourably interfere with the normal air flow through

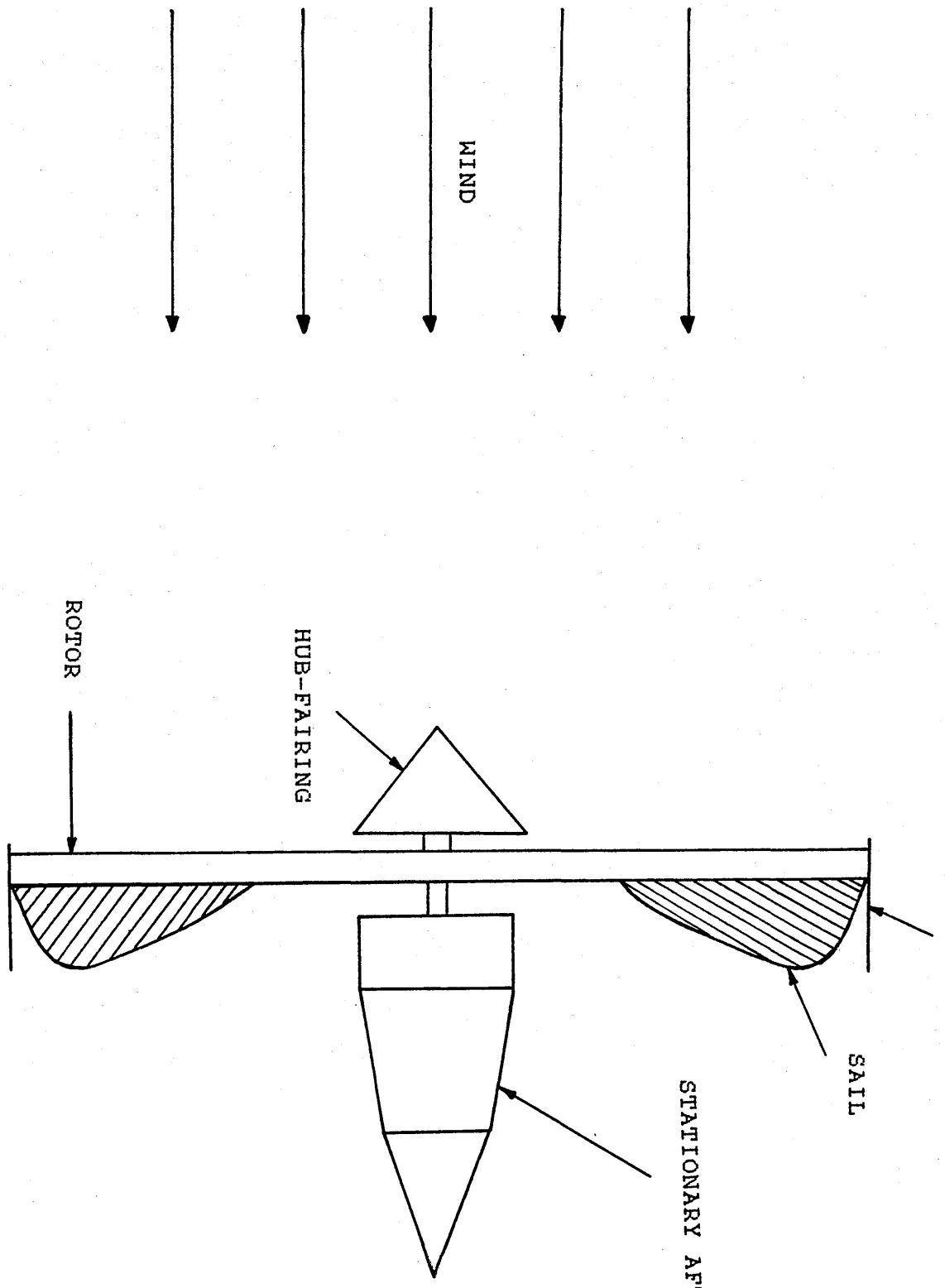

FIG. 29 Centre-body and tip-fin augmented wind-turbine.

the rotor and thus results in an increase in power output (28). If a streamlined body is positioned in a uniform airflow, the velocity of the air increases as the air passes around the body. If the body is at the centre of the wind rotor, the velocity of the air impinging on the working portion of the rotor is greater, due to centre-body interference, than it would be without a centre-body. Thus one might expect that the addition of a centre-body to a windmill rotor will increase the quantity of wind kinetic energy available for conversion into useful energy for any given wind velocity.

Since it is impossible for the sails to be extended right down to the axis of the rotor, a hole is being created at the centre of the wind rotor with a radius equal to the distance between the axis of rotation and the root of the sail, where air passes relatively unaffected by the wind rotor. In this case, the centre-body acts as a "plug" and deflects air that normally passes through the hub section of the rotor and directs it radially outwards to the sails, where it can be usefully harnessed.

The Tip-fins

Because air is deflected by the hub-fairing towards the "working zone" of the sail (i.e near the periphery of the rotor), there will be a corresponding increase in the rotor-tip losses. These occur due to a reduction of lift at the sail tips, where the sail cannot

support the lifting pressure differential between the upper and lower surfaces of each sail. The losses depend directly upon the sail loading (i.e the magnitude of the pressure differential) and are expected to increase with the hub-fairing diameter.

The tip losses can be reduced by employing tip-fins (31). The theory (32) predicting a maximum coefficient for wind turbines (i.e the so-called Betz limit) is only valid for ideal rotors applying a steady axial force to the air stream. Real wind turbines that produce radial as well as axial forces, are not accounted for by the Betz analysis and they may have much greater power outputs than the one-dimentional theory suggests.

The shrouded wind turbine, a rotor surrounded by what is essentially a cylindrical circular wing that directs an aerodynamic "lift" force radially inwards, is capable of at least trebling the power output of a wind turbine (33). As a reaction to the lift directed towards the shroud centre-line, a cross wind force acts upon the air, so deflecting the flow outwards, and causing its streamtube to widen downwind of the rotor (see Figs.30 and 31). Although the shroud is eminently capable of augmenting wind turbine power outputs, it is relatively expensive, so inhibiting its future widespread incorporation in cheap wind rotor systems.

Van Holten (34), from data obtained with a simulated propeller-type wind-rotor, showed that the diffusion ratio is dependent upon the mean radial force so

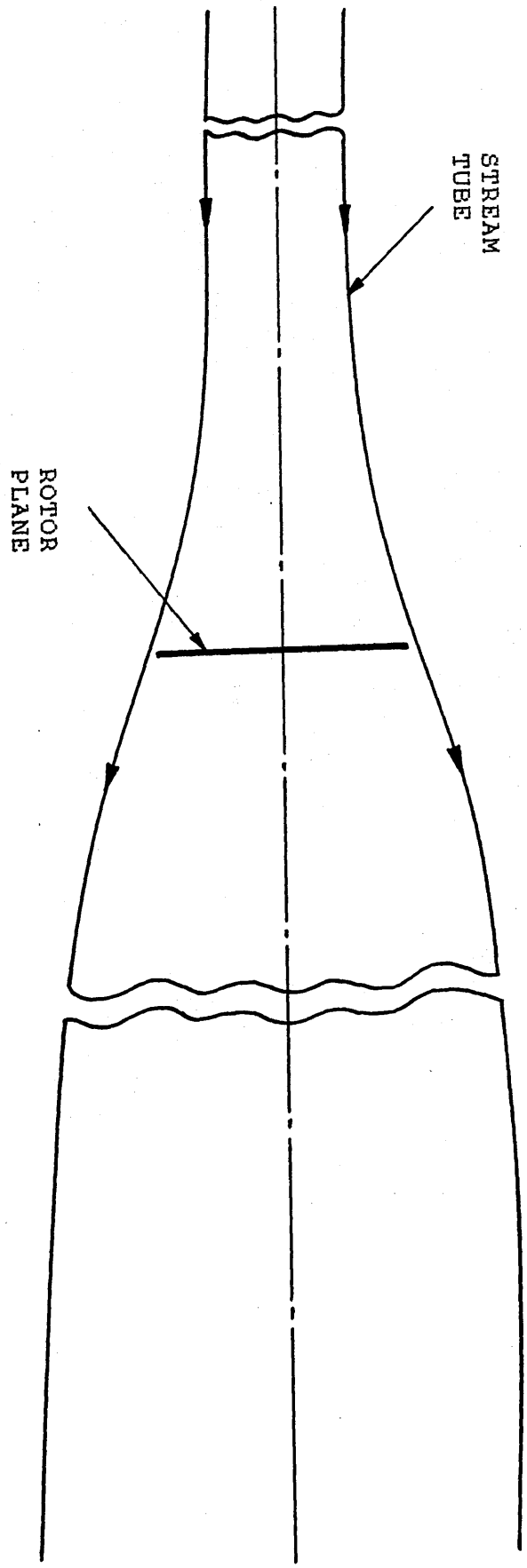

FIG. 30 Stream tube for air flowing through a conventional horizontal axis wind-turbine.

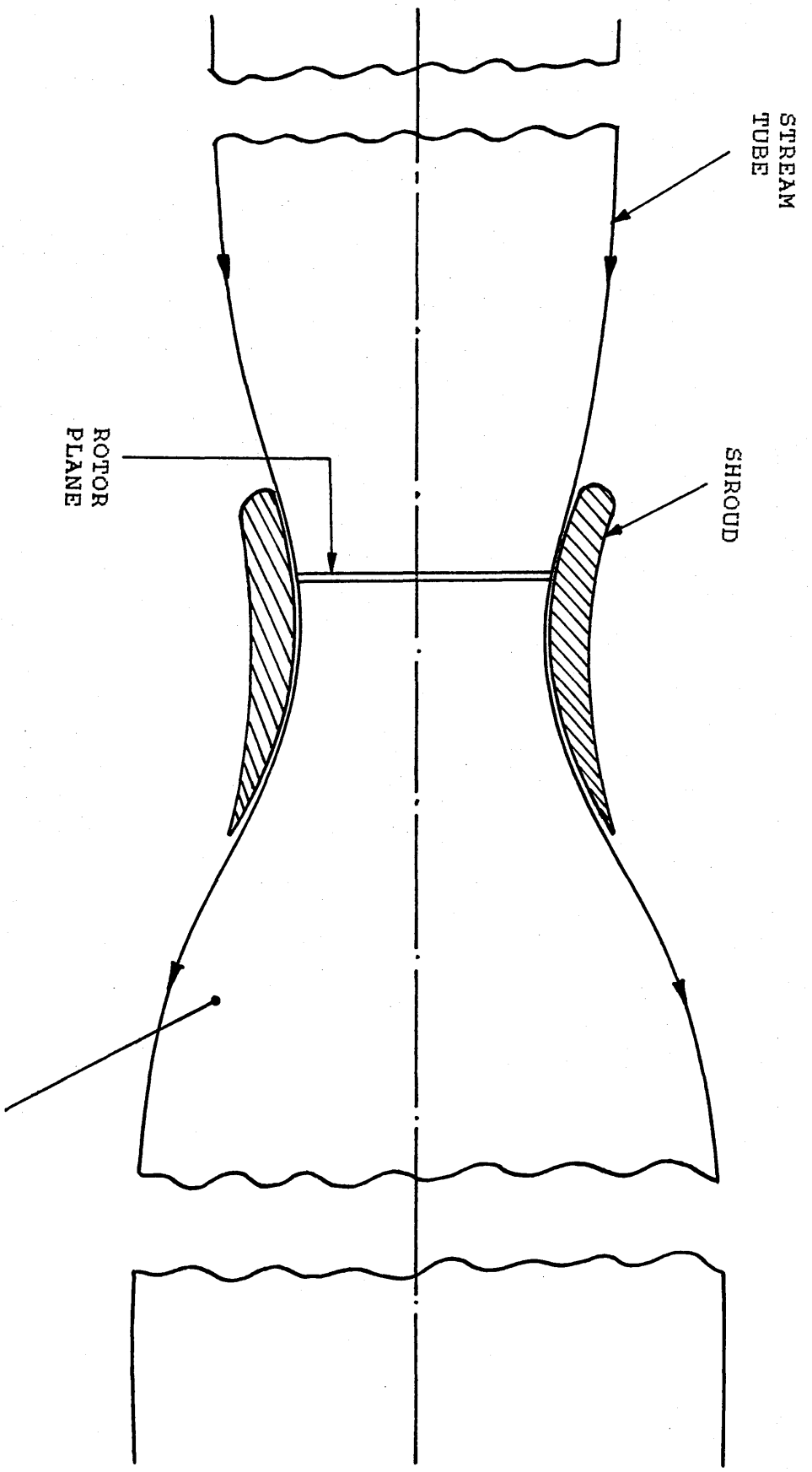

FIG. 31 Stream tube for air flowing through the wind-turbine of Fig.30 which is now enclosed by a shroud.

exerted by the wind per unit length of the circumference of the rotor plane. This suggests that to achieve diffusion of the flow, a full shroud may not be required. Replacing the shroud by tip-fins (which are also sometimes referred to as tip-vanes) concentrates the cross-wind forces onto the aerodynamic surfaces near the circular periphery of the wind turbine. This arrangement, shown in Fig.32, causes a deflection of the air stream in a manner analogous to that occurring in shrouded wind-rotors.

The power enhancement is greater for a shrouded rotor than for the rotor with tip-fin augmentors. This occurs because the drag forces on the shroud do not adversely affect the power output of the wind turbine. However, with the tip-fin augmented wind turbine, induced and viscous drag forces ensure that the power augmentation capability is less than that achieved with the shrouded wind rotor.

By utilising relatively inexpensively aerodynamically shaped tip-fins, the induced drag can be made negligible (35). As the cross-wind forces do not work on the fluid, no energy is lost in order to establish a force field, and so no torque is required to drive the tip-fins (34). This implies that they need not experience induced drag.

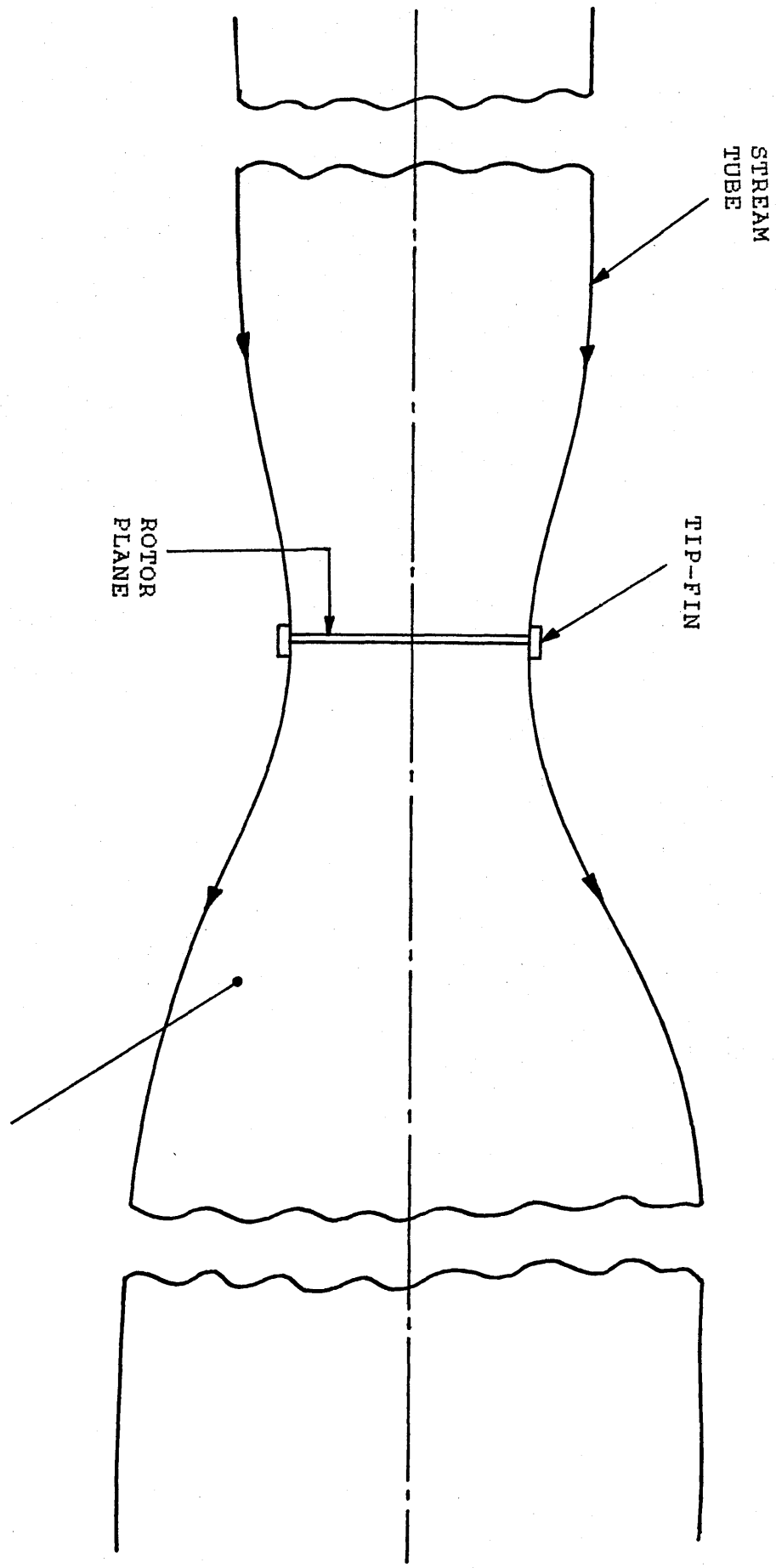

FIG.32 Stream tube for air flowing through a tip-fin augmented version of the rotor of Fig.30.

CHAPTER FIVE

PRACTICAL USE OF THE PROTOTYPE WIND TURBINE

Because up to 80% of rural electricity in the Third World Countries is used for pumping (4), disruption in such supplies often leads to crop failures. Also equally as important, in these same regions of the world, is the lifting of water for drinking.

A Cretan windwheel and a peristic pump are relatively simple devices. The main advantage is that they can be built by local unskilled labour, hence resulting in cost minimisation.

So in this project, the author has coupled the augmented wind turbine with a commercially-available peristaltic pump in order to serve the above purpose.

Owing to the varying torques and power outputs generated from wind turbines, the pumps to be coupled to them should be able to operate effectively under these conditions. However a conventional peristaltic pump possesses an almost fixed inertia and is thus designed to operate within a limited range of rotational speeds. This may therefore inhibit its effectiveness for use with wind turbines.

COUPLING OF A PUMP TO A WIND TURBINE

In order to gain the maximum energy from the wind turbine, say for pumping water, their (i.e the wind turbine

and the pump) torque characteristics would have to be matched. Sail-type wind turbines possess a nearly parabolic relationship between their power coefficient (Cp), and their tip-to-wind speed ratio (λ). This then gives an approximately linear relationship between their torque coefficient (Cq), and the tip-to-wind speed ratio (λ) as shown in Figs.33 and 34.

In order to simplify the analysis of the operation and efficiency of a wind turbine and pump combination, two assumptions are made, viz:-

1) the average torque of the pump is constant (in reality the torque of a peristaltic pump varies during operation).

2) the Cq versus λ characteristics of the wind rotor is linear (this is true for tip-speed ratios slightly below design tip-speed ratio (λ) to λ(max) (36). Hence only the starting behaviour cannot be described when using this assumption).

The first assumption then implies that the torque produced by the rotor at speed V must equal to the design torque produced at V(d) .

$$\frac{1}{2} Cq \; \rho A \; V^2 R \; = \; \frac{1}{2} Cq(d) \; \rho A \; V(d)^2 \; R \qquad (108)$$

hence

$$\frac{Cq}{Cq(d)} = \frac{V(d)^2}{V^2} \qquad (109)$$

The second assumption may be written as (see appendix 5 for proof)

$$Cq = \frac{Cq(d) \quad (\lambda(max) - \lambda)}{\lambda(max) - \lambda(d)} \qquad (110)$$

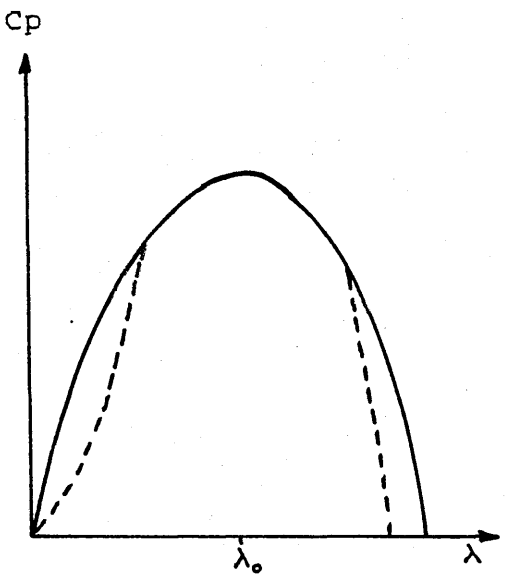

Fig.33 Power curve

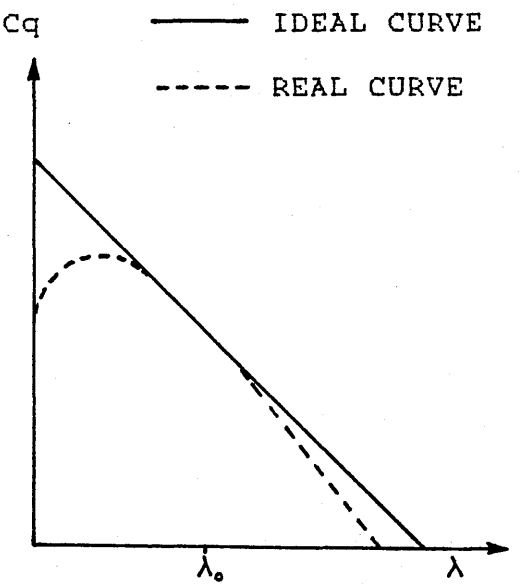

Fig.34 Torque curve

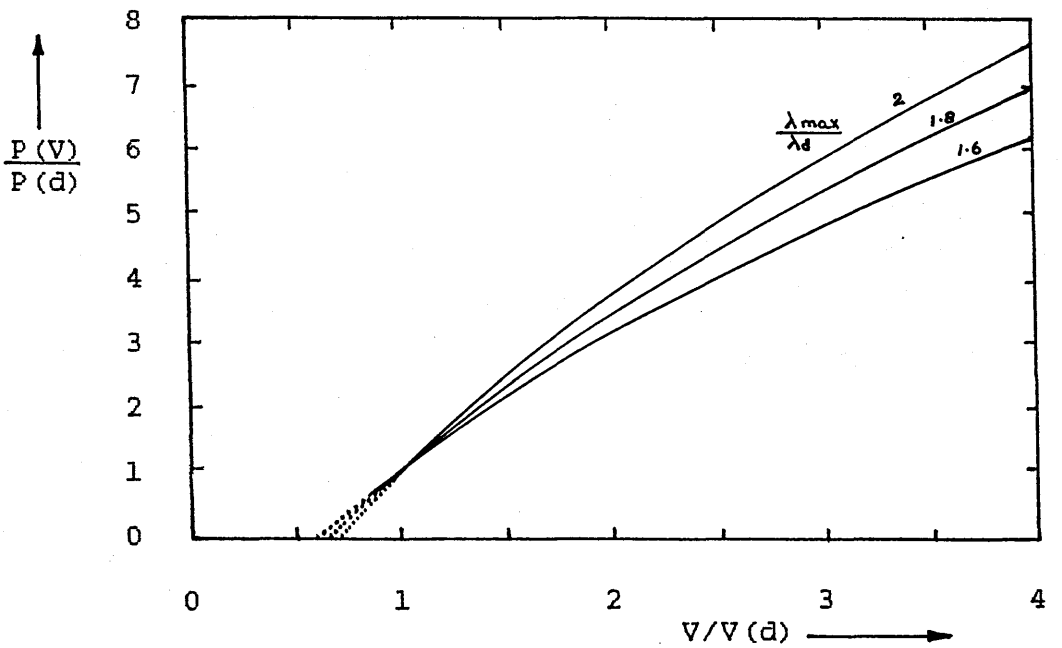

Fig.35 The output of a water pumping turbine, related to its output at the design wind speed V(d), for different values of $\lambda(max)/\lambda(d)$.

substituting equation (109) into (110)

$$\frac{V(d)^2}{V^2} = \frac{\lambda(max) - \lambda}{\lambda(max) - \lambda(d)} \quad (111)$$

which is written as,

$$\frac{\lambda}{\lambda(d)} = \frac{\lambda(max)}{\lambda(d)} - \frac{V(d)^2}{V^2} \left\{ \frac{\lambda(max)}{\lambda(d)} - 1 \right\} \quad (112)$$

Since the power $P = Q\Omega$, and $\lambda = \Omega r/V$ then:

$$\frac{P(V)}{P(d)} = \frac{Q(d)\Omega}{Q(d)\,\Omega(d)} = \frac{\Omega}{\Omega(d)} = \frac{V\lambda}{V(d)\,\lambda(d)} \quad (113)$$

substituting equation (112) into (113), we get:

$$\frac{P(V)}{P(d)} = \frac{V}{V(d)} \frac{\lambda(max)}{\lambda(d)} - \frac{V(d)}{V} \left\{ \frac{\lambda(max)}{\lambda(d)} - 1 \right\} \quad (114)$$

This is shown in Fig.35 for three values of $\lambda(max) / \lambda(d)$.

The typical shape of the Cp — V curve of Fig.36 can now be found by assuming that the efficiency of the pump η is constant. Then,

$$\frac{P(V)}{P(d)} = \frac{Cp\ V^3}{Cp(max)\ V(d)^3} \quad (115)$$

with equation (114), this gives

$$\frac{Cp}{Cp(max)} = \frac{V(d)^2}{V} \frac{\lambda(max)}{\lambda(d)} \left\{ 1 - \frac{V(d)^2}{V^2} \left(1 - \frac{\lambda(d)}{\lambda(max)} \right) \right\} \quad (116)$$

This is shown graphically in Fig.36.

From Fig.36, it is apparent that a wind turbine with a linear Cq-λ versus tip-to-speed ratio relationship, coupled to a constant torque pump, works at relatively low efficiencies. The lower the efficiency, the higher the wind speed.

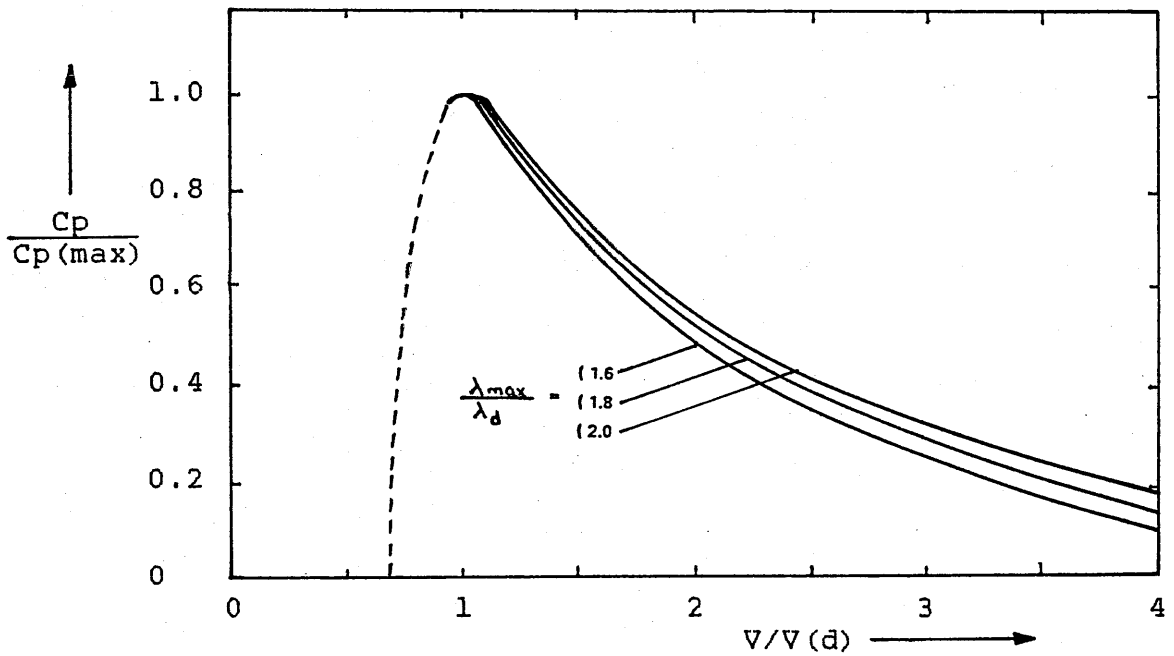

Fig.36 The power coefficient of the rotor of a water pumping wind turbine coupled to a constant torque pump with a constant efficiency, related to Cp(max) of the rotor, as a function of V/V(d) for diffirent values of λ(max)/ λ(d).

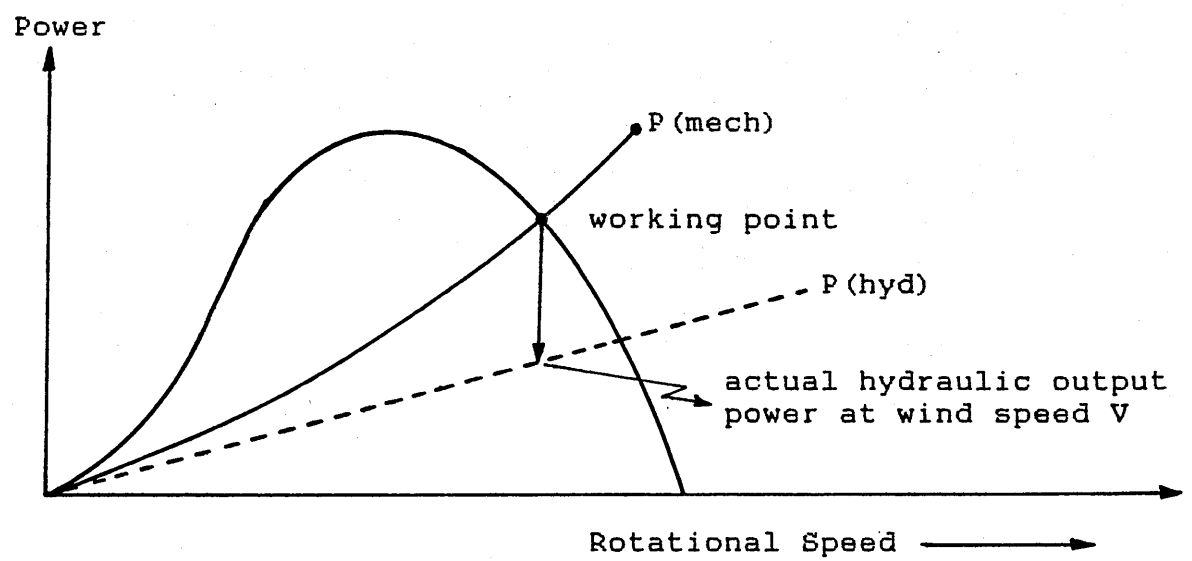

Fig.37 Working point of a rotor-pump combination at a given wind speed V.

PRACTICAL BEHAVIOUR OF WIND TURBINE AND PUMP COMBINATION

The ideal pump requires a mechanical power equal to the net power to lift the water (i.e an efficiency of 100%). In reality the mechanical power required is higher than the net water-lifting power because of mechanical losses, due to friction between rollers and tubes (for a peristaltic pump), and hydraulic losses, due to flow friction mainly in the pipes.

If a pump is coupled to a wind rotor exposed to a given wind speed V, the rotor will turn at a speed such that the mechanical power of the rotor is equal to the mechanical power exerted by the pump. This working point can be found by the intersection of the rotor power curve and the pump curve (see Fig.37).

The mechanical efficiency of the pump is defined as,

$$\eta_{(mech)} = P_{(hyd)} / P_{(mech)} \qquad (117)$$

where $P_{(hyd)}$ = nett power to lift water (= q gh)

$P_{(mech)}$ = mechanical power driving the pump (i.e the power from the rotor)

The actual flow of the water lifted by the rotor-pump combination, at the given wind speed, is found by drawing the $P_{(hyd)}$ curve (Fig.38), noting the power at the rotational speed of the working point and dividing by gh.

The hydraulic output as a function of wind speed can be found by drawing a series of rotor power curves (see Fig.38) and as a result the net output curve is found as well as the overall efficiency (i.e from wind to water) of the system.

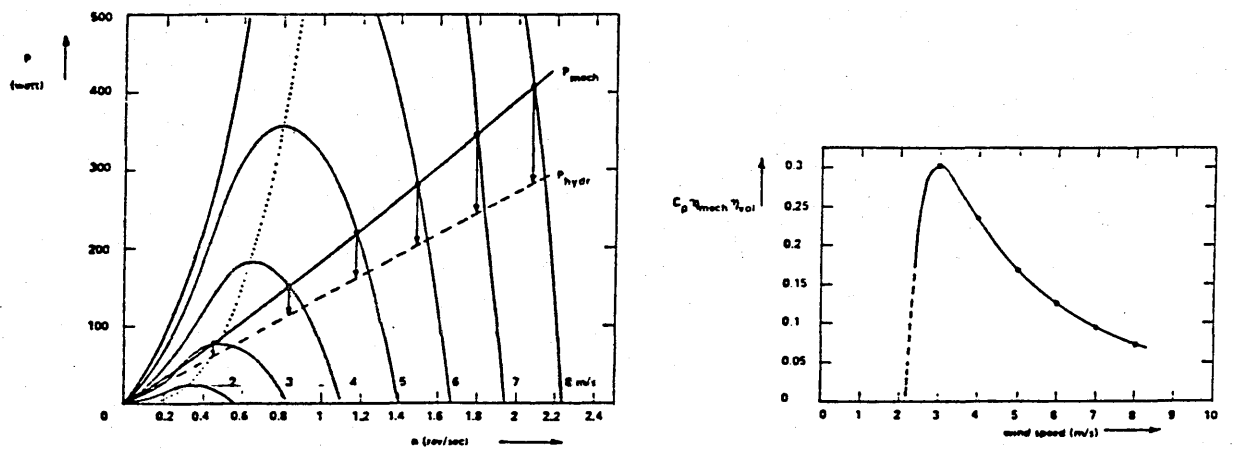

Fig.38

The wind speed at which the overall efficiency reaches a maximum is the design wind speed V(d) of the system. In practice it is the wind speed at which the Cp reaches its maximum value Cp(max). This design wind speed V(d) can also be calculated by realizing that at each wind speed, so also at V(d), the nett power supplied by the rotor-pump combination must be equal to the hydraulic power to lift the water.

i.e nett rotor-pump power = hydraulic power

$$\eta(\text{mech})\, P(\text{mech}) = P(\text{hyd})$$

$$\eta(\text{mech})\, \frac{1}{2}\, Cp\, \pi R^2\, \rho\, V^3 = q\, \rho_w\, g h$$

at $V = V(d)$

$$\eta(\text{mech})\, \frac{1}{2}\, Cp(\text{max})\, \pi R^2\, \rho\, V(d)^3 = q(d)\, \rho_w\, g h$$

therefore,

$$V(d) = \left\{ \frac{2 q(d)\, \rho_w\, g h}{\pi R\, \rho\, \eta(\text{mech})\, Cp(\text{max})} \right\}^{\frac{1}{3}}$$

Hence it can be seen that the design wind speed can be

changed by:

1) installing a different size pump

2) changing the water-lifting height

The overall efficiency of the wind turbine/pump combination is found using,

$$\eta(\text{overall}) = \frac{P(\text{mech}) \times 100\%}{P} \qquad (118)$$

where P = the power from the undisturbed wind.

THE PERISTALTIC PUMP

In order to start a fixed inertia pump a relatively high torque is required, whereas the proposed self regulating peristaltic pump shown in Fig.39 would commence operating even in low wind speeds.

Because of its design simplicity and ease of operation, the peristaltic pump can be easily adapted to regulate a wind-driven pump combination. One advantage of such a pump is that it has no mechanical drive into the pumping chamber, hence sealing problems do not occur.

The above pump consists of a flexible tube (positioned between the drive unit and the pump housing). As the rollers pass over the tubing, that part of the tube becomes flattened, thereby driving forward the liquid in the tube. The simultaneous relaxation of the tube behind the flattened portion draws in further liquid to be displaced forward by the next roller which squashes the tube. At any one time, at least one roller is pressed against the highly flexible elastic tubing thereby preventing the reverse flow of water.

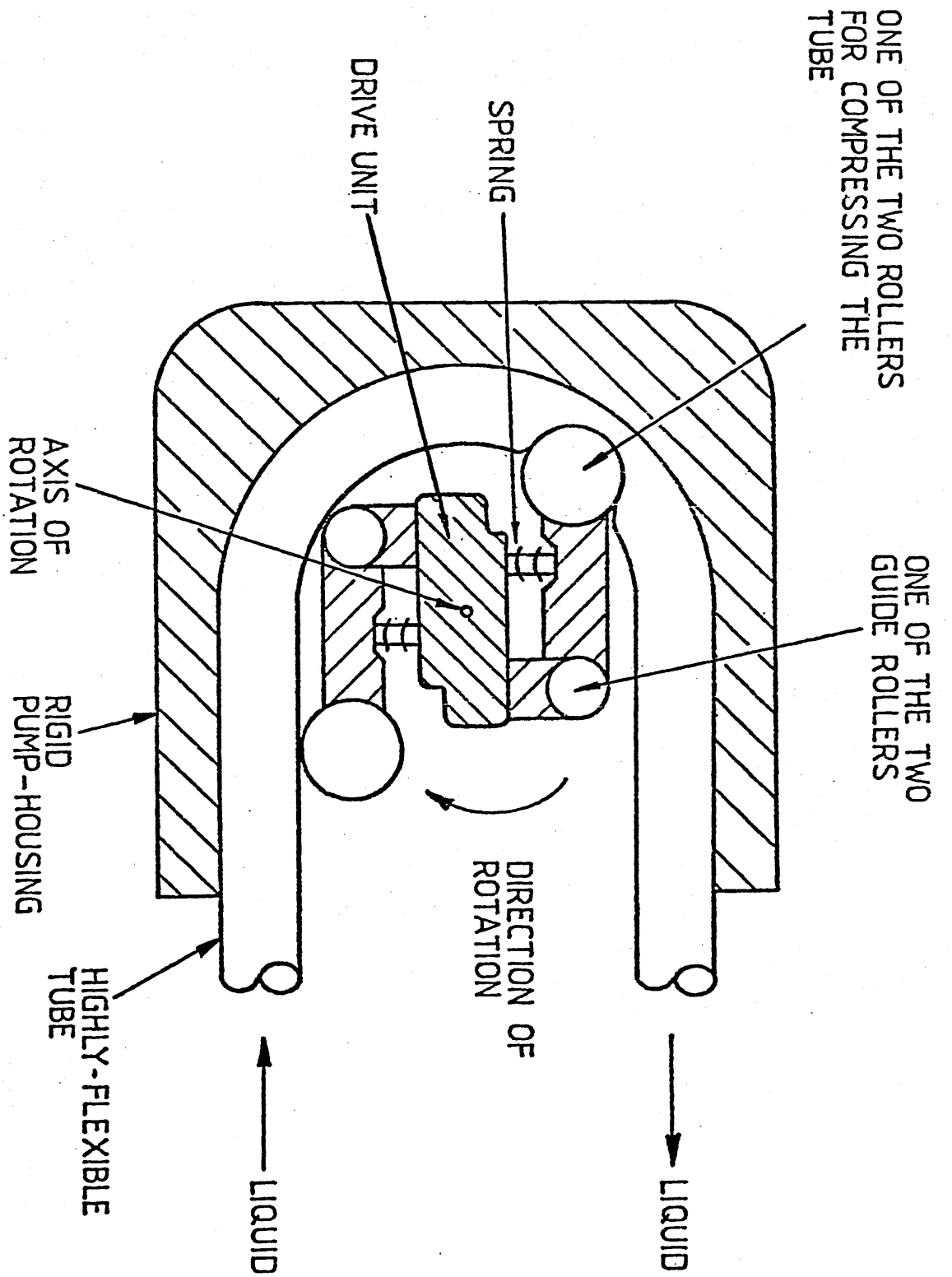

Fig.39 Schematic drawing of the peristaltic pump: its components and operation.

The flowrate is largely a function of the internal diameter of the tube and the speed at which the roller advances. The suction lift capability, however is largely determined by the restitutional power of the tube. If the tube does not restitute fully before the advance of the next roller, then the flow rate will be affected.

LOW-TECHNOLOGY PERISTALTIC PUMP

The above described pump would be rather disadvantageous in the third world because of its initial capital cost. Robertson and Leaman (37) have developed a low-technology version of the peristaltic pump that can be manufactured cheaply using indigenous materials.

The operating principles are the same as those of the peristaltic pump previously described. However, the low-technology pump (see Fig.40) has two novel features in its design, namely:-

1) the tube is externally wrapped round the drum and the roller compresses more than one revolution of the tube, for each revolution of the roller.

2) two sets of tubing are used in order to reduce the pump's starting torque. The outer tube is of a resilient material and the inner one is a highly flexible tube.

A single orbiting roller delivers fluid over the full (or nearly full) 360 degrees of rotation, with only one interruption per revolution, as the roller passes over the outlet end. This multi-turn option results in several

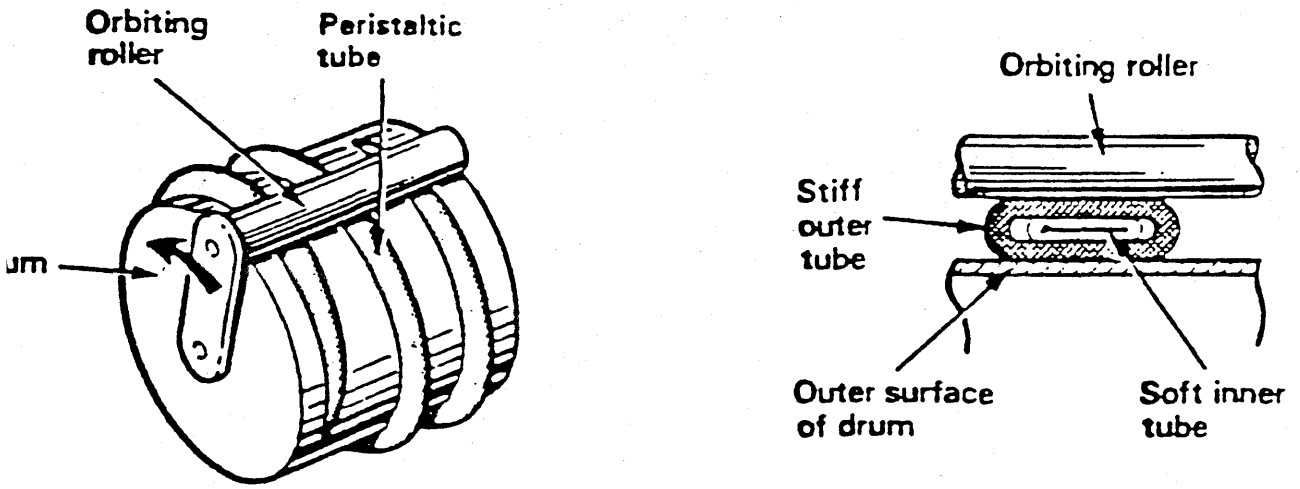

Fig.40 Low-technology peristaltic pump

compression areas of the tube with the single roller giving a multi-seal effect, whilst still allowing the time of one revolution for the compressed area of the tube to regain its shape, and so draw-in fresh fluid.

For the double tube system, the outer tube need only be compressed to the "flattened thickness" of the inner tube. This means that the outer tube is not distorted to the point of wall failure and enables the pump to operate at higher pressures, as the inner tube can only expand to a limited extent before being constrained by the outer tube. This co-axial characteristics arrangement can also be used to improve the suction characteristics. By inter-connecting the inlet end of the inner tube and the space between the tubes, the pressure differential across the wall of the inner tube can be reduced to zero, thereby improving its

recovery time before taking up further fluid. This pump can be driven in two ways:

1) driving a central shaft, where the radial arm (see Fig.40) is attached to the compression roller; or

2) driving the compression roller directly.

Because the roller is in contact with one area or another of the tube at all times, directly driving the roller becomes a practical proposition. This reduces the drag on the tubing as the roller winds itself around the drum, rather than being pushed over the surfaces. Tests have shown (37), that driving the roller directly gives far better performance than driving it indirectly.

CHAPTER SIX

EXPERIMENTAL DETAILS AND MEASUREMENTS

THE WIND TUNNEL

A purpose built open circuit wind tunnel (the air being directly exhausted and not recirculated) designed to work in the blowing mode was used for the purpose of this project. It consists of a duct of 840mm diameter and 5120mm long (see Fig.41). A general duty extraction fan is mounted at one end, capable of delivering 6.61m/s at a speed of 11.7m/s, introducing a static pressure rise of 50.8mm of water gauge. The fan diameter is 838mm. A variable-speed A.C. motor of 6.7KW is coupled to the fan through a triple V-belt drive. The maximum rpm of the motor is 1500. Starting the fan is only possible when the starter is fully wound down, giving a minimum dynamic pressure of 0.44mm of water (corresponding to 2.5m/s).

Preliminary velocity traverses across and along the test section (see Fig.42) showed a non uniform velocity distribution, later it was suspected that the three wire gauzes (used as flow straighteners) placed 1m apart along the wind tunnel were blocked. These were cleaned out with compressed air. This however did not improve the velocity profile inside the test section. Stroboscopic analyses showed an inconsistent fan speed and that parts of the seven blades had been cut away and therefore accurate, uniform velocity profiles were difficult to achieve.

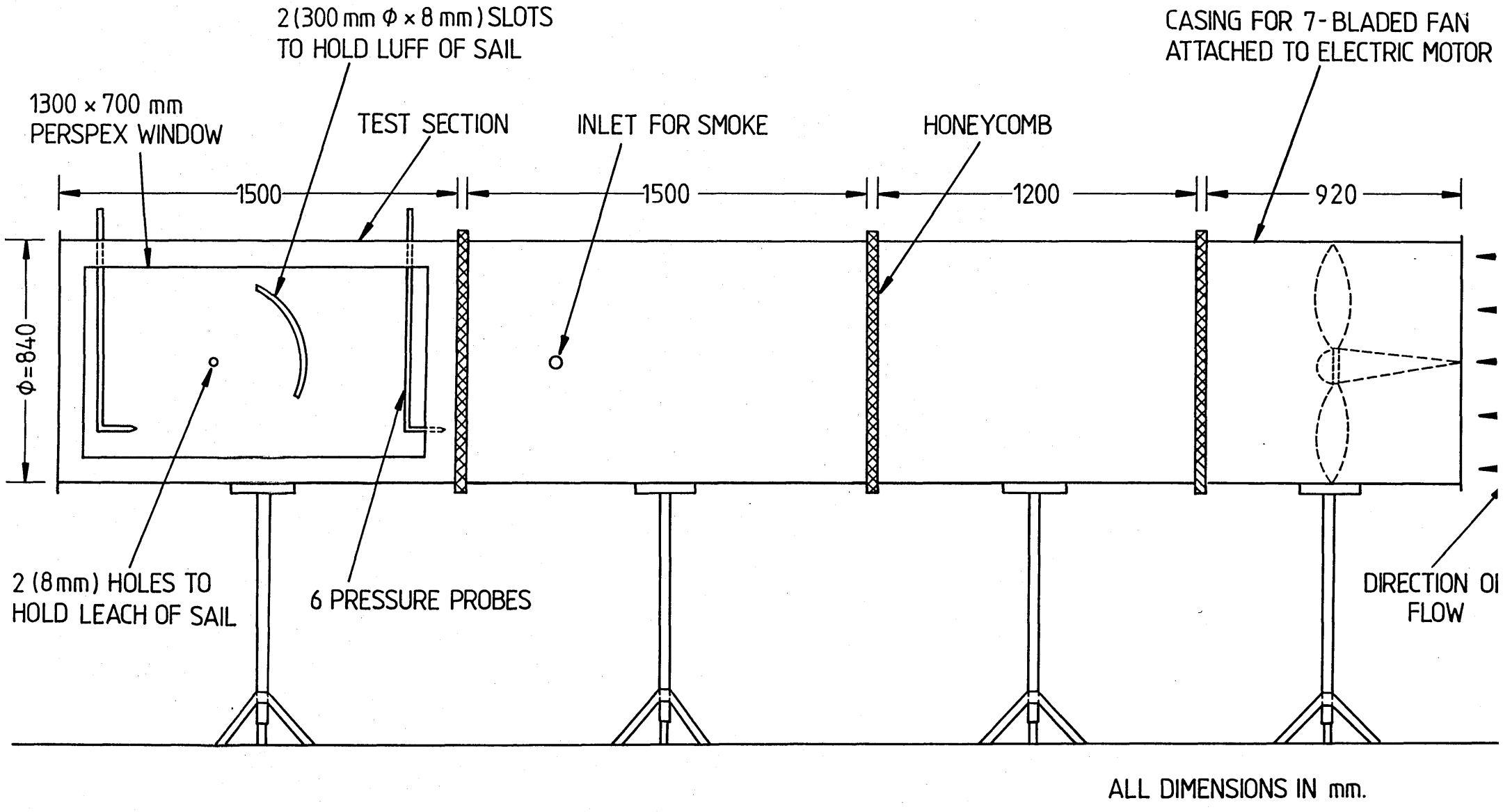

FIG. 4.1 WIND TUNNEL CONFIGURATION

TOP VIEW

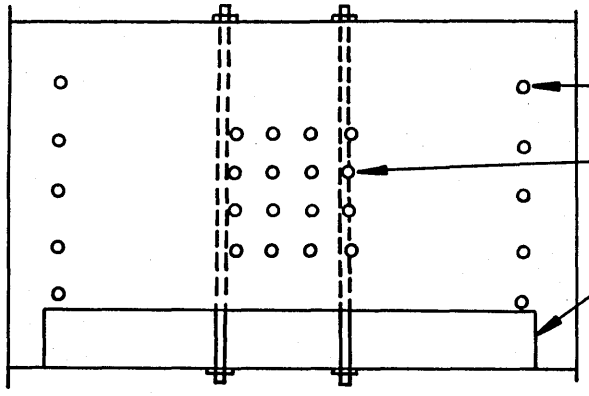

10 PORTS FOR PRESSURE PROBES

16 PORTS FOR HOT WIRE ANEMOMETERS

PART OF PERSPEX WINDOW

SIDE VIEW

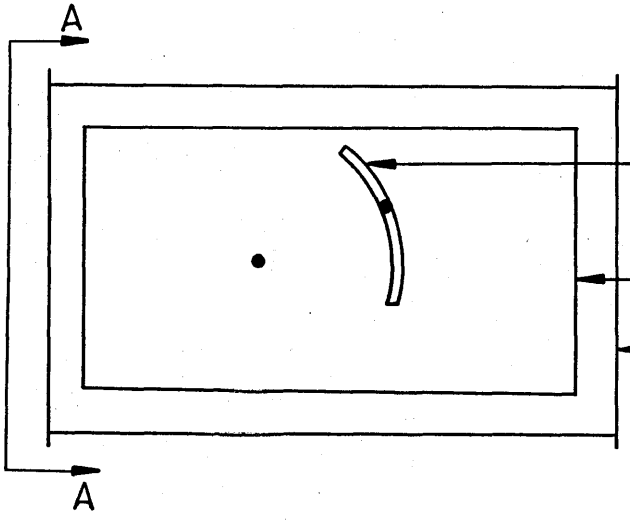

SLOT TO CARRY ROD FOR LUFF OF SAIL

PERSPEX WINDOW

TEST SECTION

VIEW FROM A-A

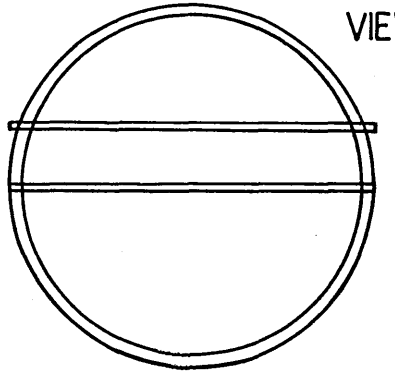

BOTTOM VIEW

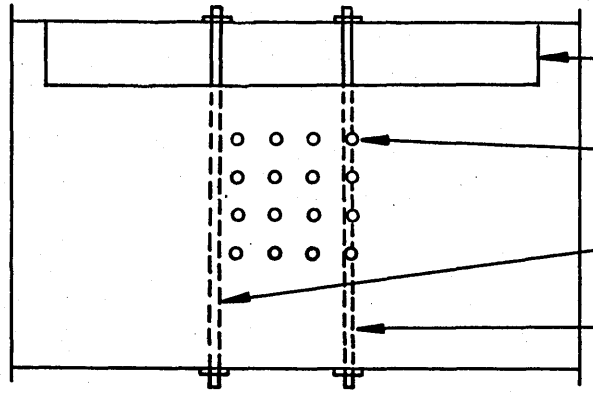

PART OF PERSPEX WINDOW

16 PORTS FOR HOT WIRE ANEMOMETERS

FIXED ROD FOR LEACH OF SAIL

MOVABLE ROD FOR LUFF OF SAIL

However the turbulence inside the test section was still fairly high and it was suspected that the entry length of the wind tunnel was too small. A 1m long, 0.8m diameter duct was designed to increase the overall length of the wind tunnel. The latter modification coupled with the three flow straighteners of thickness 50.8mm and cell size 6.35mm resulted in a near uniform velocity profile as well as a reduction in turbulence inside the test section.

THE TEST SECTION

The test section (or settling chamber) is 1.5 metres long with a diameter of 0.84 metre. It is made up of the same material as the rest of the wind tunnel, i.e 5mm cast iron (see Fig.42). Five holes of 5mm diameter were drilled on each top end of the test section so as to accommodate the pressure probes. Next, sixteen holes of 15mm diameter were drilled on both the top and bottom parts of the test section in order to take the hot wire-anemometers for velocity assessment.

A 1.3 metre by 0.7 metre Perspex sheet was cut and bent (in the oven) to the same curvature of the test section. Once set, a slot of o.3 metre diameter and 8mm thick together with an 8mm hole were made in the sheet. The same size of slot and hole were cut in the test section (see Fig.42).

A piece similar in size to the Perspex sheet was cut out of the test section. The Perspex sheet was then

mounted on to the test section with counter sunk screws, in order to serve as a window for flow visualization purposes. Two rods are inserted through the slots and holes (see Fig.42) so as to hold the luff and leach of the sail. The prepared test section was then bolted on to the rest of the wind tunnel.

WIND-TUNNEL BLOCKAGE EFFECTS

The conditions under which the proto-type wind turbine is tested in a wind tunnel are not the same as those in free-air. The effect of the wind tunnel in simulating the free air conditions produces:

1) a lateral constraint to the flow pattern about the wind turbine known as "solid blockage". In the open wind tunnel solid blockage is the same as an increase in the dynamic pressure, increasing all forces and moments at a given angle of attack of the sail. However this effect is negligible in the case of this project since the approaching air stream is free to expand as it passes through the wind turbine (see flow-visualization tests).

2) a lateral constraint to the flow pattern about the wake known as "wake blockage". Wake blockage is normally negligible with open section wind tunnels and is therefore neglected.

In this project, the blockage ratio was found to be 46%, (blockage ratio = area of wind turbine / cross-sectional area of wind tunnel) and it was concluded

from smoke test results (see discussion of results), that solid and wake blockage effects were negligible.

VELOCITY TRAVERSING

Velocity traverses have been done across and along the test section with the help of a pitot static tube and a micro manometer. Results were taken at various points inside the test section (see graphs 1 to 7).

The wind tunnel is run at various velocities and the velocity head measured through the pitot static tubes. As the flow was not quite steady, this resulted in a fluctuation of the manometer needle. Hence the mean reading at every station is recorded.

THE ROTOR

A cycle wheel was used as the rotor, being light weight, strong, readily available throughout the world (often as scrap) and providing a basic framework onto which sails could easily be attached. The particular wheel used was 0.64 metre in diameter with thirty-six spokes. The number of spokes, together with the findings of Calvert (38) and Dekker (36) indicated that nine sails would be the optimal number and that they should be relatively loose to maximise the starting torque.

The rotor was held on to the wind-turbine's shaft by the appropriate nuts. This facilitated the removal of the wind turbine in order to vary the different parameters, the

effect of which were to be tested.

THE ROTOR HOLDER

A planar tripod, made of steel, was welded to the central shaft of the wind turbine (see Fig.43), on which the wheel and its bearings were able to rotate. This arrangement enabled the rotor to be held centrally and at orthogonal to the air flow.

THE SAILS

The material used for the nine sails was ICI Melinex with a thickness of 2×10^{-4} m. The latter had the advantages of being strong, flexible, lightweight and airtight. A template was used when cutting all nine sails in order to ensure that they were all identical.

The attachment of the sails onto the wheel's spokes were as follows:

Each sail was first wrapped round the spoke and glued using Evostik. The trailing edge of the sail was then fastened onto the next fourth spoke by the use of an adjustable clamp (see Fig.44). The sail angle could be adjusted by altering the position of the bolts on the clamp. The angle was determined by simple trigonometry because the distance between the sail and the spoke was known as well as that between the four spokes covered by the sail.

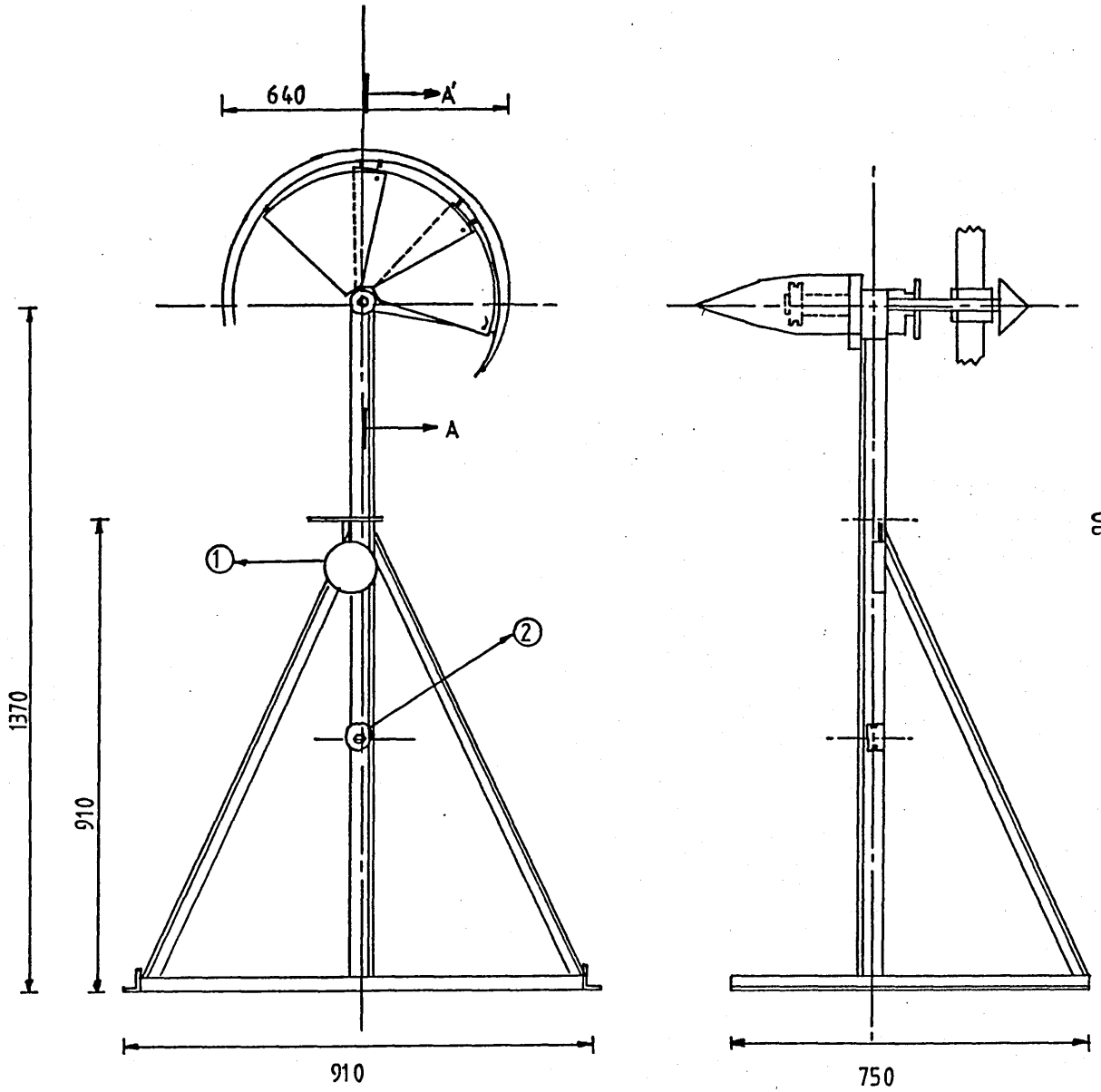

EXPLODED SECTIONAL VIEW AA'

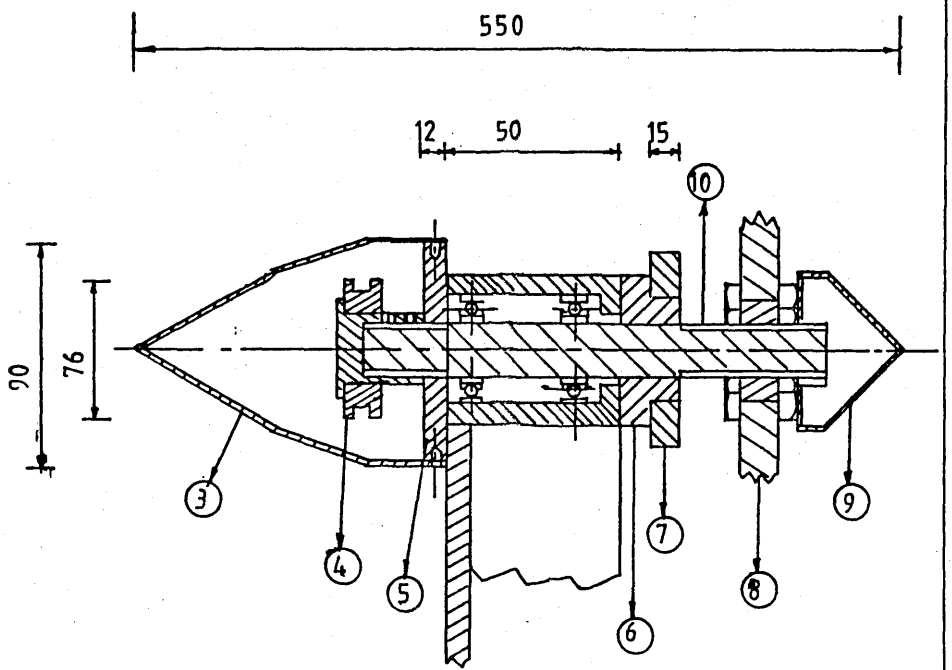

1	DYNAMOMETER
2	PULLEY
3	AFTER BODY
4	PULLEY
5	AFTERBODY SUPPORT
6	BRASS SUPPORT
7	PHOTOCELL
8	ROTOR
9	HUB-FAIRING
10	ROTOR SHAFT
	HORIZONTAL-AXIS WINDTURBINE
	SCALE 1:10

Fig.43 Schematic drawing of wind-turbine on planar tripod.

ALL DIMENSIONS IN MM

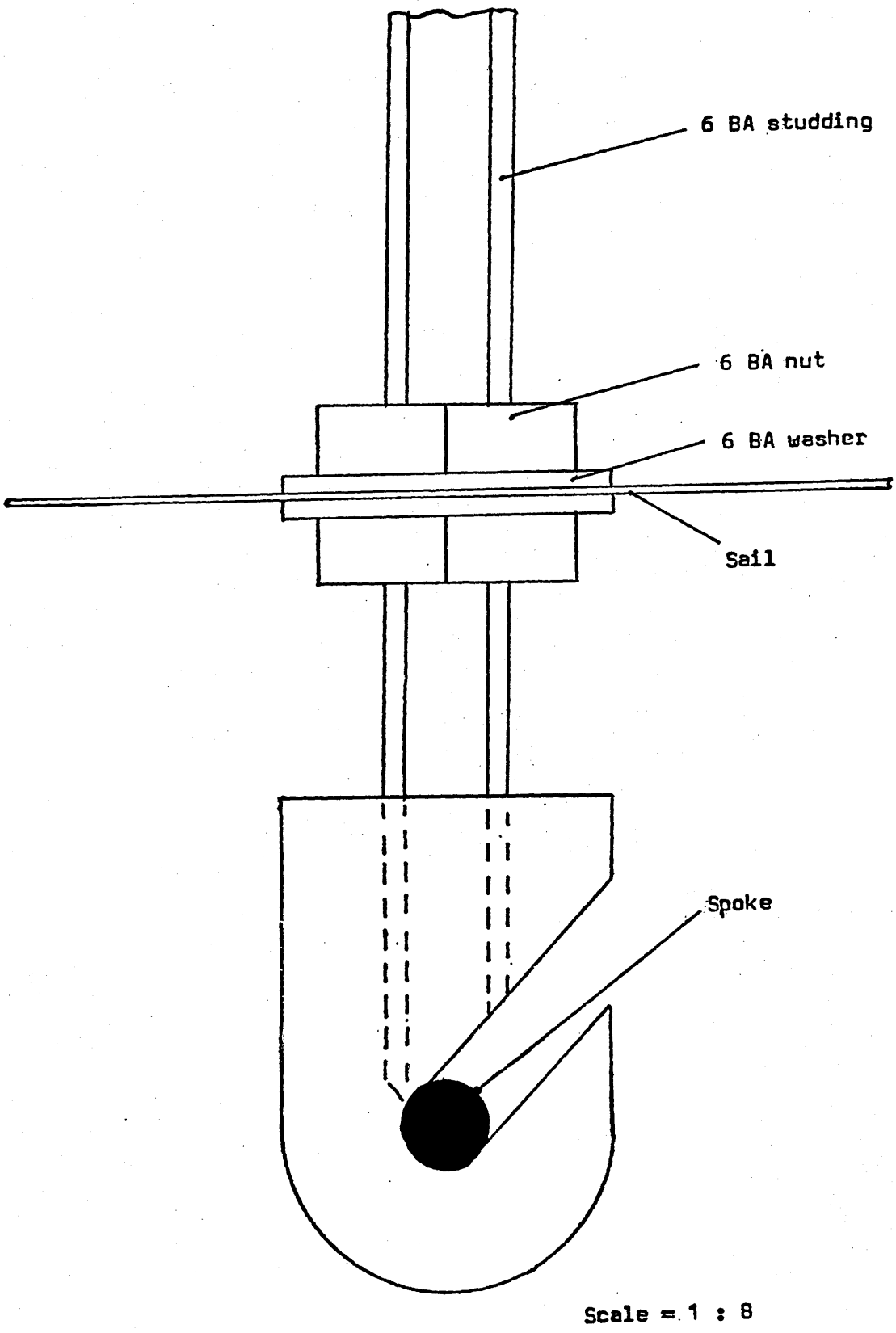

Fig.44 Sail angle adjustment clamp.

WIND-SPEED MEASUREMENT

A Pitot-static tube attached to an electronic micro-manometer was used to measure the wind speed. Following the manufacturer's instruction, two lengths of 6.4 millimetre-bore plastic tubing were connected from the pitot-static tube ports to the micro-manometer ports. The manometer read the dynamic head of the wind stream, which is $(V^2/2g)$ from which the velocity can be determined directly. The scale on the instrument is in millimetre of water. Therefore the convertion would be as follows:

$$h(air) = V^2/2g$$

$$\rho(air)\,h(air) = \rho(water)\,h(water)$$

or,
$$h(air) = \left[\rho(water)/\rho(air)\right] h(water)$$

so,
$$V(air) = \sqrt{2gh(air)}$$

Putting in the values at s.t.p.

$$V(air) = 4.1 \sqrt{h(water)}$$

where h(water) is measured in mm.

Table (18) gives the corresponding values of velocity in m/s and dynamic head in mm of water.

In order to achieve the greatest available accuracy, the micro-manometer was zeroed on the one percent scale. Since the fan could only start at a dynamic pressure of 0.44 millimetre of water, there was no actual danger of overloading. It was not necessary to make corrections for swirl when using the pitot-static tube (39); this inacuracy was small in comparison with variations in the wind speed and also in the sail tension.

ROTOR SPEED MEASUREMENT

The rotor speed was determined by the use of a photocell unit which was placed on the rotor shaft 6.4 millimetre from a duralumin torus. The latter was divided into twelve segments which were alternatively black and silver. A continuous light beam, fed from a five-volt stabilised voltage supply, was reflected on the torus. The pulses of reflected light were sensed by the photocell and the impulses relayed to the electronic counter. As the counter recorded over intervals of ten seconds, the rotor speed was displayed in revolution per minute.

TORQUE MEASUREMENT

A brake-type dynamometer (see Fig.45 and Plate 1) was used for this purpose: it included both weights and a spring balance for added stability. The simple type of brake consisted of a rope (radius r_2) passing via a guide pulley to another pulley (radius r_1) which was welded to the cycle wheel hub. Tension was produced on the rope due to the weight of the mass (m) at one end and the pull on the spring balance (M) at the other.

The torque was then determined using the relationship:

$$T = (m - M)\ (r_1 + r_2)g \qquad (119)$$

POWER DETERMINATION

Having known the speed of the rotor N(rpm) and the torque T(Nm), the power P(watt) was then worked out using

the following equation:

$$P = \frac{2\pi NT}{60} \qquad (120)$$

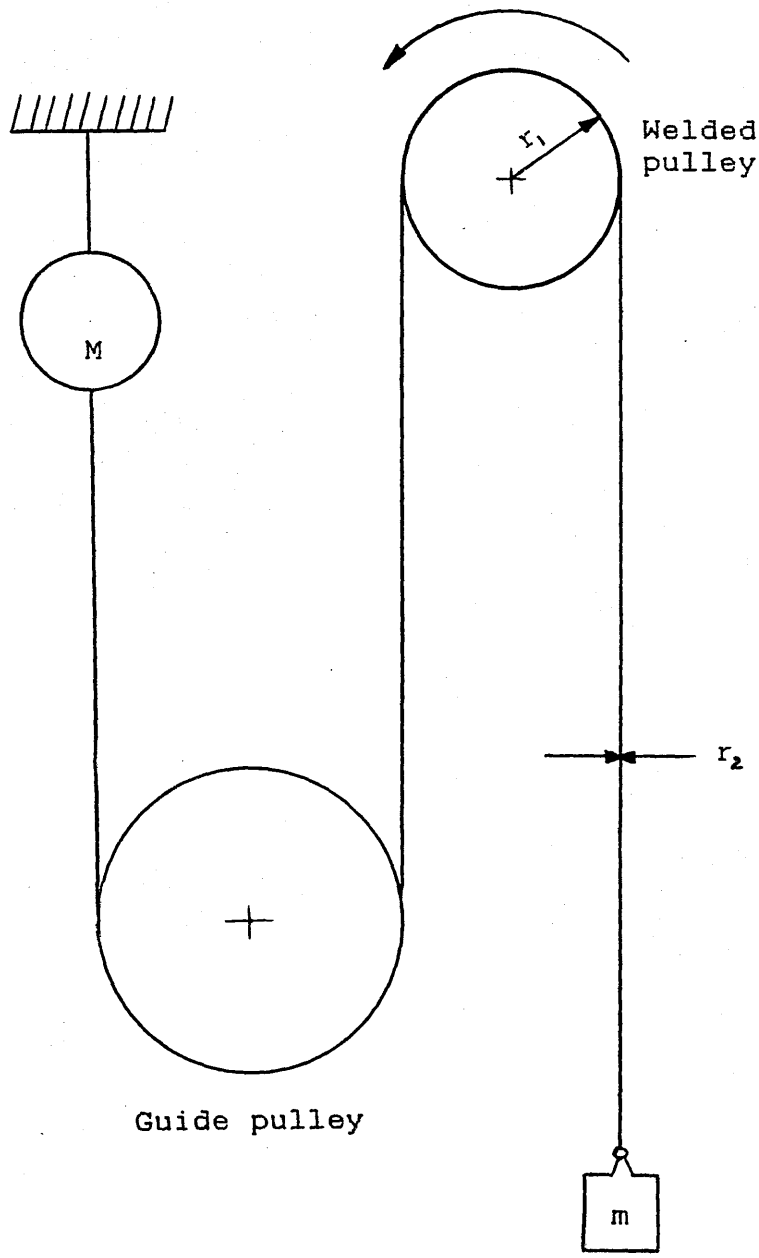

$$T = (m - M)(r_1 + r_2)g$$

Fig. 45 Dynamometer arrangement.

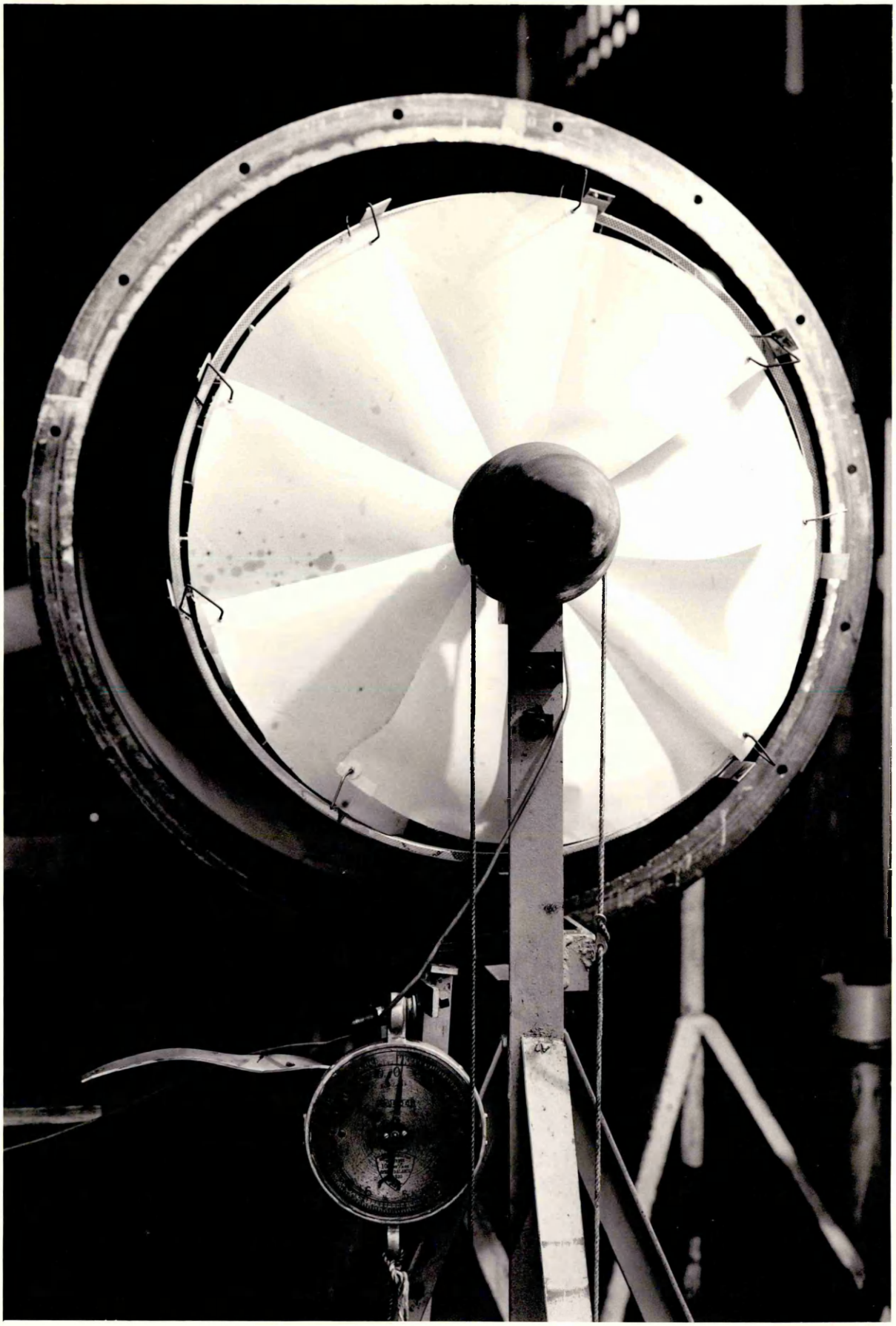

METHODS BY WHICH MEASUREMENTS WERE TAKEN

The power supply to the recording instruments was switched on and left for fifteen minutes in order to allow them to attain steady states.

A sail, 300 by 280mm with a 1% slack (i.e 1% of the length) was attached to the two rods, see Fig.41, and a wind speed was chosen. The fan could only be switched on when the started was fully wound down. The angle of incidence, α, was then varied between 0° and $+60^{\circ}$ at 2.5 degree intervals. For each value of α, (1) a photograph was taken in order to determine the shape of the sail, (2) hot-wire anemometers were inserted from both the top and bottom of the test section, so as to establish the velocity profiles on both sides of the sail.

An array of hypodermic tubes was then attached to the sail, with one set of openings facing the oncoming wind and the other connected to a set of manometers, this might be a crude method, but it gave us an indication of the pressure distribution on both sides of the sail for each angle of incidence and wind speed.

To determine the flow around the sail:

1) a set of "short lengths of wool" each 70mm long was stuck on each side of the sail using evo-stik glue. With a constant wind speed, the angle of incidence was varied at 2.5 degree intervals and a photograph was taken for each α. This method gave us an indication of the qualitative behaviour, i.e whether laminar, turbulent or mixed, flow ensued as the

air passed over and under the sail.

2) with a plain sail (i.e no tufts or hypodermic tubes), and a wind speed chosen, smoke was injected from a smoke generator via a hole in the wind tunnel. Again photographs were taken, but because of the size of the test section and the strength of the wind inside, the smoke just disintegrated and blew away, hence no comparison could be made with (1) above.

Nine sails were then attached to the wheel and set at the optimal angle, as found from above experiment, by adjusting the bolts on the variable clamp (see Fig.44).

After having made sure that ten balls (in grease) were present in the bearing at each side of the wheel, the rotor was then mounted on the rotor holder. Care was taken so as to make sure that the duralumin torus was facing the photocell with a maximum gap of 6 millimetres. The wheel was secured using a bearing nut, then a lock nut was added.

To achieve a greater accuracy, the micro-manometer was zeroed using the one per cent scale. The voltage supply to the photocell unit was checked to ensure that it was delivering 5 volts. The dynamometer

A rope was then looped round the appopriate pulleys and various weights were attached to one end of the rope whilst the other end (of the rope) was firmly fixed to the spring balance. The dynamometer arrangement is shown in Fig.45.

The fan was switched on and the following

parameters were recorded: spring balance reading (M), mass (m), rotor speed (N), and wind speed (via the dynamic head). The test was repeated with different masses.

The next step was to mount the centre-body on the rotor and the above procedures were followed. Different configurations of centre-bodies were tested and readings taken down.

More tests were completed on the rotor, but this time the turbine was augmented by various sets of tip-fins and a centre-body.

An optimised wind turbine (i.e with the best sail angle, afterbody and tip fins) was then placed in front of the wind tunnel. With a constant wind speed, the rotor was set in motion. Smoke from the smoke generator was injected at various points close to the wind turbine and photographs were taken.

Finally, the optimised wind turbine was put into practice for the purpose of water pumping. A peristaltic pump was coupled to the optimised rotor and the above procedure was repeated once again.

CHAPTER SEVEN

ERRORS ARISING FROM TESTS.

The errors in the results stem from various instruments used as well as inconsistencies of the fan speed of the wind-tunnel. It was difficult to achieve the same response with the wind-tunnel once the power was switched off. One way round this discrepancy was to perform as many tests as possible in a day.

This chapter analyses the errors that arose from the equipment used and also the effects of matching the wind-turbine with a pump.

DYNAMOMETER

The errors here arose from two major sources, namely the spring balance and the leather thong. Using the 10 lb spring balance (i.e. at high rotational speeds), the error was - 0.25 lb. (= 0.114 kg). Thus there is a maximum error of less than 3% at M = 10lb. The friction rope brake and pulley temperatures tended to increase at high rotor speeds. Therefore the torque recorded is slightly lower than that developed by the wheel. Overall, the dynamometer errors were estimated to be less than five per cent.

WIND VELOCITY

A micro-manometer and pitot-static tube were used

to measure the wind speed. The micro-manometer accuracy was $\sim$ 1%. Corrections for yaw were not necessary because the error from a pitot-static tube at twenty per cent deviation from the horizontal is below five per cent.

Fluctuations in the dynamic pressure of about ten per cent were noted. This was due to the difficulty of obtaining an even wind speed, using the fan, as described earlier.

ROTOR SPEED

This was measured using an electronic counter, its error being negligible compared with those due other sources.

COUPLING OF PUMP TO WIND/TURBINE

The hydraulic power of the pump is:

$$P(hyd) = q\ \rho_w\ g h$$

where ρ_w = density of water (= 1000 kg/m^3)

g = gravity (= 9.81 m/s^2)

q = flowrate (m^3/s)

Now 1 cc/min = 10^{-6} /60 m^3/s

= 1.67×10^{-8} m^3/s

For example,

if $q = 20$ (x 100 cc/min)

Then $P(hyd) = (20 \times 100 \times 1.67 \times 10^{-8})\ \rho_w g h$ watts

i.e. $P(hyd) = 0.45$ watts

Pumping efficiency $\eta = \frac{P(hyd)}{P(mech)}$

From the graphs of power versus rotor speed, P(mech) is

found by the intersection of the power curve at wind speed V m/s of the wind turbine when it is not connected to the pump, and the rotor speed obtained at wind speed v m/s when the pump is connected to the wind turbine.

This intersection of the wind-turbine/pump combination at wind speed V m/s is termed its working point.

ERROR ANALYSIS OF MECHANICAL POWER

The formulae for calculating the torque and power, as shown in the previous chapter, are:

$$T = (m - M)\ (r_1 + r_2)\ g \qquad (119)$$

and

$$P(mech) = 2\pi NT/60 \qquad (120)$$

Hence

$$P(mech) = \frac{2\pi N}{60}\ (m - M)\ (r_1 + r_2)\ g \qquad (121)$$

$$P(mech) = CN\ (m - M) \qquad (122)$$

where $C = \frac{2\pi}{60}\ (r_1 + r_2)\ g$

If we then differentiate eq.(122), we get:

$$dP(mech) = \frac{dP(mech)\ (dN)}{dN} + \frac{dP(mech)\ (dM)}{dM} \qquad (123)$$

$$dP(mech) = C(m - M)\,dN + (-CN)\,dM \qquad (124)$$

Therefore the error in P(mech) is

$$[dP(mech)]^2 = [-C(m - M)\,dN]^2 + [(-CN)\,dM]^2 \qquad (125)$$

The percentage error in P(mech) is,

$$\%\ \text{error in } P(mech) = \frac{dP(mech)\ \times\ 100}{P(mech)}\ \% \qquad (126)$$

Estimated errors in instruments:

M = dynamometer mass reading = $\pm$ 0.05 Kg

N = rotor revolutions = $\pm$ 5 rpm

Using eq.(125) & (126), the error in the maximum power which is available from the wind turbine is calculated as shown in table (103)

ERROR ANALYSIS OF PUMP/WIND-TURBINE COMBINATION

The mechanical efficiency of a pump is defined as:

$$\eta = P(hyd) \;/\; P(mech) \qquad (127)$$

where P(hyd) = nett power to lift the water (= $q \rho_w gh$)

P(mech) = mechanical power driving the pump

(i.e power from the rotor)

It is assumed that the error in the flowrate obtained is approximately $\pm$ 0.5 cc/min, due to friction losses in pipes and bends. This could however be eliminated by proper design and positioning of the pipes and tubes coupled to the wind-turbine.

Then since $P(hyd) = q \rho_w gh$

where ρ_w, g and h are constants and q is in m^3/s.

Then differentiating we get,

$$dP(hyd) = \frac{dp(hyd)}{dq} \times dq \qquad (128)$$

Therefore $$dP(hyd) = \rho_w gh\,(dq) \qquad (129)$$

hence error in P(hyd) is,

$$\left[dP(hyd)\right]^2 = \left[\rho_w gh\; dq\right]^2 \qquad (130)$$

Now since $$\eta = P(hyd) \;/\; P(mech)$$

Then error in pump efficiency is found by differentiating equation (127)

i.e $$d\eta = \frac{\dfrac{d\eta \times dP(hyd)}{dP(hyd)} - \dfrac{d\eta \times dp(mech)}{dP(mech)}}{\left[P(mech)\right]^2} \qquad (131)$$

Therefore $$d\eta = \frac{\frac{dP(hyd)}{P(mech)} + \frac{dP(mech)}{P(mech)}}{\left[\frac{P(mech)}{P(mech)}\right]^2} \quad (132)$$

Therefore $$d\eta = P(mech) \times dP(hyd) + dP(mech) \quad (133)$$

Hence error in pump efficiency is:

$$\left[d\eta\right]^2 = \left[P(mech) \times dp(hyd)\right]^2 + \left[dP(mech)\right]^2 \quad (134)$$

Now from the previous section (error analysis of P(mech)) and Table(103), the error in mechanical power is:

at V = 5.0 m/s error in dP(mech) = 3%

at V = 7.5 m/s error in dP(mech) = 1%

at V = 4.1 m/s error in dP(mech) = 0.4%

Then using the above data and equation (134), the error in η is calculated as shown in Table (101).

ERROR ANALYSIS OF POWER COEFFICIENT (Cp)

The power coefficient is defined by:

$$Cp = P(mech) / P \quad (135)$$

where P = the power available to the windturbine from the wind.

$$P = \frac{1}{2} \rho(air) \times V \times \pi R$$

where V = undisturbed wind velocity (m/s)

and R = windturbine radius (m)

Now the wind velocity was measured using a pitot-static tube and a micro-manometer in mm of water. This is converted to (m/s) using,

$$V^2 = 2gh / \rho(air)$$

where h = manometer reading (mm of water)

substituting, we get:

$$P = \frac{1}{2}\,\rho(\text{air})\;\pi R\left[(2\times 9.81\times h)/(1.19)\right]^{\frac{3}{2}} \qquad (136)$$

Therefore

$$P = \frac{1}{2}\,\rho(\text{air})\;\pi R\,(h)^{\frac{3}{2}}\;(66.95) \qquad (137)$$

Hence

$$P = D\,(h)^{\frac{3}{2}} \qquad (138)$$

where $D = \frac{1}{2}\,\rho(\text{air})\;\pi R\;(66.95)$

Now from equation (121)

$$P(\text{mech}) = \frac{2\pi N}{60}\,(m - M)\,(r_1 + r_2)\,g$$

Let $A = 2\pi\,(r_1 + r_2)\,g$

and $B = Am$, then

$$P(\text{mech}) = BN - ANM \qquad (139)$$

where A and B are constants.

Then substituting equations (138) & (139) into (135), we get

$$Cp = \frac{BN - ANM}{D\,(h)^{\frac{3}{2}}} \qquad (140)$$

Hence error in Cp is found by differentiating equation (140)

$$dCp = \left(\frac{Bh^{-\frac{3}{2}}}{D} - \frac{ANh^{-\frac{3}{2}}}{D}\right)dN + \left(-\frac{ANh^{-\frac{3}{2}}}{D}\right)dM + \left[\frac{BN}{D}\left(-\frac{3h^{-\frac{5}{2}}}{2}\right) + \frac{ANM}{D}\left(\frac{3h^{-\frac{5}{2}}}{2}\right)\right]dh \qquad (141)$$

$$dCp = \frac{h^{-\frac{3}{2}}}{D}\,(B - AM)\,dN + \left(-\frac{ANh^{-\frac{3}{2}}}{D}\right)dM + \frac{3Nh^{-\frac{5}{2}}}{2D}\,(B + AM)\,dh \qquad (142)$$

Then the error in Cp is,

$$\left[dCp\right]^2 = \left[\frac{h^{-\frac{3}{2}}}{D}(B - AM)\,dN\right]^2 + \left[\left(-\frac{ANh^{-\frac{3}{2}}}{D}\right)dM\right]^2 + \left[\frac{3Nh^{-\frac{5}{2}}}{2D}(B + AM)\,dh\right]^2 \qquad (143)$$

Now the values of the constant terms are calculated using the following data:

r = fixed pulley radius = 0.076m

r = rope radius = 0.002m

R = rotor radius = 0.320m

then A = 0.082

and D = 12.82

Estimated error in instruments:

M = dynamometer mass = $\pm$ 0.05 kg

h = micro-manometer reading = $\pm$ 0.2 mm of water

N = rotor revolutions = $\pm$ 5 rpm

Using the experimental results and data for maximum power, the error in the power coefficient (Cp) is calculated using equation (143), as shown in Table (104).

DISCUSSIONS OF RESULTS AND CONCLUSIONS

CHAPTER EIGHT

DISCUSSION OF EXPERIMENTAL RESULTS AND CONCLUSIONS

Great care has been taken in order to achieve, as near as possible, a consistent air-flow from the wind turbine. But due to the slightly pulsating flow in the wind-tunnel and the fact that the same flow conditions could not be repeated consistently once the power had been switched off, it was found that the wind-tunnel had to be left running for at least one hour before any sensible reading could be taken.

Experimental results were obtained from various tests, viz:- air-flow stabilization, pressure distribution on the sail at different angles of attack, flow visualization over the sail at different angles of attack, tests on both unaugmented and augmented rotor, flow visualizations around the augmented rotor, and finally tests on fully-augmented wind turbine/pump combination.

In order to study the static and dynamic behaviour of the wind turbine, when it is either rotating on its own or coupled to a peristaltic pump, its response will depend largely on the intensity of the air-flow approaching it and the corresponding shape of the air velocity-profile.

WIND VELOCITY PROFILE INSIDE THE TEST-SECTION

All tests for this part of the project were performed at a chosen wind speed of 5 m/s (the average wind speed in the U.K). Velocity traverses were done across and along the test section with the help of a pitot static tube and a micro-manometer. Readings were taken at various points inside the test section.

Initial tests (see Graph 1) showed that the velocity profile was almost parabolic, but "inwards". This indicated that the velocity was a minimum at the centre of the wind-tunnel. Graph 1 also showed that the maximum values of the velocity profile occur away from the centre, i.e.near the wall section of the wind-tunnel. Normal experimental and theoretical data suggests that the maximum air velocity for any wind tunnel, either open-ended or closed section, should occur at its centre.

Even after various modifications were considered and employed (see Chapter six) in order to improve the situation, a perfect velocity profile was very hard to achieve. This discrepancy was attributed to the fact that the fan speed was inconsistent and that parts of the seven blades (of the fan) had been cut away. Maximum values for the velocity profiles at the centre of the wind tunnel were finally attained but fluctuations still occurred at the wall section (as shown in Graphs 2 to 7).

SURFACE VISUALIZATION OF SAIL AT VARIOUS ANGLES OF ATTACK

In order to obtain an indication of the qualitative behaviour, i.e. whether laminar, turbulent or mixed flows occured when the air passes over and under the sail, a photographic technique was employed.

As adequate lighting was needed both to work on the model and for photographic purposes, three floodlights were installed round the window section of the wind-tunnel.

A sail of 300 x 280 mm with a 1% slack (i.e. 1% of the length) was cut out. A set of "short lengths of wool" of 70 mm long and approximately 2 mm in diameter was then stuck on each side of the sail using Evo-stick glue. Wool was chosen because it is a basically light-flexible material that aligns itself with the local surface flow. The prepared sail was then mounted on to the two rods inside the test-section (see Fig.41). With a constant wind speed of 5 m/s, the angle of incidence, α, was varied at 2.5 degree intervals and a photograph was taken for each value of (see Plates 2 to 17).

From Plate 2, at an angle of attack of zero degrees, it is seen that the air flows smoothly at the leading edge of the sail. But at about three-quarters of the way down, the shape of the airfoil changes to an inward

curve. This is because the pressure on the upper surface (in that region) exceeds that of the lower surface and what then results is a negative lift.

As the angle of incidence is increased to 2.5° (Plate 3), the sail has taken the shape of a typical aerofoil. The lift is now positive and the flow around the sail appears to be in a smooth stream line except at the trailing edge, where some form of disruption seems to occur.

This disruption at the trailing edge is witnessed for all angles of incidence between 2.5 and 15° (Plate 3 to 8). The reason for the latter behaviour is that the fluid has the tendency to "go round" the sharp edge. However, it can be said that the fluid does not like this process, because a relatively high velocity is required at the trailing edge where the two fluid streams meet each other (22). Instead, a vortex is created at the sharp edge, and it is followed by a discontinuity, or vortex sheet.

As the angle of incidence is further increased from 2.5 to 15 degrees (Plates 3 to 8) the lift increased gradually and no seperation of the flow was noticed on either side of the sail (apart from the trailing edge). The maximum angle of attack that could be attained without any any disturbance on the main body of the sail was 15°.

When α was set at 17.5°, (Plate 9) slight fluctuation on the top surface of the sail became apparent. This was probably due to the fact that the sail had stalled and that flow separation had taken precedence.

The effect of this flow separation became more noticeable at higher angles of attack (Plates 10 to 12). It quickly spread upstream from the trailing edge and consequently destroyed the suction peak. This caused a loss of lift and any increase in the angle of attack reduced the lift still further (Plates 13 to 17).

From Plates 14 to 17, it can be seen, that as the contour of the sail became highly curved, particularly over the rear portion, the more readily did the air flow cease to follow the contour, and transition to turbulence occurred over that part of the sail. At these angles of incidence (i.e. for $\alpha > 35^{\circ}$), the shape of the sail as an aerofoil was completely destroyed and the whole configuration was flappling quite violently.

FLOW-VISUALIZATION ON SAIL (SMOKE-TEST)

With a plain sail (i.e. no tufts) of the same dimension as above, and a wind speed (5 m/s) chosen, smoke was injected from a smoke generator via a hole in the wind tunnel (see Fig.41). Again photographs were taken, but

because of the size of the test-section and the strength of the wind inside it, the smoke just disintegrated and blew away. Hence, no comparison could be made with the above tests. It was also hoped that the smoke combined with aluminium dust particles would help in tracing the flow pattern around the sail.

PRESSURE DISTRIBUTION OVER AND UNDER SAIL SURFACES.

For this part of the experiment, a sail of the same dimensions as that used previously (see surface-visualization tests). A set of hypodermic tubes (ten in all) were glued to each side of the sail and their ends connected to a multi-manometer. The wind speed was set at 5 m/s and the angle of attack of the sail was varied from 0 to 20° at 2.5° intervals.

All pressure reading were converted (22) into corresponding values for the pressure coefficient (Cp) using the simple equation:-

$$Cp = \frac{P - P_{\infty}}{1/2\ \rho\ V_{\infty}^2} = 1 - \left[\frac{V}{V_{\infty}}\right]$$

where P and V are local pressure and velocity,
and P_{∞} and V_{∞} are free-ream pressure and velocity respectively.

The pressure coefficients were then plotted against X/C, where X and C are the distance from the leading

edge and the chord length respectively. By convention, negative values of Cp were plotted above the horizontal axis (see Graphs 8 to 16).

It was seen in the surface-visualization techniques (see Plates 2 to 17) that the load (i.e. pressure) over and under the sail surfaces varied with the angles of incidence. Graphs 8 to 16 show the pressure distributions round the sail as the angle of attack was varied. These graphs should be interpreted as showing the general nature of the variations and not as being quantitatively accurate in detail (because of the weight and probable interference of the hypodermic tubed).

From Graph 1, with $\alpha = 0^{\circ}$ it is seen that the pressure on the upper surface exceeds that on the lower surface and as a conseqence, a negative lift is produced. The same effect can be seen in Plate 2, where the rear half of the sail curved inwards.

As the angle of incidence was increased to 2.5° (Graph 9), the shape of the sail changed and the readings indicated that a reversal in pressure difference had occurred. This time the lift was positive and as before (see Plate 2) the sail took the shape of a typical aerofoil.

However, between α = 0 and 2.5° (see Plate 2 and 3, and Graphs 8 and 9), a transition in the shape of the rear half of the sail ensued, i.e. from an inward curve to an outward one, had occured. This would have been the region where the net area enclosed by the curve of Cp versus X/C would have been zero. What really happens is that both surfaces of the sail experience both positive and negative lift. These lifts cancel each other and what then results is a zero lift situation.

In Graphs 9 to 14, the lift increases steadily with the angle of incidence up to a certain value, α = 15° in our case. This rise in lift is mainly due to circulation which creates a higher velocity (lower pressure) at the upper surface, and a lower velocity (higher pressure) at the lower surface of the sail. In this manner a positive lift is produced. Before the experiments, the impression was that the air hits the inclined sail and the sail is therefore pushed up by the air below. It is now seen, Graphs 10 to 14, that the sail is at least partially sucked up by the air passing along the upper surface. As a matter of fact, the contribution to the total lift from the negative pressure or suction developed at the upper surface is larger than the contribution from the positive pressure at the lower surface.

The pressure started to drop once the angle of incidence exceeds 15°. From there on (Graphs 15 and 16) the sail began to lose its lift. This is depicted by the decrease in the size of the Cp for values of α beyond 15°. This sudden flattening of the upper surface pressure distribution at high incidence is due to flow separation. The effect of this separation quickly spreads upstream from the trailing edge, and destroys the suction peak. This causes a loss of lift, and further increases in incidence reduce the lift stillfurther.

THE LIFT CURVE

The Cp against X/C curve (see Graphs 8 to 16), helped in drawing a curve of the lift coefficient (C_L) versus angle of attack (α). The reason for this is that the total area enclosed by the Cp versus X/C curve gives directly the value of the lift coefficient, C_L (see the proof presented in Appendix 7). A planimeter was used to measure the areas of both the upper and lower surfaces in each graph (8 to 16). The difference between the two gave the lift coefficient for that particular angle of attack. The whole graph of C_L versus α, which is known as the lift curve, is shown in Graph 17.

This graph indicates the way in which the lift coefficient of the flexible aerofoil varies with angle of incidence.

At an angle of attack of zero degrees, it is seen that the lift is negative. As the incidence increases, the curve behaves in a linear fashion over a considerable range (i.e. between $\alpha = 2.5$ and 15°), reaching a maximum value of $C_L \approx 1.075$. As the effect of separation begins to be felt, the slope of the curve begins to fall off. The angle at which the curve begins to decrease is the stalling angle.

One important point to note is that no tests were done on the pressure distribution over and under the sail surfaces for values of α between 0 and 2.5°. From Graph 17, it is apparent that the curve crosses the horizontal axis at an angle of attack which lies between the two. This angle would have been the position at which zero lift occurred.

TESTS ON THE FULLY-AUGMENTED WIND-ROTOR

In order to ascertain the effectiveness of the tested augmentation devices (i.e. centre-bobies and tip-fins), all performance curves include the power characteristics of the unaugmented rotor for direct comparison.

TESTS USING CENTRE-BODIES: Three hub-fairing and two after-bodies (see Fig.48) were tested on the flexible-sail type wind rotor; Graphs 18, 19 and 20 show their power characteristics. The rotor was augmented using rotating and stationary hub-fairings, with and without stationary after-bodies. Compared with the performance of the unaugmented rotor, the presence of the centre-bodies led to increased maximum power outputs. Stationary hub-fairings resulted in greater power increases than rotating ones, whereas all three fairings gave virtually the same power augmentation. The system consisting of a rotating hub-fairing and after-body gave a power increase of approximately 28% over the unaugmented rotor, but when the hub-fairing was stationary the resulting power augmentation was approximately 41%.

From graphs 18, 19 and 20,it is apparent that the presence of an after-body also contributes to the rotor's power harnessing capabilities. But as Blaha (28) suggested,

its exact shape is relatively unimportant - the after-bodies tested in this investigation (see Graphs 19 and 20) resulted in almost similar performance curves and corroborate Blaha's contention.

These graphs also indicate that the shapes of the three hub-fairings, chosen as the most suitable of those available, are relatively unimportant despite their different weights and size ratios, because their power outputs are virtually identical. Graphs 19 and 20 show that the power characteristics from the wind-rotor and after-body only are almost identical to those for the rotor with the rotating hub-fairing, suggesting that a relatively cheap alternative to the conventional centre-body is the use of an after-body only.

The differences between the power outputs from the rotating and stationary hub-fairing augmented rotors are due partly to the rotating fairing increasing the mass of the rotor and partly to the increase in the frictional forces compared with those incurred by stationary hub-fairings.

As it was found that the shapes of the centre-bodies had little effect in enhancing the power outputs of sail-type wind-turbines, only one configuration i.e. with the hub-fairing S2 and after-body A2 (see Fig.48, and Plate 18), was subsequently used.

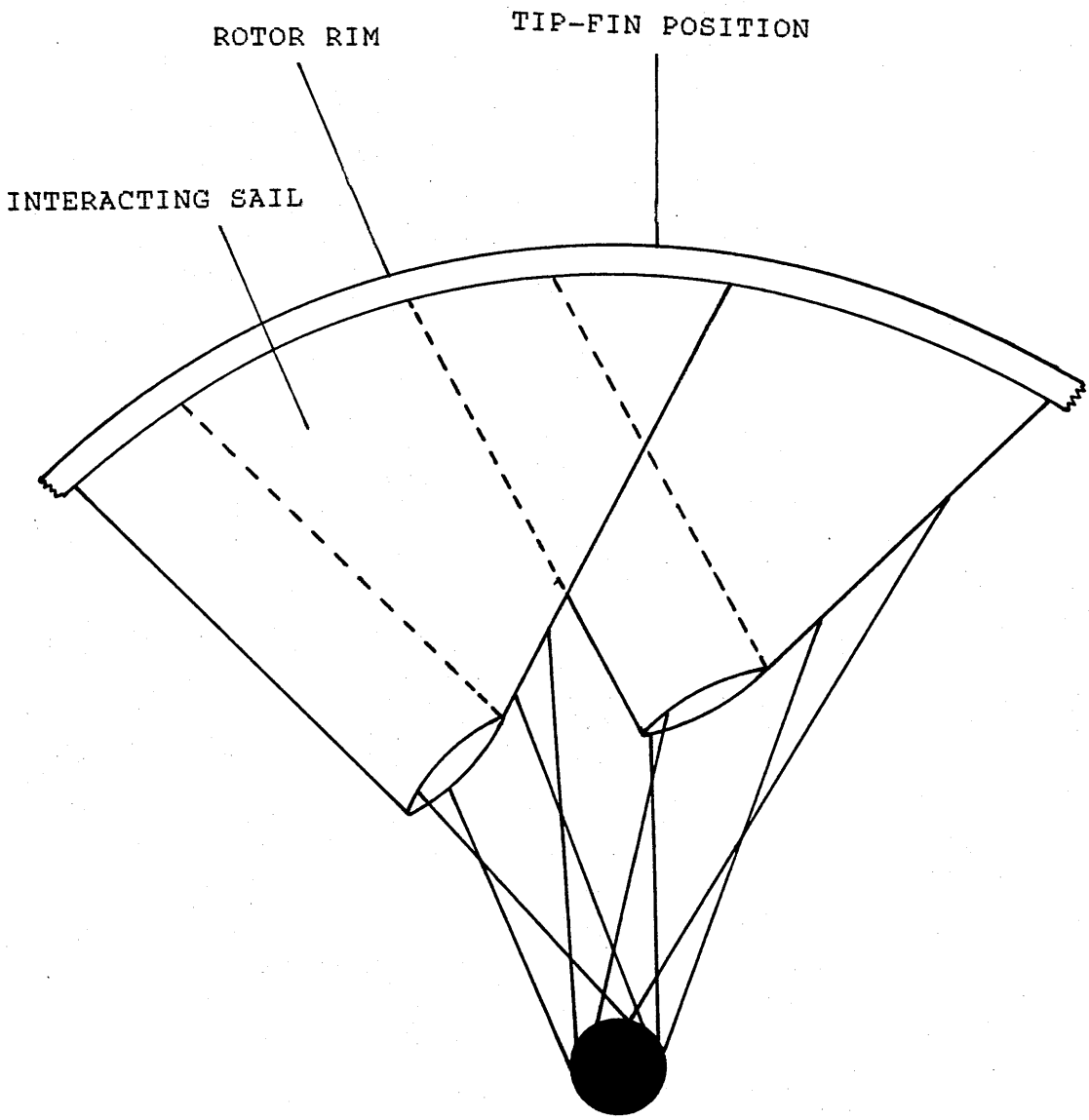

Fig. 46 Rotor segment showing tip-fin position.

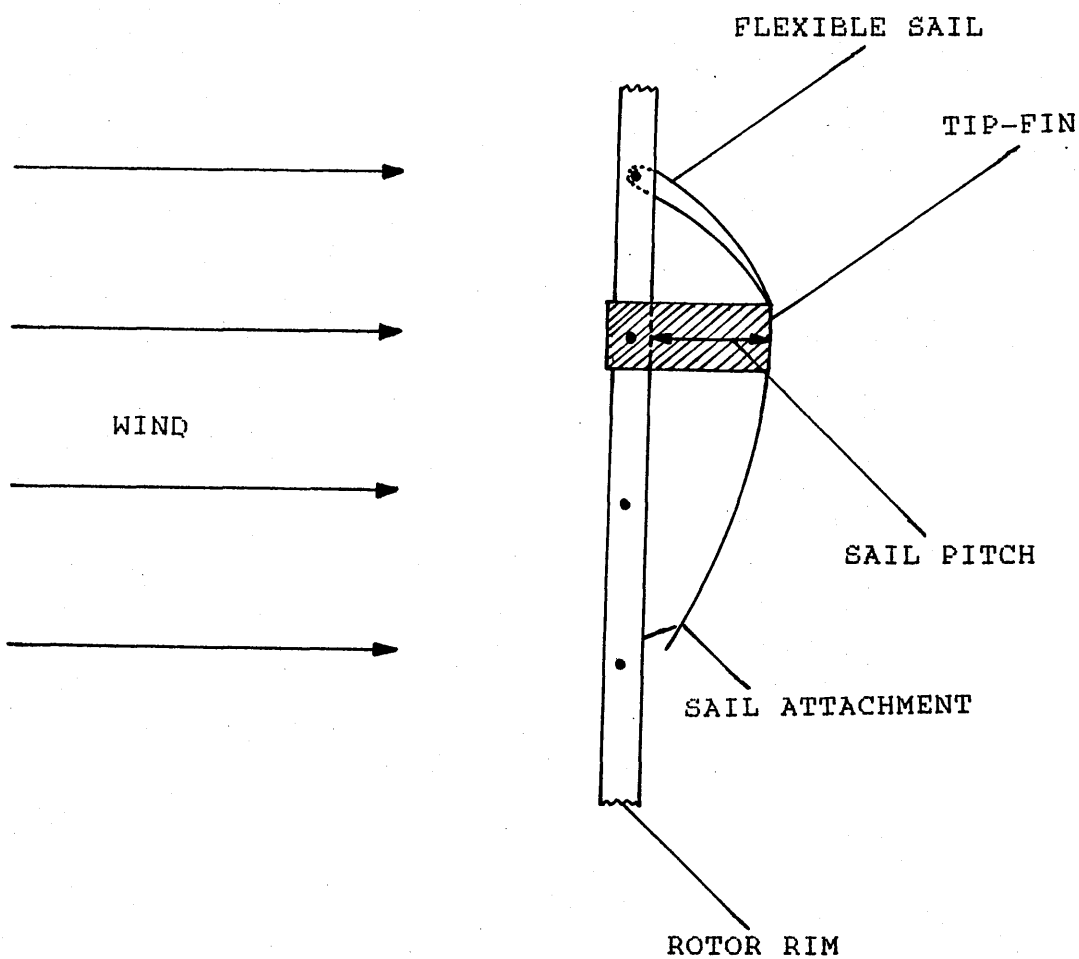

Fig. 47 Tip-fin position tested and sail profile (the four dots on the rim represent anchorage points for the wheel spokes).

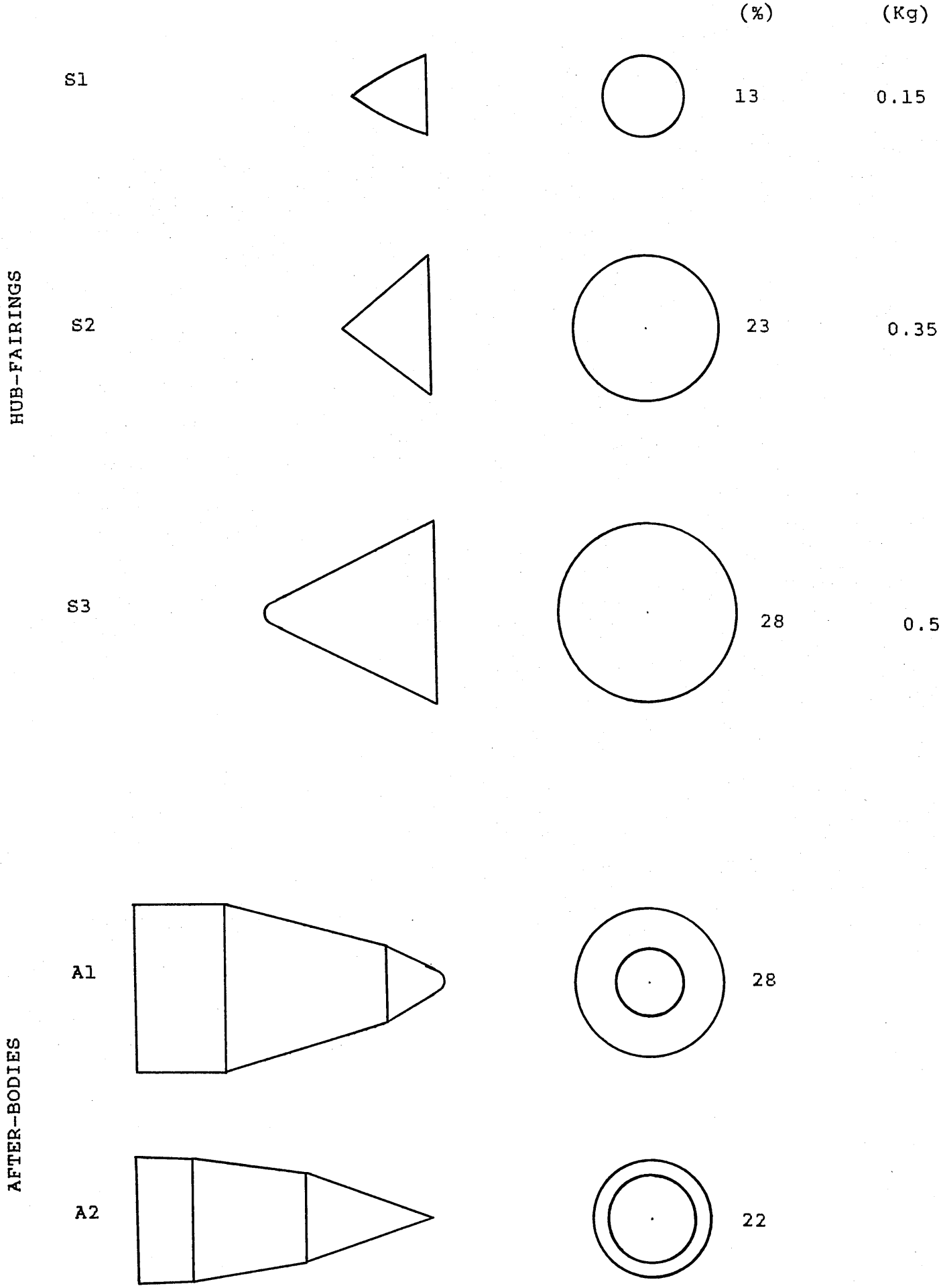

FIG. 48 Dimensions of tested hub-fairings and after-bodies.

TESTS USING TIP-FINS: The tip-fin tests were performed with the wind-rotor augmented by tip-fins as shown in Fig.46 and 47. Fleming and Probert (31) found that the tip-fins resulted in increased power if they were placed in the position shown in Fig.46. It corresponded to where the sail displacement - the horizontal distance between the rim and the considered zone of the sail - was anticipated to be greatest (this is conveniently referred to as the sail pitch (see Fig.47)).

The cycle wheel utilised as a framework for the sails contained thirty-six spokes. Nine sails were adopted, each overlapping the next (sail) one by three spoke spaces (i.e. the distance between three spokes). One tip-fin was bolted on to the wheel rim where the sails start to overlap each other (and hence the adoption of nine tip-fins) as shown in Plate 1.

Fifteen different types of tip-fins, designated 1 to 15 (see Fig.49) were tested, with each tip-fin located as shown in Fig.46. The power characteristics are plotted in Graphs 21 to 30. In all these graphs it is apparent that if the rotor is augmented with tip-fins an increase in power output is achieved. The use of rotating hub-fairing, centre-bodies (with rotating hub-fairings), after-bodies and stationary hub-fairing, all lead to improvements in the performance of the tip-fin augmented rotor. As can be seen

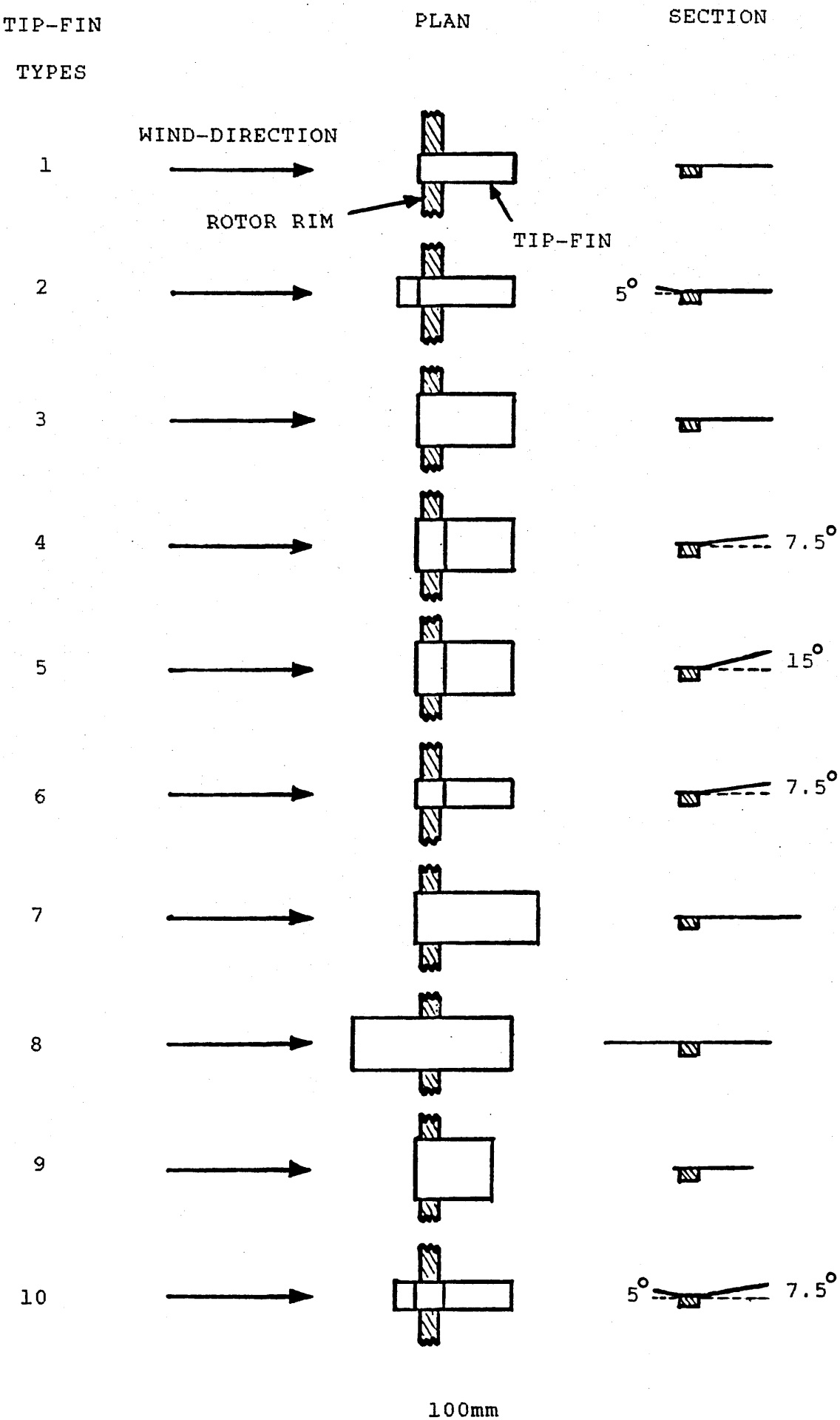

Fig.49 Tested tip-fins (actual thickness is 1.5mm).

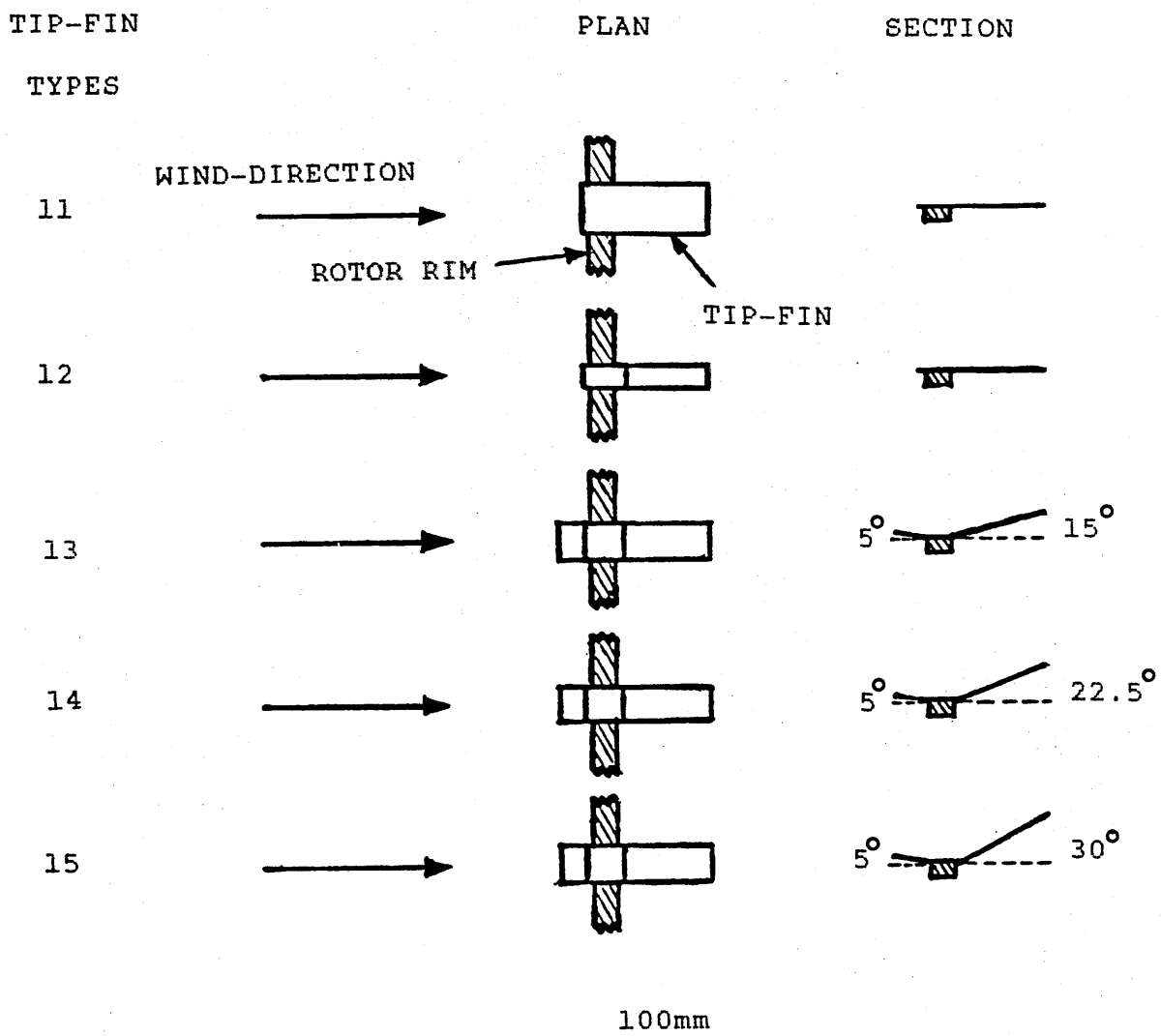

Fig.49(ctd) Tested tip-fins.

from graphs 21 and 30, the maximum powers were obtained when the rotor was augmented with tip-fins, a stationary hub-fairing and a stationary after-body.

The first test was carried out with tip-fin type 3 (Fig.49), which is flat with the dimensions 100 x 50mm, projecting downwind of the rotor. Previous investigations (31) on the latter fin has shown that it gave the maximum power of those investigated. From graph 23, we see that there is an increase in power output over the unaugmented rotor of about 69%. The reasons for this power increase are because the fins were approximately the same length as the sail pitch (Fig.47) and that they interacted with the trailing vortices emanating from the rotor sails thus deflecting the air that would normally spill out of the sail, towards the centre-line i.e. on to the sail. When the above tip-fin width was halved (tip-fin type 1, Fig.49), an even bigger increase was recorded (graph 21). This was due to the overall mass being reduced and hence a reduction in induced drag forces. The type 7 tip-fin being longer but of the same width (50mm) induced greater drag forces on the rotor, reduced its rotational speed and so harnessed slightly less wind energy (i.e. leading to a 66% increase in maximum power output). Tip-fins type 8 (see Fig.49) protruding from both sides of the windwheel were tested . A power enhancement of about 64% was obtained (graph 28). This tip-fin was of the same width (50mm) as type 3. The lower

power enhancement was again due to a larger drag force being caused by the tip-fin protruding from both sides of the windwheel. With tip-fin type 9, which was of the same width as type 3 but shorter in length, a smaller increase in power output was also noticed (graph 29) i.e. a maximum power enhancement of 60%. Due to their relatively short projection over the rotor rim, air was able to spill out of the sail, over the fin and so be less diffused downstream.

The effect on the performance of the wind rotor when augmented with angled tip-fins projecting downstream (i.e. tip-fins type 4, 5 and 6) was next investigated. Types 4 and 5 were of the same dimensions as type 3 but angled at 7.5° and 15° respectively. They both resulted in a reduced power output compared with that from type 3. Tip-fin type 6 (width 25mm) configuration involved the fin projecting downwind at an angle of 7.5° and gave still less power enhancement than type 3 (Graph 26).

As type 1 gave the maximum power, considerable attention was given into optimising this shape in order to improve the performance of the wind rotor still further. Five sets of nine tip-fins were cut, each with the same length (100mm) as type 1 projecting downwind but with an additional length of 20mm upwind angled at 5° (see tip-fins type 2,10,13,14, and 15 (Fig.49). The upwind angle (i.e. 5°) was kept constant but the downwind angle was varied. What

then resulted was a venturi effect. The incoming wind converged towards the sails due to the slight upwind angle. Acceleration of the wind then occurred at the rotor and finally the wind was diffused behind the rotor. In just the same manner in which the diffused angle of the venturi meter is determined according to the diameter of its throat, the optimal tip-fin angle is also determined according to the rotor diameter. For the rotor tested it was found that the best angle downwind was 7.5° (tip-fin type 10).

When an optimisation of the tip-fins were done using the data for the fifteen tip-fins tested, it was apparent (Graphs 31 and 32) that the best shape would be the one of width 25mm, length 100mm, projecting downwind at an angle of 7.5° and a short length upwind (say 20mm) at a slight angle (say 5°).

FLOW BEHAVIOUR ACROSS A FULLY-AUGMENTED WIND-TURBINE.

Having fully optimised the wind-rotor, an attempt was made in order to understand the air-flow behaviour as it passes through the rotating turbine. To achieve our aim, a smoke-tube was used together with the equipment shown in Plate 19. The smoke obtained was not as dense as was expected but sufficiently visible to be photographed.

All the flow-visualisation tests were done when the wind-turbine was fully augmented, and the magnitude of the approaching air was 5 m/s. The sail angle of attack was 15 degrees.

From the smoke test obtained (see Plates 20 to 31), it is found that the results agree to a fair extent with the theory of air-flow through a wind-turbine.

Plates 20 to 23 show the behaviour of the air through the interacting sails from the rotor hub to the tip of the rotor. It is found that the flow is fairly laminar and that flow separation occurs at the edge of the over-lapped sail. The air flow starts to become turbulent and speed is reduced after it has passed through the sails. This can be seen by the expansion of the smoke streams towards the edge of the over-lapped sail.

From Plates 23 to 28 it can be seen that the air flow near the rotor tip diverges away from the main stream flow and flows away from the top of the sails. This enforces the argument that the effect of using tip-fins does help in widening the stream-tube downwind of the rotor as explained in chapter four (see also Fig.32). Plate 25 shows a similar phenomenon which occurs when the wind-turbine is rotating.

Another reason for the deflection of the air flow may be due to the high pressure-differential across the sail and across the air in the mainstream and rotor. The pressure on the windward side of the sail is higher than the mainstream air pressure and hence at the rotor tips, the air tends to flow outwards.

The wake of the wind-turbine is shown in Plates 24 to 31, which consists of a different head from the mainstream. This wake is made up of a vortex tube of increasing radius downstream together with a central vortex and free vortices at the rotor tips, which produce the induced velocity components.

The flow around the stationary after-body is a vortex flow which is rather turbulent, as shown by the smoke trace in Plates 29 to 31.

APPLICATION OF FULLY-AUGMENTED WIND-ROTOR FOR WATER PUMPING

All tests in this section were performed with the rotor augmented with the best devices found in the previous set of experiments (i.e. stationary fairing S2, after-body and Tip-fins 10 as shown in Figs.48 & 49).

All graphs of the augmented wind-turbine/pump combination are represented at different wind speeds, varying from 3.7 m/s to 11 m/s.

The peristaltic pump used for this purpose (i.e. water pumping) is shown in Fig.39 and its description is outlined in chapter 5.

In order to examine the pumping characteristics of the wind-turbine, the combined system was tested at different wind speeds with the sail angle of attack set at 15 degrees. Graph 34 shows that the output of the pump behaves linearly with the rotor speed. This is expected due to the following relationship:

$$\eta = P(hyd) \;/\; P(mech) \qquad (117)$$

where $P(hyd) = q\,\rho_w g h$

and $P(mech) = 2\pi i N T/60$

$$= 2\pi i N\,(m - M)(r_1 + r_2)g \;/\; 60$$

Therefore $$\eta = \frac{q\,\rho_w g h}{2\pi i N\,(m - M)(r_1 + r_2)g \;/\; 60} \qquad (144)$$

Or $$\eta\,(m - M)(r_1 + r_2)g\pi i N = 30 q\,\rho_w g h \qquad (145)$$

From equation (145), it can therefore be seen that the flow-rate q is proportional to the rotor speed N.

Table (100), shows that as the wind speed is changed from 3.7 m/s to 4.1 m/s, only a slight increase (i.e. 9%) in water flow-rate is noticed. However, as the wind speed is further increased from 4.1 m/s to 5 m/s, a 73% rise in flow-rate is achieved. From there on, i.e. from 5 m/s to 11 m/s, the output increased steadily but not to such change.

It was observed that the combined system operated when the wind speed was adjusted to 3.7 m/s (i.e. the cut-in wind speed). At this speed, visual observation confirmed that the shape of the sail was not fluctuating at any point. Smoke-test results (see Plates 20 to 31) show that at 5 m/s, the sail behaved in a manner similar to that of a rigid aerofoil and that the air flow through the interacting sails was nearly uniform and flow separation occured towards the edge of the overlapped sail. The results gave an insight into the behaviour of the system.

At higher wind speeds, i.e. V > 5 m/s, it was observed that as the wind speed was increased, the bottom of the sail began to fluctuate quite moderately and became very violent at the maximum tested wind speed of 11 m/s. At V = 11 m/s, the centre of some of the sails became

"indented", and it was suspected that this behaviour was either due to the high level of turbulence in the wake or the back-flow of air from the pump mounting. The rotor shaft vibrations at this speed were large and this was mainly due to the rotor shaft mounting design (see Fig.43).

It is explained in Chapter five how the wind-turbine/pump system behaves at different wind speeds. Graph 35 shows the matching of the fully-augmented wind-turbine's power curve to the power curve of the combined system at different wind speeds. The aim of illustrating these curves is to determine the working point of the wind-turbine/pump combination at different wind speeds.

From table (101) and graph 35, it is found that at low wind-speeds (i.e., < 4.1 m/s) no worthwhile power can be harnessed from the wind. The power curve, for that particular wind speed, reaches its maximum value at a lower rotor speed as compared to the curves for wind speeds of 5 m/s and over. However, as the wind speed is increased to 5 m/s, the power curve remained the same shape but its output has nearly trebled. The maximum output (10.25 watts) is reached at a rotor speed of around 145 m/s. As the wind speed is further increased to 7.5 m/s, distortion in the power curve is noticed, this was probably due to the vibration in the rotor shaft together with back-flow of air from the pump mounting.

CONCLUSIONS.

The various investigations carried out, on both the flexible sail and the horizontal-axis flexible sails wind-turbine, gave an insight into their behaviours when faced with an oncoming wind. The conclusions thus drawn may be summarized as follows:

The sail

The sail behaves fairly well over relatively small ranges of angles of incidence, i.e. for lying between 2.5 and 15°. Beyond $\alpha = 15^{\circ}$, flow separation takes precedence and at higher angles of attack (namely $\alpha > 25^{\circ}$), the shape of the sail as an aerofoil becomes distorted and the flow is highly turbulent over its surface.

For an angle of incidence of zero degrees, the lift is negative. The lift curve crosses the α-axis between 0 and 2.5° suggesting a zero lift with a positive angle of attack. The lift increases linearly with further increase in α until $\alpha = 15^{\circ}$ where the magnitude of the lift starts to decrease.

FULLY AUGMENTED WIND-ROTOR

The rotor investigations suggest the following:

1. Rotating hub-fairings are capable of augmenting the

power outputs of sail-type wind-turbines.

2. Holding the hub-fairings stationary results in even greater power outputs.

3. An after-body on its own (without a hub-fairing) gives approximately the same power-harnessing capabilities as a conventional centre-body configuration (i.e. rotating hub-fairing and static after-body).

4. The shapes of the hub-fairing and after-body are relatively unimportant with respect to augmenting wind rotor power outputs.

5. The best shape of tip-fin was the one that was about the same length as the sail pitch. This tip-fin had the dimensions 100mm x 25mm. Tip-fins that were much shorter than the sail pitch led to tip losses.

6. Tip-fins that were too long, too wide or protruded from both sides of the rotor, experienced a drag force which reduced their power enhancement.

7. Tip-fins are most effective when placed downwind of the rotor, where they reduce the energy dissipated as trailing vortices.

8. Tip-fins having short length (say 20mm) at a slight angle (say 5°) upwind and a length of 100mm at an angle of 7.5° downwind resulted in a power enhancement of about 60% over the unaugmented windwheel.

9. It is recommended that a centre-body, combination of stationary hub-fairing and stationary after-body, together with the tip-fin mentioned in section 8 above, will lead to power enhancement for the sail-type wind-turbine tested.

FLOW-VIZ. ACROSS FULLY AUGMENTED WIND-TURBINE

The flow is mainly laminar through the interacting sails. Flow separation only occurs at the edge of the over-lapped sail. The use of tip-fins does help in widening the stream-tube downwind of the rotor. The flow around the stationary after-body is a vortex one and rather turbulent.

WIND-TURBINE/PUMP COMBINATION

The tested wind-turbine and pump combination works fairly efficiently from its cut-in wind speed of 3.71 m/s to its cut-out wind speed of 11 m/s. The output of the pump behaves almost linearly with the rotor speed. The minimum rate at which water is pumped by the system is 0.4 l/min at a wind speed of 3.71 m/s and at its maximum wind speed of 11 m/s, the pumping rate is 3.2 l/min.

REFERENCES

REFERENCES

1. W.BRANDT & A.SAMPSON, "North South: A programme for survival", Pan Books, London, 1981.

2. R.RAMAKUMAR, "Harnessing wind power in developing countries", Tenth Inter-society Energy Conversion Engineering Conference, Delaware University, Newark, USA, 1975, pp966-73.

3. E.F.SHUMACHER, "Social and economic problems calling for the development of Intermediate Technology", UNESCO, Conference on the applications of science and technology to the Development of Latin America, Sept'65.

4. S.K.TEWARI, "Economics OF Wind Energy Use for Irrigation in India", Science, vol.202, pp98-122, 3rd Nov'78.

5. SPUR, "The Newspaper of the World Development Movement", New York, Aug'81.

6. M.E.HURTADA & L.JOSEPH, "Third World Water Crisis", the Guardian, 15th April 1981.

7. S.K.TEWARI, "An evaluation of the strategy of low-cost horizontal-axis windmills", Proceedings of the International

Solar energy Congress, Mankind's future source of Energy from the Sun, New Delhi, Vol.3, Pergamon Press, New York, 1948, pp1848-53.

8. E.P.WARNER & S.OBER, "The aerodynamics of yacht sails", Transactions of the society of Naval Architects, Vol.33, pp207-232, 1925.

9. V.CISOTTI, "Moto con scia di un profilo-flessible", Nota I & II, Rendiconti della reale, Acad.Nat.dei Lincei, Vol.15, pp166-173 & pp253-257, 1932.

10. K.VOELZ, "Profil und auftrieb eines segels", Z.A.M.M (30), 301-317, 1950.

11. J.W.BUGLER, "On the application of potential-flow theory to the aerodynamics of sails", Ph.D thesis, College of Aeronautics, C.I.T., Bedford, 1979.

12. B.THWAITES, "The aerodynamic theory of sails I:2-D sails", Proceedings of the Royal Society, Vol.A261, 1961, pp402-422.

13. J.N.NIELSEN, "Theory of flexible aerodynamic surfaces", Journal of Applied Mechanics, Vol.30, pp435-442, 1963.

14. L.G.CHAMBERS, "A variational formulation of the THWAITES

sail equation", Quarterly Journal of applied mathematics, 9(1966), pp221-231.

15. R.BARAKAT, "Incompressible flow around porous 2-D sails and wings", Journal of mathematics and physics, 47(1968) pp327-49.

16. J.P.DUGAN, "A free-stream model of the 2-D sail", Journal of fluid mechanics, 42, pt3(1970), pp433-446.

17. J.O.MYALL & S.A.BERGER, "Recent progress in the analytical study of sails", Aeronautical Sciences Division, University of California, Berkeley, 1969.

18. J.M.VANDEN BROECK, "Non-linear 2-D sail theory", the physics of fluids, 25(3) (1982) pp420-423.

19. C.A.MARCHAJ, "Sailing theory and practice", Adlard Coles Ltd., London, 1979.

20. "Seminar on problems associated with mast design", S.U.Y.C., Southampton University, 1962.

21. C.A.MARCHAJ, "Aero Hydrodynamics of sailing", Adlard Coles Ltd., London, 1979.

22. H.GLAUERT, "The elements of aerofoil and airscrew

theory", Cambridge University Press, London, 1983.

23. E.H.LYSEN, "Introduction to wind energy", Steering Committee for Wind Energy in Developing Countries, Amersfoort, The Netherlands, 1983.

24. R.E.WILSON, P.B.S.LISSAMAN & S.N.WALKER, "Aerodynamic performance of wind turbines", June 1976, Energy Research and Development Administration (Division of Solar Energy).

25. H.GLAUERT & W.F.DURAND(ed), "Aerodynamic theory 'Airplane Propellers', Vol.5, Division J-M, chapter 5, section 4, pp169-360, Julius Springer, Berlin, 1935.

26. W.JANSEN & P.SMULDERS, "Rotor design for horizontal axis windmills", Steering Committee for Wind Energy in Developing Countries, Amersfoort, The Netherlands, 1977.

27. W.JANSEN, "Horizontal-axis fast running wind turbines for developing countries", Steering Committee for Wind Energy in Developing Countries, Amersfoort, The Netherlands, 1976.

28. R.BLAHA, "The effect of a centre body on axial flow windmill performance", AMS Report 1266, Princeton University, New Jersey, 1978.

29. H.J.STEWART, "A simplified Two-Dimensional theory of thin aerofoils", Journal of the Aeronautical Sciences, Vol.9, 1942, pp452-456.

30. L.PRANDTL, The essential of fluid dynamics", Blackie, New York, 1952.

31. P.D.FLEMING & S.D.PROBERT, "Power augmentation of cheap, sail type, horizontal axis wind turbines", School of Mech. Eng., Cranfield Inst. of Technology, Cranfield, Bedford, Great Britain.

32. A.BETZ, "Windmill in the light of modern research", N.A.C.A. Technical Memorandum, No.474, from: Die Naturwissenschaften, XV(46), 1927.

33. O.IGRA, "Research and development for shrouded wind turbines", Energy Conservation and Management, 21(1)1981, pp.13-48.

34. TH.VAN HOLTEN, "Performance analysis of a windmill with increased power due to tip-vane diffusion of the air stream", Memorandum M-224, Techniche Hogeschool, Delft, the Netherlands, 1974.

35. TH.VAN HOLTEN, "Concentrator systems for wind energy, with emphasis on tip-vanes", Wind Engineering, 5(1)(1981),

pp.29-45.

36. A.H.DEKKER, "Performance characteristics of some sail and steel bladed wind-rotors", Steering Committee for Wind Energy in developing countries, Amersfoot, the Netherlands, 1977.

37. T.J.ROBERTSON "Private Communication", January 1984.

38. N.G.CALVERT, "The characteristics of a sail mill", Transactions of the Newcomen Society, 1972, London.

39. A.POPE & J.J.HARPER, "Low Speed Wind Tunnel Testing", John Wiley & sons, New York, 1984.

40. S.N.WALKER, "Performance and optimum design analysis / computation for propeller_type wind turbines", Ph.D thesis, Oregon State University, May 1976.

41. B.THWAITES, "Incompressible aerodynamics", Southampton University, 1959.

42. G.W.W.PONTIN, "A first-order mathematical model of the lift/drag characteristics of aerofoil sections", Wind Engineering, Vol.5, No.3, 1981, pp147-153.

43. U.S.NASA, "Aerodynamic design of axial flow

compressors", 1952.

44. I.E.JONES, "Power augmentation of a Savonius-type wind turbine for water-pumping applications", MSc thesis, 1982, Cranfield Institute of Technology.

45. A.D.GARRAD, "Dynamics of wind turbines", E.T.S.U. Harwell, January 1985.

46. R.W.MILLER, "Flow measurement engineering handbook", the Macmillan Press Ltd., 1979.

47. A.VOLLAN, "Aeroelastic stability and dynamic response calculations for wind-energy convertors", Wind Engineering, 3(1) (1979), pp427-444.

48. C.A.MARCHAJ, "Sailing theory and practice", Adlard Coles Ltd., London, 1976.

49. P.W.O'CALLAGHAN, "Energy SCENE", C.I.T. Computer Programme, S.M.E. Cranfield, 1984.

50. D.W.BRYER & R.C.PANKHURST, "Pressure-probe methods for determining wind speed and flow direction", Pergamon Press, New York, 1976.

51. B.McWILLIAMS, M.M.NEWMAN & D.SPREVAK, "The probability

distribution of wind velocity and wind direction", Wind Engineering, V3, 4, pp465-87, 1979.

52. B.McWILLIAMS & D.SPREVAK, "The estimation of the parameters of the distribution of wind speed and direction", Wind Engineering, V4, 4, pp321-49, 1980.

53. I.CEBETI & P.BRADSHAW, "Momentum transfer in boundary layer", Hemisphere, Washington D.C., 1977.

54. R.BETCHOV, "Transition", Handbook of turbulence, Vol.1, pp147-164, Plenum Press, New York, 1977.

55. J.ROBERT & B.G.NEWMAN, "Lift and drag of a sail aerofoil", Wind Engineering, 3(1) (1979), pp1-22.

56. E.O.TUCK & M.HASELGROVE, "An extention of 2-D sail theory", Journal of Ship Research, 16(1972) pp148-52.

57. A.M.De PAOR, "A new theory for the actuator disc and the windmill", Technology Ireland Journal, Institute for Industrial Research and Standards, Dublin, July/August, 1980.

58. C.J.WOOD & S.H.TAN, "Towards an optimum yacht sail", Journal of Fluid Mechanics, 1978, Vol.85, pt3, pp459-477.

59. M.K.HASELGROVE & E.O.TUCK, "Stability properties of 2-D sail model", Society of Naval Architects and Marine Engineers, New England Sailing Yacht Symposium, New London, Connecticut, January 1976.

60. L.W.APPERLEY, "On the improved aerodynamic efficiency of a sailing vessel", 5th. Australian Conference on hydraulics and fluid mechanics, University of Canterbury, Christchurch, New Zealand, December 9 to 13, 1974.

61. T.E.SWEENEY, "Exploratory sail wing research at Princeton", Report 578, Dept. of Eng., Princeton University, 1961.

62. B.S.SHENSTONE, "Unconventional flight", Aeronautical Journal, (72), 655-666 (1968).

63. M.I.GUREVICH, "The theory of jets in an ideal fluid", 1966, New York, Pergamon.

64. L.RALEIGH, "On the resistance of fluids", (1876), Phil. Mag.(5)2,430-41.

65. J.P.DUGAN, "Two-Dimensional potential flow around a flexible membrane", 1966, M.S.Thesis, North Western University.

66. W.E.ARNOLDI, "The principle of minimized iterations in the solution of the matrix igenvalue problem", Hamilton standard division, united aircraft corporation, East Hartford, Conn.,1950.

67. L.PRANDTL, "Hydro Aeromechanics", Dover, New York, 1957.

68. L. PRANDTL & J.TIETJENS, "Applied hydro and Aeromechanics", McGraw-Hill, California, 1934.

69. L.PRANDTL & J.TIETJENS, "Fundamentals of Hydro and Aeromechanics", McGraw-Hill, California, 1934.

70. A.J.SHUTLER, "Cretan Windmill studies", Cranfield Institute of technology, M.Sc. Thesis, Sept. 1979.

71. M.A.BIOT, "Some simplified methods in airfoil theory", California Institute of Technology, Journal of Aeronautical Sciences, vol.9, 1941, pp185-90.

72. L.PRANDTL, "Ueber neuere arbeiten zur theorie der tragenden flache", Proceedings of International Congress for Applied Mechanics, Cambridge, USA, pp478-82, 1938. English translation, NACA, Technical Memorandum, No.962, Dec'40.

73. T.V.KARMAN, "Aerodynamics selected topics in the light of their historical development", Cornell University Press,

Ithaca, New York, 1941.

74. E.D.CHARLES, "Flight theory and aerodynamics", A practical guide for Operational safety, Institute of Safety and Systems Management, University of South California, 1981.

75. M.VAN DYKE, "An album of fluid motion", Department of Mechanical Engineering, Stanford University, Stanford, California, 1984.

76. I.H.ABBOTT & A.E.VON DOENHOFF, "Theory of wing sections", Dover, New York, 1948.

77. R.V.SOUTHWELL, "Relaxation methods in Engineering Sciences", Oxford University Press, Oxford, 1940.

78. O.C.ZIENKIEWICZ & K.MORGAN, "Finite elements and approximation", J.Wiley & sons, New York, 1983.

79. W.C.OSBORNE, "Fans", Pergamon Press Ltd., Oxford, 1977.

80. R.J.GOLDSTEIN, "Fluid mechanics measurements", Hemisphere Publishing, Washington, 1983.

APPENDICES

APPENDIX (1)

WIND TUNNEL

Ac commutator motor (serial number R212480)

Speed 1259/400/20 rpm

Power 9/2/0.1 horse power

Manufactured by:

Thomson-Houston & company Ltd,

Rugby.

Reconditioned by:

R.R.Burton,

Shepton,Mallet,Somerset.

INSTRUMENTS USED

Micro-manometer MDC FC001

Stabilized voltage supply

Electronic counter 15MHz TC12A

Pitot-static tube

Pressure probes

Multi-manometer

Hot-wire anemometers AVM501TC

Smoke generator

Pentax MV1 and tripod

APPENDIX (2)

MICRO-MANOMETER DATA

Calibration temperature	23°C
Input voltage	240V
Output voltage	0-1.00V
Dial marking pressure	0-30% & 0-100%
Slow time constant	2 secs.

Accuracy of 1% in any range (1,3,10,30 & 100%)

Manufacturer:

Furnace control Ltd.,
Beeching road south,
Bexhill on sea,
Sussex TN39 3LJ.

Mode of operation:

1. Place total pressure tubing on right-hand side (looking from the front of the instrument) and the static pressure tubing to the left hand port.
2. Switch the mains supply on with the instrument switch in the off position.
3. Set the "zero" dial to zero.
4. Switch on the rotary selector switch to the 1% range and zero the meter control after the 15 minutes warm up period.
5. Put the equalizing valve in the "out" position to allow

the dynamic pressure to be read.

6. When the instrument is not in use, the rotary switch should be turned to the "off" position, the equalizing valve put in the "in" position and mains supply switched off.

APPENDIX (3)

PITOT-STATIC TUBE

A standard pitot static tube has two sets of orifices: one large one at the tip of the tube and several smaller ones located on the side of the shaft (these are the static holes of which there are eight equally spaced around the periphery of the tube). The pressure at the large orifice indicates the total head ($p + \frac{\rho U^2}{2}$) and at the smaller orifices the static pressure (p). If the pressure from the two sets of orifices are connected across a micro-manometer, then the pressure difference is the dynamic pressure ($\frac{\rho U^2}{2}$).

The position of the static holes are critical because:

1) the crowding of the stream lines near the tip reduces the pressure along the shaft so that the static pressure at the static holes may be low;

2) a high-pressure region exists ahead of the stem that tends to make the indicated static pressure too high.

To reduce these two effects would require the static holes to be so close to the tip that small deviations in manufacture could make a relatively large error in the static pressure.

APPENDIX (4)

HOT WIRE ANEMOMETER

Manufacturer:

Prosser Scientific Instrument Ltd.,
Hadliegh, Suffolk,
England.

General Description

Hot-wire anemometers commonly used are made in two basic forms: the constant-current type and the constant temperature type. Both utilize the same principle, but in different ways. In the constant current type, a fine resistance wire carrying a fixed current is exposed to the flow velocity. The wire attains an equilibrium temperature when the I^2R heat generated in it is just balanced by the convective heat loss from its surface. The circuit is designed so that the I^2R heat is essentially constant; thus the wire temperature must adjust itself to change the convective loss until equilibrium is reached. Since the convection film coefficient is a function of flow velocity, the equilibrium wire temperature is a measure of velocity. The wire temperature can be measured in terms of its electrical resistance. In the constant-temperature form, the current through the wire is adjusted to keep the wire temperature (as measured by its resistance) constant. The current required to do this then becomes a measure of flow

velocity.

For equilibrium conditions, an energy balance for a hot wire would be:

$$I^2 R_w = hA(T_w - T_f)$$

where,

I = Wire current.

R_w = Wire resistance.

T_w = Wire temperature.

T_f = Temperature of flowing fluid.

h = Film coefficient of heat transfer.

A = Heat transfer area.

Now h is mainly a function of flow velocity for a given fluid density. For a range of velocities, this function (sometimes called King's Law) has the general form:

$$h = C_o + C_1 \sqrt{v}$$

For the measurement of average velocities in an incompressible flow, a constant temperature anemometer is used, while a constant current anemometer would be preferred in compressible flow.

Fig.(50) shows the circuit arrangement of the constant temperature anemometer used in this project. For accurate work, a given hot-wire probe must be calibrated in the fluid in which it is to be used. That is, it is exposed to "known" velocities (measured accurately by some other means) and its output is recorded over a range of velocities. See Fig.(51) for the calibration curve of the constant temperature anemometer used.

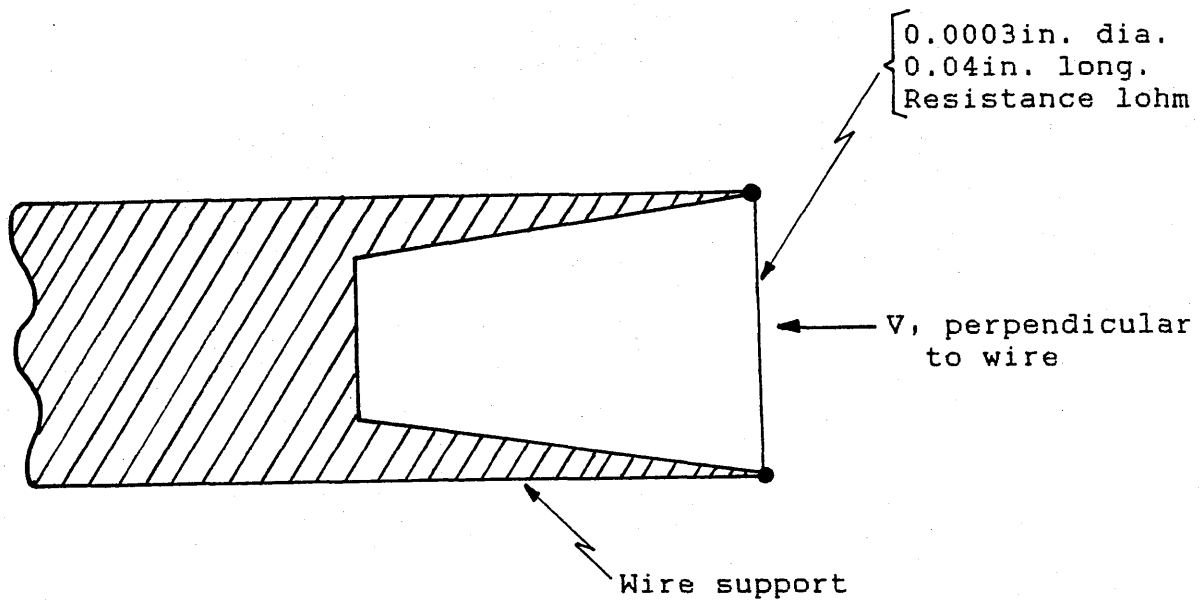

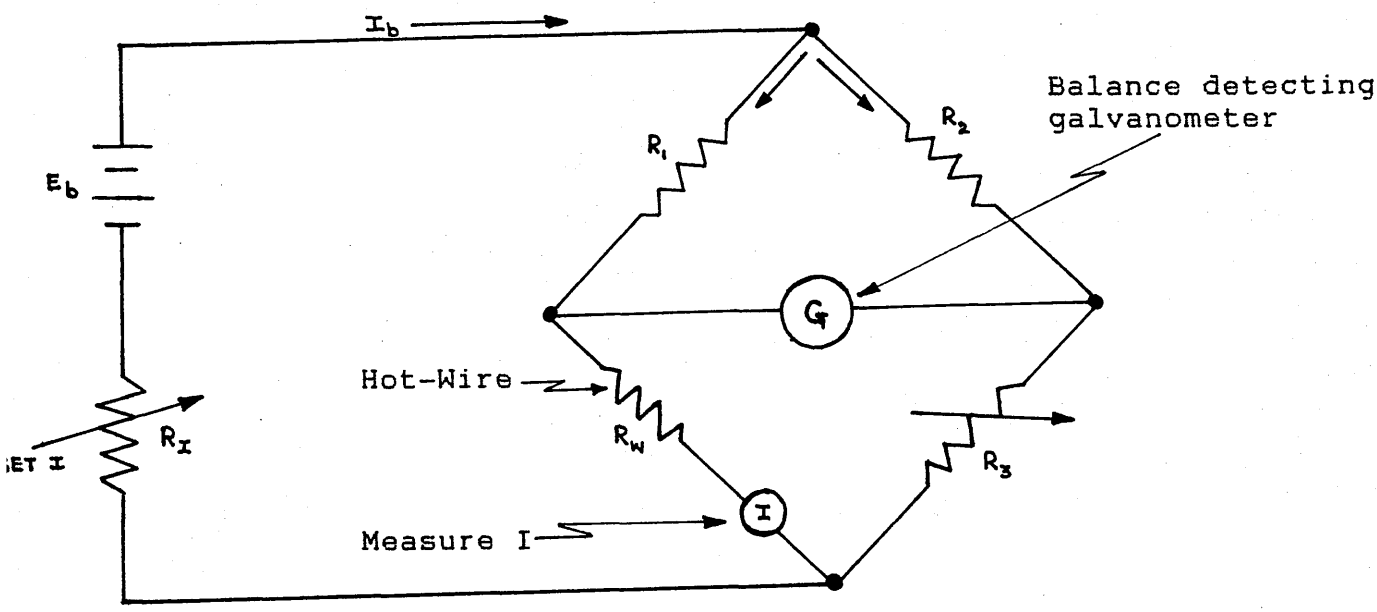

$R_I >> R_1, R_2, R_3, R_W$

Fig.50 Circuit arrangement for constant temperature anemometer.

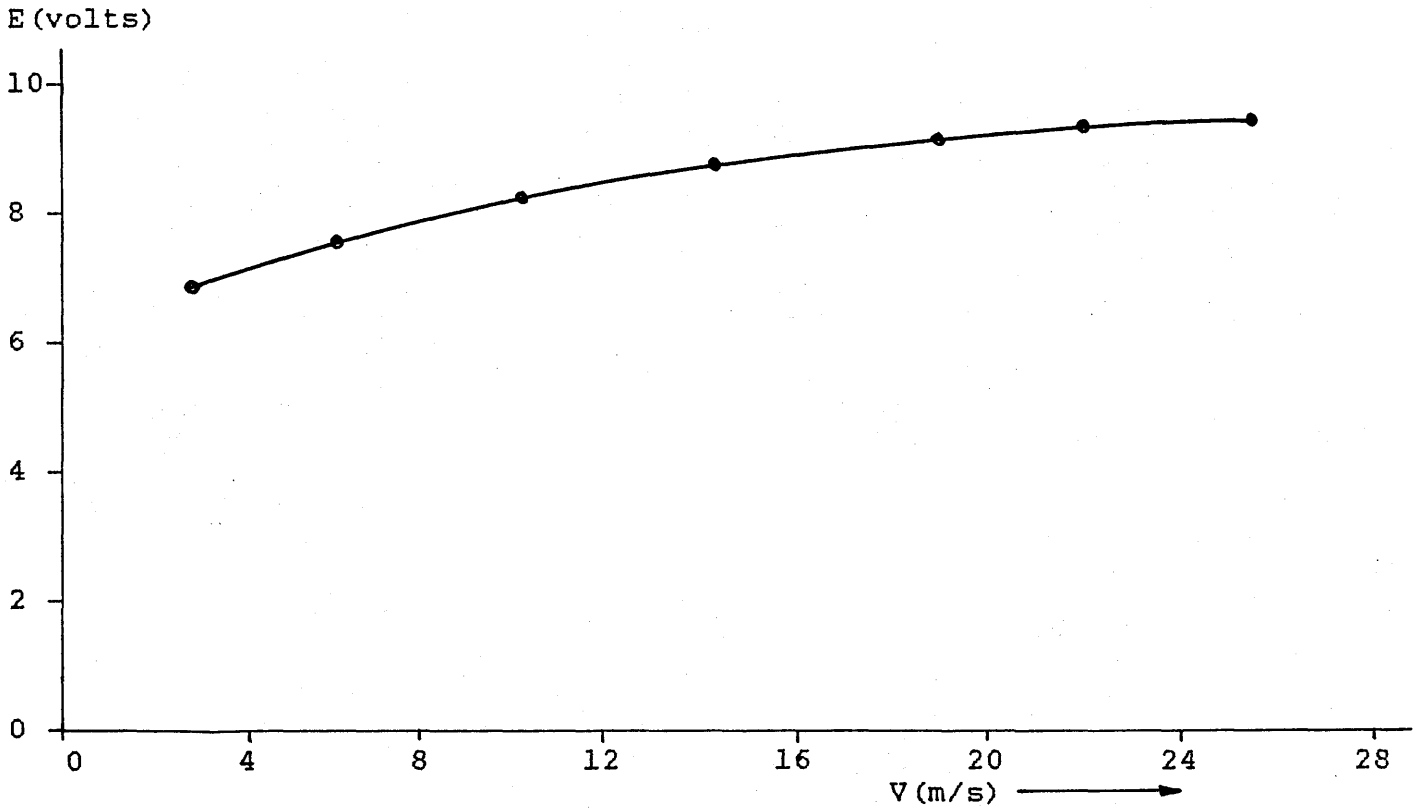

Fig.51 Constant-temperature anemometer calibrated in air at 20°C.

APPENDIX (5)

Proof for equation (110)

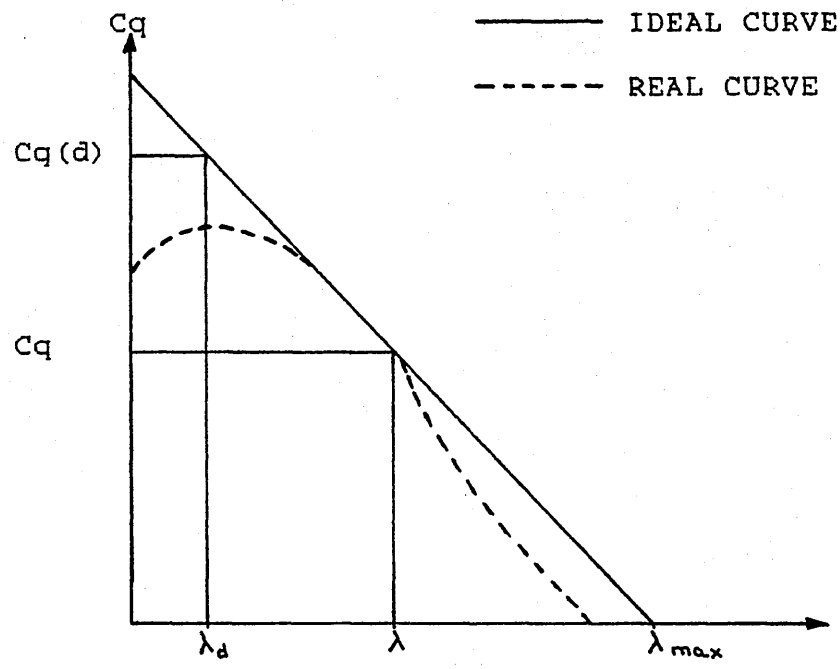

Fig.52

From Fig.(52) above, the torque can be interpreted by using similar triangles as follows:

$$\frac{\lambda(max) - \lambda}{Cq} = \frac{\lambda(max) - \lambda(d)}{Cq(d)}$$

hence

$$Cq = Cq(d) \frac{(\lambda(max) - \lambda)}{\lambda(max) - \lambda(d)} \qquad (110)$$

APPENDIX (6)

WATSON & MARLOW PUMPHEAD-SPECIFICATIONS.

501R Pumphead Specifications

MATERIALS OF CONSTRUCTION

TRACK: Aluminium casting
Aluminium side-guard
Kematal hinges

ROTOR: Anodised aluminium extrusions
Stainless steel collet and fittings
Molybdenum filled nylon rollers
Kematal guide rollers

GUARD: Polycarbonate injection moulding

VOLUME DELIVERED PER REVOLUTION

TUBING ID (mm)	0.5	0.8	1.6	3.2	4.8	6.4	8.0
VOLUME (ml)	0.042	0.0124	0.43	1.86	4.05	6.35	10.8

DIMENSIONS

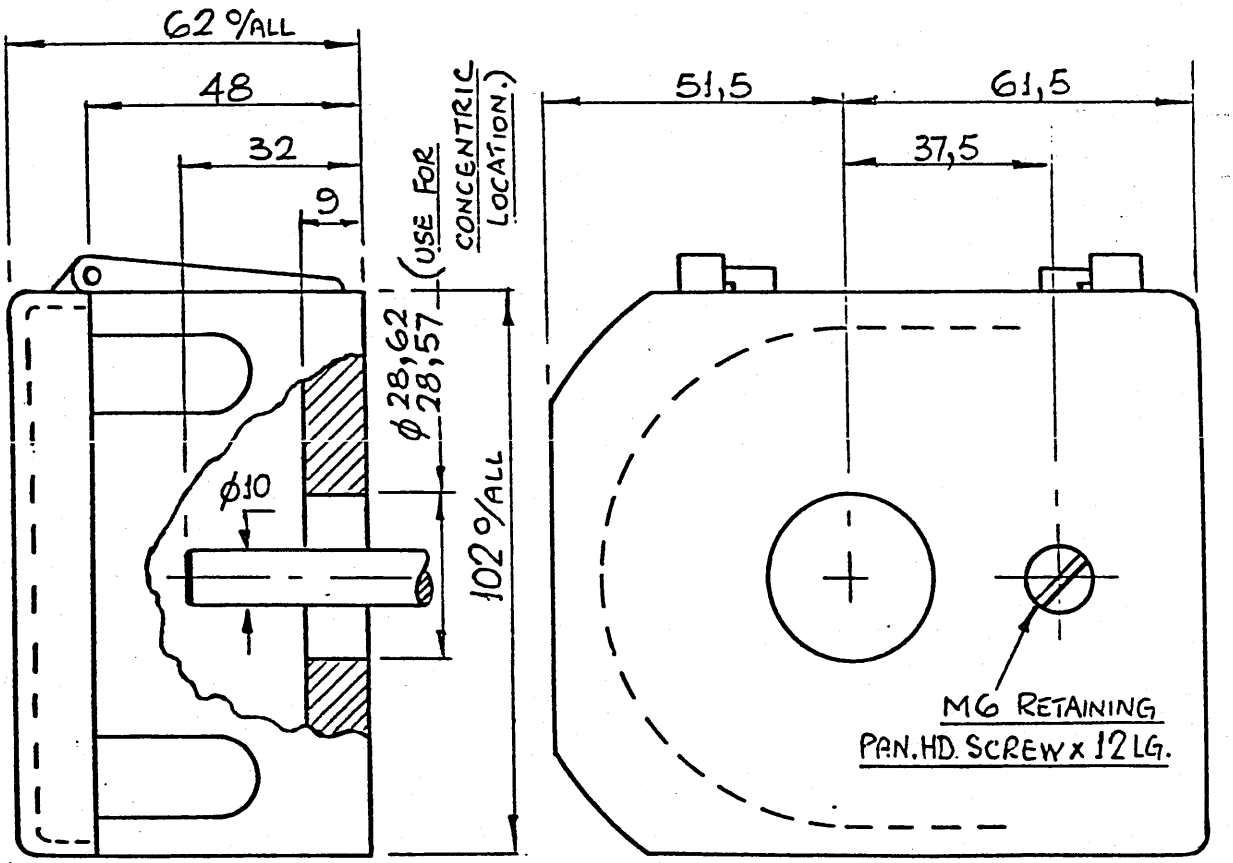

WATSON-MARLOW LIMITED

PRODUCT(S)	SUBJECT	REF.
501R	Pumphead Specifications — OEM	~~2-23/6~~

WATSON-MARLOW LIMITED
Falmouth, Cornwall, TR11 4RU, England.
Telephone: Penryn 73461 (STD 0326)
Telex: 45594 Triflo G

501 MODULAR PERISTALTIC PUMP SYSTEM

The tables shown below indicate typical flow rates obtainable from the 501 pumpheads fitted with silicone tubing when pumping water at normal room temperature with negligible suction and delivery pressures. The minimum will be 1/20 of the values indicated.

It is stressed that the flow rates given relate to conditions indicated. The flow rate on a particular application depending on the duty should be determined under operating conditions. Other important factors affecting flow rates are, suction and delivery pressures, temperature, fluid viscosity and the material of the tube in use.

501R PUMPHEAD

ml/min

DRIVE MODULE SPEED RPM	BORE SIZE OF TUBE mm WALL THICKNESS OF TUBE 1.6 mm 0.5	0.8	1.6	3.2	4.8	6.4	8.0
10	0.4	1.3	4.2	19	39	64	96
50	2.1	6.1	22	92	200	315	520
100	4.2	12.4	43	186	405	635	1080
170	7.1	21	73	320	700	1080	1820

501D PUMPHEAD

ml/min

DRIVE MODULE SPEED RPM	BORE SIZE OF TUBE mm 1.0	1.5	2.0	2.5	3.0	4.0
	WALL THICKNESS OF TUBE mm 0.35	0.5	0.5	0.5	0.5	0.7
10	0.3	0.6	0.9	1.2	2.0	2.8
50	1.4	2.9	4.5	6.2	10	14

501M PUMPHEAD

ml/min

DRIVE MODULE SPEED RPM	BORE SIZE OF TUBE mm 1.0	1.5	2.0	2.5	3.0	4.0
	WALL THICKNESS OF TUBE mm 0.35	0.5	0.5	0.5	0.5	0.7
10	0.5	2.9	1.9	3.1	4.8	7.8
50	2.6	5.8	9.6	15	24	39
100	5.2	11.6	19	31	48	79
170	8.8	20	32	52	82	134

WATSON-MARLOW LIMITED
Falmouth, Cornwall, TR11 4RU, England.
Telephone: Penryn (STD 0326) 73461
Telex: 45594 Triflo G
A Member of The Smith & Nephew Group of Companies

PRICE LIST 5/240/2
(exclusive of V.A.T.)
NET EX. WORKS

for tubing see list MTP/20

501 MODULAR PERISTALTIC PUMP SYSTEM

OPERATIONAL SPEED	DRIVE UNITS	PRICE
170 rpm	Standard Drive Unit 501S/170. Please specify voltage and case finish (enamel or stainless steel).	£270.00
100 rpm	Standard Drive Unit 501S/100. Please specify voltage and case finish (enamel or stainless steel).	£270.00
50 rpm	Standard Drive Unit 501S/50. Please specify voltage and case finish (enamel or stainless steel).	£270.00
10 rpm	Standard Drive Unit 501S/10. Please specify voltage and case finish (enamel or stainless steel).	£270.00
170 rpm	Universal Drive Unit 501U/170. Please specify voltage, case finish, as well as control input signal and signal source impedance e.g. 4 - 20 mA 500 ohms.	£326.00
100 rpm	Universal Drive Unit 501U/100. Please specify voltage, case finish, as well as control input signal and signal source impedance e.g. 4 - 20 mA 500 ohms.	£326.00
50 rpm	Universal Drive Unit 501U/50. Please specify voltage, case finish, as well as control input signal and signal source impedance e.g. 4 - 20 mA 500 ohms.	£326.00
10 rpm	Universal Drive Unit 501U/10. Please specify voltage, case finish, as well as control input signal and signal source impedance e.g. 4 - 20 mA 500 ohms.	£326.00

501U ADDITIONAL OPTIONS		
	Failsafe	£30.00
	Failsafe with Alarm	£33.00
	Switched Guard	£15.00
	Switched Guard with Alarm	£18.00

PUMPHEAD TYPE REF.	PUMPHEAD TYPE	
501R	Roller Pumphead	£53.00
501D	Delta Multi-channel Module	£84.00
501DX	Delta-multichannel Extension	£45.00
501M	Multi-channel Module	£100.00
501MX	Multi-channel Module Extension	£68.00

ACCESSORIES TYPE REF.	Specify voltage, time scales and case finish on Timers.	
501T	Timer Module for 999.9 seconds time scale.	£250.00
501T	Timer Module for 59 minutes 59 seconds time scale.	£250.00
501T/F	Footswitch Assembly for Timers.	£20.00
501U/F	Footswitch Assembly for 501U.	£20.00

NOTE *The prices indicated above for the Drive Units DO NOT include a pumphead. Pumphead must be ordered separately when required.*

WATSON-MARLOW LIMITED

Falmouth, Cornwall, TR11 4RU, England.
Telephone: Penryn (STD 0326) 73461
Telex: 45594 Triflo G

A Member of the Smith & Nephew Group of Companies

PRICE LIST MTP/20
(exclusive of V.A.T.)
NET EX. WORKS

TUBING for 501 MODULAR SYSTEM & MHRE/K Mk.4 SERIES

PRICE PER METRE

TUBE BORE SIZE	Neoprene	Butyl Rubber	Silicone	Elastic P.V.C.	Viton
0.5 mm	–	–	£0.60	–	–
0.8 mm (1/32")	£0.70	–	£0.70	–	–
1.6 mm (1/16")	£0.75	£0.75	£0.90	£0.55#	£3.75#
3.2 mm (1/8")	£0.80	£0.80	£1.10	£0.75	£4.50#
4.8 mm (3/16")	£0.85	£0.90	£1.20	£0.90	£6.00#
6.4 mm (1/4")	£0.90	£0.95	£1.55	£1.00	£7.25#
8.0 mm (5/16")	£1.00	£1.15	£1.75	–	£9.00#

# Denotes tubing with wall thickness 0.8 mm. All others have wall thicknesses of 1.6 mm.

NOTE 9.6 mm bore Neoprene and 8.0 and 9.6 mm bore Elastic P.V.C. tubing are available on request. Advice should be sought before use with Watson-Marlow pumps.

501M and 501D MC 10, DELTA, Multi-channel Module Silicone Tubing

PRICE PER METRE

PART NO.	TUBE BORE SIZE	TUBE WALL THICKNESS	PRICE
TU 100	1.0 mm	0.35 mm	£0.25
TU 101	1.5 mm	0.50 mm	£0.30
TU 102	2.0 mm	0.50 mm	£0.35
TU 103	2.5 mm	0.50 mm	£0.45
TU 104	3.0 mm	0.50 mm	£0.55
TU 105	4.0 mm	0.70 mm	£0.70

TUBING ACCESSORIES

DE 254	Nipple Type P	Autoclavable polypropylene nipple for use with tube bore sizes up to 2.0 mm.	each	£0.25
DE 255	Nipple Type T	Autoclavable polypropylene nipple for use with tube bore sizes up to 2.5 mm and above.	each	£0.25
MS4		Tube of silicone grease.		£3.30

APPENDIX (7)

Proof that the area under the "Pressure Coefficient (Cp) versus X/C" curve is the lift coefficient (Cl).

Consider an aerofoil as shown in the Figure below. Take the chord line as the x-axis, and a normal to it through the leading edge as the y-axis. Let X, Y be the components of aerodynamic force in these directions, and C_x, C_y be these forces reduced to coefficient form. Let α be the incidence of the aerofoil.

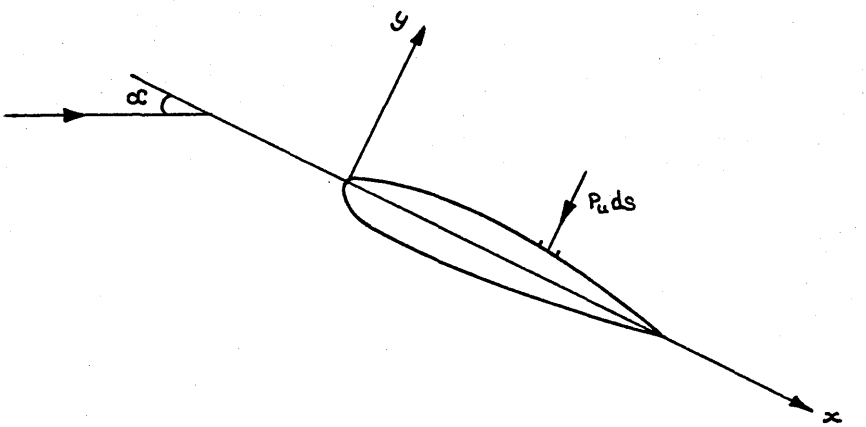

Consider an element of length ds on the upper surface of the aerofoil. The force on this element is $p_u.ds$ normal to the surface, where p_u represents the pressure on the upper surface. The component of this force in the y-direction is then $-p_u.dx$. Thus the pressure forces on the upper surface contribute:

$$-\int_0^c p_u \, dx$$

to the net force per unit span in the y-direction.

Similarly, the pressure forces on the lower

surface contribute:

$$\int_0^c p_l \, dx$$

where p_l is the lower surface pressure. The total force per unit span in the y-direction is then:

$$Y = \int_0^c (p_l - p_u) \, dx,$$

and the force coefficient is:

$$C_Y = \frac{Y}{1/2 \, \rho \, V_\infty^2 c.1}$$

$$= \int_0^c \left\{ \frac{p_l - p_\infty}{1/2 \rho V_\infty^2} - \frac{p_u - p_\infty}{1/2 \rho V_\infty^2} \right\} \frac{1}{c} \, . dx$$

$$= \int_0^1 (C_{PL} - C_{Pu}) \, d\left(\frac{x}{c}\right)$$

where C_{Pu}, C_{PL} are the pressure coefficients on the upper and lower surfaces respectively.

In this way, C_x may be obtained by intergrating C_P with respect to y/c. Then, since α is small, and C_x is much smaller than C_y, we may write:

$$C_L = C_y \cos\alpha - C_x \sin\alpha \doteqdot C_y \text{ , and}$$

$$C_D = C_y \sin\alpha + C_x \cos\alpha \doteqdot C_y . \alpha + C_x .$$

Thus, using this approximation,

$$C_L = \int_0^1 (C_{PL} - C_{Pu}) \, d\left(\frac{x}{c}\right)$$

which are the areas enclosed by the curves in Graphs 8 - 16.

APPENDIX (8)

DEFINITIONS OF VARIOUS TERMS USED

Term	Definition
Aspect ratio	The measure of the narrowness of an aerofoil planform. It is usually defined as the ratio of the span squared over the area.
Viscosity	The "stickiness" of a fluid and its tendency to resist sliding between layers.
Density	The density of a material is a measure of the amount of the material contained in a given volume.
Camber	The curvature of the surface of an aerofoil, relative to the chord line.
Angle of incidence	The angle between the chord line of a given aerofoil section and the direction of the undisturbed stream.
Angle of stall	The angle of incidence corresponding to the maximum lift coefficient.
Form drag	That part of the drag represented by the components of the pressures at points on the surface of an aerofoil, resolved normal to the surface.

Induced drag	That fraction of the total drag of a part inevitably induced by its lift.
Profile drag	The sum of the surface-friction and form drags.
Pressure drag	The part of the drag due to the resolved component of the pressures normal to the surface.
Surface-friction drag	The part of the drag due to the tangential forces on the surface.
Interference	The aerodynamic influence of bodies on one another.
Boundary layer	The thin layer of fluid adjacent to the surface in which the viscous forces exert a noticeable influence on the motion of the fluid.
Transition point	The point at which the flow in a boundary layer begins to change from laminar to turbulent.
Circulation	The integral of the component of the fluid velocity along any closed path with respect to the distance round the path.
Eddy	Motion in which there is circulation round a

limited region of intense vorticity.

Dynamic pressure	The increase in pressure which arises when a stream of fluid is brought to rest.
Reference pressure	Half the product of the density and the square of the velocity of a fluid.
Static pressure	The pressure at a point on a body moving with the fluid.
Total head	The sum of the dynamic and static pressures.
Stagnation point	A point on the surface of a body in motion through an inviscid fluid where the fluid is at rest relative to the body, and where positive pressure on the body is a maximum.
Line vortex	A vortex in which the vorticity is concentrated in a line.
Point vortex	The section of a straight-line vortex in two-dimensional motion.
Vortex sheet	A thin layer of fluid with intense vorticity.

Vorticity — The vorticity at any point in a fluid is twice the mean angular velocity of a small element of fluid surrounding the point.

Aerofoil — A body so shaped as to produce aerodynamic reaction normal to its motion through the air without excessive drag.

Centre line — Of an aerofoil; a line, each point of which is equidistant from the upper and lower boundaries of the aerofoil section, the distances being measured normal to the line itself.

Chord line — The straight line through the centres of curvature at the leading and trailing edges of an aerofoil section.

PLATES 2 to 17

SURFACE-VISUALIZATION OF THE FLOWS AROUND A FLEXIBLE-SAIL AT VARIOUS ANGLES OF ATTACK, α.

(By the use of tufts)

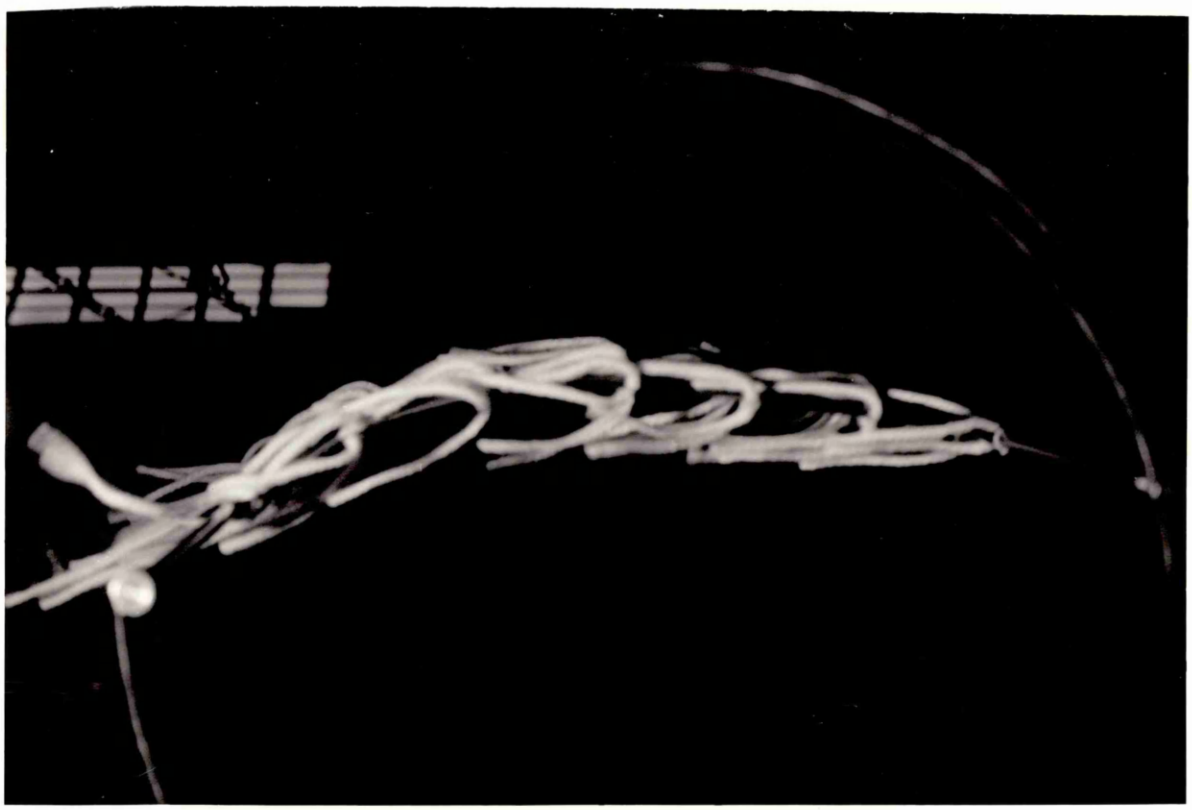

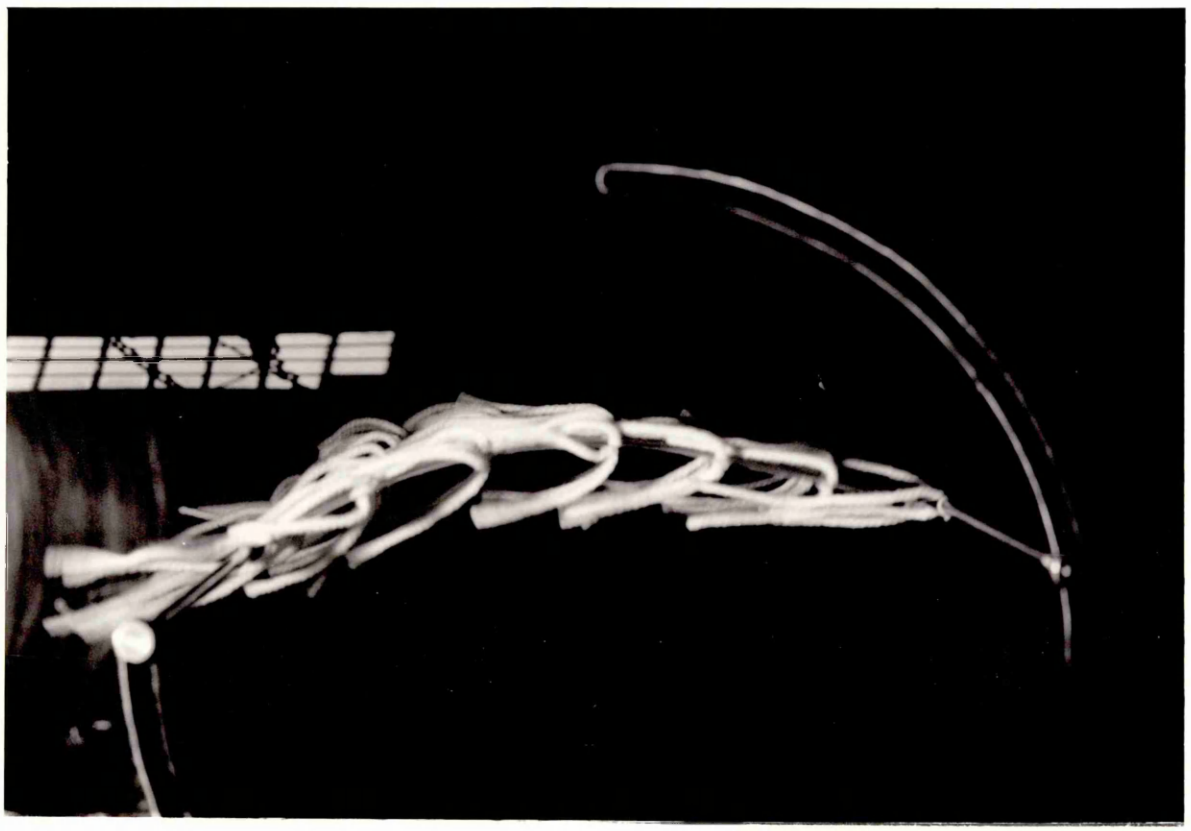

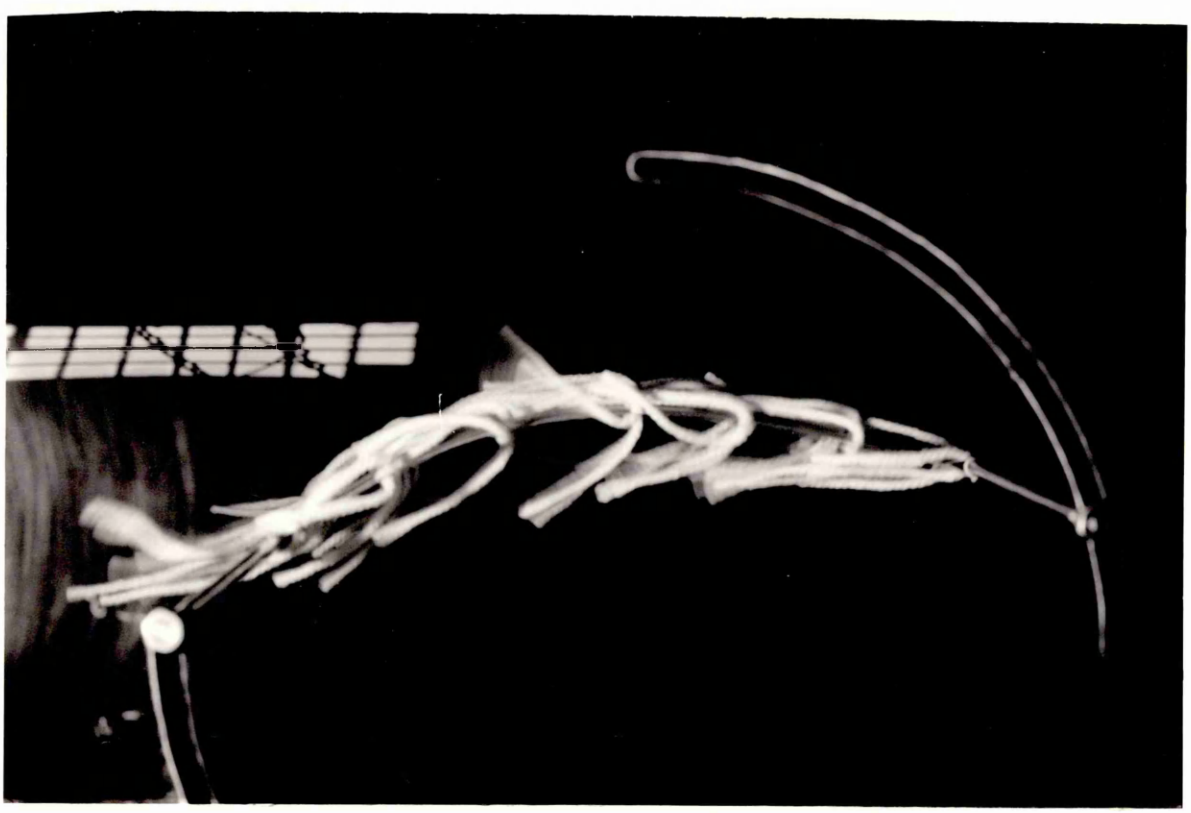

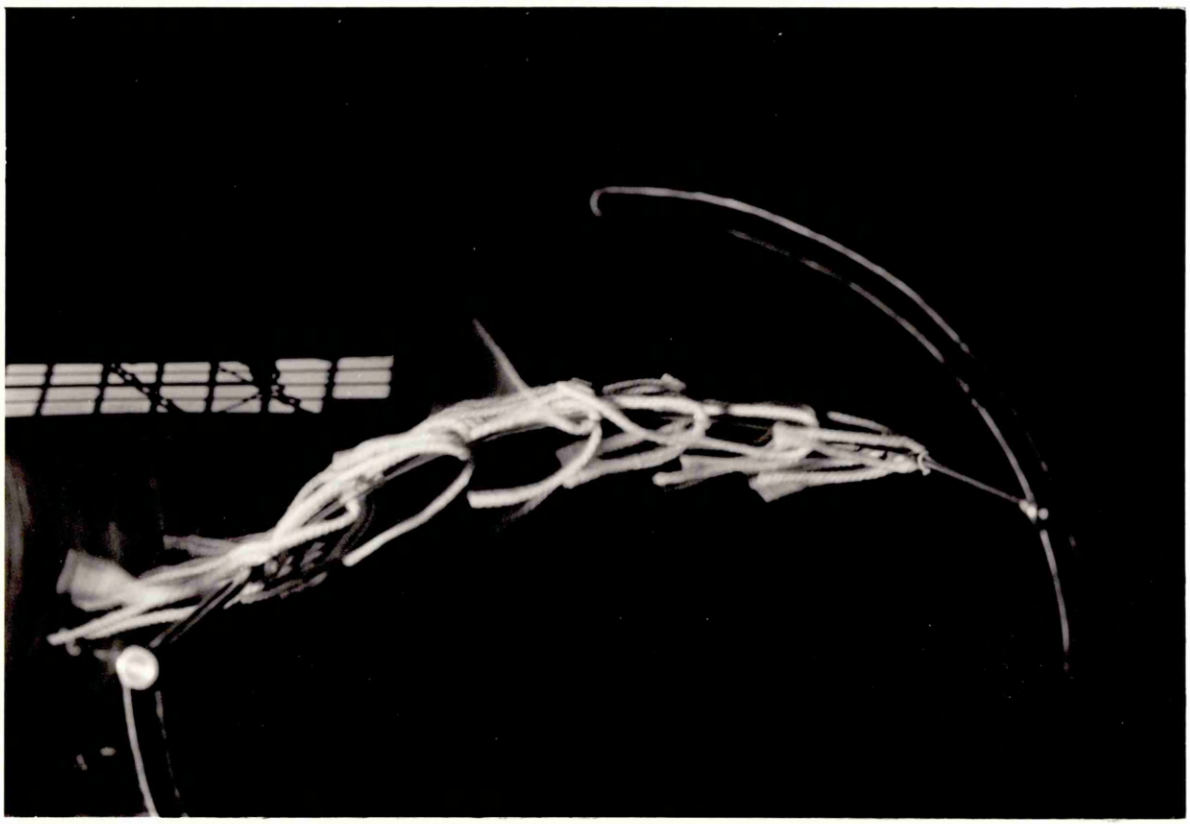

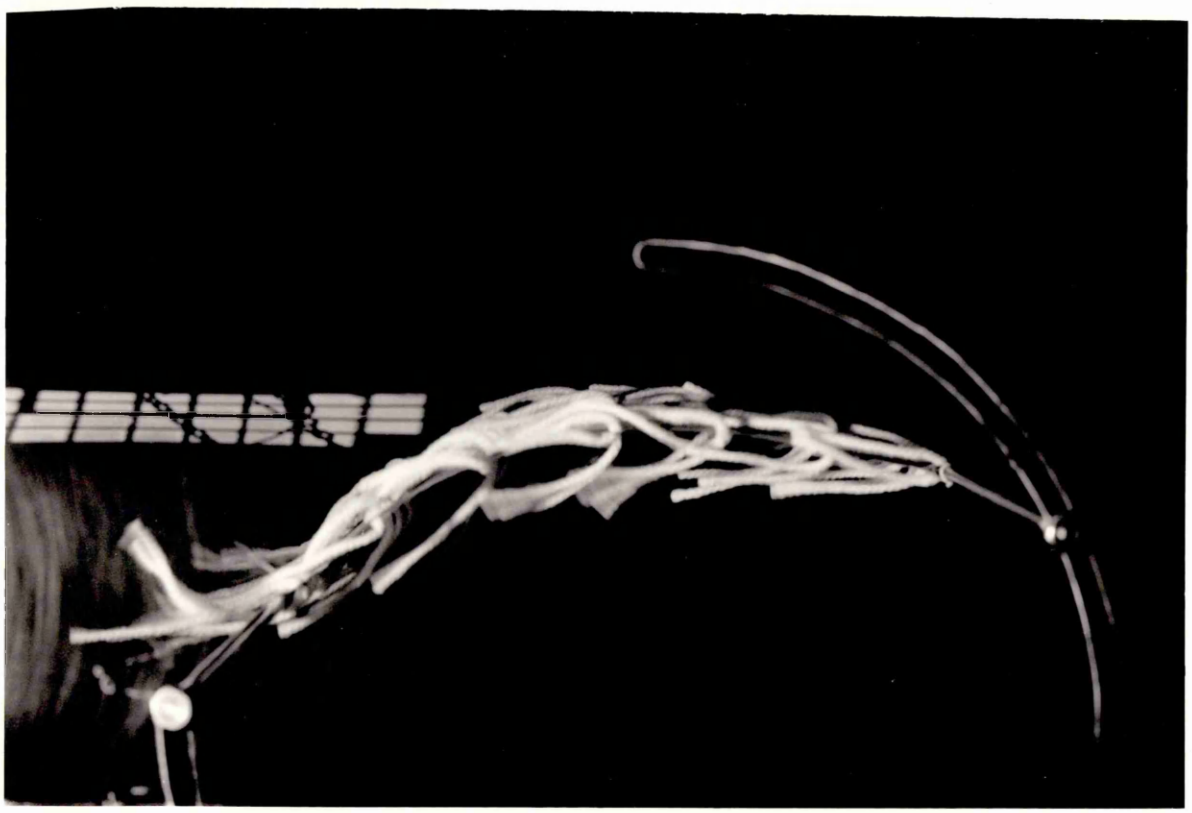

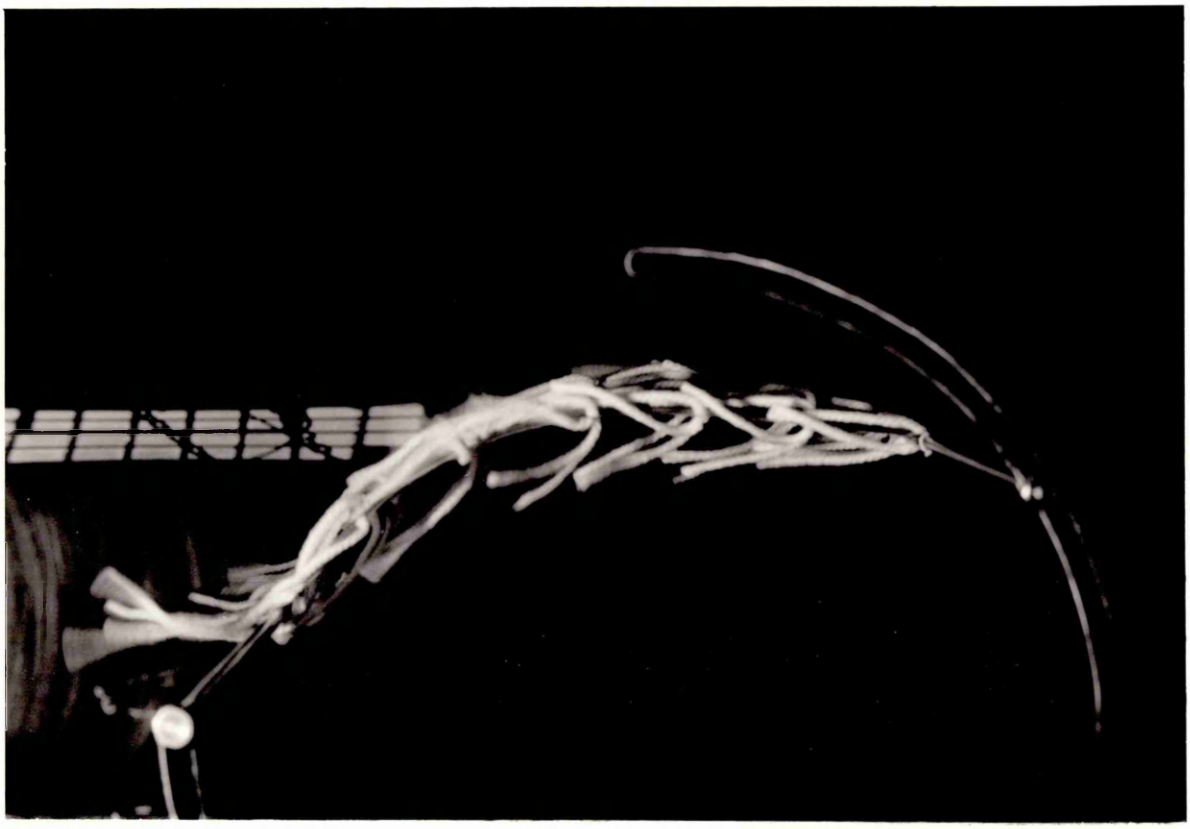

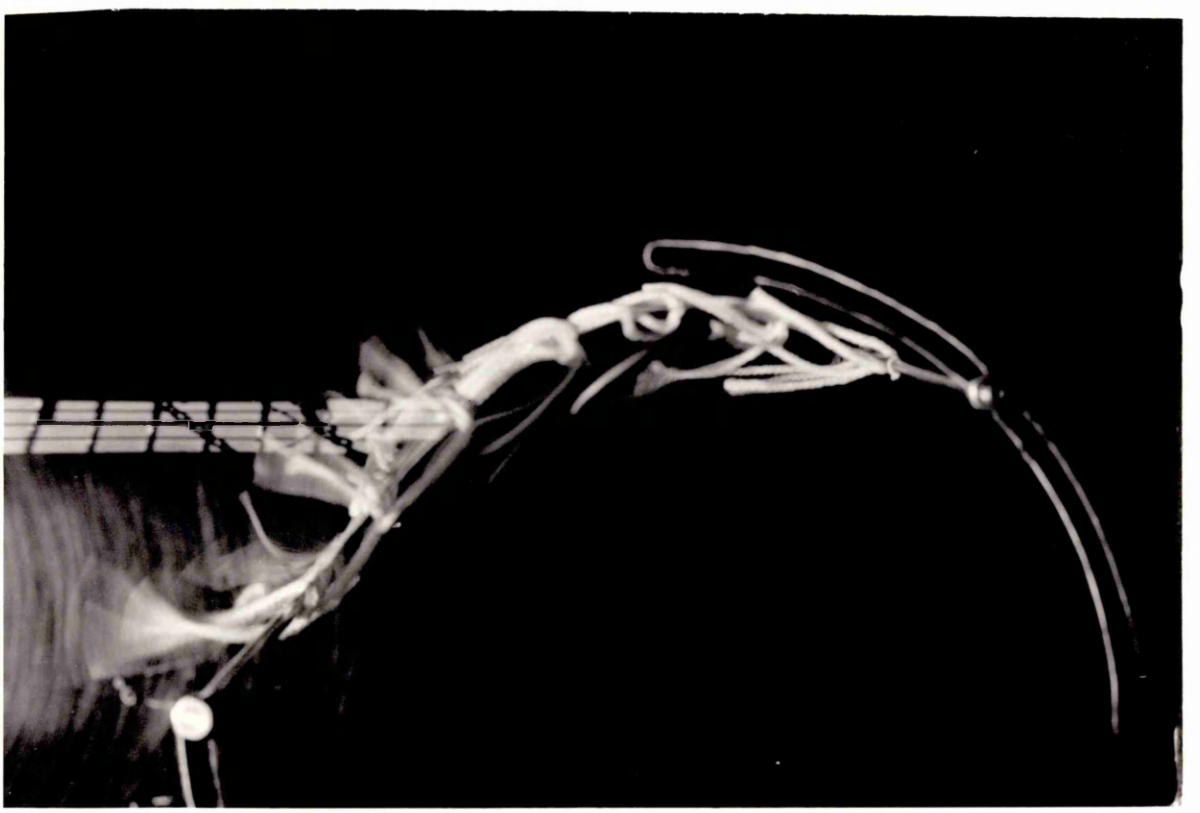

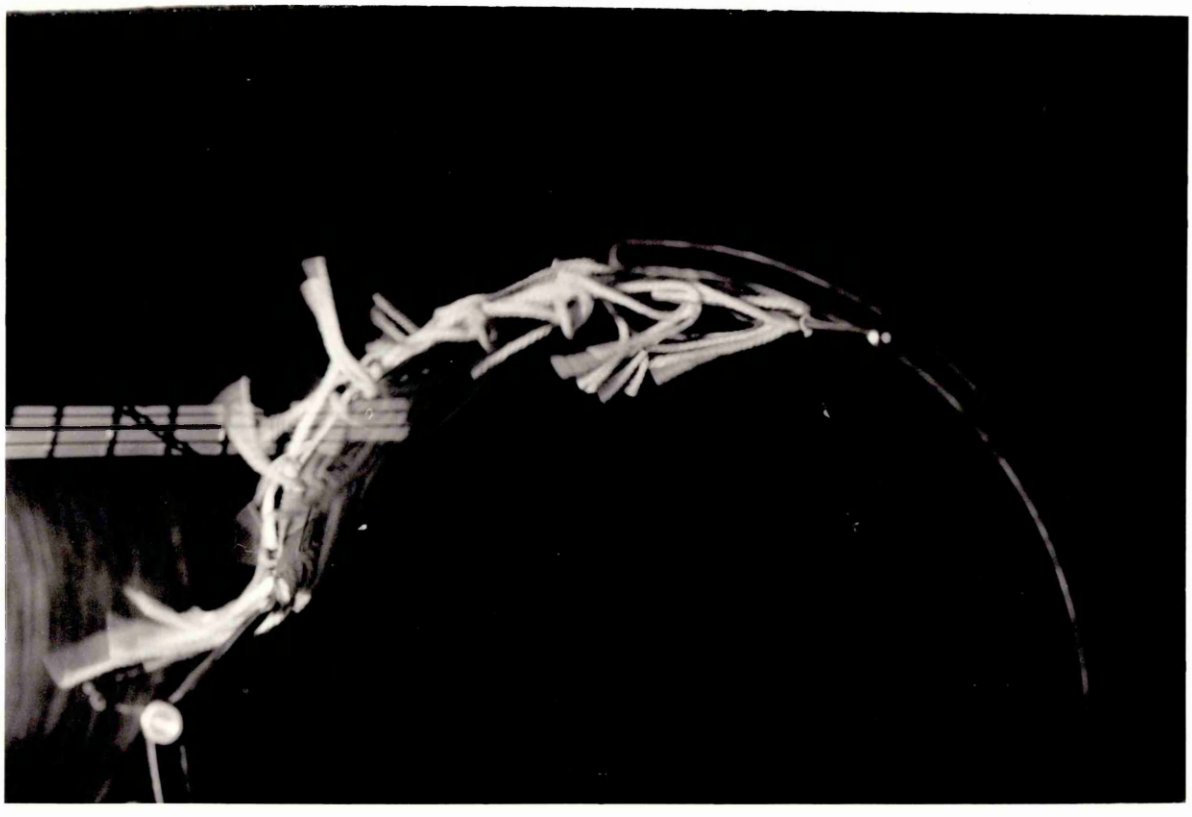

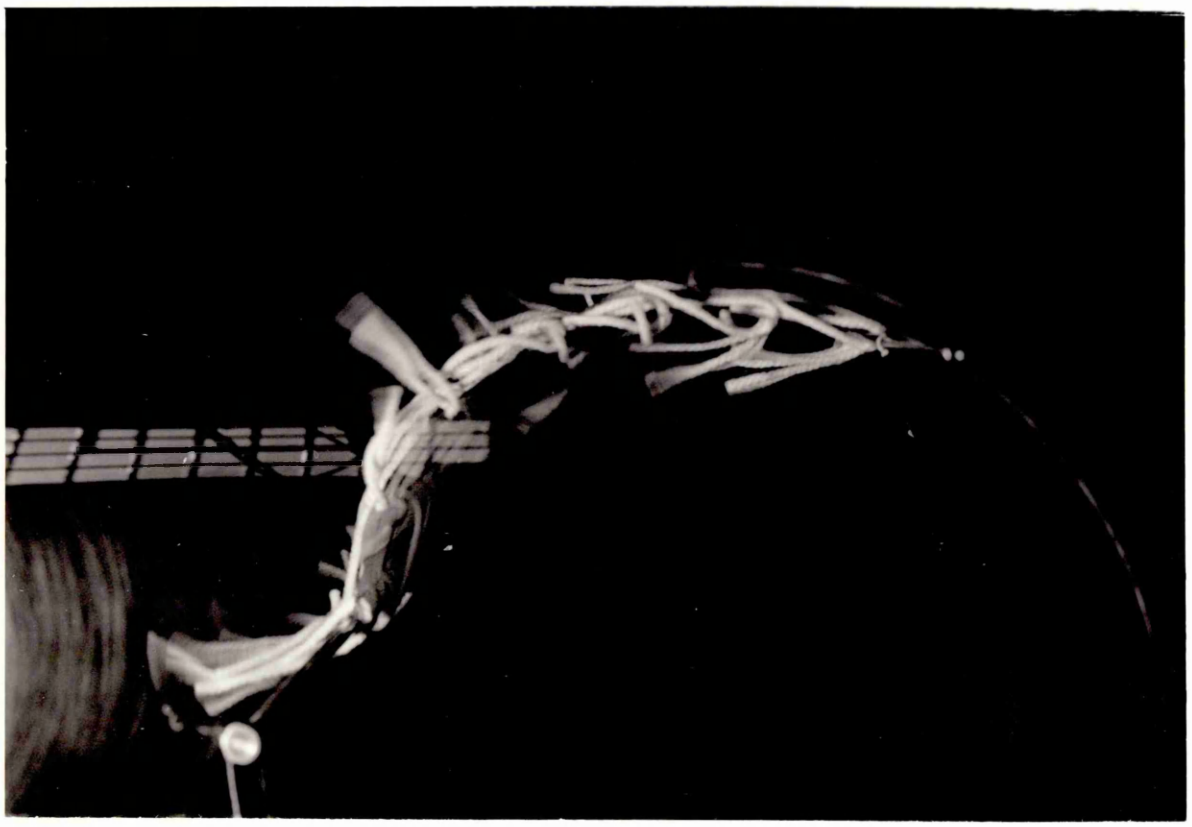

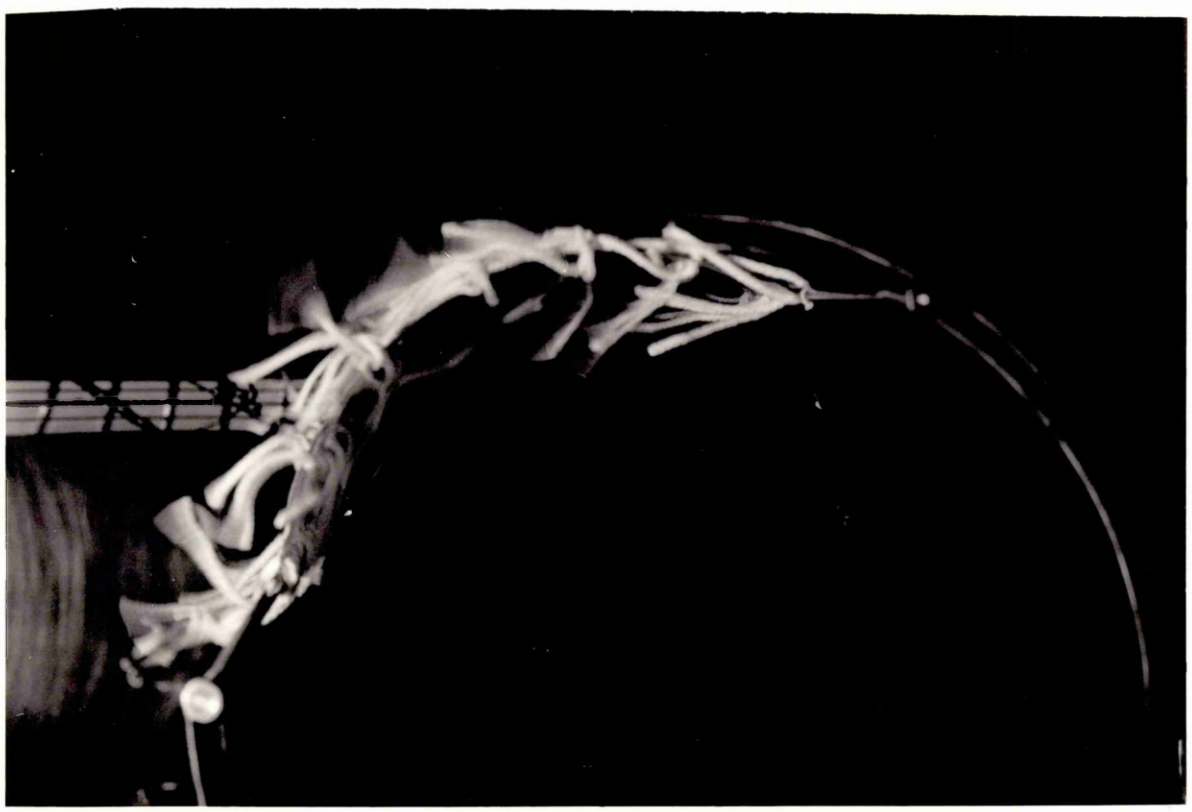

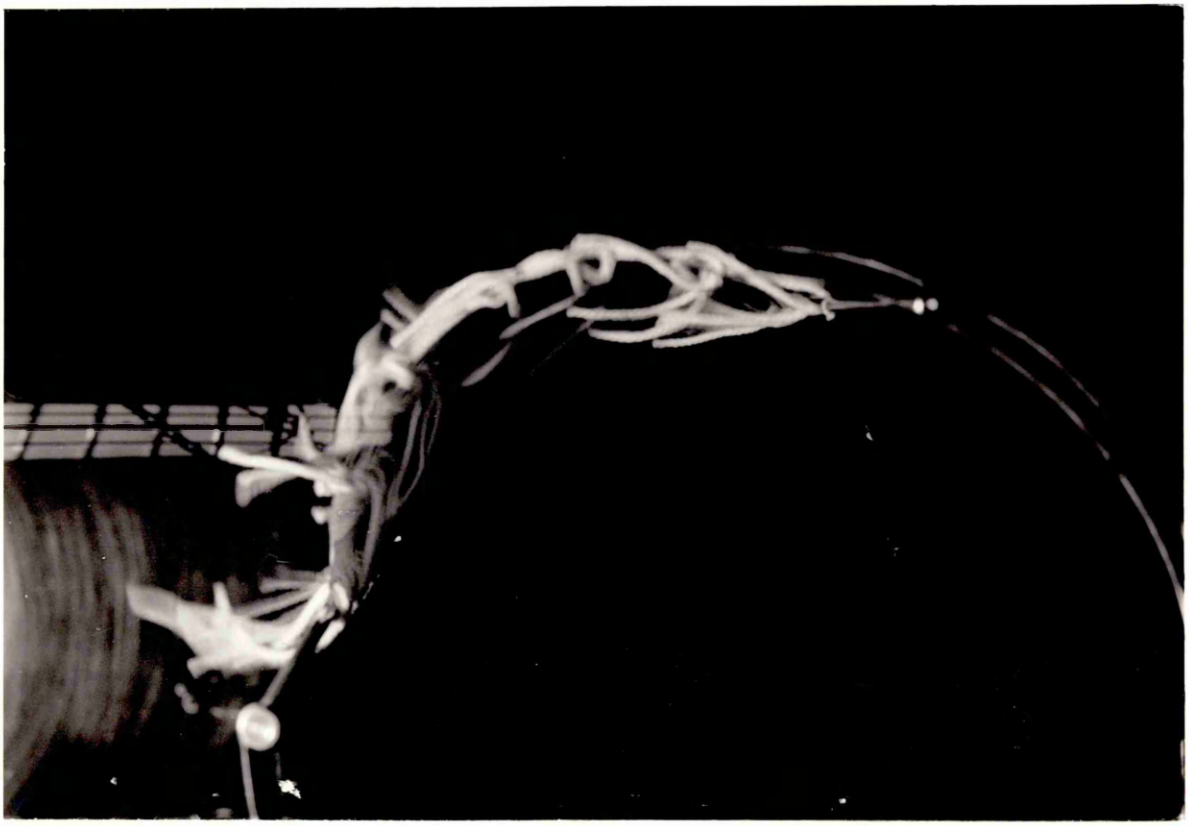

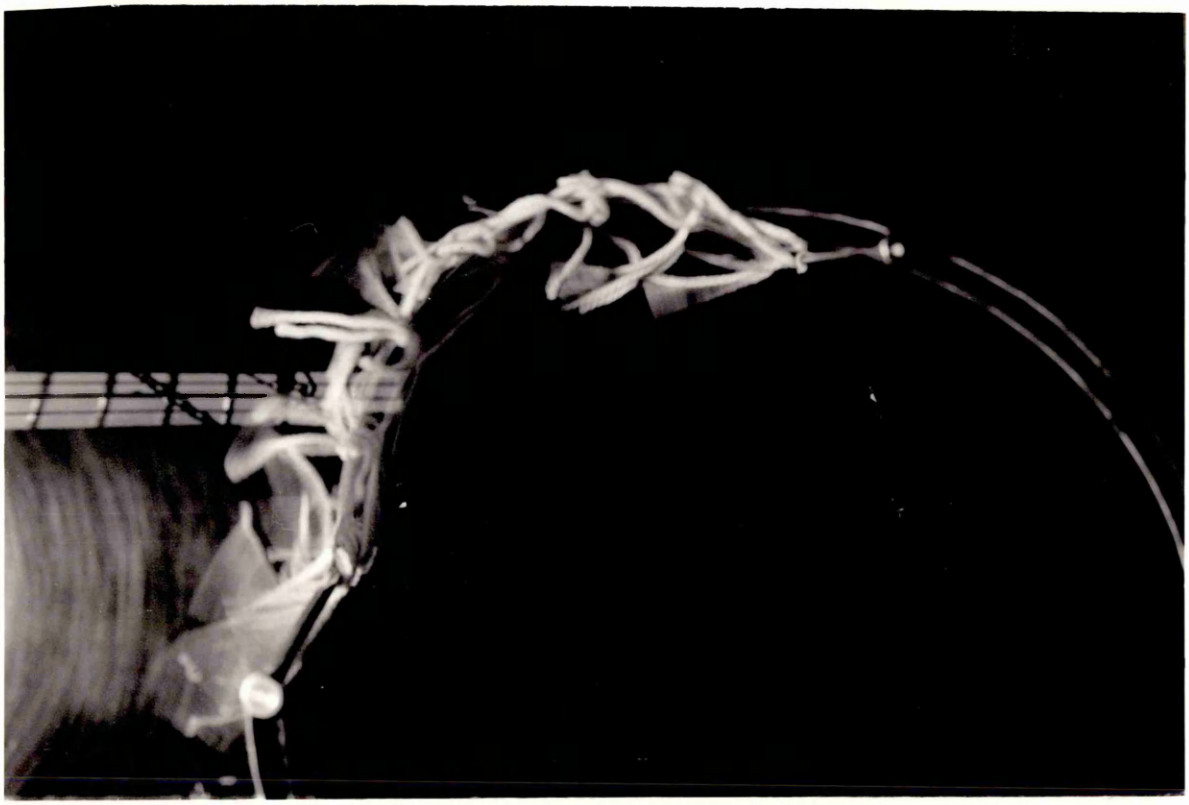

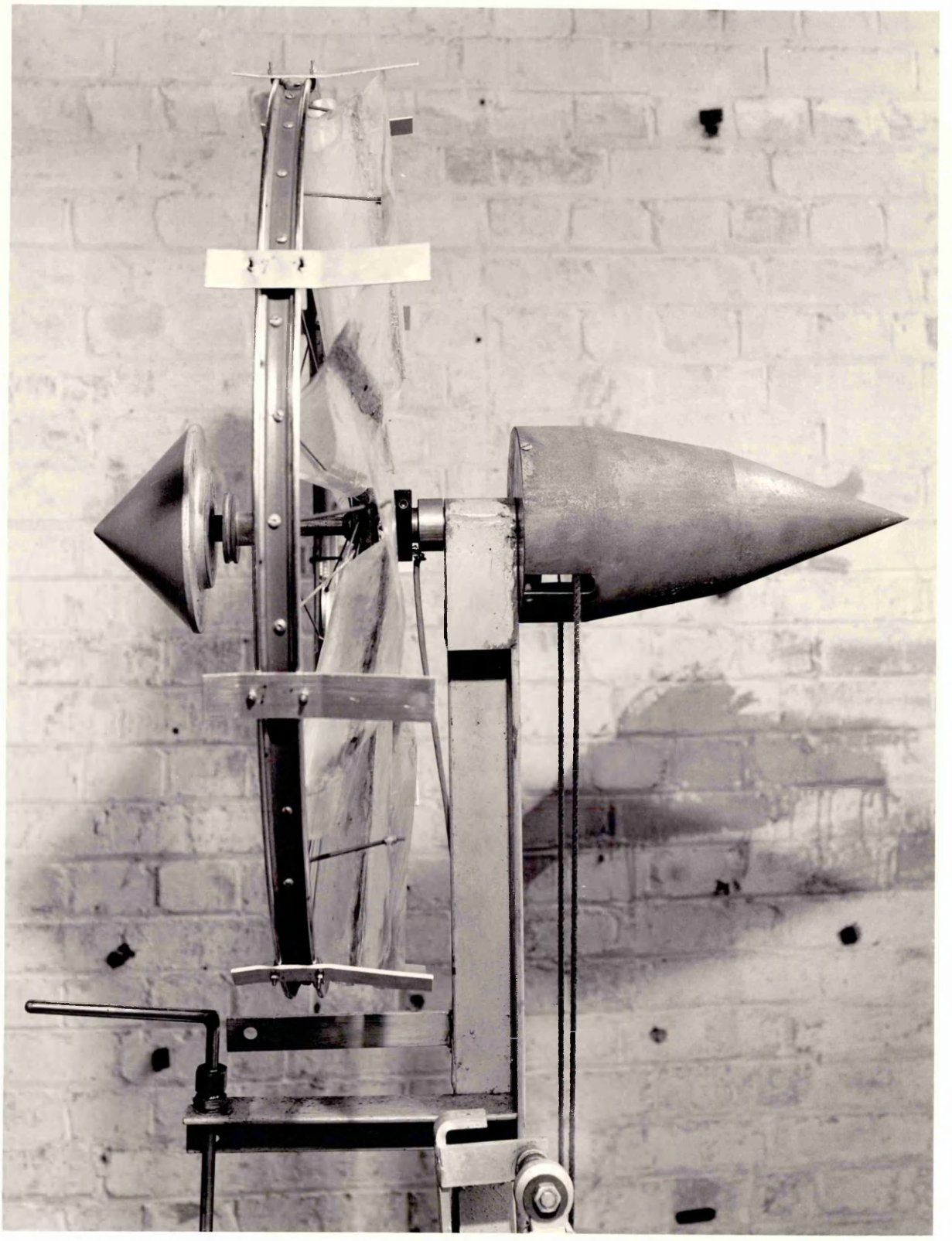

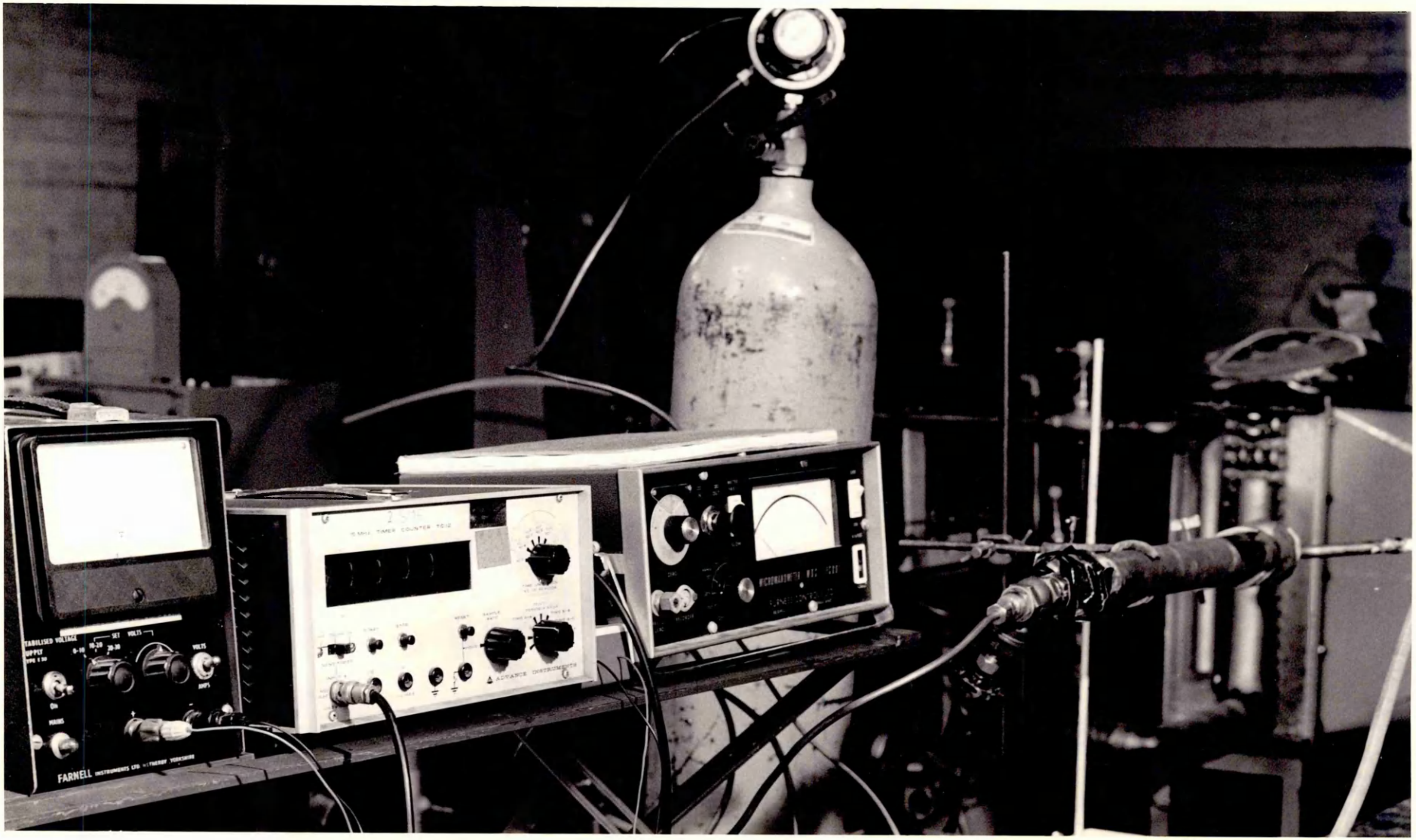
FARNELL

PLATES 20 to 31

FLOW-VISUALIZATION OF AUGMENTED WIND-TURBINE.

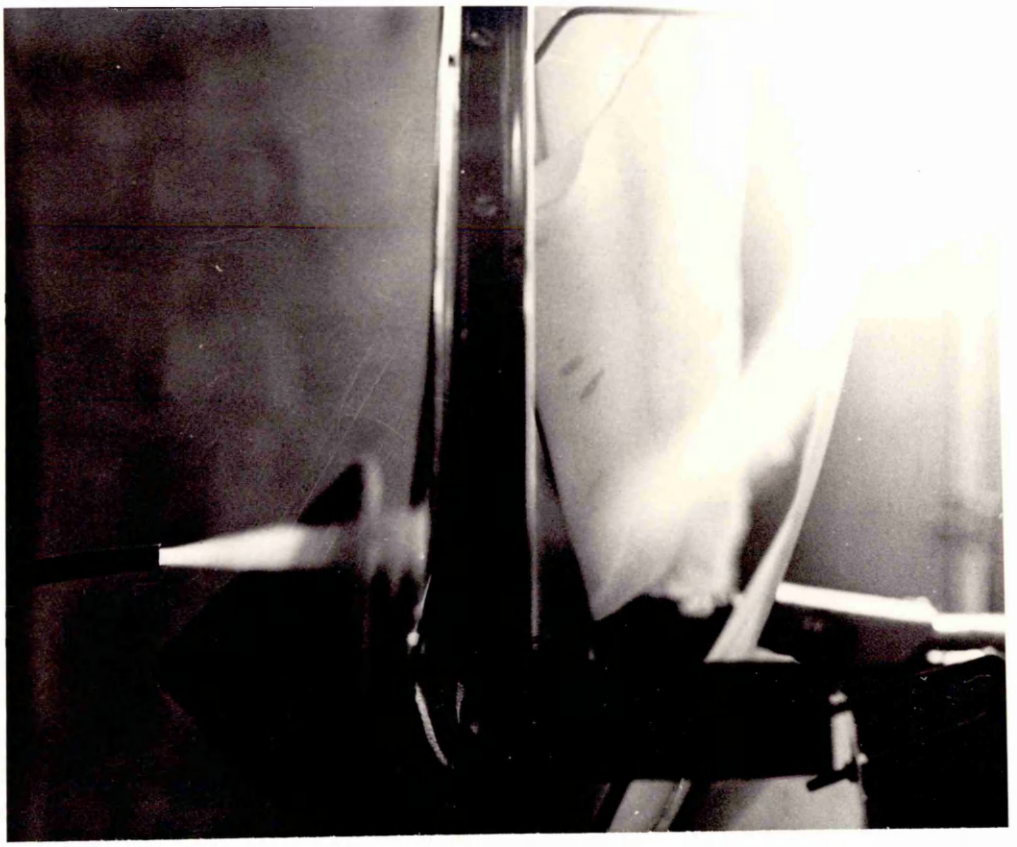

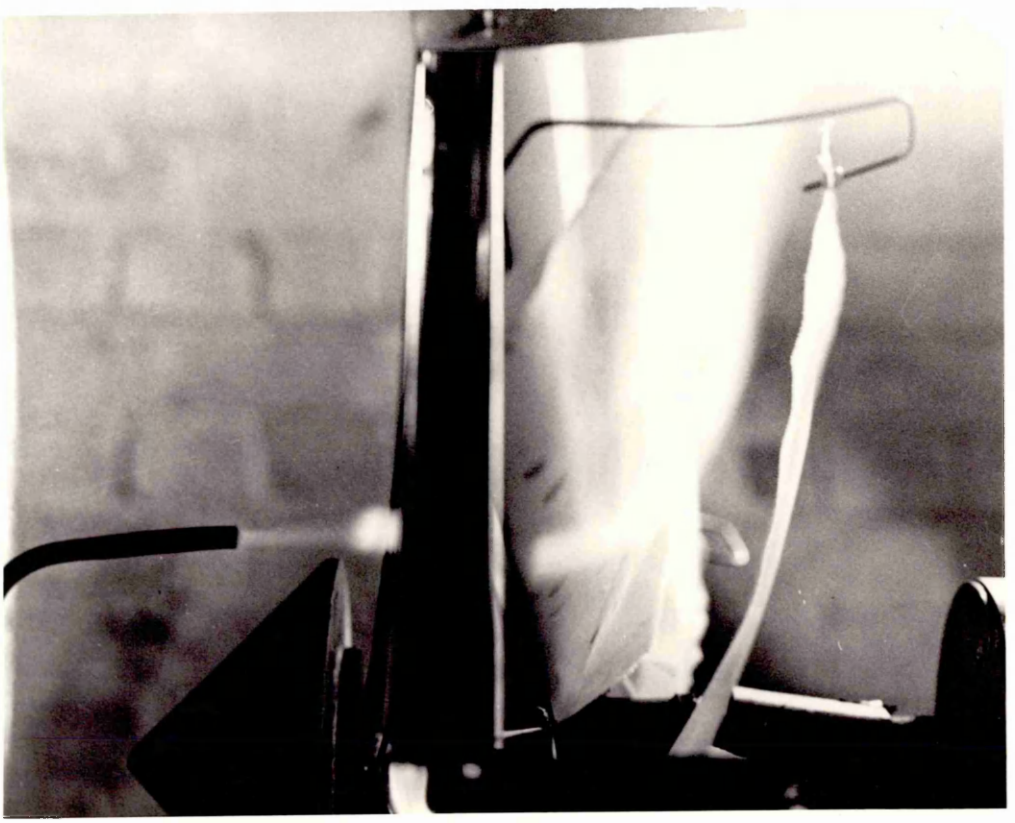

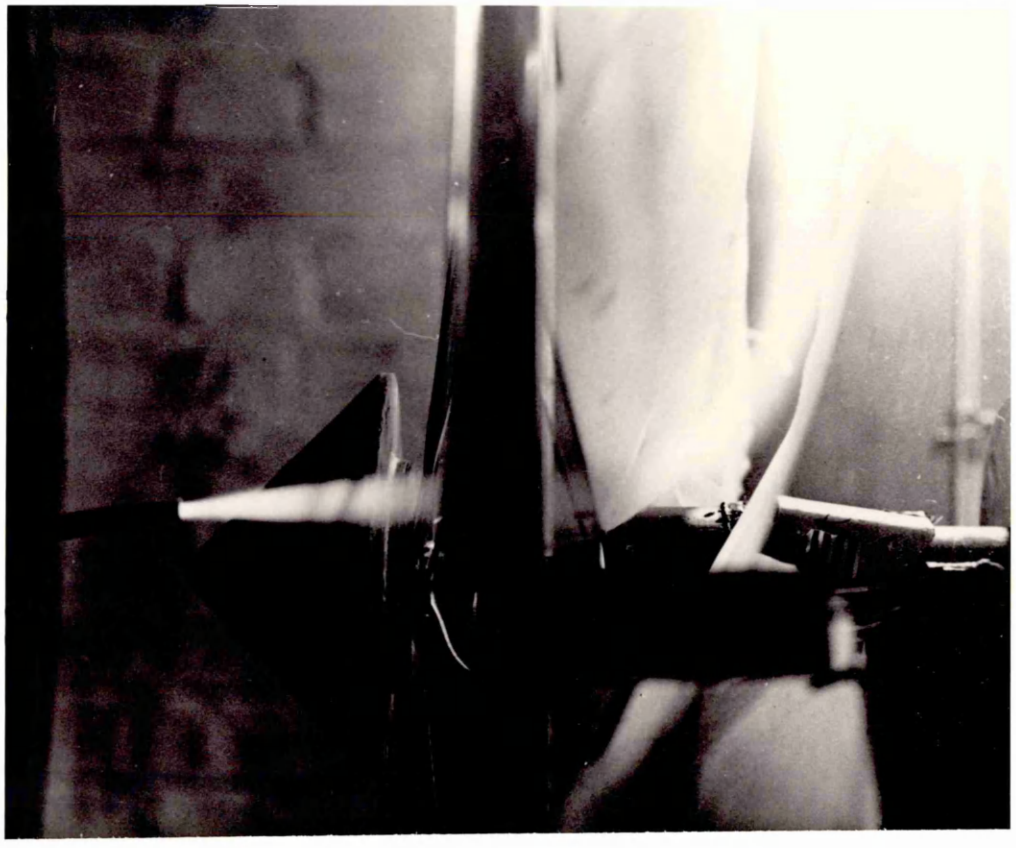

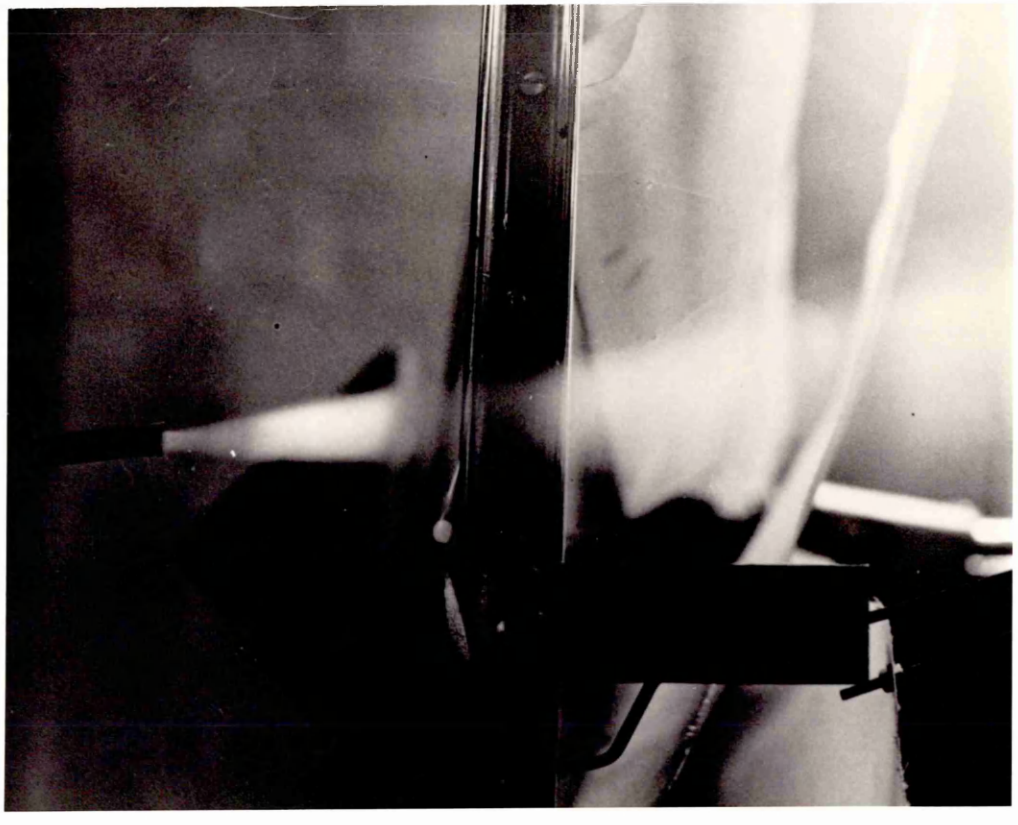

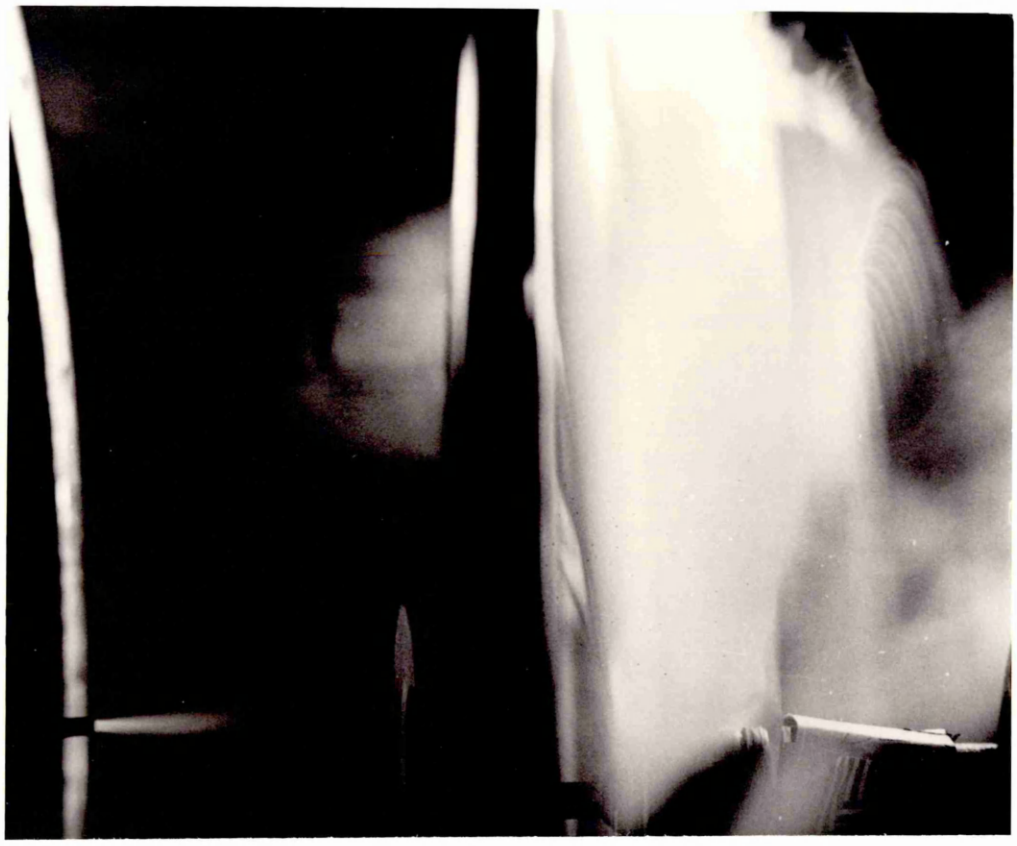

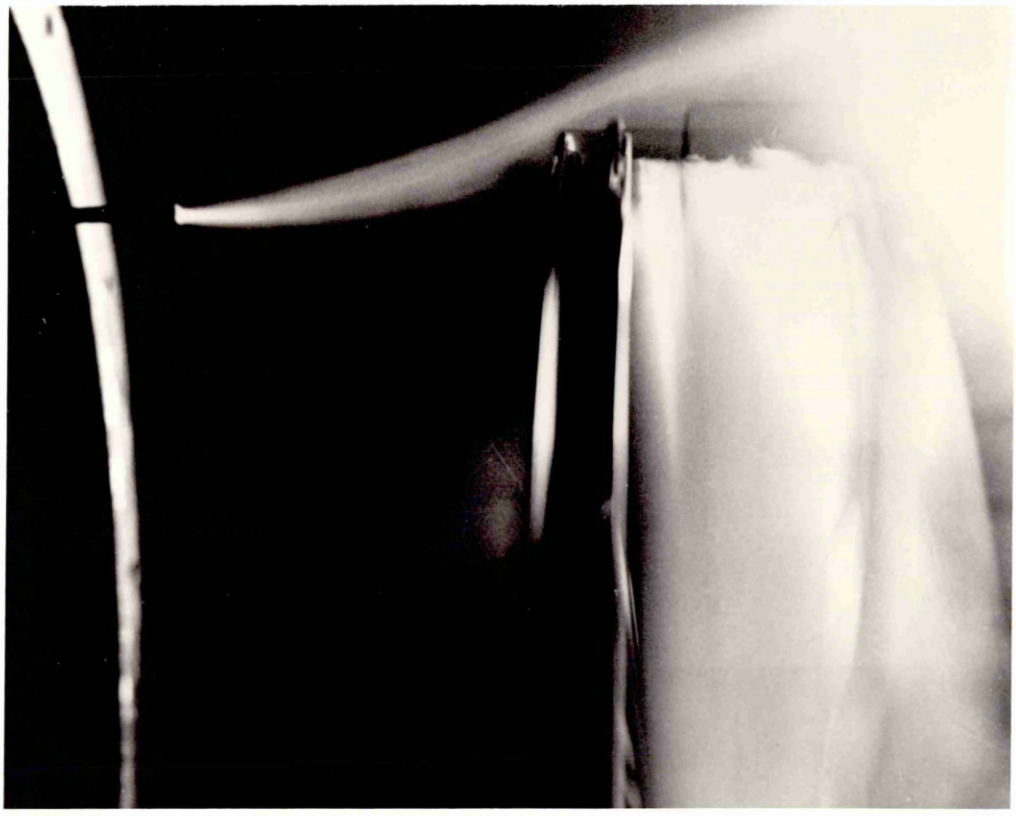

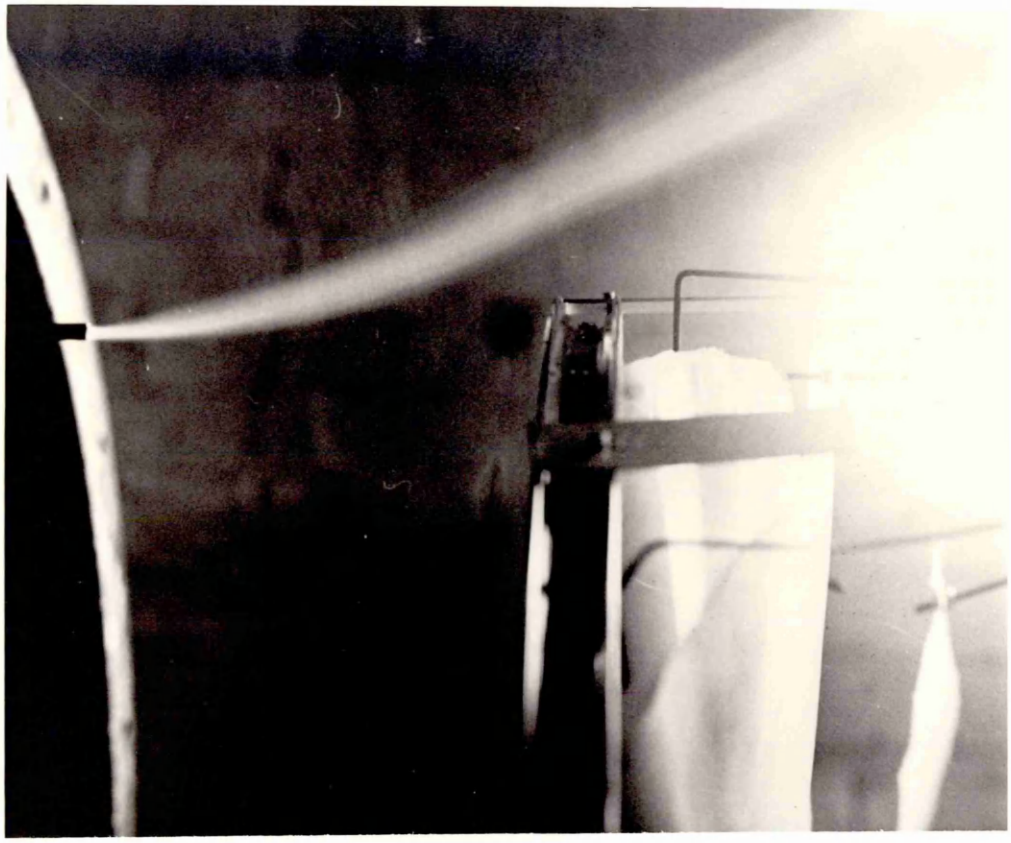

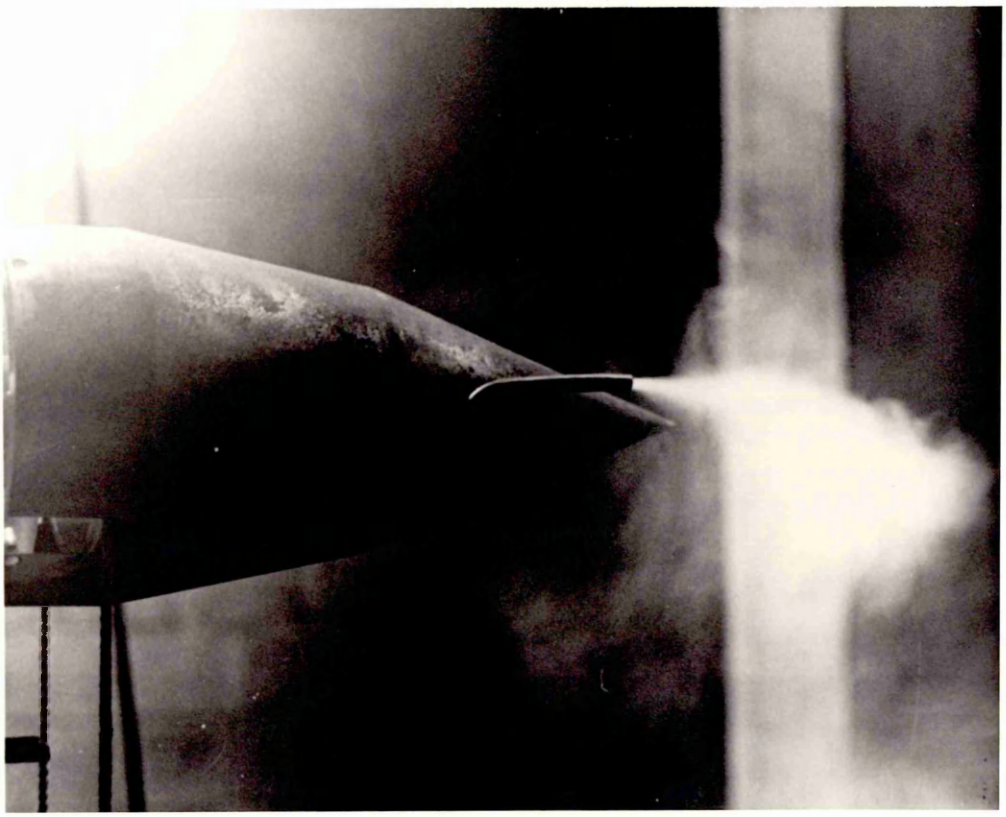

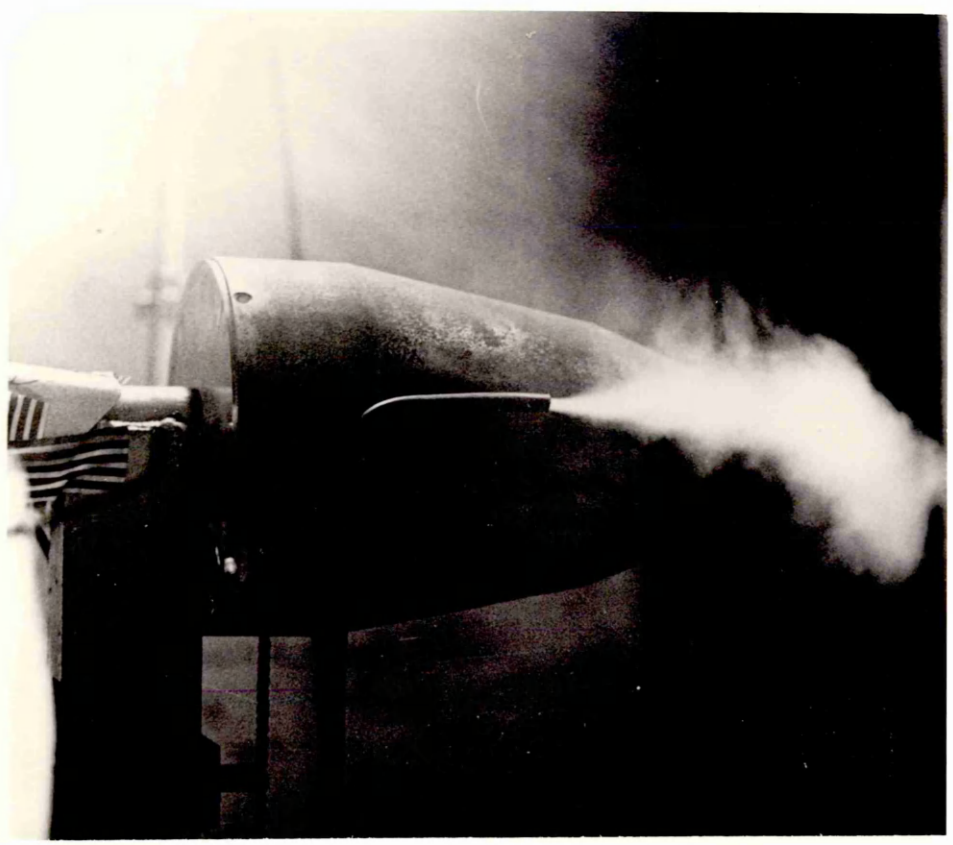

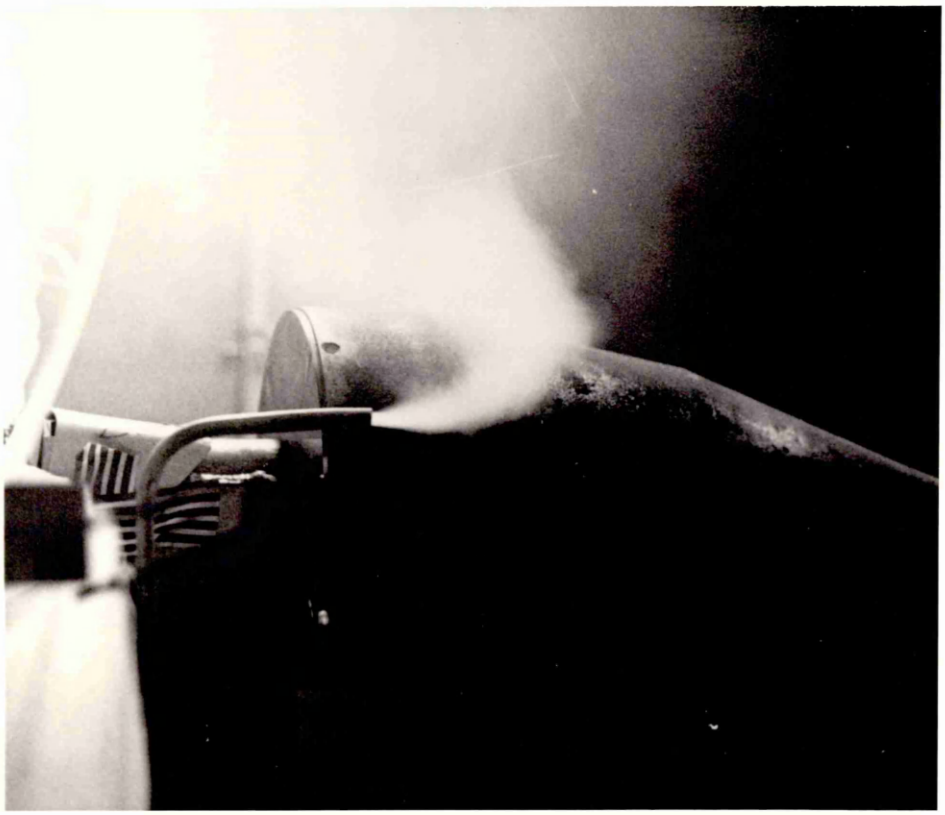

GRAPHS

GRAPH (1) VELOCITY PROFILE INSIDE DUCT AT 5m/s

(before wind-tunnel modification)

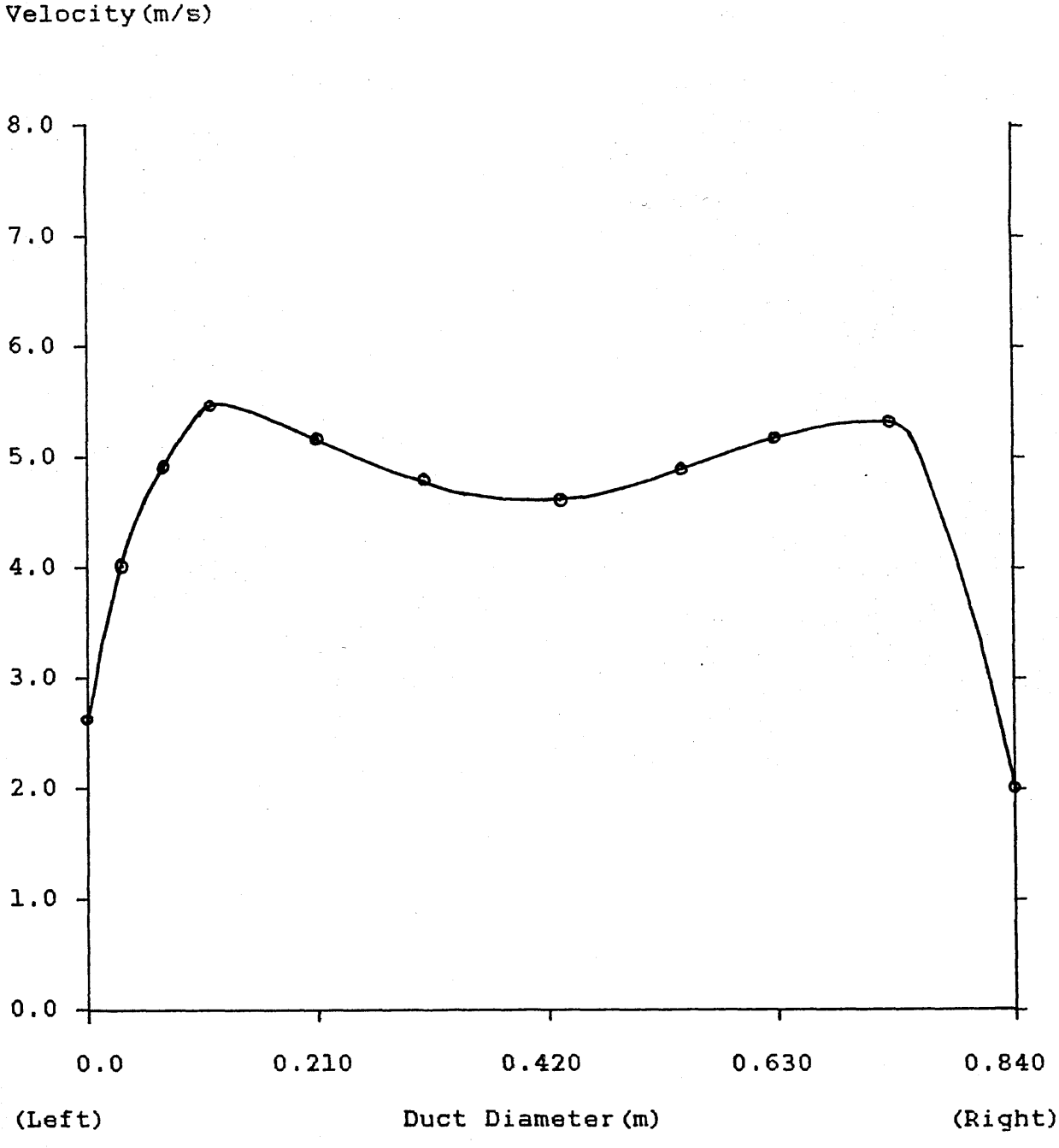

GRAPH (2) VELOCITY PROFILE INSIDE DUCT AT 5m/s

(Plane 1 at Y=0.420m (vertical distance))

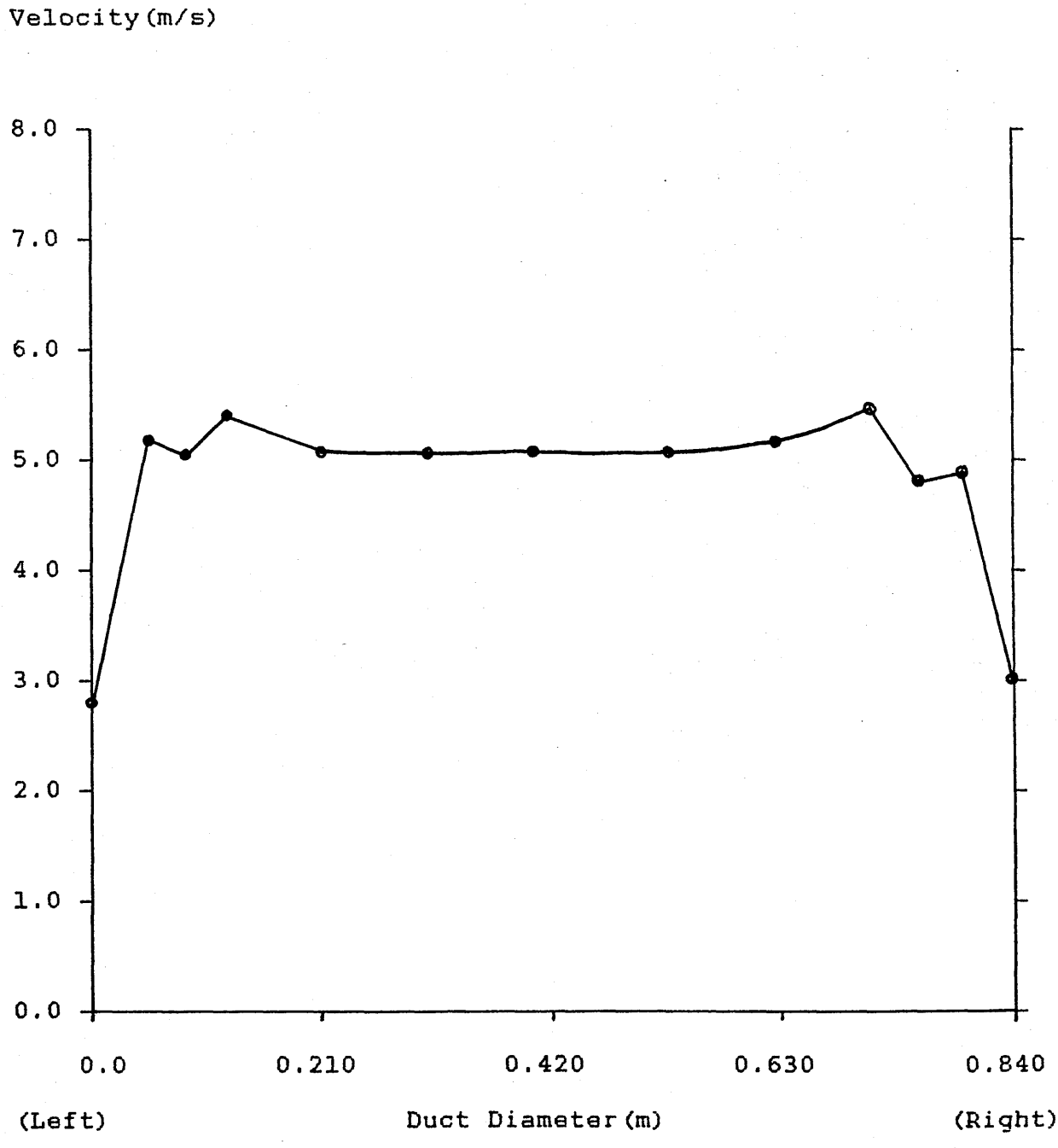

GRAPH (3) VELOCITY PROFILE INSIDE DUCT AT 5m/s

(Plane 2 at Y=0.420m (vertical distance))

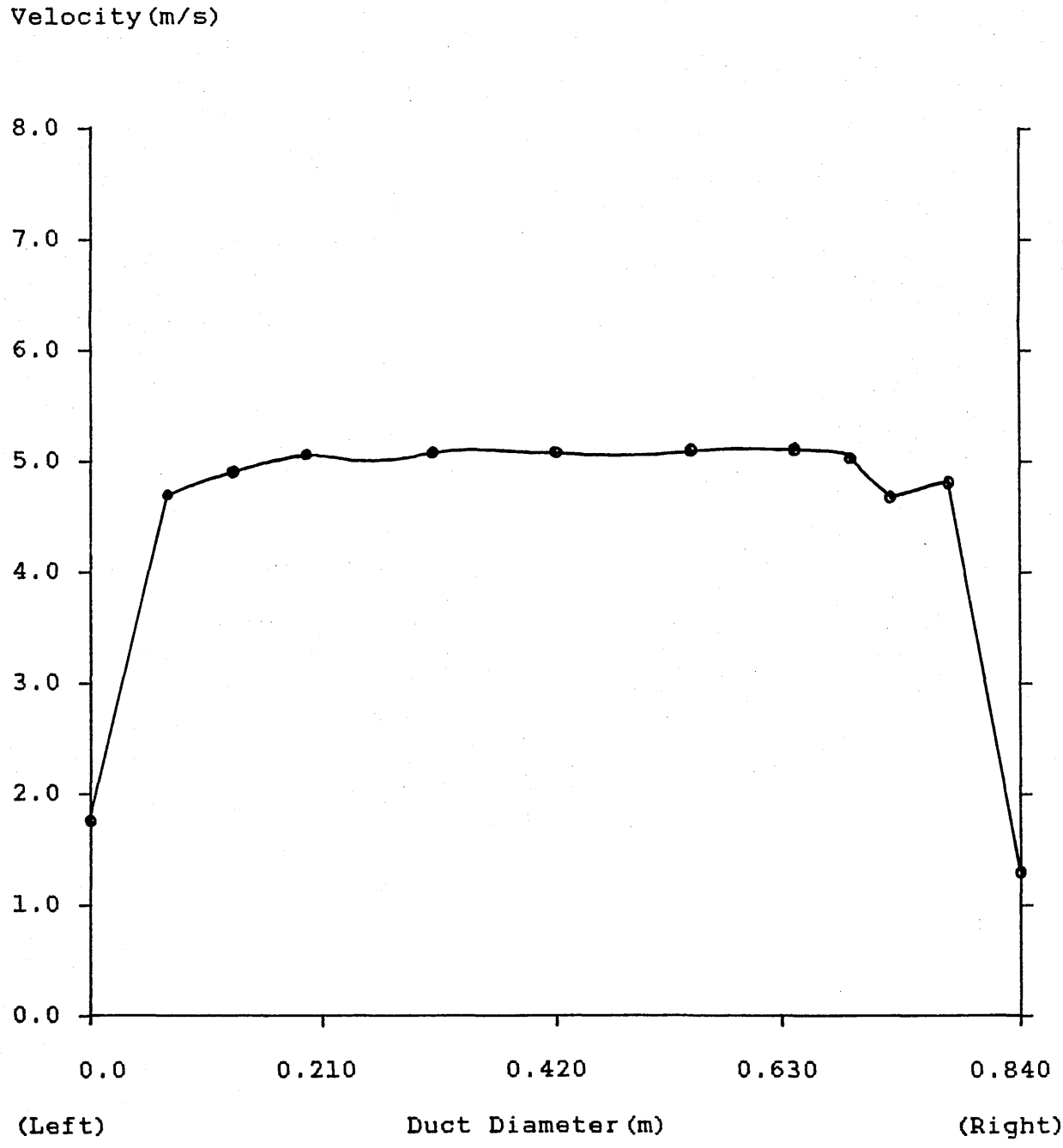

GRAPH (4) VELOCITY PROFILE INSIDE DUCT AT 5m/s

(Plane 3 at Y=0.420m (vertical distance))

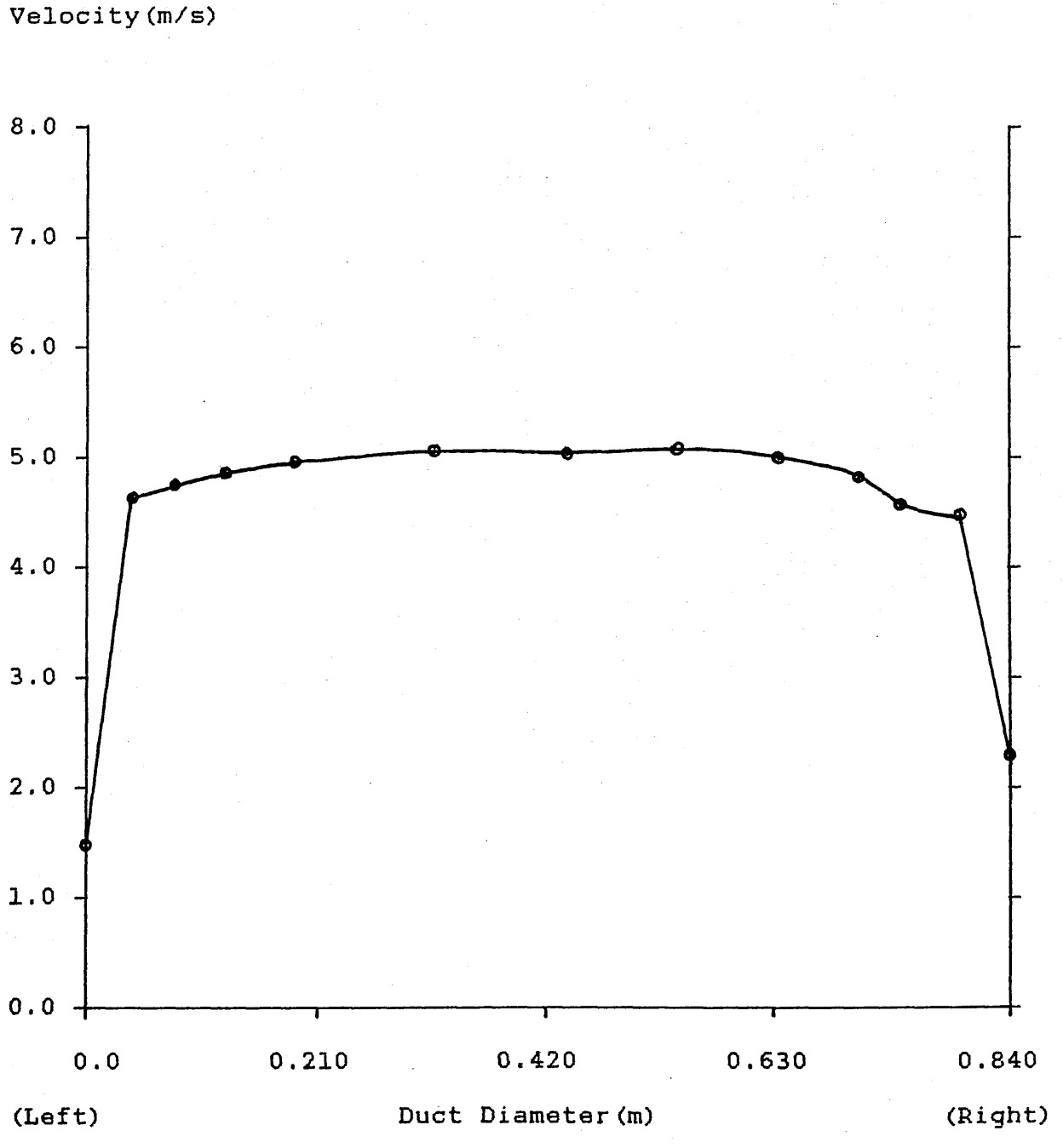

GRAPH (5) VELOCITY PROFILE INSIDE DUCT AT 5m/s

(Plane 4 at Y=0.420m (vertical distance))

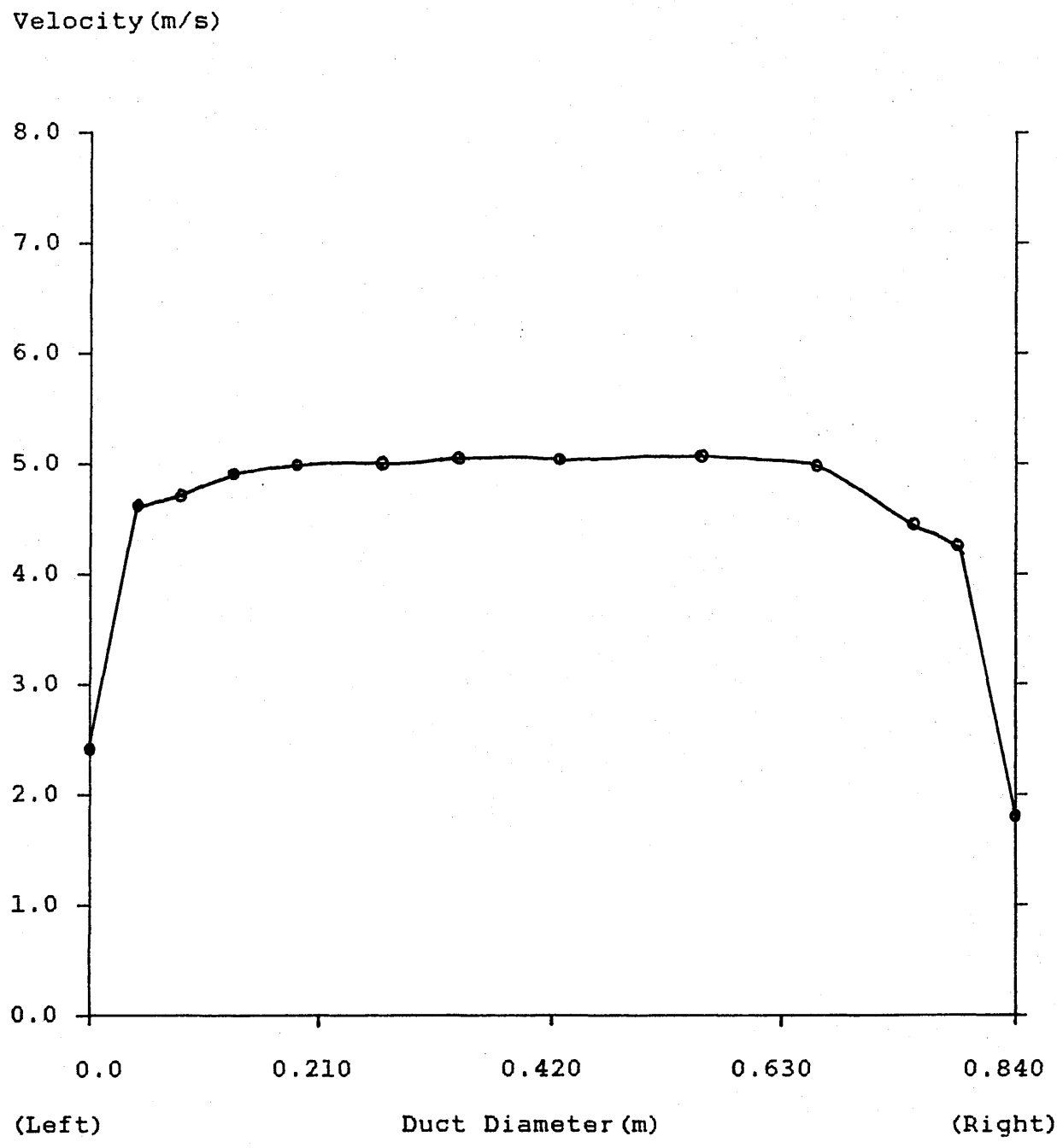

GRAPH (6) VELOCITY PROFILE INSIDE DUCT AT 5m/s

(Plane 5 at Y=0.420m (vertical distance))

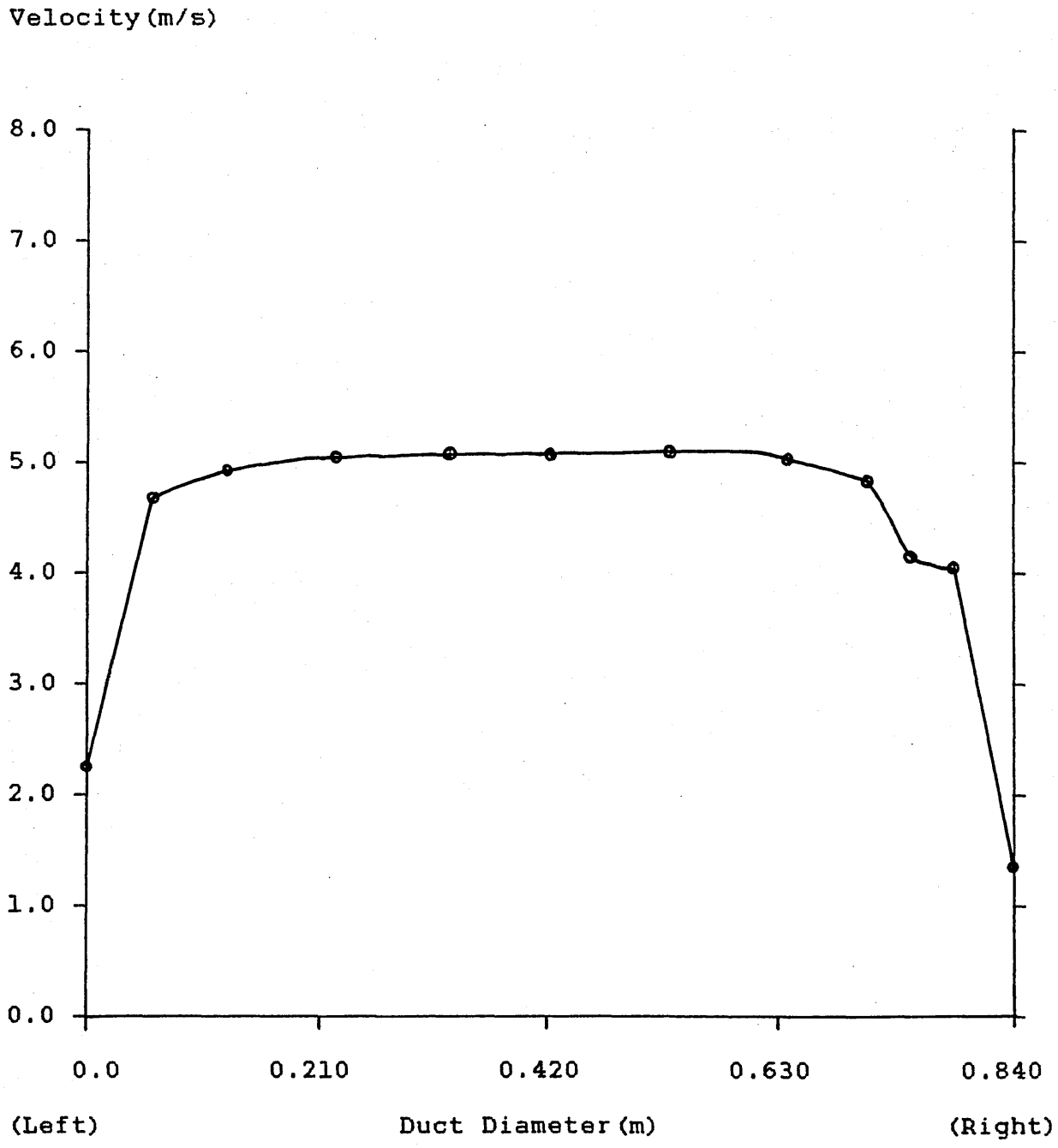

GRAPH (7) VELOCITY PROFILE INSIDE DUCT AT 5m/s

(Plane 6 at Y=0.420m (vertical distance))

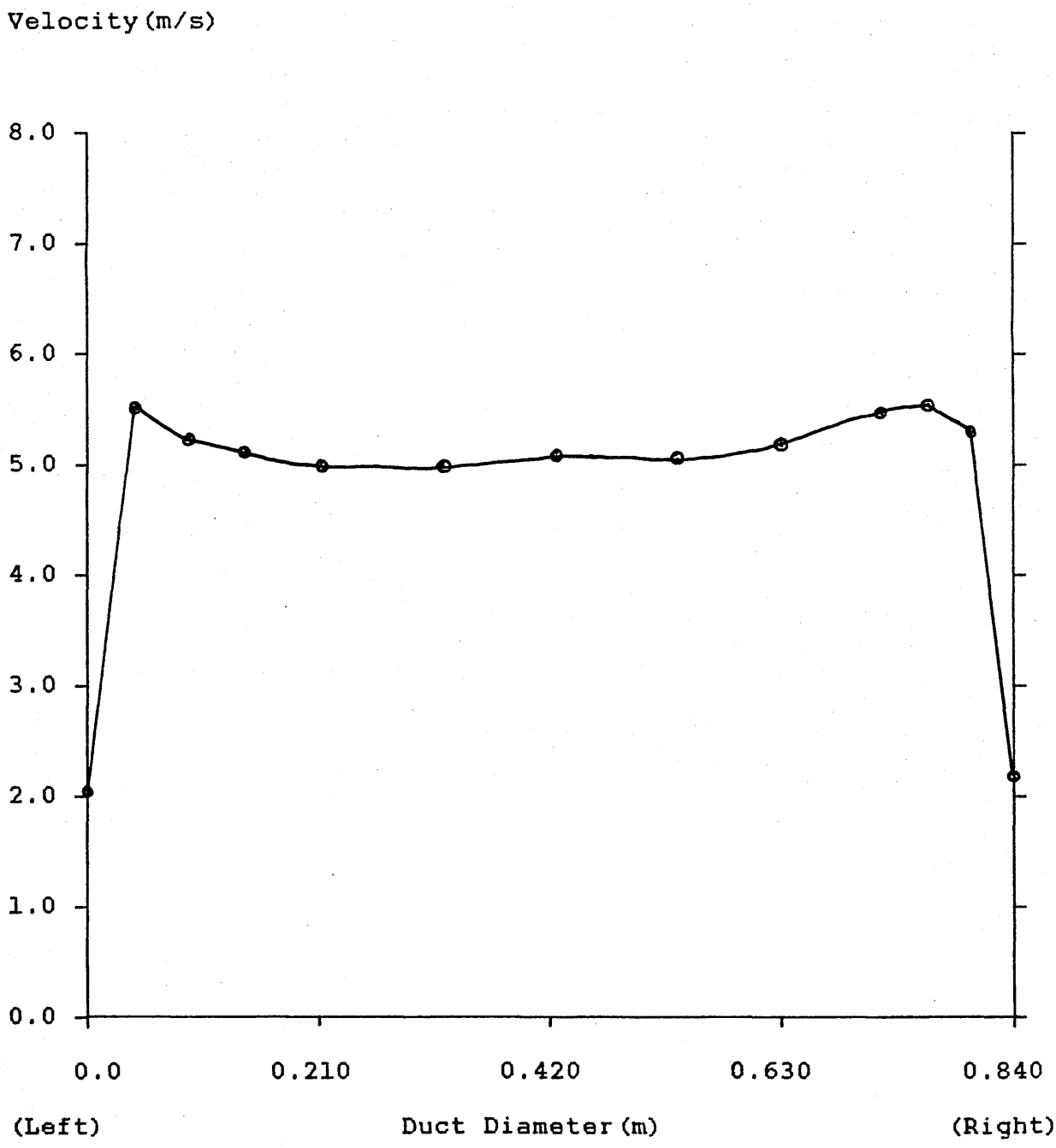

GRAPH (8) PRESSURE DISTRIBUTION ON SAIL AT $\alpha = 0^{\circ}$

(X=distance along leading edge)

(C=chord length)

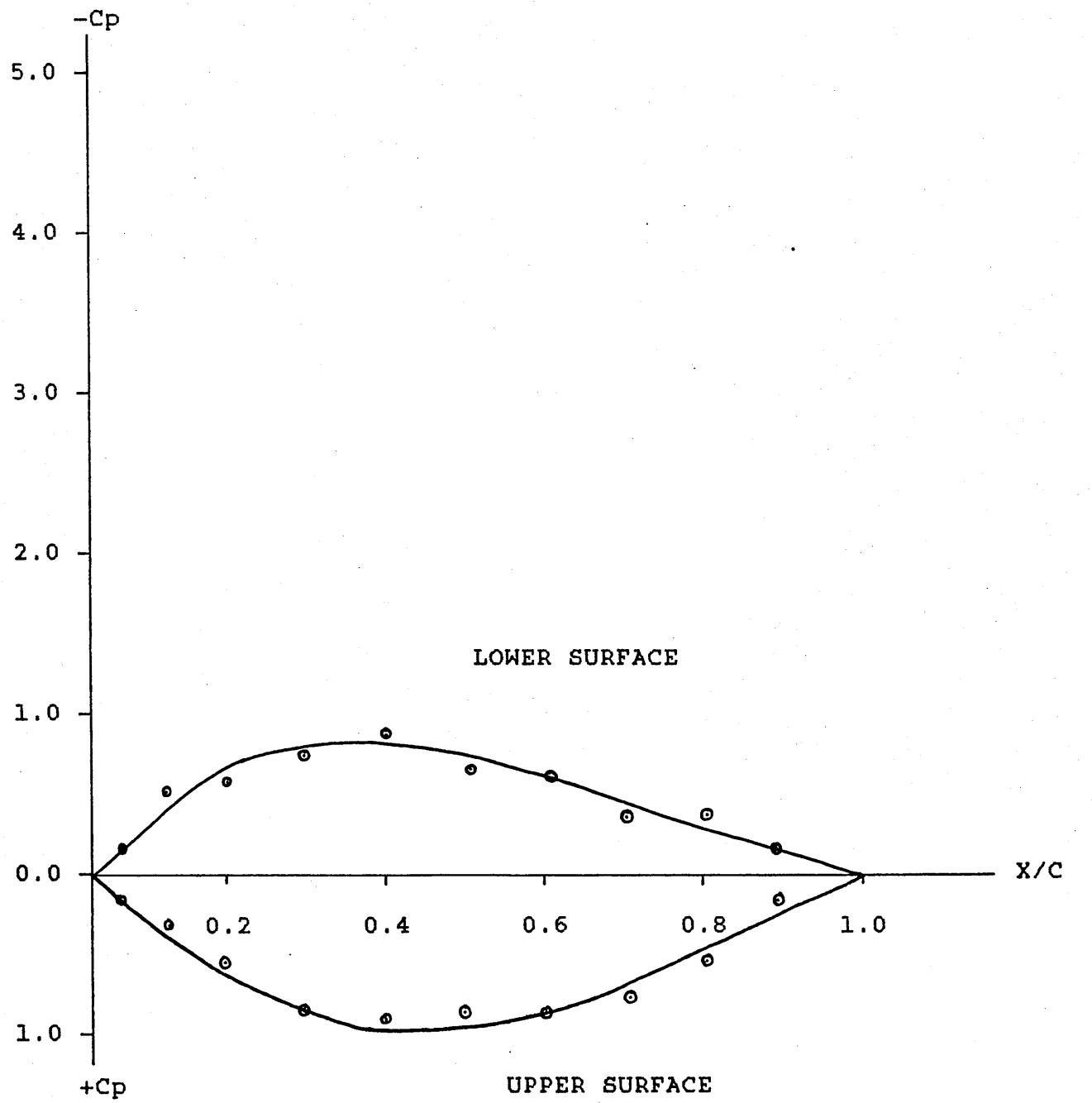

GRAPH (9) PRESSURE DISTRIBUTION ON SAIL AT $\alpha = 2.5^{\circ}$

(X=distance along leading edge)

(C=chord length)

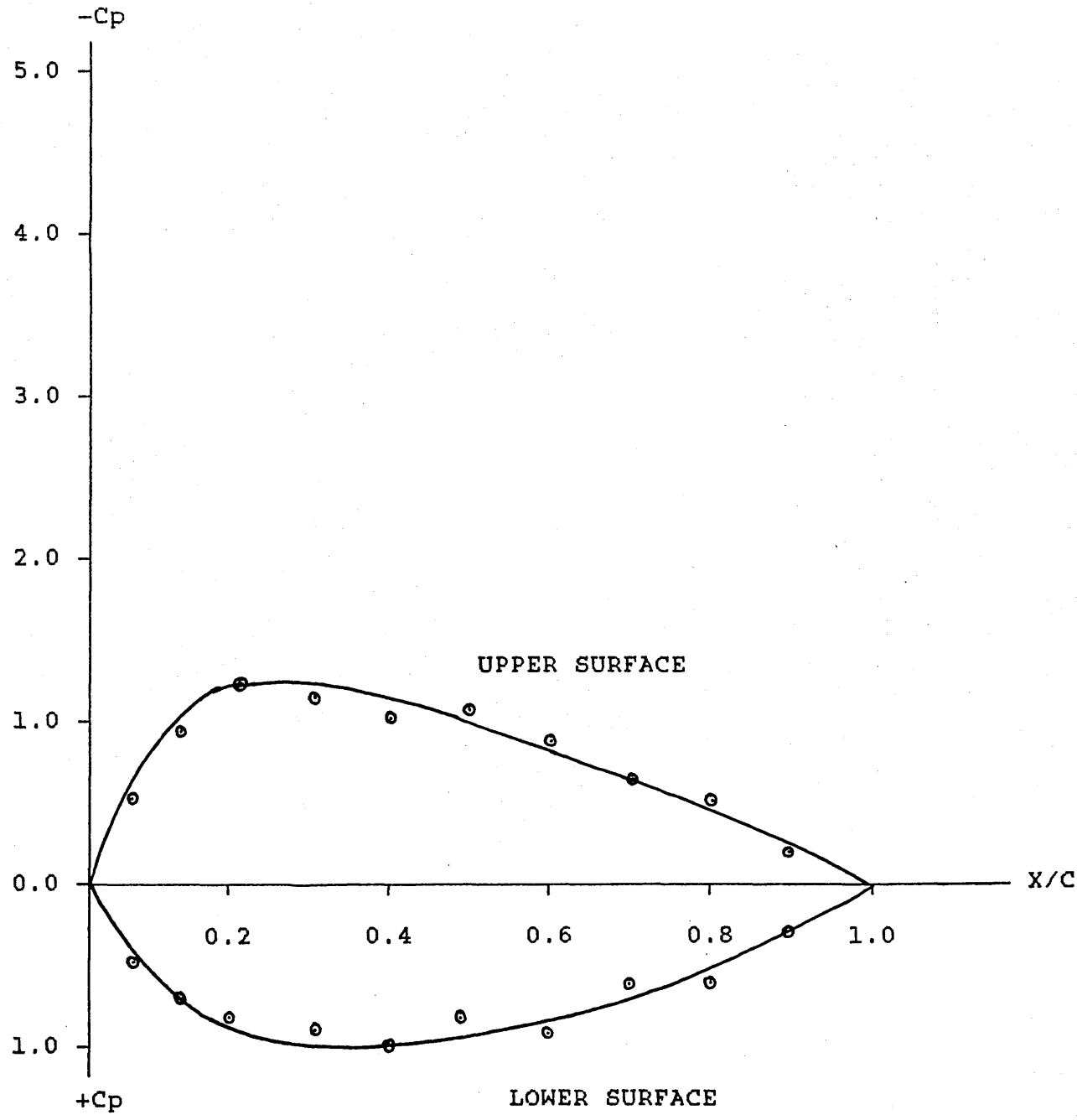

GRAPH (10) PRESSURE DISTRIBUTION ON SAIL AT $\alpha = 5.0^{\circ}$

(X=distance along leading edge)

(C=chord length)

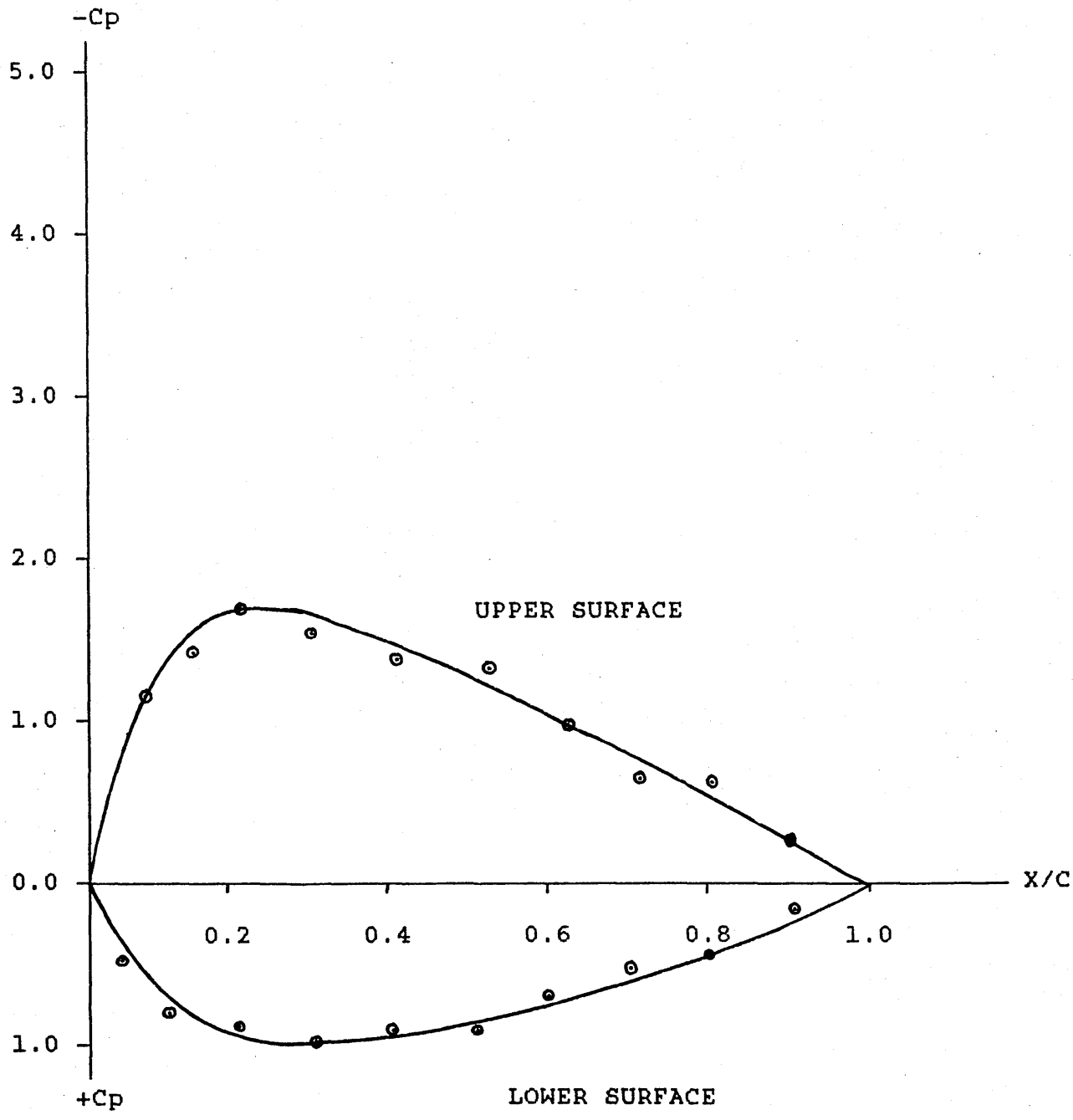

GRAPH (11) PRESSURE DISTRIBUTION ON SAIL AT $\alpha = 7.5^{\circ}$

(X=distance along leading edge)

(C=chord length)

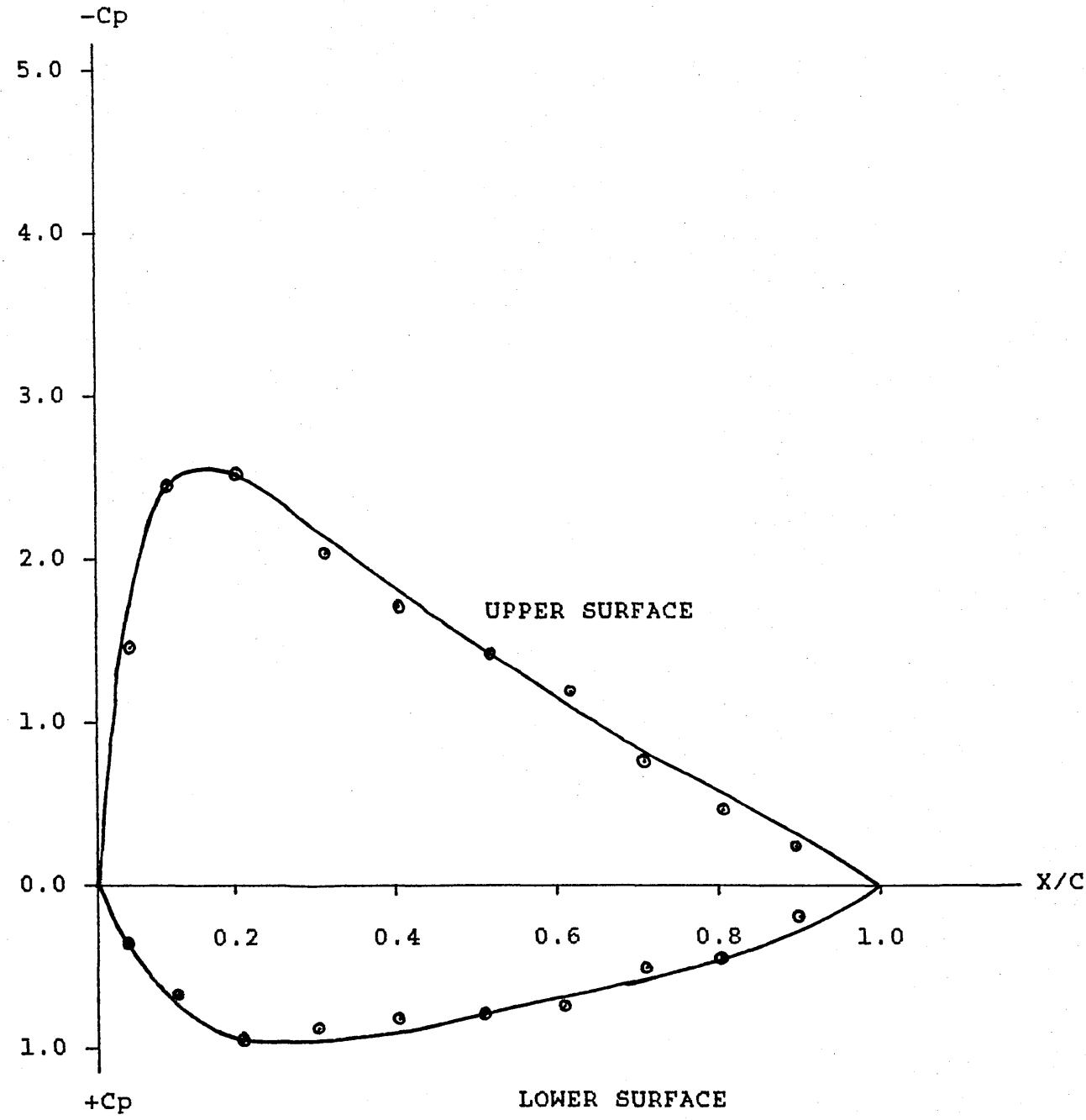

GRAPH (12) PRESSURE DISTRIBUTION ON SAIL AT $\alpha=10^{\circ}$

(X=distance along leading edge)

(C=chord length)

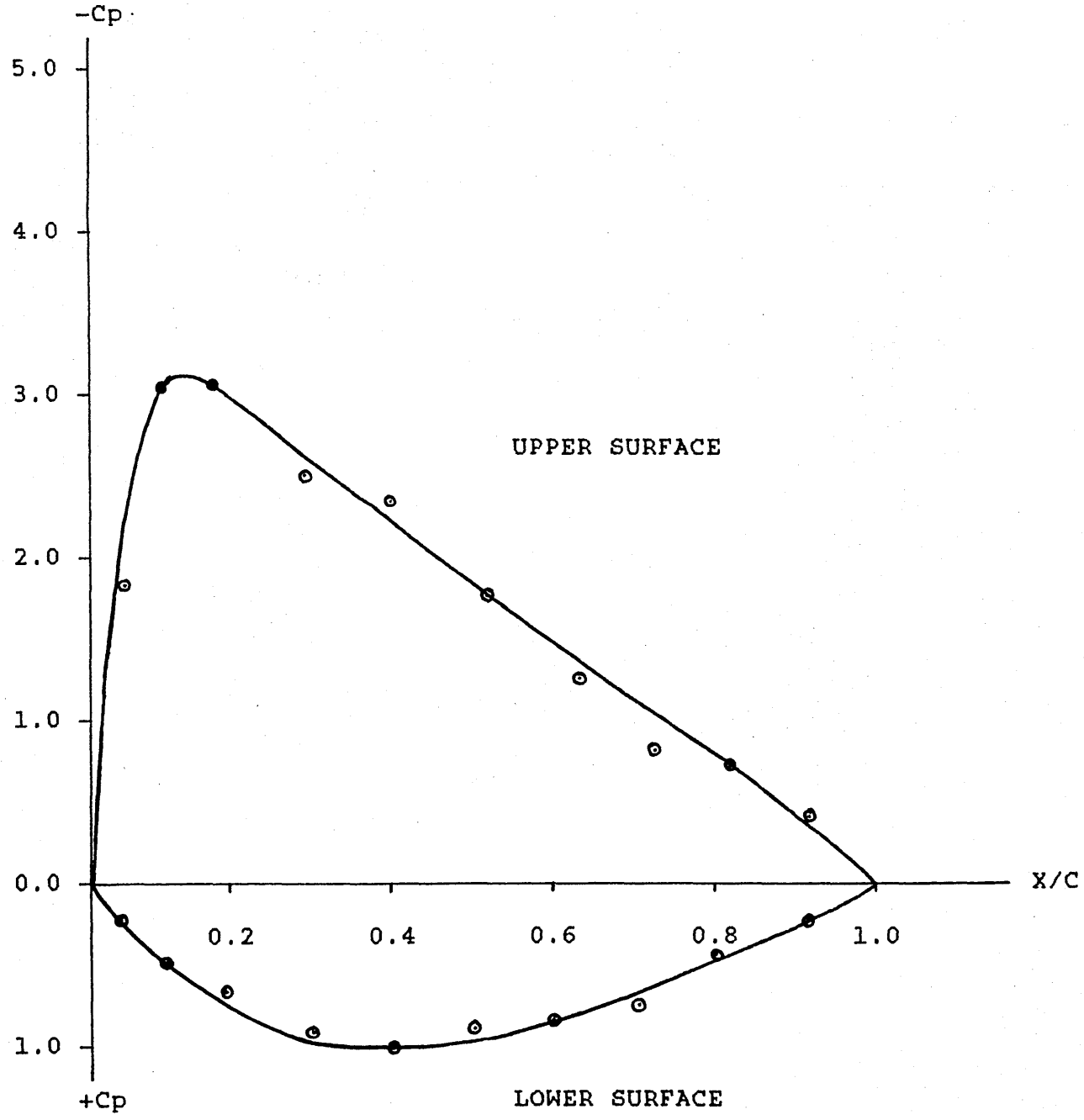

GRAPH (13) PRESSURE DISTRIBUTION ON SAIL AT $\alpha = 12.5^{\circ}$

(X=distance along leading edge)

(C=chord length)

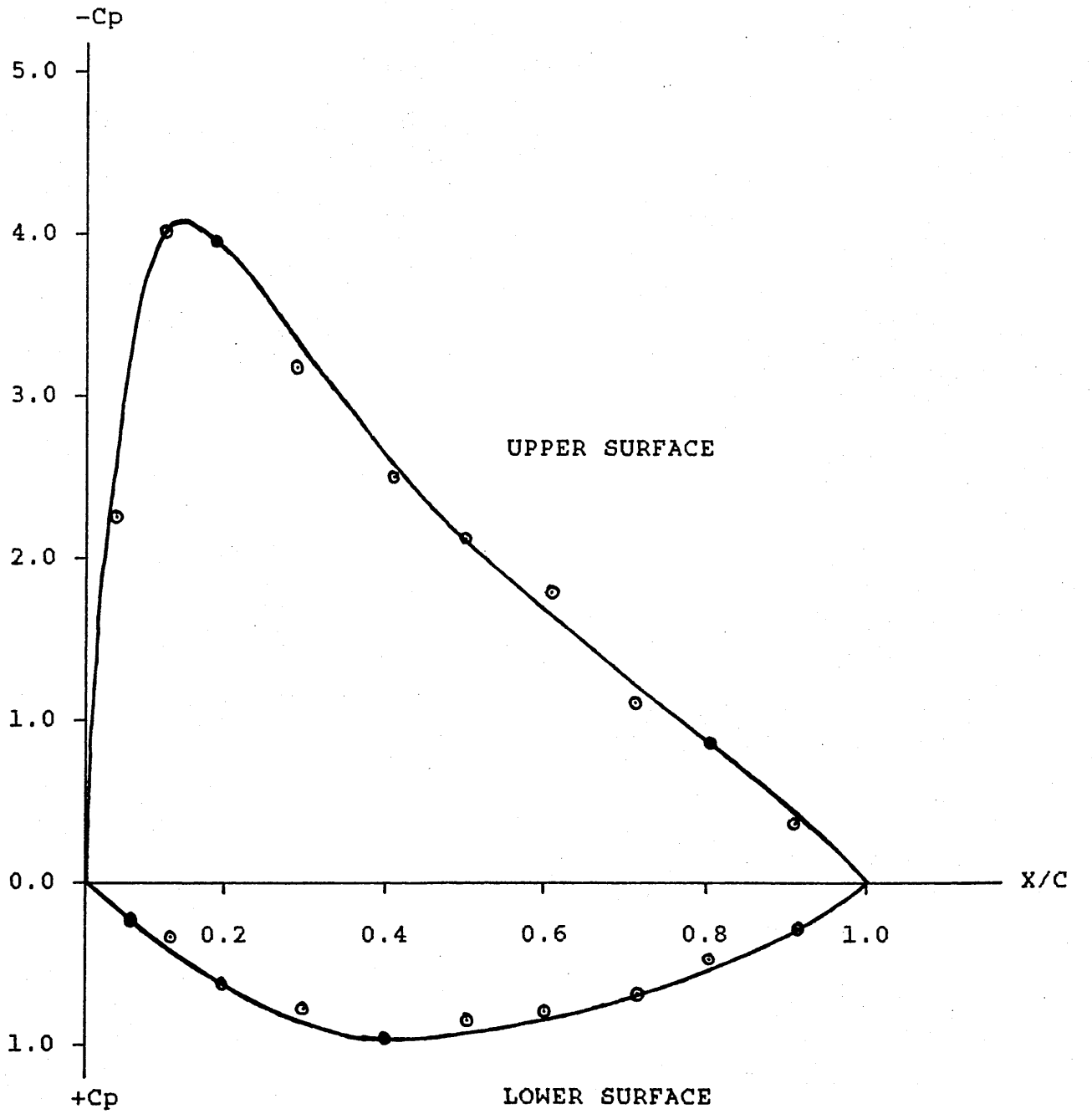

GRAPH (14) PRESSURE DISTRIBUTION ON SAIL AT $\alpha = 15^{\circ}$

(X=distance along leading edge)

(C=chord length)

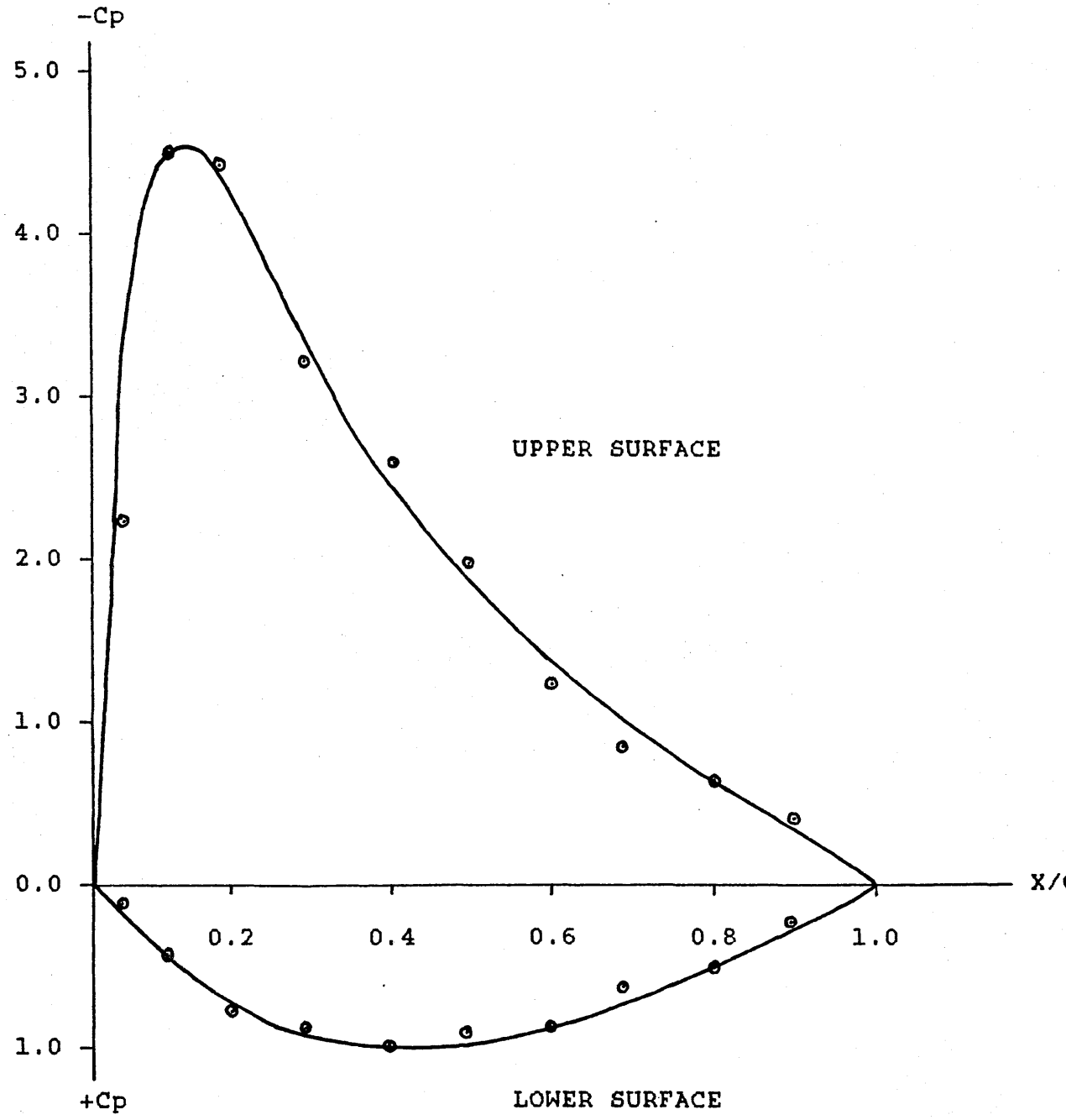

GRAPH (15) PRESSURE DISTRIBUTION ON SAIL AT $\alpha = 17.5^{\circ}$

(X=distance along leading edge)

(C=chord length)

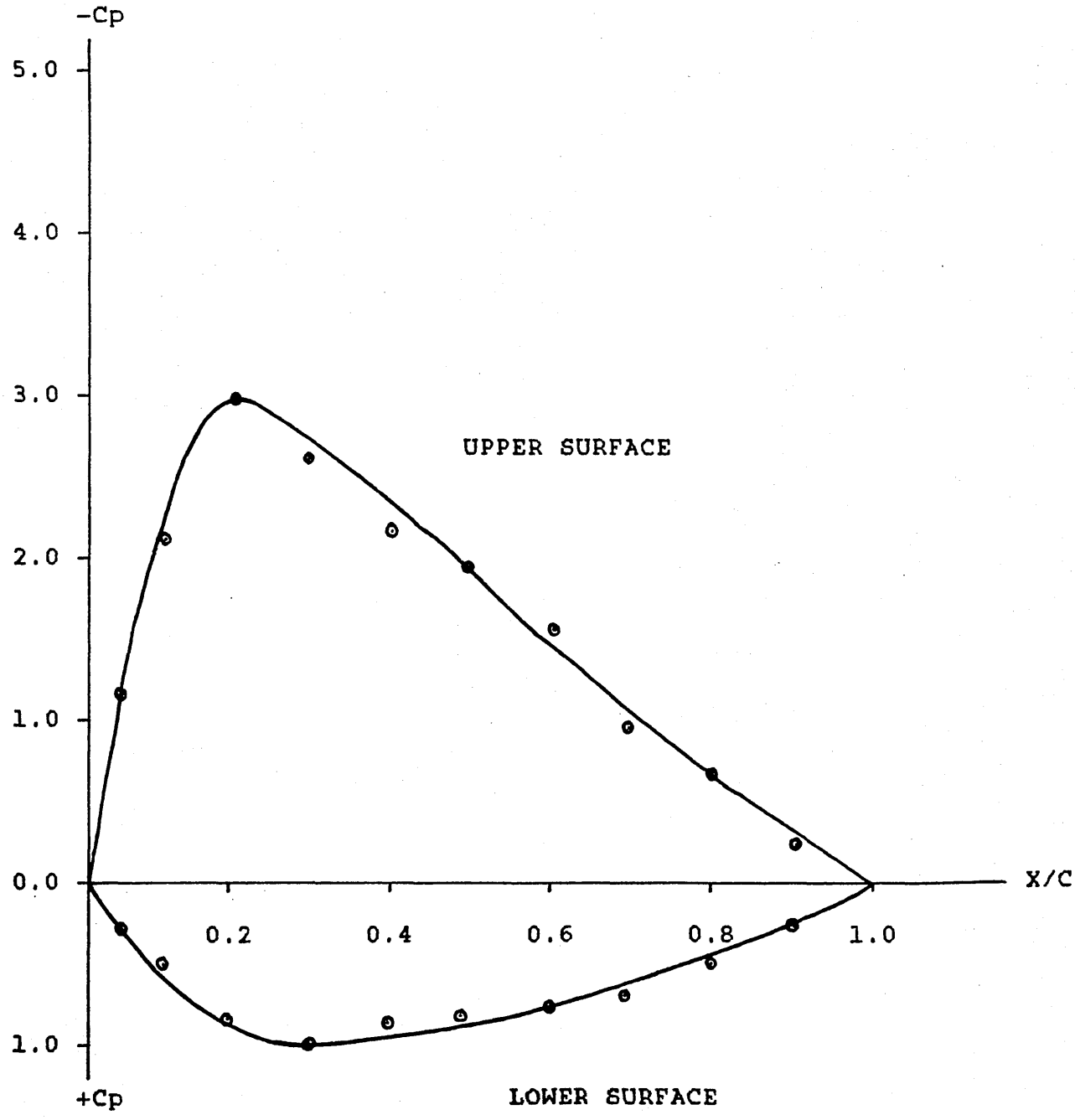

GRAPH (16) PRESSURE DISTRIBUTION ON SAIL AT $\alpha=20^{\circ}$

(X=distance along leading edge)

(C=chord length)

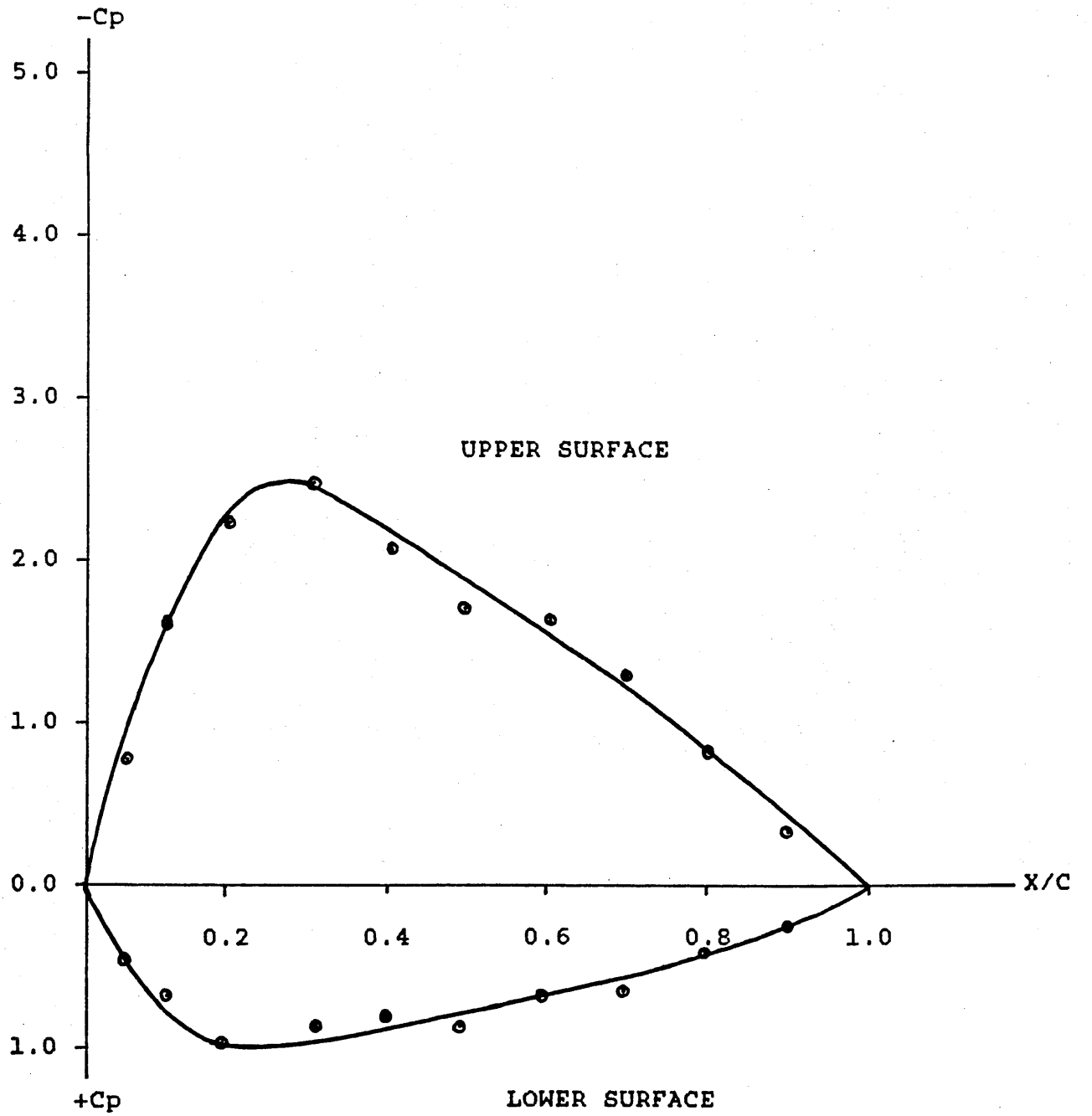

GRAPH (17) LIFT COEFFICIENT C_L AGAINST ANGLE OF ATTACK α

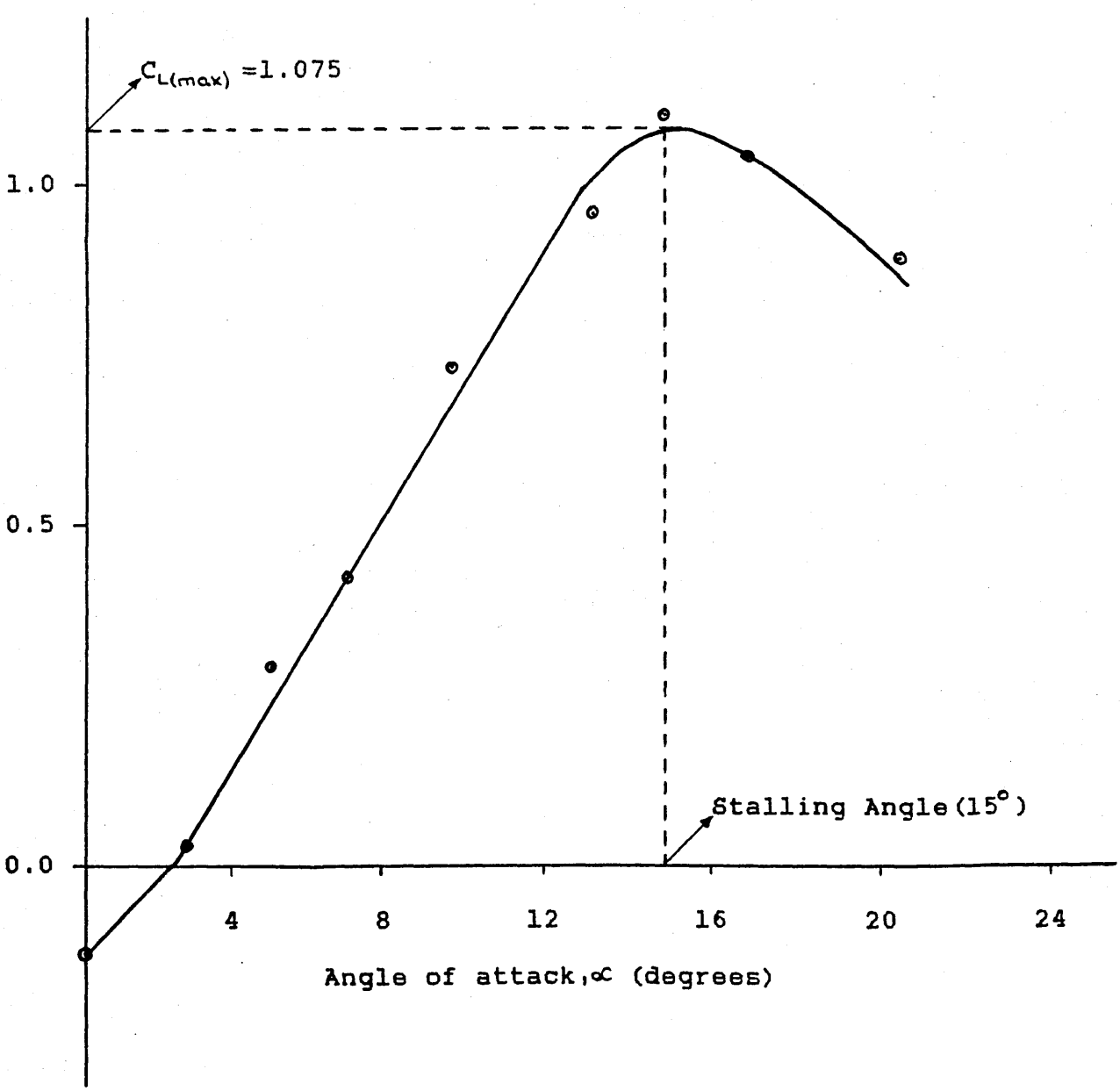

GRAPH (18) THE EFFECT OF HUB-FAIRINGS (NO AFTER-BODY) ON WIND-TURBINE POWER OUTPUT.

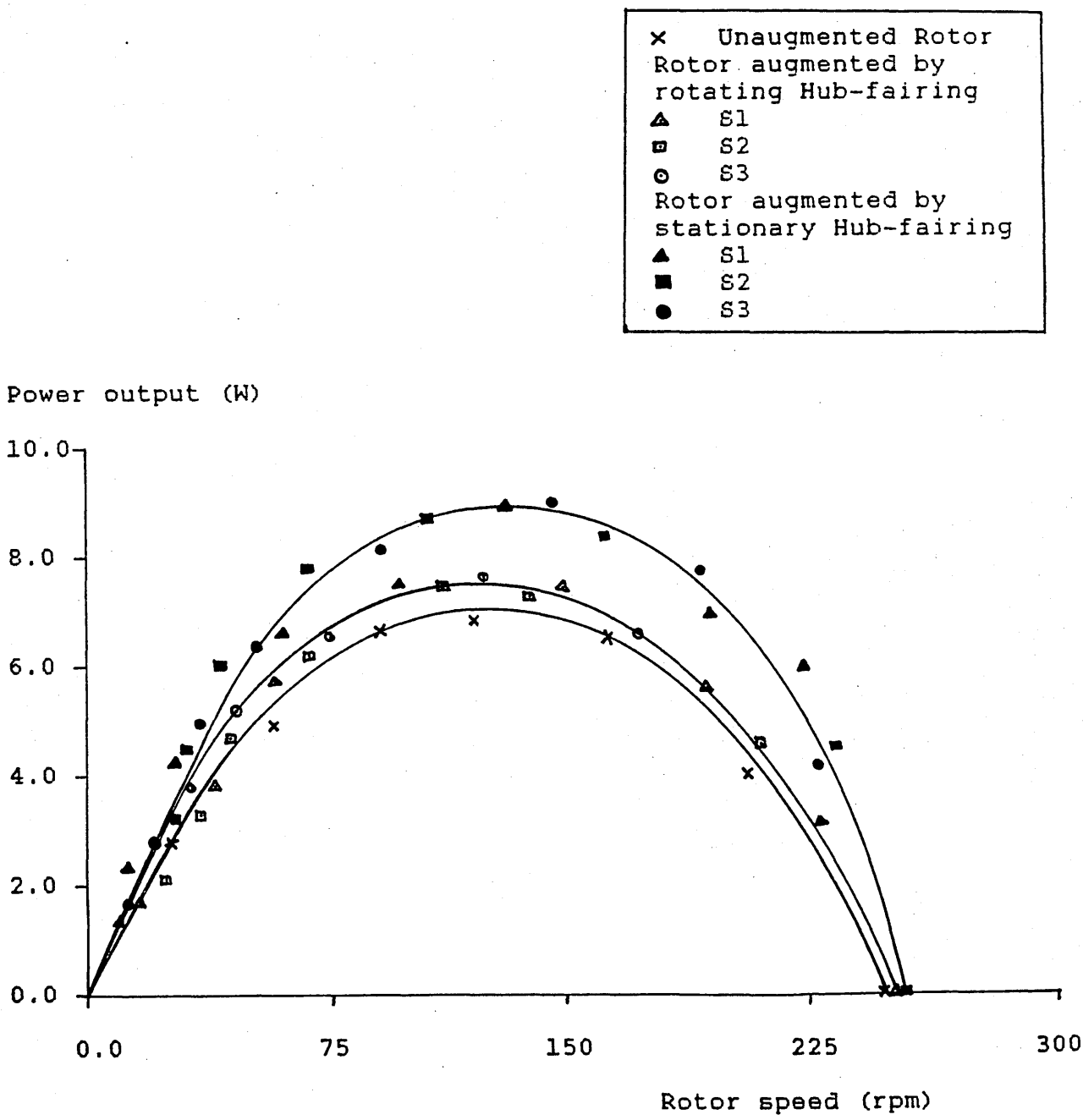

GRAPH (19) THE EFFECT OF HUB-FAIRINGS AND AFTER-BODY A1 ON WIND-TURBINE POWER OUTPUT.

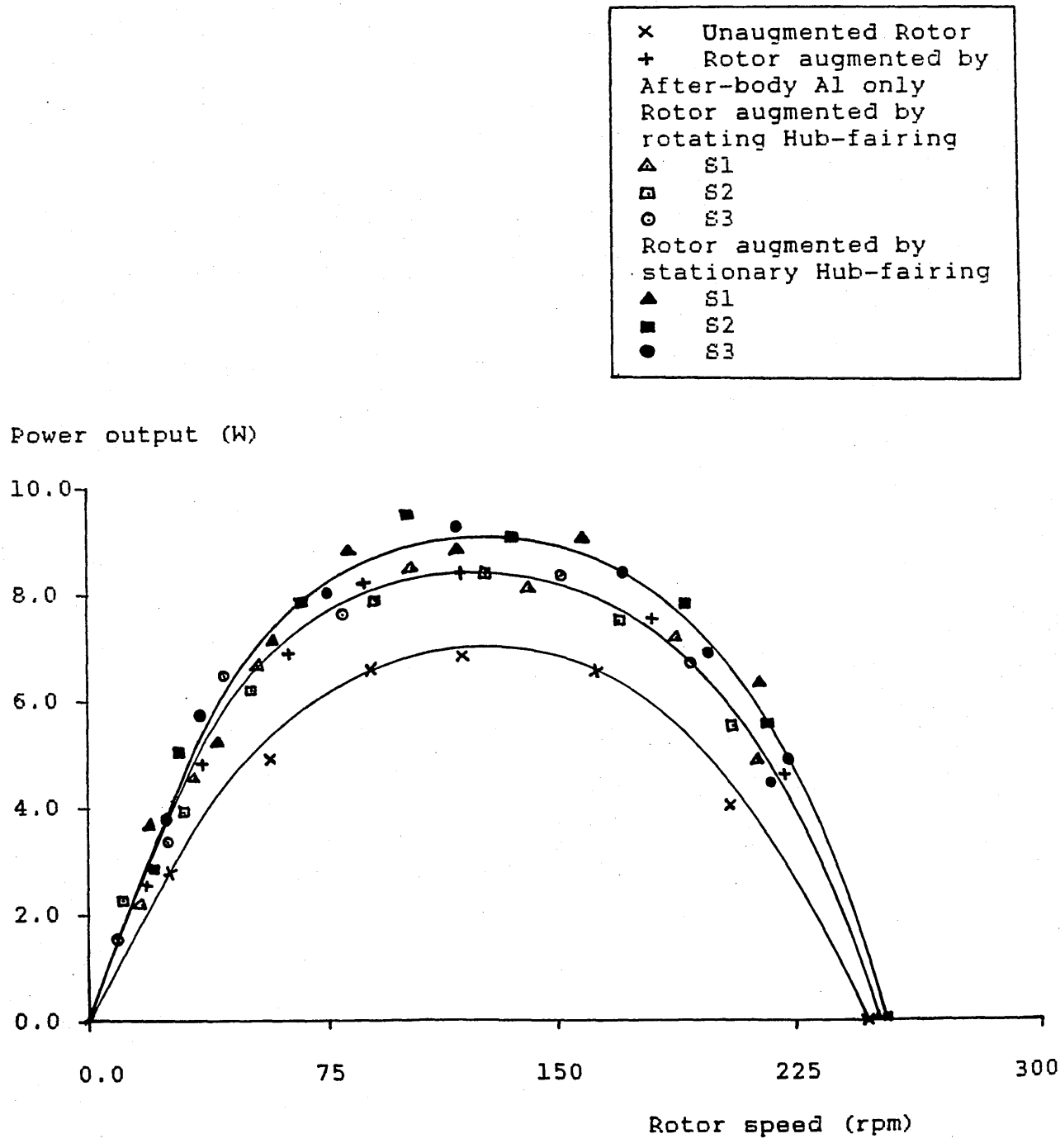

GRAPH (20) THE EFFECT OF HUB-FAIRINGS AND AFTER-BODY A2 ON WIND-TURBINE POWER OUTPUT.

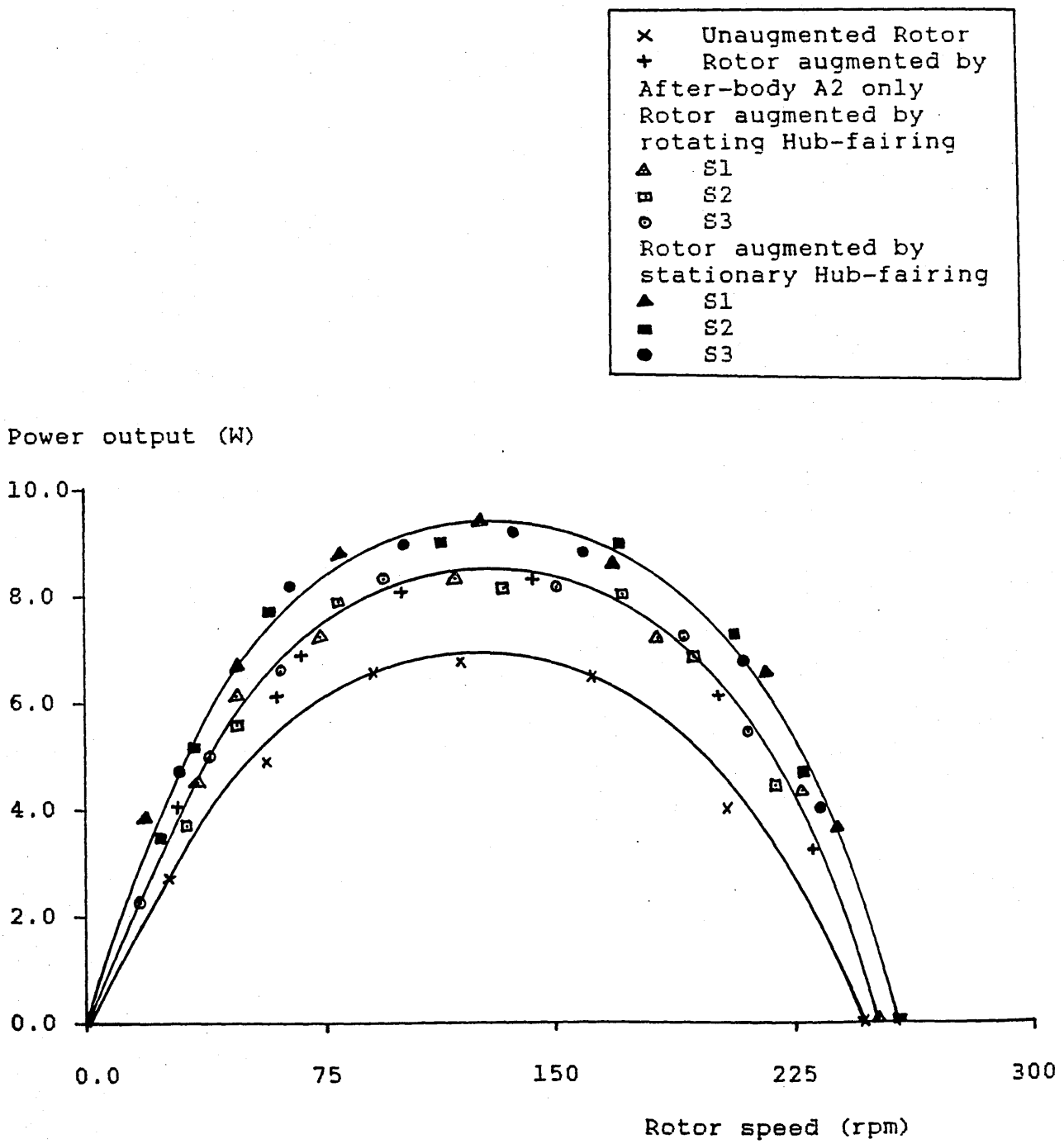

GRAPH (21) THE EFFECT OF TIP-FINS AND CENTRE-BODIES ON WIND-TURBINE POWER OUTPUT, FIN(1).

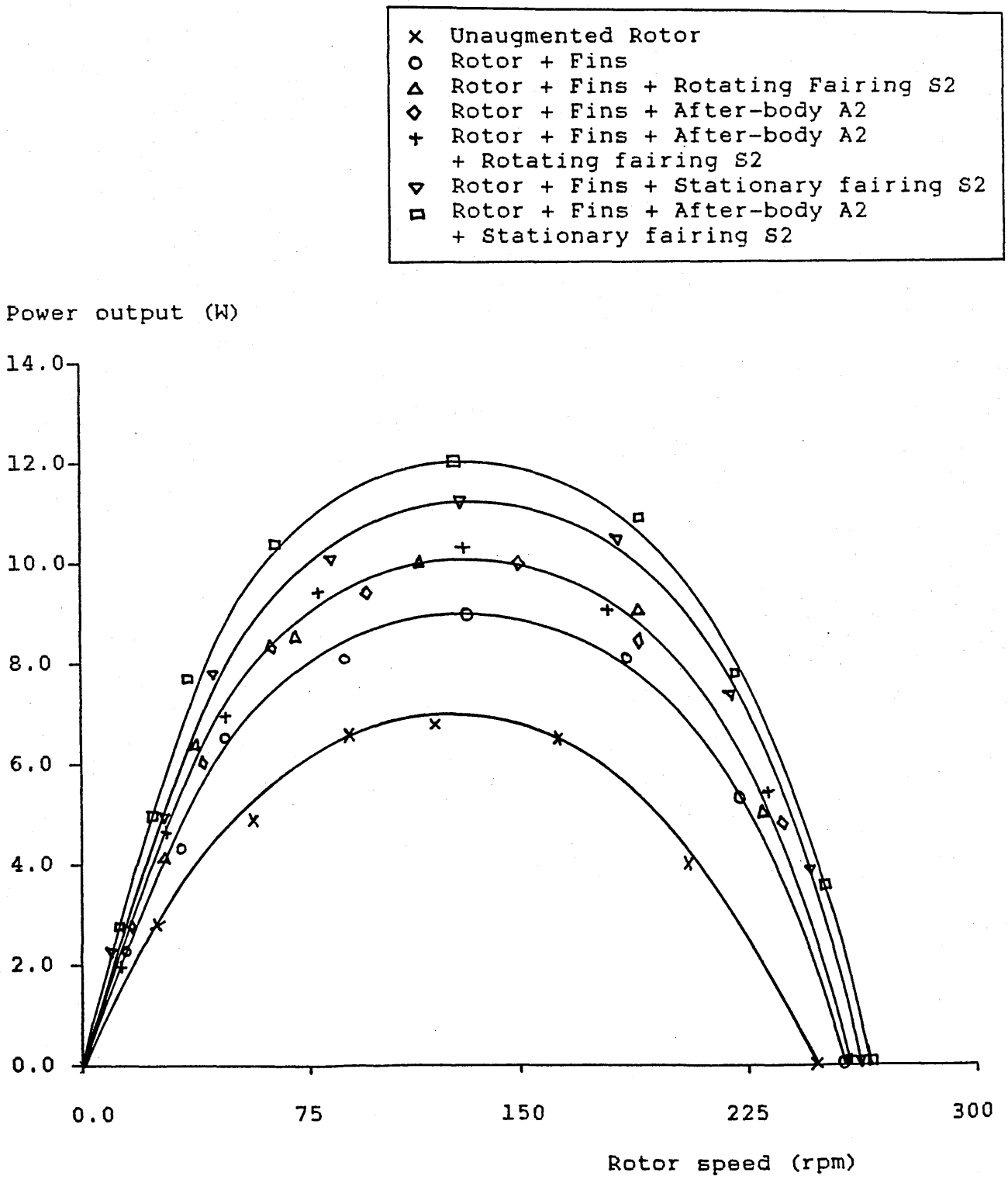

GRAPH (22) THE EFFECT OF TIP-FINS AND CENTRE-BODIES ON WIND-TURBINE POWER OUTPUT, FIN(2).

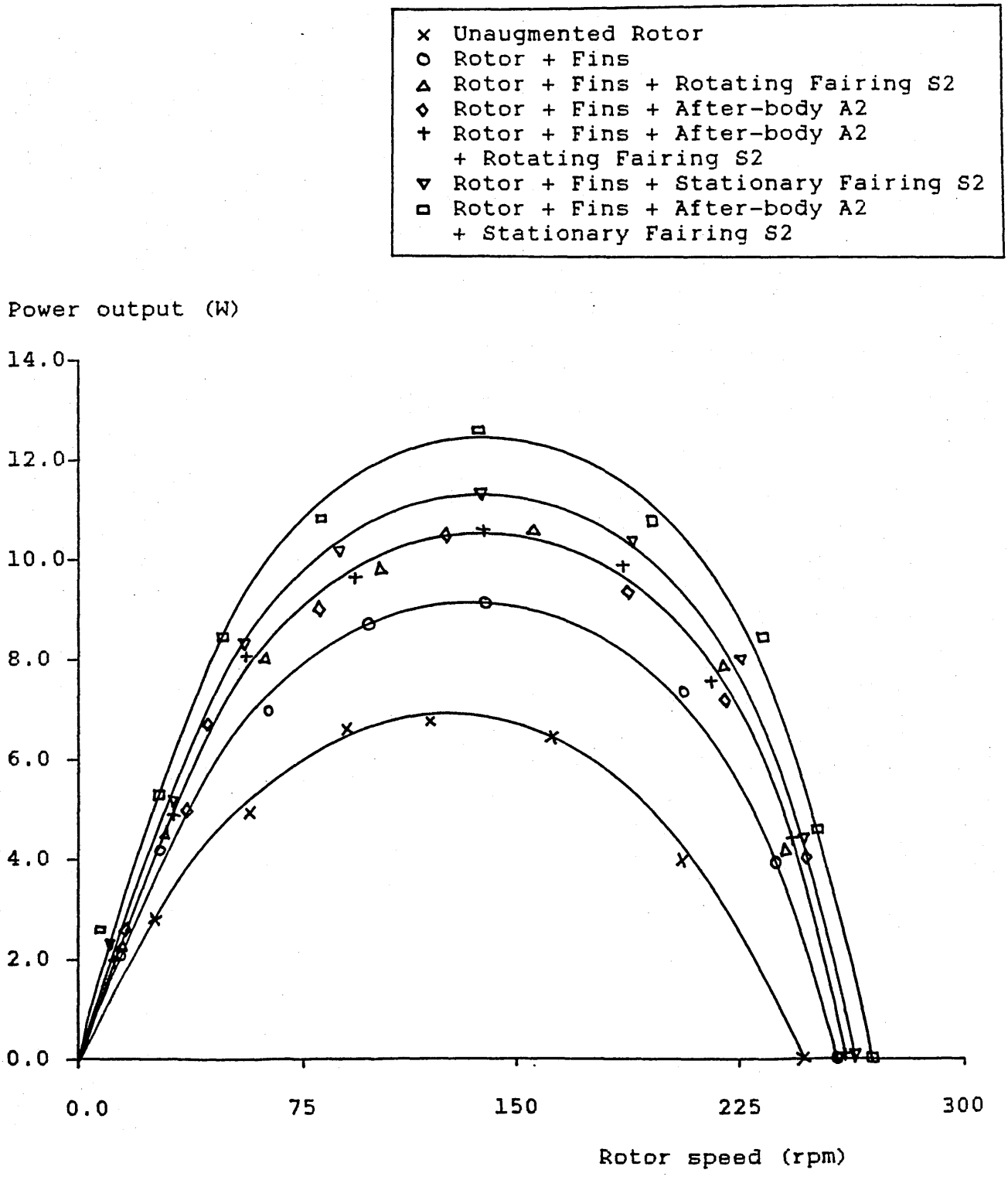

GRAPH (23) THE EFFECT OF TIP-FINS AND CENTRE-BODIES ON WIND-TURBINE POWER OUTPUT, FIN(3).

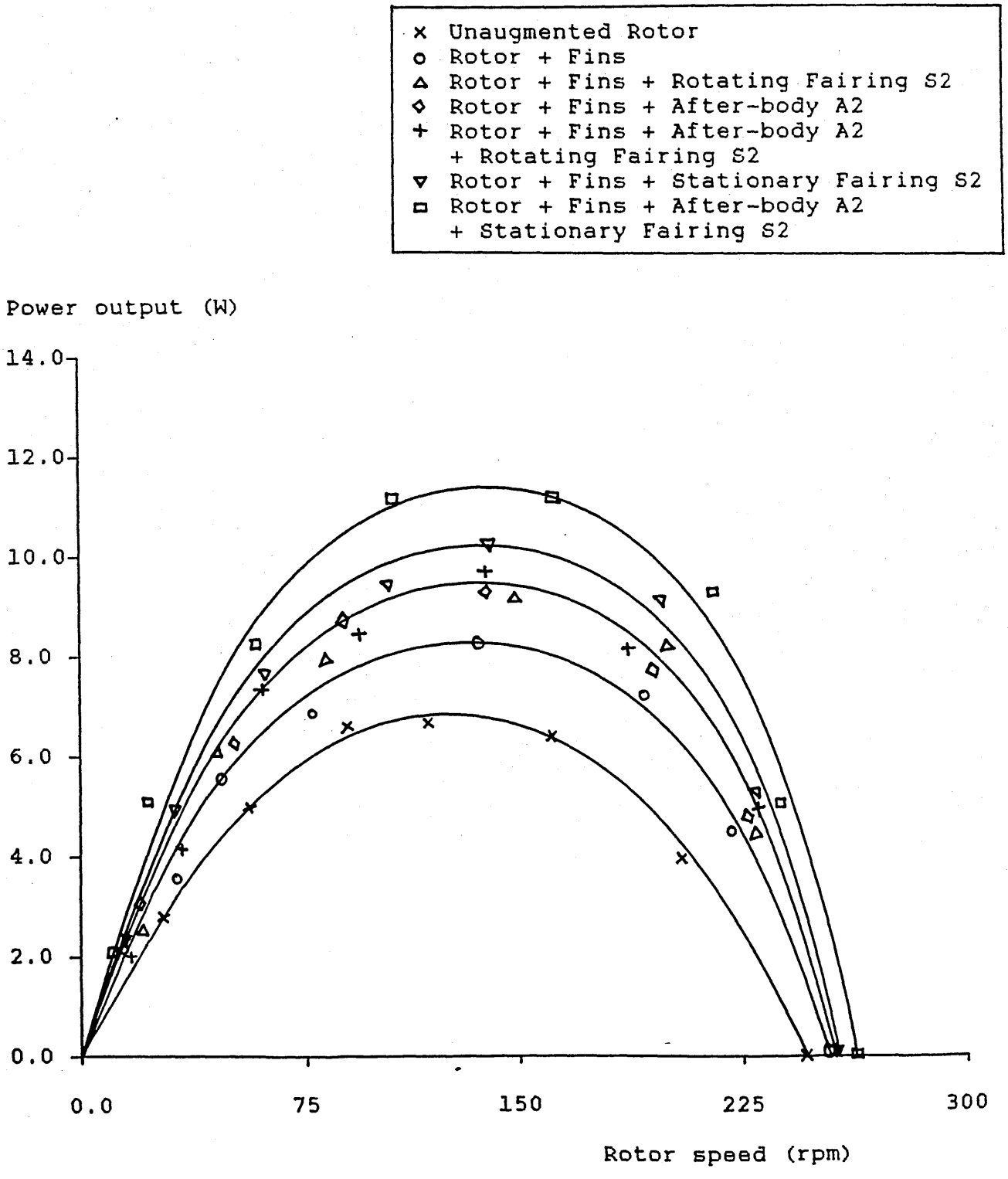

GRAPH (24) THE EFFECT OF TIP-FINS AND CENTRE-BODIES ON WIND-TURBINE POWER OUTPUT, FIN(4).

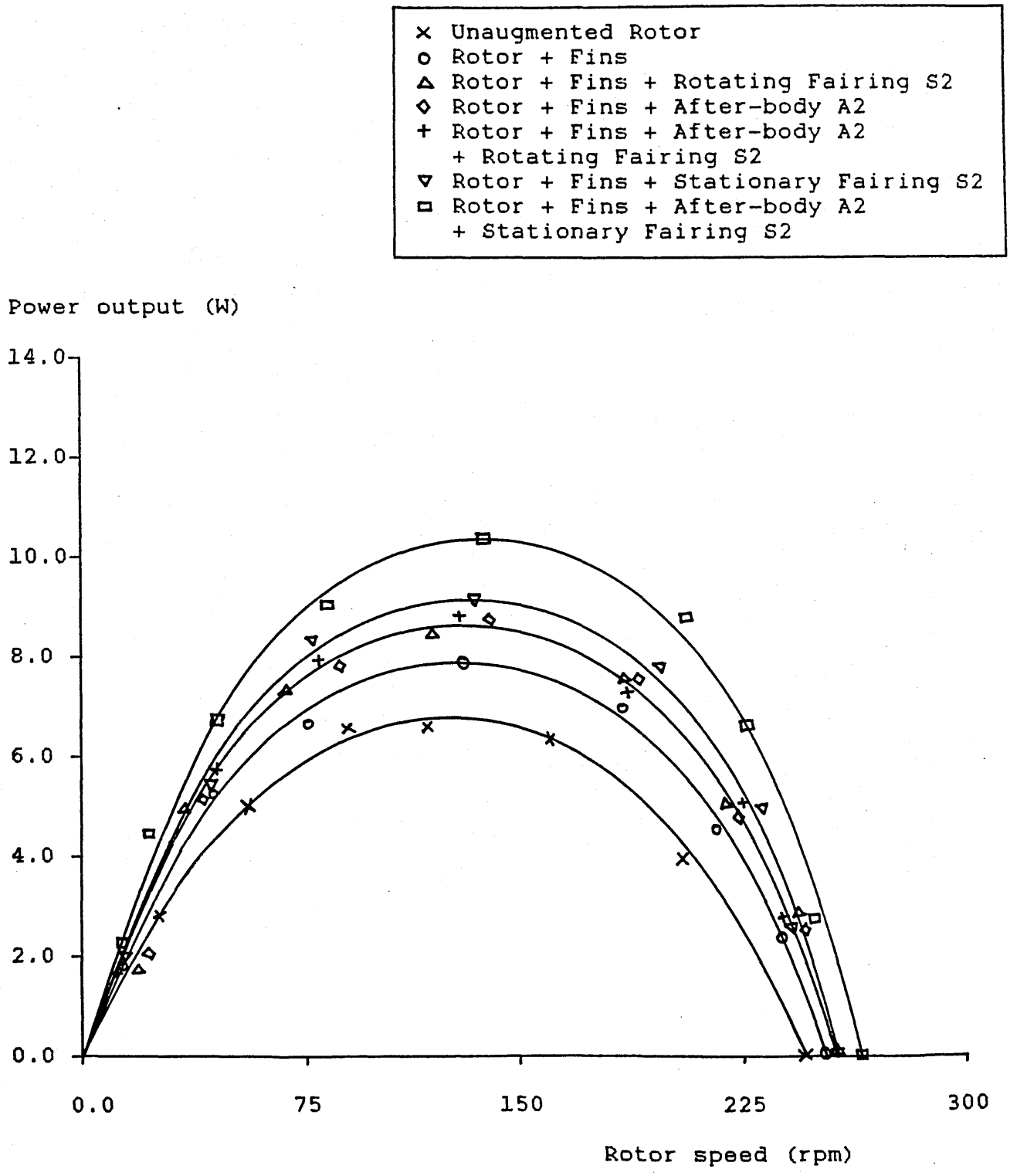

GRAPH (25) THE EFFECT OF TIP-FINS AND CENTRE-BODIES ON WIND-TURBINE POWER OUTPUT, FIN(5).

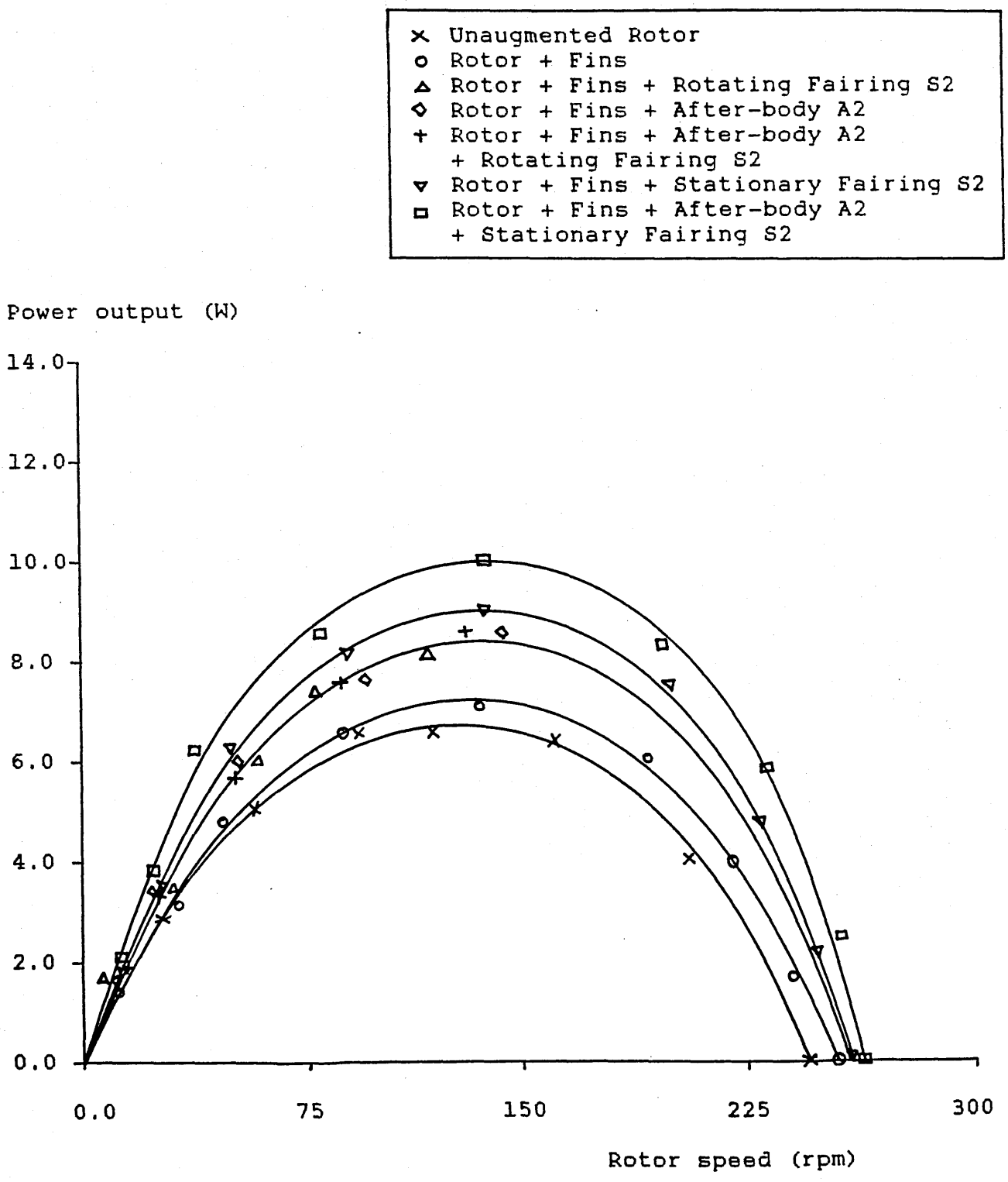

GRAPH (26) THE EFFECT OF TIP-FINS AND CENTRE-BODIES ON WIND-TURBINE POWER OUTPUT, FIN(6).

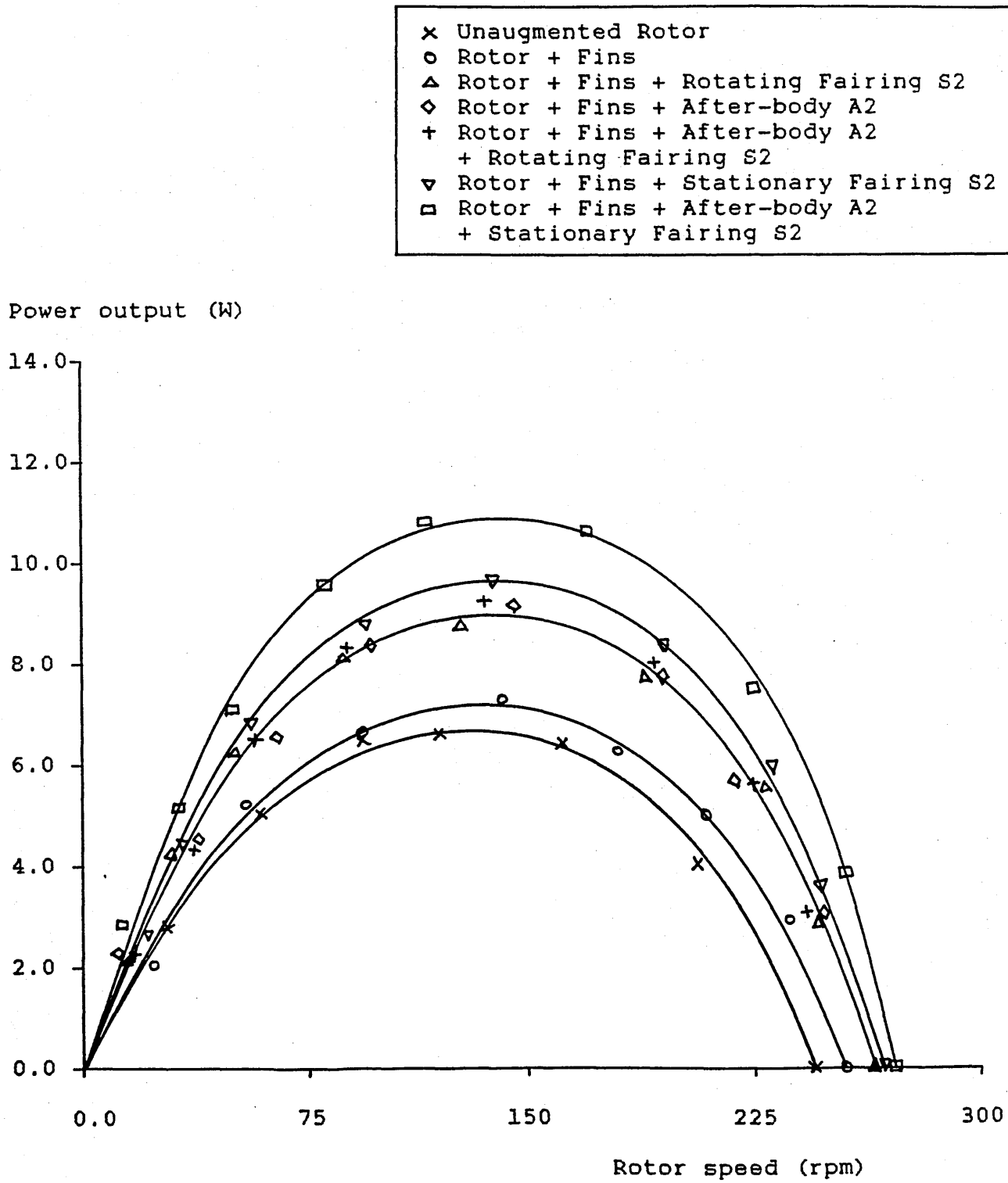

GRAPH (27) THE EFFECT OF TIP-FINS AND CENTRE-BODIES ON WIND-TURBINE POWER OUTPUT, FIN(7).

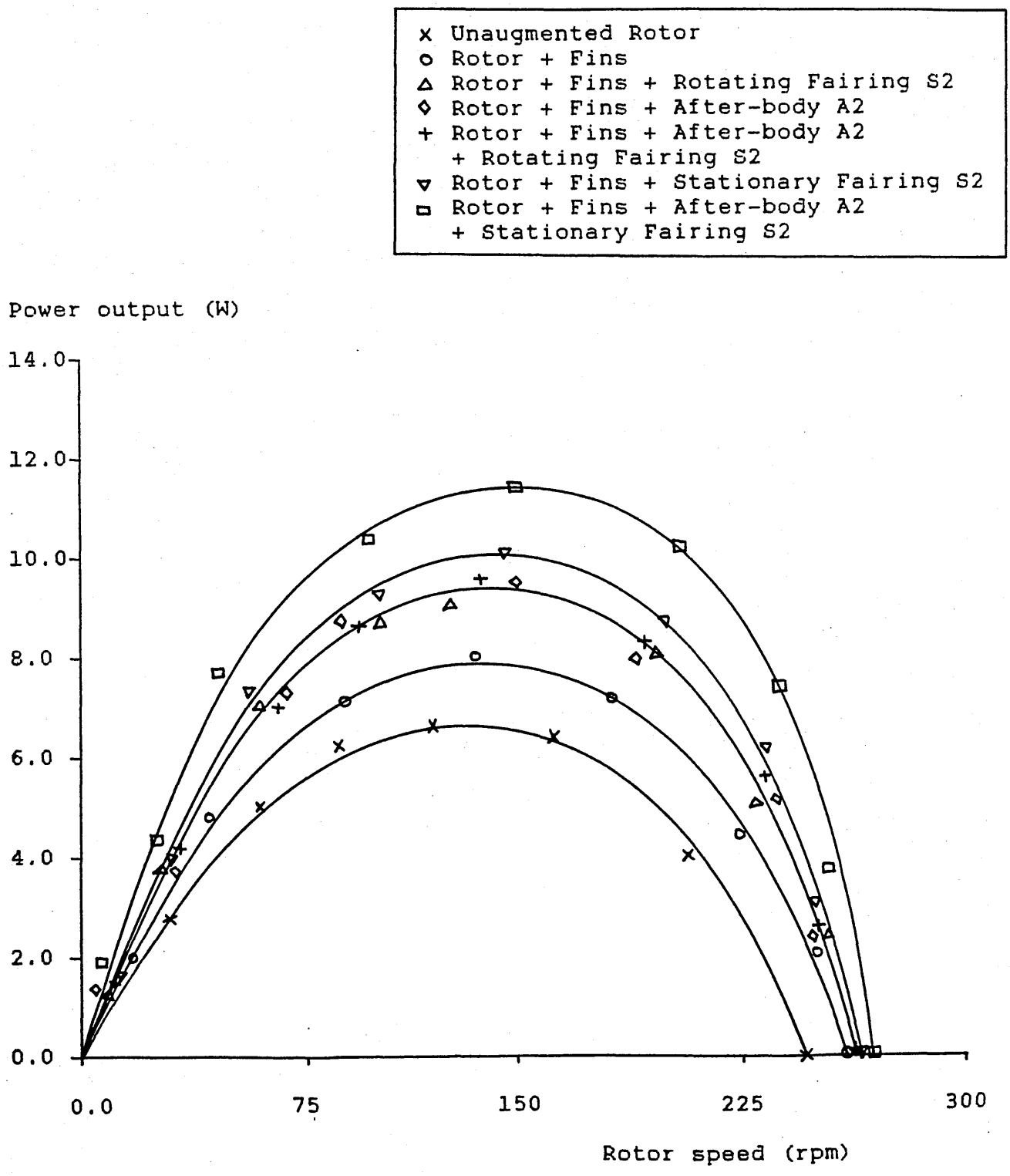

GRAPH (28) THE EFFECT OF TIP-FINS AND CENTRE-BODIES ON WIND-TURBINE POWER OUTPUT, FIN(8).

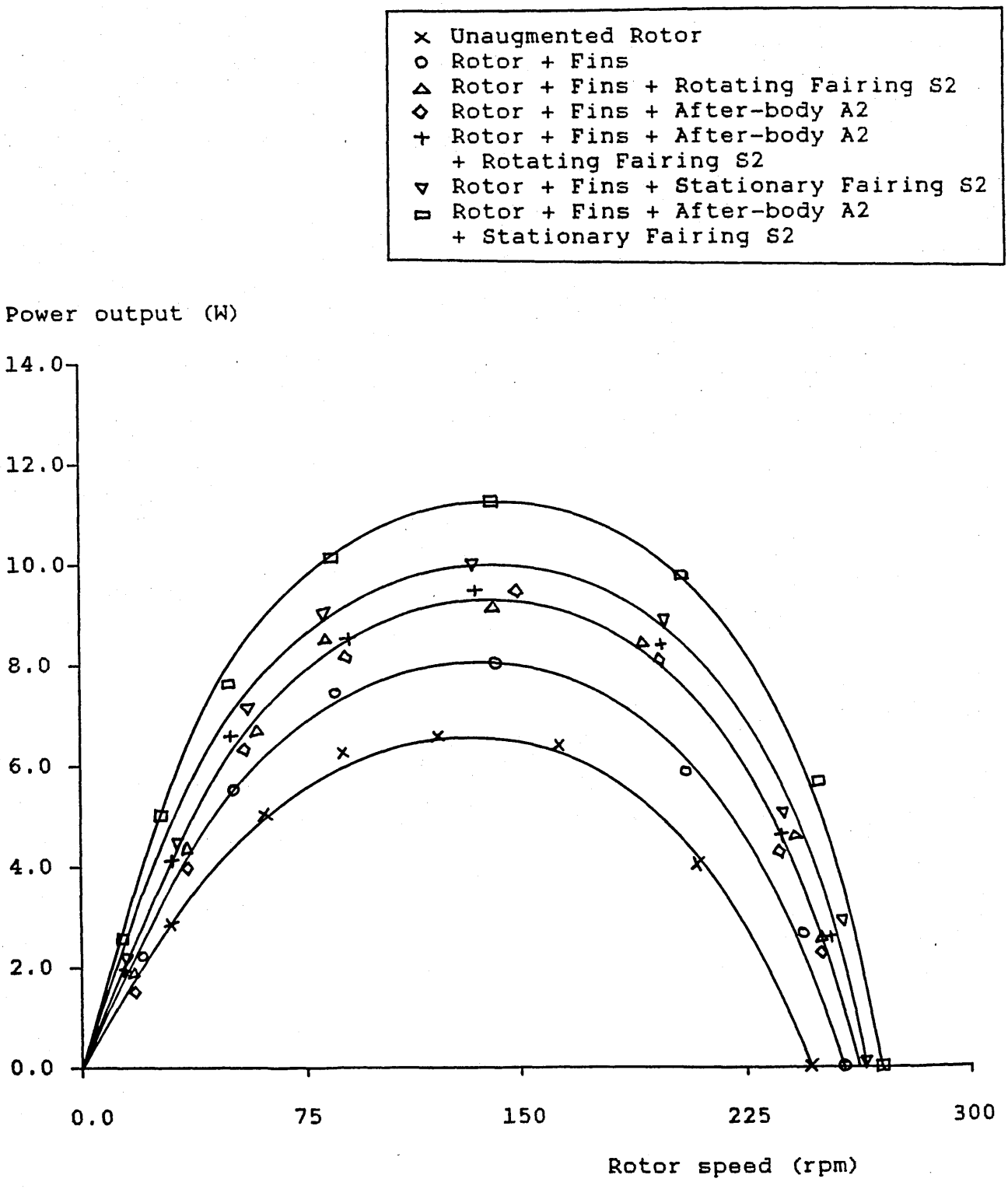

GRAPH (29) THE EFFECT OF TIP-FINS AND CENTRE-BODIES ON WIND-TURBINE POWER OUTPUT, FIN(9).

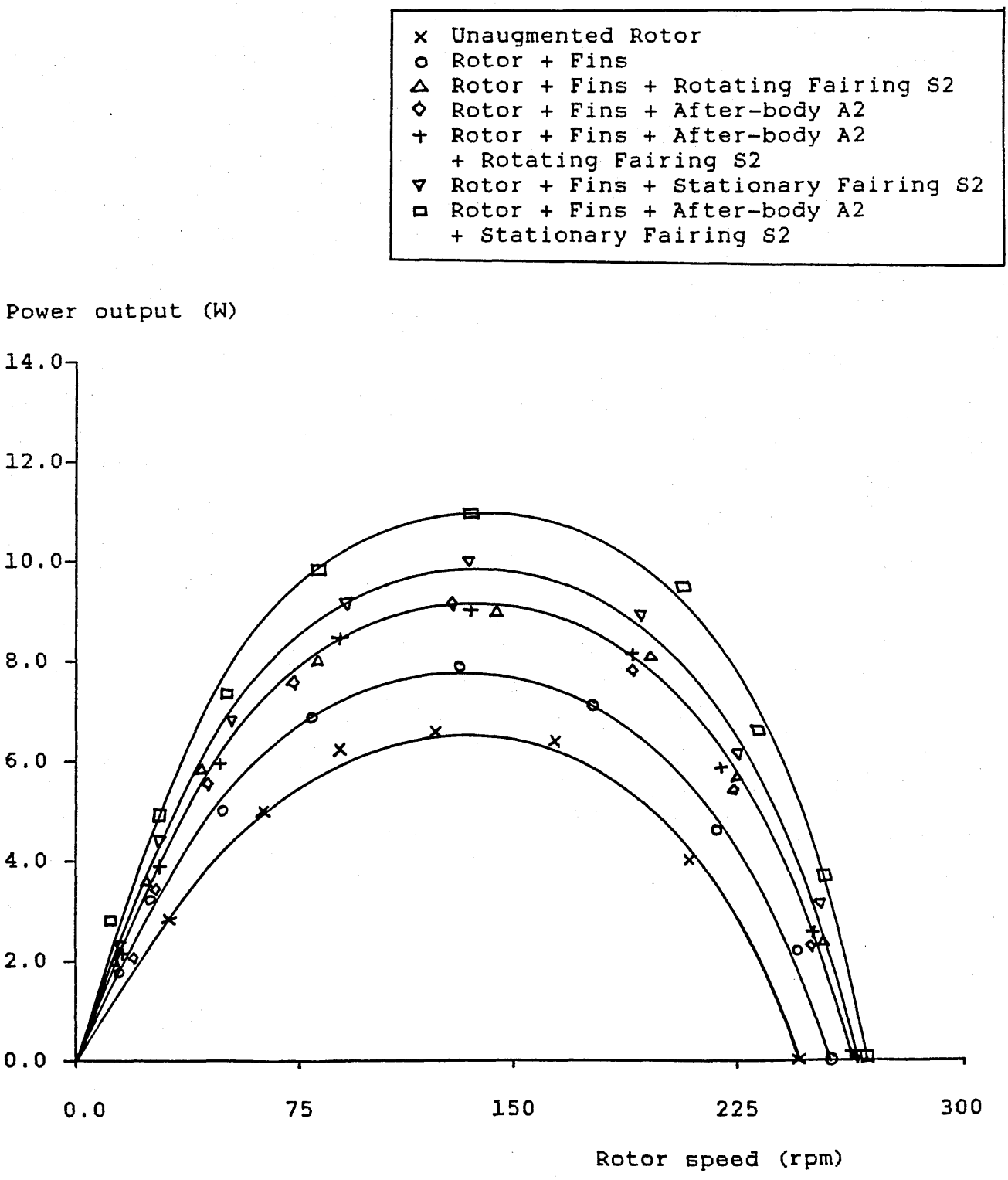

GRAPH (30) THE EFFECT OF TIP-FINS AND CENTRE-BODIES ON WIND-TURBINE POWER OUTPUT, FIN(10).

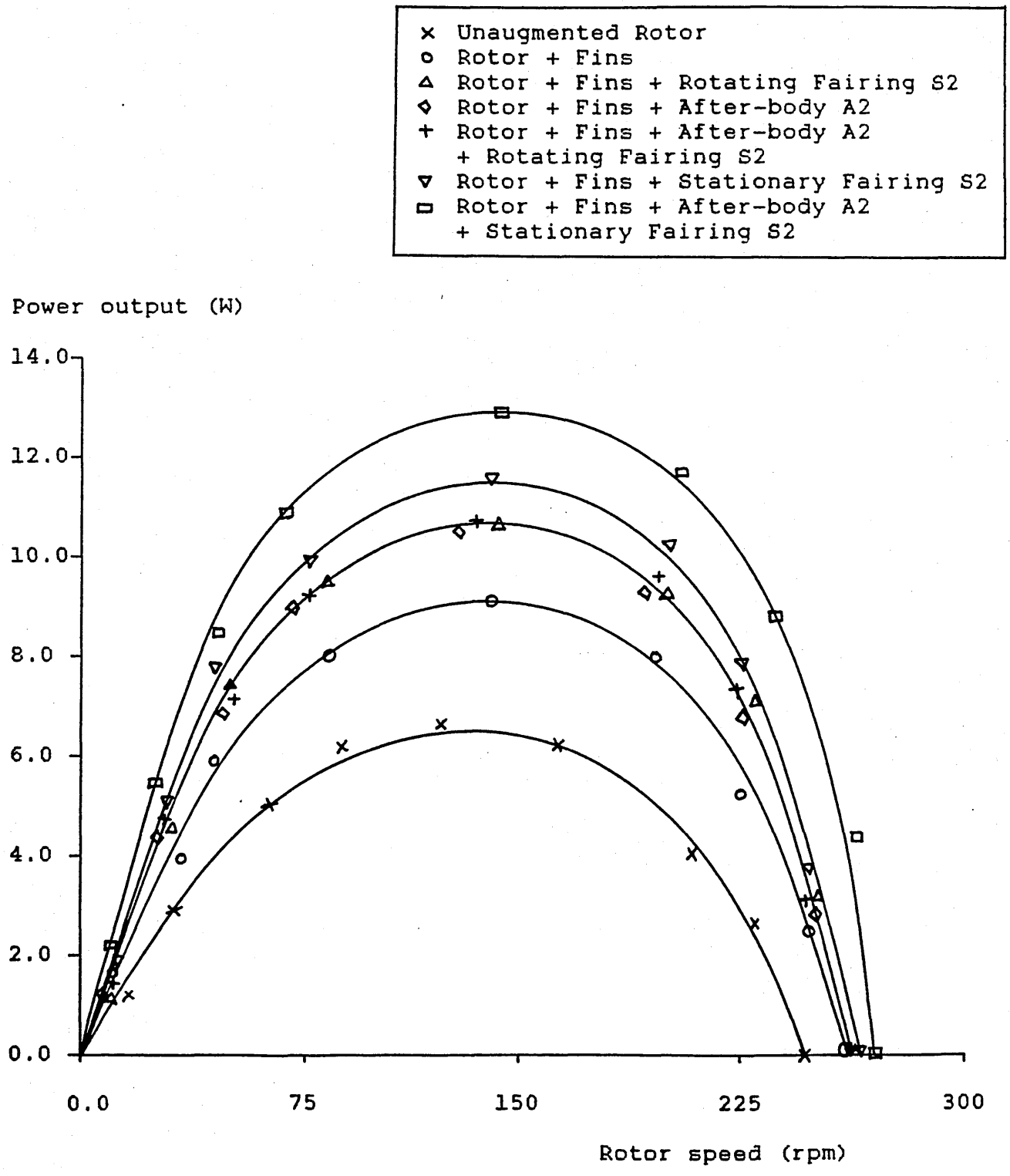

GRAPH (31) THE EFFECT OF TIP-FIN ANGLE (DOWNWIND) ON WIND-TURBINE POWER OUTPUT.
(Both length (20mm) and angle (5°) upwind are kept constant).

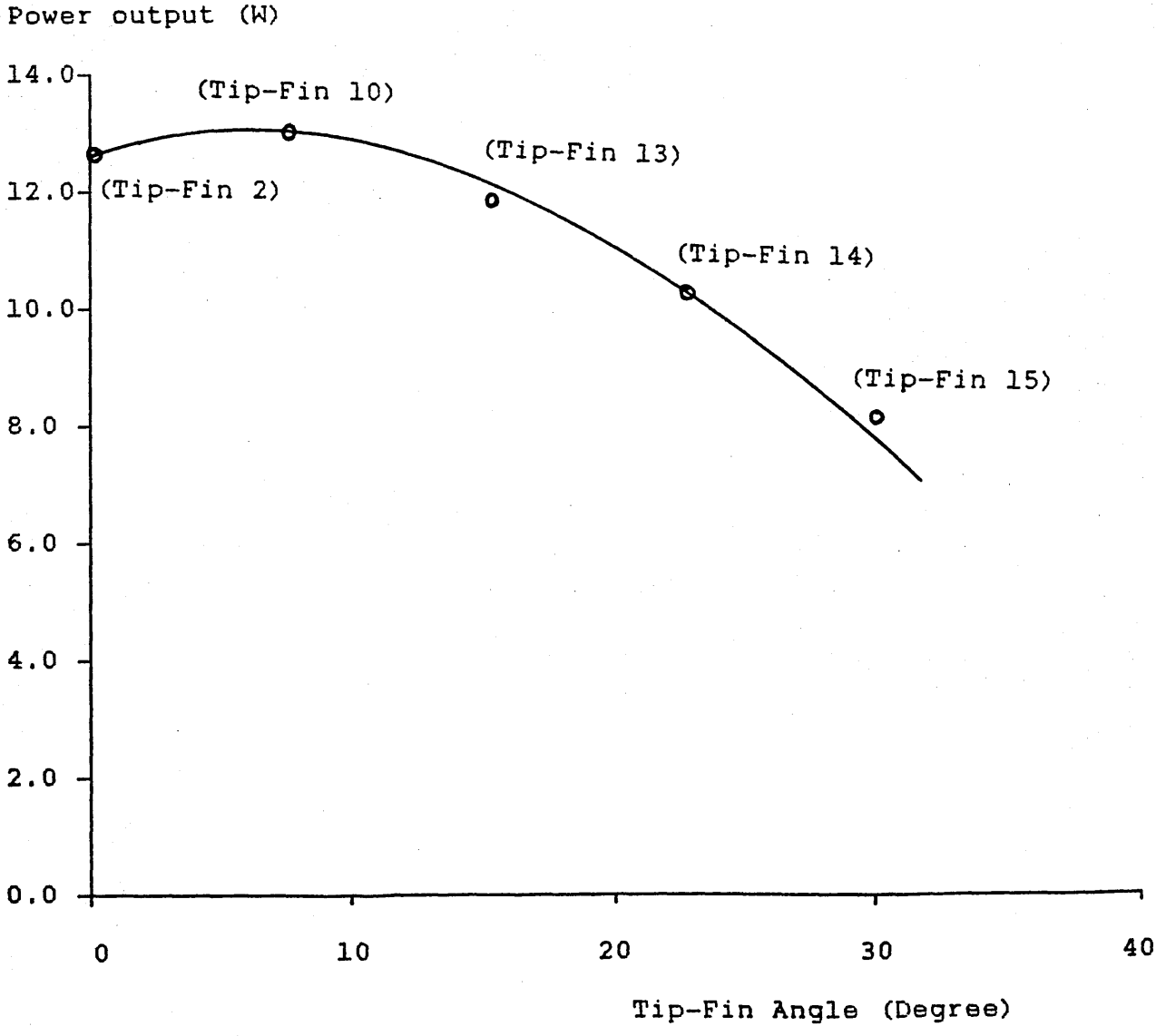

GRAPH (32) THE EFFECT OF TIP-FIN WIDTH ON WIND-TURBINE POWER OUTPUT.

(length (100mm) downwind is kept constant with zero length upwind).

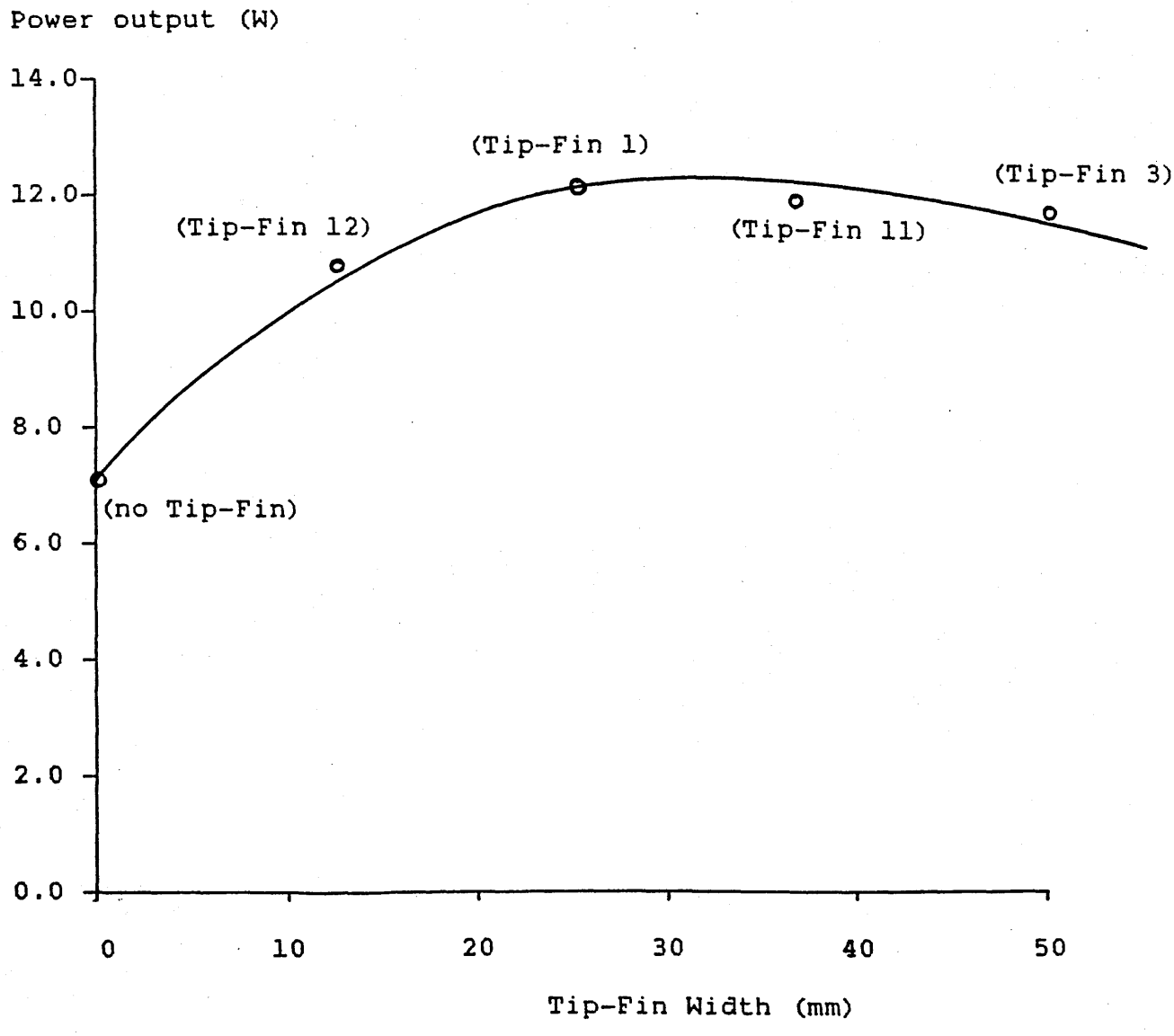

GRAPH (33) PERFORMANCE OF WIND-TURBINE/PUMP COMBINATION FOR A HEAD h = 1.37m and $\alpha = 15^{\circ}$.

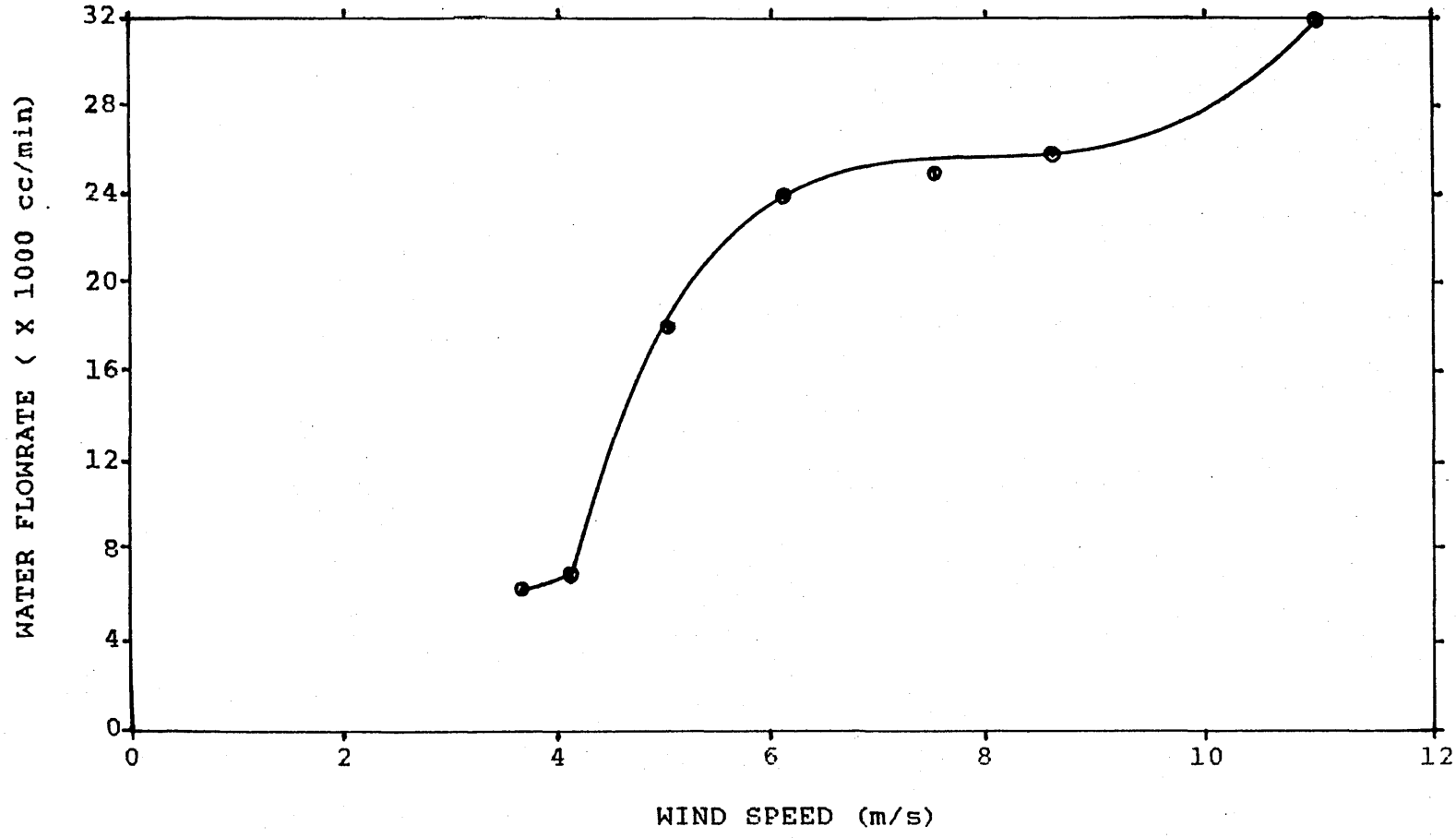

GRAPH (34) COMBINATION OF WIND-TURBINE/PUMP CHARACTERISTICS AT $\alpha = 15^{\circ}$.

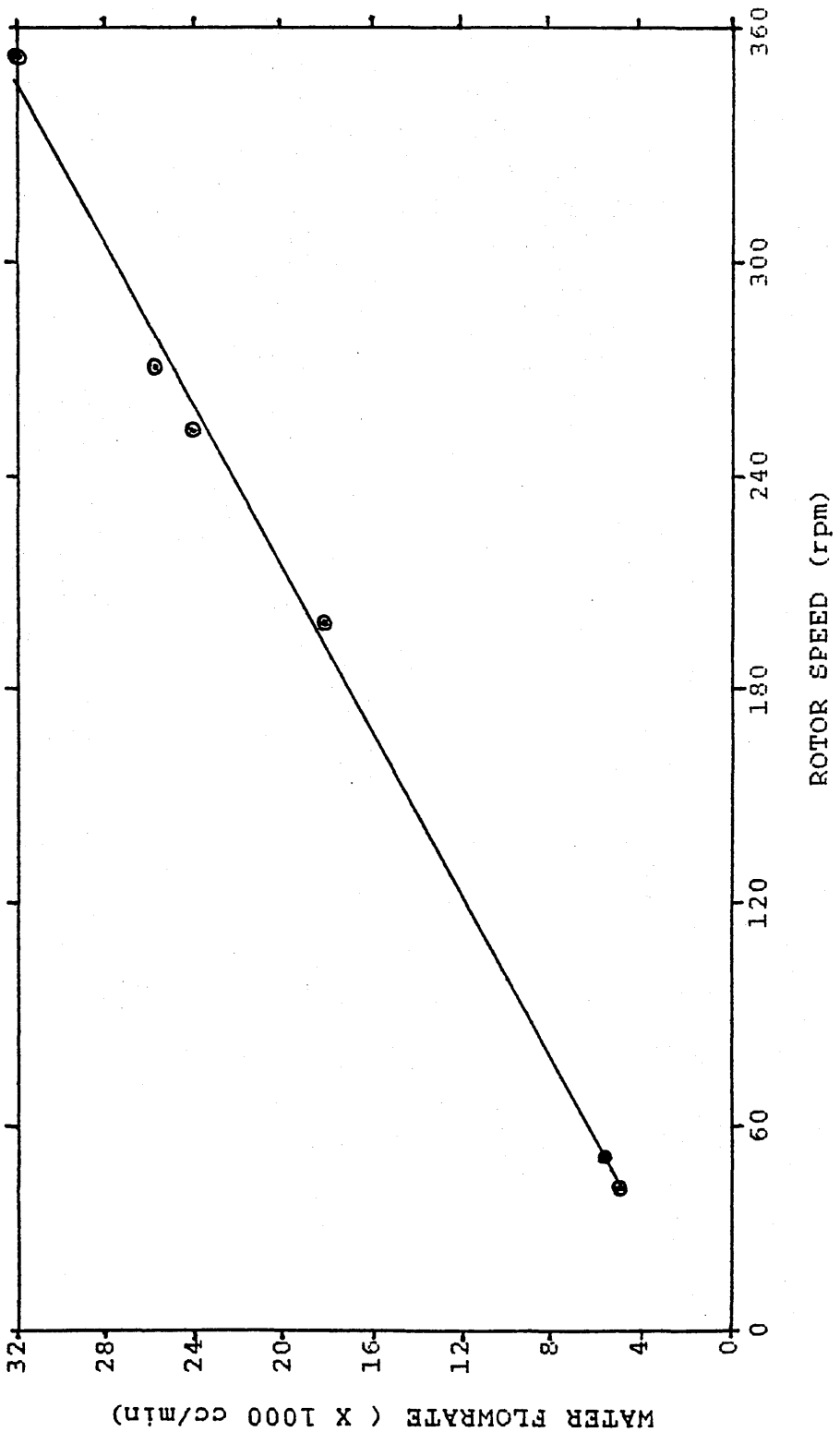

GRAPH (35) POWER CHARACTERISTICS OF WIND-TURBINE/PUMP COMBINATION AT $\alpha = 15^{\circ}$.

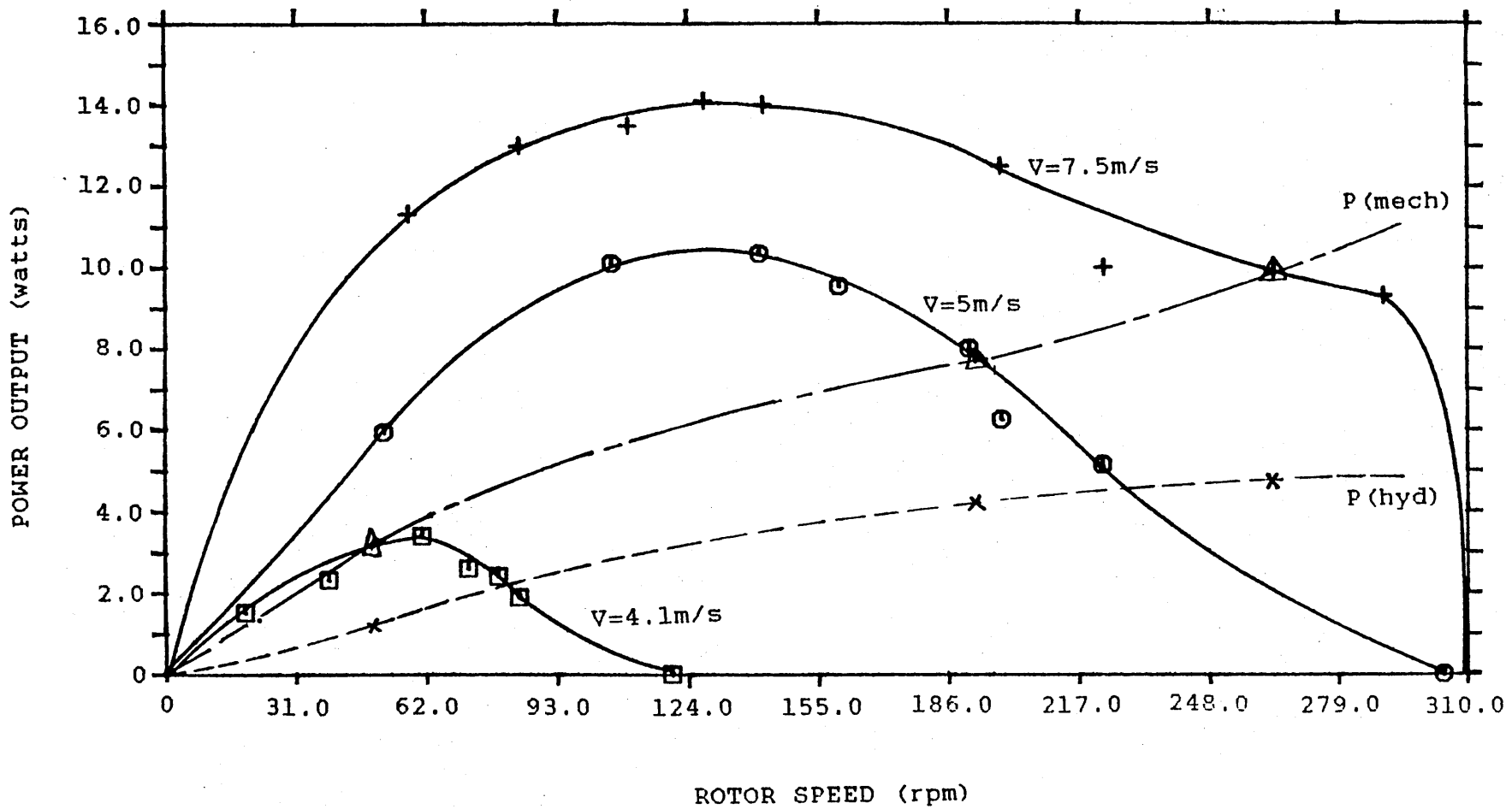

TABLES

TABLE(1) Velocity profile inside duct at 5m/s.

(Before duct modification).

Distance across duct (m)	Air velocity (m/s)
0.000	2.63
0.033	4.10
0.065	4.83
0.103	5.21
0.210	5.05
0.313	4.77
0.420	4.70
0.525	4.97
0.630	5.20
0.728	5.17
0.770	4.67
0.807	3.73
0.840	2.00

TABLE(2) Velocity profile inside duct at 5m/s.

(Plane 1 at Y=0.420 (vertical distance))

Distance across duct (m)	Air velocity (m/s)
0.000	2.90
0.033	5.20
0.065	5.10
0.103	5.30
0.210	5.96
0.313	5.97
0.420	5.01
0.525	5.00
0.630	4.93
0.728	5.17
0.770	4.83
0.807	3.87
0.840	3.00

TABLE(3) Velocity profile inside duct at 5m/s.

(Plane 2 at Y=0.420 (vertical distance))

Distance across duct (m)	Air velocity (m/s)
0.000	1.77
0.033	3.86
0.065	4.57
0.103	4.87
0.210	4.93
0.313	4.97
0.420	5.00
0.525	5.01
0.630	4.91
0.728	4.83
0.770	4.70
0.807	4.77
0.840	1.33

TABLE(4) Velocity profile inside duct at 5m/s.

(Plane 3 at Y=0.420 (vertical distance))

Distance across duct (m)	Air velocity (m/s)
0.000	1.60
0.033	4.50
0.065	4.63
0.103	4.93
0.210	5.00
0.313	4.92
0.420	5.00
0.525	5.00
0.630	4.94
0.728	4.86
0.770	4.55
0.807	4.50
0.840	2.30

TABLE(5) Velocity profile inside duct at 5m/s.

(Plane 4 at Y=0.420 (vertical distance))

Distance across duct (m)	Air velocity (m/s)
0.000	2.33
0.033	4.53
0.065	4.60
0.103	4.83
0.210	4.87
0.313	4.97
0.420	5.00
0.525	5.02
0.630	5.06
0.728	4.83
0.770	4.60
0.807	4.50
0.840	1.90

TABLE(6) Velocity profile inside duct at 5m/s.

(Plane 5 at Y=0.420 (vertical distance))

Distance across duct (m)	Air velocity (m/s)
0.000	2.20
0.033	3.53
0.065	4.80
0.103	4.87
0.210	4.96
0.313	4.95
0.420	5.00
0.525	4.96
0.630	4.95
0.728	4.70
0.770	4.01
0.807	3.93
0.840	1.27

TABLE(7) Velocity profile inside duct at 5m/s.

(Plane 6 at Y=0.420 (vertical distance))

Distance across duct (m)	Air velocity (m/s)
0.000	2.00
0.033	5.46
0.065	5.40
0.103	5.33
0.210	5.10
0.313	4.96
0.420	4.97
0.525	5.01
0.630	5.06
0.728	5.37
0.770	5.30
0.807	5.10
0.840	2.33

TABLE(8) Pressure distribution over sail at $\alpha = 0^{\circ}$.

X/C	PRESSURE COEFFICIENT (Cp)	
	Upper Surface	Lower Surface
0.05	0.30	0.25
0.1	0.65	0.55
0.2	0.80	0.55
0.3	0.95	0.57
0.4	0.85	0.75
0.5	0.86	0.45
0.6	0.80	0.50
0.7	0.85	0.30
0.8	0.60	0.40
0.9	0.15	0.20
1.0	0.00	0.00

TABLE(9) Pressure distribution over sail at $\alpha = 2.5^{\circ}$

X/C	PRESSURE COEFFICIENT (Cp)	
	Upper Surface	Lower Surface
0.05	0.75	0.50
0.1	1.20	0.60
0.2	1.15	0.80
0.3	1.00	0.95
0.4	1.00	0.95
0.5	1.10	0.75
0.6	0.95	0.85
0.7	0.70	0.50
0.8	0.60	0.60
0.9	0.20	0.25
1.0	0.00	0.00

TABLE(10) Pressure distribution over sail at $\alpha = 5^{\circ}$

X/C	PRESSURE COEFFICIENT (Cp)	
	Upper Surface	Lower Surface
0.05	1.15	0.60
0.1	1.35	0.90
0.2	1.70	0.85
0.3	1.45	1.00
0.4	1.25	0.85
0.5	1.35	0.90
0.6	1.10	0.65
0.7	1.25	0.45
0.8	1.25	0.50
0.9	0.35	0.20
1.0	0.00	0.00

TABLE(11) Pressure distribution over sail at $\alpha = 7.5^{\circ}$

X/C	PRESSURE COEFFICIENT (Cp)	
	Upper Surface	Lower Surface
0.05	1.50	0.50
0.1	2.58	0.75
0.2	2.50	1.00
0.3	2.01	0.85
0.4	1.65	0.82
0.5	1.52	0.85
0.6	1.25	0.80
0.7	0.85	0.55
0.8	0.50	0.50
0.9	0.35	0.22
1.0	0.00	0.00

TABLE(12) Pressure distribution over sail at $\alpha = 10^{\circ}$

X/C	PRESSURE COEFFICIENT (Cp)	
	Upper Surface	Lower Surface
0.05	1.91	0.45
0.1	3.20	0.65
0.2	3.15	0.82
0.3	2.55	0.98
0.4	2.45	0.90
0.5	1.85	0.85
0.6	1.40	0.80
0.7	0.92	0.75
0.8	0.71	0.41
0.9	0.45	0.30
1.0	0.00	0.00

TABLE(13) Pressure distribution over sail at $\alpha = 12.5^{\circ}$

X/C	PRESSURE COEFFICIENT (Cp)	
	Upper Surface	Lower Surface
0.05	2.25	0.50
0.1	3.75	0.51
0.2	3.90	0.85
0.3	3.25	0.83
0.4	2.70	0.95
0.5	2.35	0.80
0.6	2.01	0.75
0.7	1.30	0.76
0.8	1.00	0.49
0.9	0.51	0.35
1.0	0.00	0.00

TABLE(14) Pressure distribution over sail at $\alpha = 15^{\circ}$

X/C	PRESSURE COEFFICIENT (Cp)	
	Upper Surface	Lower Surface
0.05	2.45	0.20
0.1	4.00	0.51
0.2	4.40	0.91
0.3	3.50	0.85
0.4	3.25	0.90
0.5	2.50	0.75
0.6	1.45	0.81
0.7	1.00	0.50
0.8	0.75	0.51
0.9	0.50	0.20
1.0	0.00	0.00

TABLE(15) Pressure distribution over sail at $\alpha = 17.5^{\circ}$

X/C	PRESSURE COEFFICIENT (Cp)	
	Upper Surface	Lower Surface
0.05	1.51	0.45
0.1	2.35	0.65
0.2	2.93	0.95
0.3	2.48	0.96
0.4	2.09	0.82
0.5	1.80	0.75
0.6	1.55	0.76
0.7	1.00	0.73
0.8	0.75	0.55
0.9	0.30	0.30
1.0	0.00	0.00

TABLE(16) Pressure distribution over sail at $\alpha = 20^{\circ}$

X/C	PRESSURE COEFFICIENT (Cp)	
	Upper Surface	Lower Surface
0.05	0.95	0.53
0.1	1.83	0.65
0.2	2.20	0.98
0.3	2.45	0.85
0.4	2.05	0.76
0.5	1.65	0.91
0.6	1.75	0.75
0.7	1.45	0.72
0.8	0.80	0.35
0.9	0.35	0.25
1.0	0.00	0.00

TABLE(17) Angle of attack, α against lift coefficient, C_L.

Angle of attack, α (degrees)	Lift coefficient, C_L
0.0	-0.150
2.5	0.025
5.0	0.208
7.5	0.475
10.0	0.750
12.5	0.983
15.0	1.083
17.5	1.016
20.0	0.892

TABLE(18) Wind speed and corresponding dynamic head.

Dynamic head (mm of water)	Wind speed (m/s)
0.5	2.90
1.0	4.10
1.5	5.02
2.0	5.80
2.5	6.48
3.0	7.10
3.5	7.67
4.0	8.20
4.5	8.70
5.0	9.17
5.5	9.62
6.0	10.04
6.5	10.45
7.0	10.85
7.5	11.23

TABLE(19) Power characteristics of unaugmented rotor.

Mass(m) (kg)	Balance Reading(M) (kg)	Average Rotor Speed(N) (rpm)	Torque(T) (Nm)	Power(P) (Watt)
0.00	0.000	241.2	0.000	0.00
0.32	0.178	227.3	0.109	2.61
0.45	0.184	204.5	0.183	3.92
0.65	0.198	165.5	0.377	6.54
0.77	0.210	122.8	0.543	6.98
1.10	0.243	83.4	0.739	6.43
1.25	0.266	64.2	0.727	4.89
1.57	0.289	35.5	0.798	2.97
2.00	0.352	20.3	0.527	1.12

TABLE(20) Power characteristics of rotor augmented with rotating fairing S1.

Mass(m) (kg)	Balance Reading(M) (kg)	Average Rotor Speed(N) (rpm)	Torque(T) (Nm)	Power(P) (Watt)
0.00	0.000	247.3	0.000	0.00
0.32	0.184	233.2	0.133	3.25
0.45	0.197	187.5	0.280	5.50
0.65	0.202	150.0	0.472	7.42
0.77	0.232	94.2	0.741	7.31
1.10	0.267	75.1	0.826	6.50
1.25	0.378	54.2	1.007	5.72
1.57	0.489	37.5	1.027	3.85
2.00	0.566	17.1	1.148	1.48

TABLE(21) Power characteristics of rotor augmented with rotating fairing S2.

Mass(m) (kg)	Balance Reading(M) (kg)	Average Rotor Speed(N) (rpm)	Torque(T) (Nm)	Power(P) (Watt)
0.00	0.000	247.1	0.000	0.00
0.32	0.116	225.3	0.128	3.02
0.45	0.127	205.7	0.209	4.52
0.65	0.148	187.2	0.282	5.53
0.77	0.200	134.7	0.518	7.31
1.10	0.268	106.1	0.652	7.25
1.25	0.372	67.5	0.876	6.19
1.57	0.419	43.9	1.003	4.61
2.00	0.571	29.8	1.121	2.98

TABLE(22) Power characteristics of rotor augmented with rotating fairing S3.

Mass (m) (kg)	Balance Reading (M) (kg)	Average Rotor Speed (N) (rpm)	Torque (T) (Nm)	Power (P) (Watt)
0.00	0.000	246.8	0.000	0.00
0.32	0.045	226.3	0.146	3.48
0.45	0.098	195.8	0.269	5.52
0.65	0.158	171.8	0.361	6.49
0.77	0.182	120.3	0.597	7.52
1.10	0.243	75.8	0.805	6.39
1.25	0.331	45.7	1.089	5.21
1.57	0.375	28.3	1.238	3.67
2.00	0.496	15.4	1.160	1.87

TABLE(23) Power characteristics of rotor augmented with stationary fairing S1.

Mass (m) (kg)	Balance Reading (M) (kg)	Average Rotor Speed (N) (rpm)	Torque (T) (Nm)	Power (P) (Watt)
0.00	0.000	249.7	0.000	0.00
0.32	0.054	232.5	0.167	4.07
0.45	0.097	217.5	0.260	5.93
0.65	0.162	193.2	0.401	6.89
0.77	0.183	125.6	0.676	8.89
1.10	0.233	91.7	0.834	8.01
1.25	0.341	63.9	0.974	6.52
1.57	0.373	30.3	1.352	4.29
2.00	0.499	13.3	1.709	2.38

TABLE(24) Power characteristics of rotor augmented with stationary fairing S2.

Mass (m) (kg)	Balance Reading (M) (kg)	Average Rotor Speed (N) (rpm)	Torque (T) (Nm)	Power (P) (Watt)
0.00	0.000	249.0	0.000	0.00
0.32	0.062	228.3	0.188	4.50
0.45	0.089	195.2	0.343	7.01
0.65	0.166	160.3	0.499	8.39
0.77	0.193	102.4	0.816	8.75
1.10	0.242	67.5	1.098	7.76
1.25	0.353	41.2	1.395	6.02
1.57	0.377	29.3	1.463	4.49
2.00	0.523	15.7	1.487	2.17

TABLE(25) Power characteristics of rotor augmented with stationary fairing S3.

Mass(m) (kg)	Balance Reading(M) (kg)	Average Rotor Speed(N) (rpm)	Torque(T) (Nm)	Power(P) (Watt)
0.00	0.000	249.9	0.000	0.00
0.32	0.053	227.1	0.178	4.23
0.45	0.079	207.3	0.285	6.19
0.65	0.098	188.3	0.390	7.69
0.77	0.142	148.6	0.577	8.98
1.10	0.189	88.7	0.872	8.10
1.25	0.242	51.8	1.171	6.35
1.57	0.297	34.5	1.378	4.98
2.00	0.489	17.3	1.496	2.71

TABLE(26) Power characteristics of rotor augmented with after-body A1

Mass(m) (kg)	Balance Reading(M) (kg)	Average Rotor Speed(N) (rpm)	Torque(T) (Nm)	Power(P) (Watt)
0.00	0.000	247.9	0.000	0.00
0.32	0.053	232.5	0.061	1.49
0.45	0.079	217.6	0.193	4.39
0.65	0.098	176.3	0.411	7.58
0.77	0.142	112.5	0.719	8.48
1.10	0.189	84.2	0.933	8.23
1.25	0.242	53.4	1.207	6.75
1.57	0.297	36.2	1.221	4.63
2.00	0.489	17.8	1.400	2.61

TABLE(27) Power characteristics of rotor augmented with after-body A1 and rotating fairing S1.

Mass (m) (kg)	Balance Reading (M) (kg)	Average Rotor Speed (N) (rpm)	Torque (T) (Nm)	Power (P) (Watt)
0.00	0.000	248.0	0.000	0.00
0.32	0.064	228.1	0.124	2.98
0.45	0.089	210.3	0.219	4.82
0.65	0.145	186.4	0.360	7.03
0.77	0.182	136.6	0.569	8.14
1.10	0.213	98.8	0.823	8.52
1.25	0.252	52.5	1.181	6.49
1.57	0.297	34.6	1.242	4.50
2.00	0.479	16.2	1.385	2.35

TABLE(28) Power characteristics of rotor augmented with after-body A1 and rotating fairing S2.

Mass(m) (kg)	Balance Reading(M) (kg)	Average Rotor Speed(N) (rpm)	Torque(T) (Nm)	Power(P) (Watt)
0.00	0.000	248.3	0.000	0.00
0.32	0.072	229.6	0.124	2.99
0.45	0.096	202.5	0.258	5.49
0.65	0.124	168.2	0.425	7.48
0.77	0.175	114.6	0.705	8.46
1.10	0.215	88.9	0.833	7.75
1.25	0.242	48.4	1.233	6.25
1.57	0.311	29.9	1.268	3.97
2.00	0.484	12.3	1.840	2.37

TABLE(29) Power characteristics of rotor augmented with after-body A1 and rotating fairing S3.

Mass (m) (kg)	Balance Reading (M) (kg)	Average Rotor Speed (N) (rpm)	Torque (T) (Nm)	Power (P) (Watt)
0.00	0.000	249.2	0.000	0.00
0.32	0.074	232.5	0.093	2.28
0.45	0.098	215.6	0.194	4.39
0.65	0.115	190.3	0.327	6.52
0.77	0.164	152.9	0.521	8.35
1.10	0.218	82.5	0.881	7.52
1.25	0.242	42.3	1.449	6.42
1.57	0.314	24.5	1.520	3.49
2.00	0.494	10.3	1.621	1.46

TABLE(30) Power characteristics of rotor augmented with after-body A1 and stationary fairing S1.

Mass (m) (kg)	Balance Reading (M) (kg)	Average Rotor Speed (N) (rpm)	Torque (T) (Nm)	Power (P) (Watt)
0.00	0.000	248.9	0.000	0.00
0.32	0.087	234.6	0.079	1.95
0.45	0.104	210.2	0.288	6.35
0.65	0.125	157.5	0.547	9.03
0.77	0.187	112.5	0.753	8.87
1.10	0.223	80.6	1.057	8.92
1.25	0.278	55.8	1.220	7.13
1.57	0.346	40.7	1.239	5.28
2.00	0.478	20.4	1.760	3.76

TABLE(31) Power characteristics of rotor augmented with after-body A1 and stationary fairing S2.

Mass(m) (kg)	Balance Reading(M) (kg)	Average Rotor Speed(N) (rpm)	Torque(T) (Nm)	Power(P) (Watt)
0.00	0.000	251.8	0.000	0.00
0.32	0.078	233.5	0.121	2.95
0.45	0.106	212.5	0.248	5.52
0.65	0.135	187.5	0.390	7.65
0.77	0.195	131.6	0.670	9.23
1.10	0.232	97.5	0.929	9.49
1.25	0.298	67.5	1.096	7.75
1.57	0.357	30.2	1.420	4.49
2.00	0.482	20.3	1.467	2.48

TABLE(32) Power characteristics of rotor augmented with after-body A1 and stationary fairing S3.

Mass (m) (kg)	Balance Reading (M) (kg)	Average Rotor Speed (N) (rpm)	Torque (T) (Nm)	Power (P) (Watt)
0.00	0.000	250.9	0.000	0.00
0.32	0.054	220.8	0.201	4.48
0.45	0.088	195.6	0.318	6.52
0.65	0.102	168.5	0.481	8.49
0.77	0.169	112.5	0.793	9.35
1.10	0.217	76.8	1.007	8.10
1.25	0.299	36.9	1.462	5.65
1.57	0.348	24.3	1.474	3.75
2.00	0.479	10.1	1.481	1.52

TABLE(33) Power characteristics of rotor augmented with after-body A2

Mass (m) (kg)	Balance Reading (M) (kg)	Average Rotor Speed (N) (rpm)	Torque (T) (Nm)	Power (P) (Watt)
0.00	0.000	252.3	0.000	0.00
0.32	0.045	227.5	0.141	3.35
0.45	0.068	199.8	0.294	6.15
0.65	0.112	140.6	0.567	8.35
0.77	0.170	97.8	0.786	8.05
1.10	0.213	67.5	0.955	6.75
1.25	0.307	60.8	0.972	6.19
1.57	0.359	31.6	1.254	4.15
2.00	0.499	15.7	1.342	1.99

TABLE(34) Power characteristics of rotor augmented with after-body A2 and rotating fairing S1.

Mass(m) (kg)	Balance Reading(M) (kg)	Average Rotor Speed(N) (rpm)	Torque(T) (Nm)	Power(P) (Watt)
0.00	0.000	251.8	0.000	0.00
0.32	0.066	224.6	0.185	4.35
0.45	0.084	182.9	0.378	7.23
0.65	0.114	157.8	0.513	8.48
0.77	0.160	112.7	0.713	8.42
1.10	0.213	67.8	1.018	7.23
1.25	0.327	46.2	1.279	6.19
1.57	0.369	36.8	1.173	4.52
2.00	0.499	16.3	1.185	1.98

TABLE(35) Power characteristics of rotor augmented with after-body A2 and rotating fairing S2.

Mass(m) (kg)	Balance Reading(M) (kg)	Average Rotor Speed(N) (rpm)	Torque(T) (Nm)	Power(P) (Watt)
0.00	0.000	253.4	0.000	0.00
0.32	0.072	217.5	0.194	4.46
0.45	0.085	193.6	0.333	6.76
0.65	0.125	172.5	0.443	8.00
0.77	0.175	128.6	0.613	8.25
1.10	0.245	80.5	0.921	7.76
1.25	0.348	48.2	1.102	5.56
1.57	0.398	32.5	1.146	3.56
2.00	0.489	17.2	1.183	2.13

TABLE(36) Power characteristics of rotor augmented with after-body A2 and rotating fairing S3.

Mass (m) (kg)	Balance Reading (M) (kg)	Average Rotor Speed (N) (rpm)	Torque (T) (Nm)	Power (P) (Watt)
0.00	0.000	250.9	0.000	0.00
0.32	0.068	232.5	0.126	3.07
0.45	0.089	209.9	0.249	5.48
0.65	0.125	189.2	0.363	7.19
0.77	0.170	153.9	0.506	8.15
1.10	0.218	94.6	0.844	8.36
1.25	0.344	62.4	0.996	6.51
1.57	0.368	36.6	1.336	5.12
2.00	0.496	17.3	1.491	2.34

TABLE(37) Power characteristics of rotor augmented with after-body A2 and stationary fairing S1.

Mass(m) (kg)	Balance Reading(M) (kg)	Average Rotor Speed(N) (rpm)	Torque(T) (Nm)	Power(P) (Watt)
0.00	0.000	253.3	0.000	0.00
0.32	0.103	235.8	0.143	3.52
0.45	0.149	215.6	0.287	6.48
0.65	0.185	168.9	0.482	8.52
0.77	0.220	120.0	0.754	9.48
1.10	0.258	79.5	1.055	8.78
1.25	0.364	46.7	1.337	6.54
1.57	0.388	22.5	1.596	3.76
2.00	0.489	10.4	1.827	1.99

TABLE(38) Power characteristics of rotor augmented with after-body A2 and stationary fairing S2.

Mass(m) (kg)	Balance Reading(M) (kg)	Average Rotor Speed(N) (rpm)	Torque(T) (Nm)	Power(P) (Watt)
0.00	0.000	254.6	0.000	0.00
0.32	0.093	226.2	0.193	4.58
0.45	0.138	200.8	0.345	7.25
0.65	0.184	171.3	0.503	9.02
0.77	0.225	110.5	0.788	9.12
1.10	0.260	58.6	1.242	7.62
1.25	0.371	38.9	1.291	5.26
1.57	0.410	23.3	1.430	3.49
2.00	0.496	10.3	1.808	1.95

TABLE(39) Power characteristics of rotor augmented with after-body A2 and stationary fairing S3.

Mass (m) (kg)	Balance Reading (M) (kg)	Average Rotor Speed (N) (rpm)	Torque (T) (Nm)	Power (P) (Watt)
0.00	0.000	255.2	0.000	0.00
0.32	0.098	230.8	0.170	4.10
0.45	0.127	207.6	0.300	6.52
0.65	0.190	159.2	0.531	8.86
0.77	0.236	131.8	0.670	9.25
1.10	0.265	97.5	0.884	9.03
1.25	0.382	65.4	1.202	8.23
1.57	0.421	31.2	1.433	4.68
2.00	0.501	10.4	1.791	1.95

TABLE(40) Power characteristics of rotor augmented with tip-fin 1.

Mass(m) (kg)	Balance Reading(M) (kg)	Average Rotor Speed(N) (rpm)	Torque(T) (Nm)	Power(P) (Watt)
0.00	0.000	253.3	0.000	0.00
0.32	0.102	240.6	0.101	2.56
0.45	0.128	220.8	0.227	5.25
0.65	0.190	185.2	0.418	8.10
0.77	0.238	127.5	0.674	9.00
1.10	0.285	85.3	0.923	8.24
1.25	0.322	39.4	1.173	6.49
1.57	0.454	33.5	1.212	4.25
2.00	0.501	15.0	1.420	2.23

TABLE(41) Power characteristics of rotor augmented with tip-fin 1 and rotating fairing.

Mass (m) (kg)	Balance Reading (M) (kg)	Average Rotor Speed (N) (rpm)	Torque (T) (Nm)	Power (P) (Watt)
0.00	0.000	256.5	0.000	0.00
0.32	0.110	228.6	0.213	5.10
0.45	0.130	210.8	0.314	6.92
0.65	0.192	187.5	0.463	9.10
0.77	0.241	111.6	0.854	9.98
1.10	0.287	69.8	1.166	8.52
1.25	0.374	37.5	1.604	6.30
1.57	0.456	24.5	1.633	4.19
2.00	0.520	10.4	2.066	2.25

TABLE(42) Power characteristics of rotor augmented with tip-fin 1 and after-body.

Mass(m) (kg)	Balance Reading(M) (kg)	Average Rotor Speed(N) (rpm)	Torque(T) (Nm)	Power(P) (Watt)
0.00	0.000	258.3	0.000	0.00
0.32	0.102	238.6	0.131	3.28
0.45	0.128	227.4	0.229	5.46
0.65	0.188	178.2	0.495	9.23
0.77	0.231	125.3	0.781	10.25
1.10	0.276	78.4	1.156	9.49
1.25	0.369	47.8	1.377	6.89
1.57	0.441	28.4	1.550	4.61
2.00	0.501	15.1	1.594	2.52

TABLE(43) Power characteristics of rotor augmented with tip-fin 1, rotating fairing and after-body.

Mass(m) (kg)	Balance Reading(M) (kg)	Average Rotor Speed(N) (rpm)	Torque(T) (Nm)	Power(P) (Watt)
0.00	0.000	257.2	0.000	0.00
0.32	0.098	232.5	0.195	4.75
0.45	0.129	187.5	0.434	8.53
0.65	0.179	150.6	0.640	10.10
0.77	0.230	95.6	0.947	9.48
1.10	0.278	64.3	1.257	8.46
1.25	0.371	39.3	1.470	6.05
1.57	0.444	28.5	1.582	4.72
2.00	0.510	16.6	1.599	2.78

TABLE(44) Power characteristics of rotor augmented with tip-fin 1 and stationary fairing.

Mass(m) (kg)	Balance Reading(M) (kg)	Average Rotor Speed(N) (rpm)	Torque(T) (Nm)	Power(P) (Watt)
0.00	0.000	259.6	0.000	0.00
0.32	0.091	243.8	0.152	3.89
0.45	0.127	217.5	0.323	7.35
0.65	0.178	181.6	0.553	10.51
0.77	0.233	125.2	0.858	11.25
1.10	0.276	82.5	1.165	10.06
1.25	0.372	45.3	1.634	7.75
1.57	0.445	28.4	1.678	4.99
2.00	0.509	10.3	2.086	2.25

TABLE(45) Power characteristics of rotor augmented with tip-fin 1, stationary fairing, and after-body.

Mass(m) (kg)	Balance Reading(M) (kg)	Average Rotor Speed(N) (rpm)	Torque(T) (Nm)	Power(P) (Watt)
0.00	0.000	260.4	0.000	0.00
0.32	0.120	246.2	0.136	3.51
0.45	0.148	218.4	0.339	7.75
0.65	0.198	188.3	0.556	10.96
0.77	0.254	123.6	0.935	12.10
1.10	0.299	64.6	1.532	10.35
1.25	0.380	36.9	1.975	7.63
1.57	0.476	24.5	1.945	4.99
2.00	0.515	12.2	2.254	2.88

TABLE(46) Power characteristics of rotor augmented with tip-fin 2.

Mass (m) (kg)	Balance Reading (M) (kg)	Average Rotor Speed (N) (rpm)	Torque (T) (Nm)	Power (P) (Watt)
0.00	0.000	255.8	0.000	0.00
0.32	0.090	233.6	0.163	3.99
0.45	0.113	202.5	0.342	7.25
0.65	0.168	177.6	0.438	8.15
0.77	0.201	135.2	0.653	9.24
1.10	0.276	96.5	0.862	8.71
1.25	0.315	63.4	1.051	6.98
1.57	0.465	27.3	1.487	4.25
2.00	0.502	15.5	1.549	2.19

TABLE(47) Power characteristics of rotor augmented with tip-fin 2 and rotating fairing.

Mass(m) (kg)	Balance Reading(M) (kg)	Average Rotor Speed(N) (rpm)	Torque(T) (Nm)	Power(P) (Watt)
0.00	0.000	256.6	0.000	0.00
0.32	0.093	234.8	0.172	4.23
0.45	0.116	217.5	0.343	7.82
0.65	0.170	186.2	0.487	9.49
0.77	0.212	156.2	0.642	10.50
1.10	0.279	98.6	0.941	9.72
1.25	0.321	62.1	1.239	8.06
1.57	0.468	30.0	1.426	4.48
2.00	0.504	16.1	1.435	2.25

TABLE(48) Power characteristics of rotor augmented with tip-fin 2 and after-body.

Mass (m) (kg)	Balance Reading (M) (kg)	Average Rotor Speed (N) (rpm)	Torque (T) (Nm)	Power (P) (Watt)
0.00	0.000	258.6	0.000	0.00
0.32	0.096	245.2	0.156	4.02
0.45	0.114	217.5	0.313	7.12
0.65	0.178	186.3	0.479	9.35
0.77	0.218	120.1	0.834	10.49
1.10	0.282	80.1	1.083	9.08
1.25	0.345	42.3	1.488	6.59
1.57	0.479	37.5	1.268	4.98
2.00	0.510	17.6	1.416	2.61

TABLE(49) Power characteristics of rotor augmented with tip-fin 2, rotating fairing and after-body.

Mass(m) (kg)	Balance Reading(M) (kg)	Average Rotor Speed(N) (rpm)	Torque(T) (Nm)	Power(P) (Watt)
0.00	0.000	258.8	0.000	0.00
0.32	0.101	240.6	0.178	4.48
0.45	0.121	212.8	0.337	7.52
0.65	0.180	185.2	0.503	9.75
0.77	0.221	134.8	0.744	10.50
1.10	0.290	91.2	1.006	9.61
1.25	0.351	54.6	1.420	8.12
1.57	0.482	33.1	1.431	4.82
2.00	0.516	13.2	1.453	1.98

TABLE(50) Power characteristics of rotor augmented with tip-fin 2 and stationary fairing.

Mass(m) (kg)	Balance Reading(M) (kg)	Average Rotor Speed(N) (rpm)	Torque(T) (Nm)	Power(P) (Watt)
0.00	0.000	259.8	0.000	0.00
0.32	0.113	245.4	0.174	4.48
0.45	0.145	223.1	0.348	8.13
0.65	0.199	187.3	0.522	10.23
0.77	0.242	130.4	0.825	11.26
1.10	0.301	85.6	1.131	10.14
1.25	0.373	53.9	1.425	8.39
1.57	0.499	34.1	1.484	5.09
2.00	0.529	13.7	1.659	2.38

TABLE(51) Power characteristics of rotor augmented with tip-fin 2, stationary fairing and after-body.

Mass(m) (kg)	Balance Reading(M) (kg)	Average Rotor Speed(N) (rpm)	Torque(T) (Nm)	Power(P) (Watt)
0.00	0.000	264.8	0.000	0.00
0.32	0.138	247.9	0.174	4.51
0.45	0.166	230.4	0.351	8.48
0.65	0.208	194.2	0.527	10.72
0.77	0.269	133.6	0.895	12.52
1.10	0.319	80.4	1.272	10.71
1.25	0.390	48.2	1.688	8.52
1.57	0.516	28.1	1.805	5.31
2.00	0.548	9.4	2.661	2.62

TABLE(52) Power characteristics of rotor augmented with tip-fin 3.

Mass (m) (kg)	Balance Reading (M) (kg)	Average Rotor Speed (N) (rpm)	Torque (T) (Nm)	Power (P) (Watt)
0.00	0.000	250.2	0.000	0.00
0.32	0.085	241.3	0.079	1.99
0.45	0.104	218.2	0.197	4.49
0.65	0.149	188.6	0.364	7.18
0.77	0.170	128.2	0.615	8.25
1.10	0.211	76.4	0.839	6.71
1.25	0.289	46.1	1.144	5.52
1.57	0.354	32.4	1.334	3.51
2.00	0.489	15.5	1.362	2.21

TABLE(53) Power characteristics of rotor augmented with tip-fin 3 and rotating fairing.

Mass(m) (kg)	Balance Reading(M) (kg)	Average Rotor Speed(N) (rpm)	Torque(T) (Nm)	Power(P) (Watt)
0.00	0.000	251.4	0.000	0.00
0.32	0.089	225.2	0.187	4.42
0.45	0.110	198.6	0.396	8.23
0.65	0.150	151.4	0.583	9.25
0.77	0.173	105.8	0.856	9.48
1.10	0.221	81.4	0.936	7.98
1.25	0.291	46.1	1.272	6.14
1.57	0.365	30.5	1.412	4.51
2.00	0.491	20.6	1.458	2.51

TABLE(54) Power characteristics of rotor augmented with tip-fin 3 and after-body.

Mass(m) (kg)	Balance Reading(M) (kg)	Average Rotor Speed(N) (rpm)	Torque(T) (Nm)	Power(P) (Watt)
0.00	0.000	252.8	0.000	0.00
0.32	0.078	240.4	0.099	2.49
0.45	0.099	223.6	0.201	4.71
0.65	0.121	193.4	0.377	7.64
0.77	0.152	165.2	0.521	9.01
1.10	0.189	133.7	0.661	9.25
1.25	0.212	88.4	0.934	8.65
1.57	0.271	50.5	1.180	6.24
2.00	0.498	21.5	1.417	3.19

TABLE(55) Power characteristics of rotor augmented with tip-fin 3, rotating fairing and after-body.

Mass(m) (kg)	Balance Reading(M) (kg)	Average Rotor Speed(N) (rpm)	Torque(T) (Nm)	Power(P) (Watt)
0.00	0.000	254.5	0.000	0.00
0.32	0.075	247.5	0.061	1.59
0.45	0.096	228.6	0.188	4.49
0.65	0.119	186.2	0.420	8.19
0.77	0.148	132.1	0.668	9.24
1.10	0.178	94.4	0.861	8.51
1.25	0.203	60.9	1.137	7.25
1.57	0.278	35.4	1.130	4.19
2.00	0.497	17.2	1.160	2.01

TABLE(56) Power characteristics of rotor augmented with tip-fin 3 and stationary fairing.

Mass (m) (kg)	Balance Reading (M) (kg)	Average Rotor Speed (N) (rpm)	Torque (T) (Nm)	Power (P) (Watt)
0.00	0.000	253.5	0.000	0.00
0.32	0.075	244.4	0.077	1.98
0.45	0.096	226.2	0.222	5.25
0.65	0.119	196.1	0.447	9.18
0.77	0.148	134.6	0.727	10.24
1.10	0.178	99.6	0.909	9.49
1.25	0.203	60.4	1.203	7.61
1.57	0.278	31.2	1.518	4.96
2.00	0.497	14.6	1.446	2.21

TABLE(57) Power characteristics of rotor augmented with tip-fin 3, stationary fairing and after-body.

Mass (m) (kg)	Balance Reading (M) (kg)	Average Rotor Speed (N) (rpm)	Torque (T) (Nm)	Power (P) (Watt)
0.00	0.000	258.6	0.000	0.00
0.32	0.105	246.5	0.112	2.89
0.45	0.149	232.5	0.205	4.98
0.65	0.180	212.6	0.416	9.25
0.77	0.211	159.8	0.673	11.26
1.10	0.256	103.4	1.034	11.19
1.25	0.321	59.6	1.322	8.25
1.57	0.389	22.5	1.974	4.99
2.00	0.589	10.3	2.118	2.13

TABLE(58) Power characteristics of rotor augmented with tip-fin 4.

Mass(m) (kg)	Balance Reading(M) (kg)	Average Rotor Speed(N) (rpm)	Torque(T) (Nm)	Power(P) (Watt)
0.00	0.000	248.9	0.000	0.00
0.32	0.087	233.3	0.102	2.49
0.45	0.109	215.4	0.199	4.51
0.65	0.156	184.6	0.358	6.92
0.77	0.187	125.6	0.600	7.89
1.10	0.212	75.2	0.827	6.51
1.25	0.278	44.4	1.116	5.19
1.57	0.301	28.6	1.172	3.51
2.00	0.487	14.2	1.210	1.74

TABLE(59) Power characteristics of rotor augmented with tip-fin 4 and rotating fairing.

Mass(m) (kg)	Balance Reading(M) (kg)	Average Rotor Speed(N) (rpm)	Torque(T) (Nm)	Power(P) (Watt)
0.00	0.000	254.6	0.000	0.00
0.32	0.078	240.4	0.113	2.84
0.45	0.099	217.5	0.221	5.04
0.65	0.137	185.6	0.387	7.52
0.77	0.177	157.5	0.517	8.52
1.10	0.198	114.2	0.709	8.48
1.25	0.232	67.5	1.026	7.25
1.57	0.345	35.2	1.218	4.49
2.00	0.465	19.4	1.431	1.62

TABLE(60) Power characteristics of rotor augmented with tip-fin 4 and after-body.

Mass (m) (kg)	Balance Reading (M) (kg)	Average Rotor Speed (N) (rpm)	Torque (T) (Nm)	Power (P) (Watt)
0.00	0.000	254.5	0.000	0.00
0.32	0.069	245.6	0.097	2.49
0.45	0.098	228.5	0.198	4.75
0.65	0.135	187.6	0.383	7.52
0.77	0.166	135.2	0.615	8.71
1.10	0.189	87.4	0.847	7.75
1.25	0.229	60.5	1.102	6.98
1.57	0.351	38.4	1.291	5.19
2.00	0.471	20.6	1.324	1.99

TABLE(61) Power characteristics of rotor augmented with tip-fin 4, rotating fairing and after-body.

Mass (m) (kg)	Balance Reading (M) (kg)	Average Rotor Speed (N) (rpm)	Torque (T) (Nm)	Power (P) (Watt)
0.00	0.000	254.6	0.000	0.00
0.32	0.070	234.4	0.111	2.72
0.45	0.101	223.5	0.215	5.02
0.65	0.139	185.2	0.373	7.23
0.77	0.172	125.6	0.664	8.73
1.10	0.193	80.4	0.931	7.84
1.25	0.239	45.9	1.184	5.69
1.57	0.364	31.2	1.374	4.49
2.00	0.489	12.5	1.436	1.88

TABLE(62) Power characteristics of rotor augmented with tip-fin 4 and stationary fairing.

Mass(m) (kg)	Balance Reading(M) (kg)	Average Rotor Speed(N) (rpm)	Torque(T) (Nm)	Power(P) (Watt)
0.00	0.000	254.5	0.000	0.00
0.32	0.068	238.6	0.102	2.54
0.45	0.096	226.8	0.189	4.49
0.65	0.125	195.9	0.374	7.68
0.77	0.166	168.6	0.484	8.54
1.10	0.187	127.5	0.693	9.25
1.25	0.221	78.2	1.036	8.48
1.57	0.362	42.4	1.237	5.49
2.00	0.486	18.2	1.346	1.68

TABLE (63) Power characteristics of rotor augmented with tip-fin 4, stationary fairing and after-body.

Mass (m) (kg)	Balance Reading (M) (kg)	Average Rotor Speed (N) (rpm)	Torque (T) (Nm)	Power (P) (Watt)
0.00	0.000	260.4	0.000	0.00
0.32	0.094	245.1	0.106	2.72
0.45	0.113	225.4	0.276	6.51
0.65	0.132	203.5	0.409	8.73
0.77	0.188	133.4	0.739	10.34
1.10	0.212	82.5	1.048	9.05
1.25	0.267	45.6	1.369	6.54
1.57	0.398	22.5	1.524	4.48
2.00	0.496	14.1	1.902	2.25

TABLE(64) Power characteristics of rotor augmented with tip-fin 5.

Mass (m) (kg)	Balance Reading (M) (kg)	Average Rotor Speed (N) (rpm)	Torque (T) (Nm)	Power (P) (Watt)
0.00	0.000	249.6	0.000	0.00
0.32	0.084	238.4	0.066	1.65
0.45	0.109	217.6	0.177	4.04
0.65	0.126	191.5	0.304	6.10
0.77	0.175	128.7	0.529	7.14
1.10	0.208	84.5	0.736	6.51
1.25	0.256	46.4	0.971	4.72
1.57	0.389	32.3	1.110	3.24
2.00	0.488	13.5	1.146	1.34

TABLE(65) Power characteristics of rotor augmented with tip-fin 5 and rotating fairing.

Mass (m) (kg)	Balance Reading (M) (kg)	Average Rotor Speed (N) (rpm)	Torque (T) (Nm)	Power (P) (Watt)
0.00	0.000	256.4	0.000	0.00
0.32	0.088	239.6	0.108	2.72
0.45	0.115	210.5	0.274	6.05
0.65	0.134	175.4	0.411	7.54
0.77	0.189	112.5	0.689	8.12
1.10	0.216	78.2	0.885	7.25
1.25	0.267	58.2	1.014	6.18
1.57	0.396	31.6	1.054	3.49
2.00	0.494	9.9	1.466	1.52

TABLE(66) Power characteristics of rotor augmented with tip-fin 5 and after-body.

Mass(m) (kg)	Balance Reading(M) (kg)	Average Rotor Speed(N) (rpm)	Torque(T) (Nm)	Power(P) (Watt)
0.00	0.000	256.7	0.000	0.00
0.32	0.092	240.6	0.100	2.54
0.45	0.120	210.5	0.278	6.12
0.65	0.151	177.2	0.421	7.82
0.77	0.193	137.5	0.598	8.61
1.10	0.221	95.2	0.753	7.51
1.25	0.279	50.8	1.133	6.03
1.57	0.412	23.4	1.424	3.49
2.00	0.507	10.2	1.452	1.47

TABLE(67) Power characteristics of rotor augmented with tip-fin 5, rotary fairing and after-body.

Mass(m) (kg)	Balance Reading(M) (kg)	Average Rotor Speed(N) (rpm)	Torque(T) (Nm)	Power(P) (Watt)
0.00	0.000	257.2	0.000	0.00
0.32	0.118	239.4	0.108	2.72
0.45	0.142	209.6	0.276	6.06
0.65	0.189	175.2	0.420	7.71
0.77	0.240	127.5	0.622	8.31
1.10	0.288	84.5	0.849	7.52
1.25	0.339	50.9	0.961	5.12
1.57	0.455	24.5	1.267	3.25
2.00	0.523	10.4	1.488	1.62

TABLE(68) Power characteristics of rotor augmented with tip-fin 5 and stationary fairing.

Mass (m) (kg)	Balance Reading (M) (kg)	Average Rotor Speed (N) (rpm)	Torque (T) (Nm)	Power (P) (Watt)
0.00	0.000	258.8	0.000	0.00
0.32	0.120	245.6	0.087	2.25
0.45	0.155	228.5	0.198	4.75
0.65	0.197	200.4	0.358	7.51
0.77	0.259	129.4	0.675	9.15
1.10	0.297	88.6	0.885	8.21
1.25	0.360	48.2	1.250	6.31
1.57	0.489	27.4	1.227	3.52
2.00	0.530	14.6	1.328	1.72

TABLE(69) Power characteristics of rotor augmented with tip-fin 5, stationary fairing and after-body.

Mass(m) (kg)	Balance Reading(M) (kg)	Average Rotor Speed(N) (rpm)	Torque(T) (Nm)	Power(P) (Watt)
0.00	0.000	260.4	0.000	0.00
0.32	0.128	248.6	0.096	2.51
0.45	0.162	228.4	0.229	5.47
0.65	0.209	195.6	0.409	8.39
0.77	0.270	131.7	0.722	9.95
1.10	0.311	80.2	1.015	8.52
1.25	0.377	37.5	1.489	6.24
1.57	0.491	23.4	1.518	3.72
2.00	0.544	12.3	1.662	2.14

TABLE(70) Power characteristics of rotor augmented with tip-fin 6.

Mass (m) (kg)	Balance Reading (M) (kg)	Average Rotor Speed (N) (rpm)	Torque (T) (Nm)	Power (P) (Watt)
0.00	0.000	250.6	0.000	0.00
0.32	0.091	232.5	0.124	3.02
0.45	0.118	207.8	0.229	4.99
0.65	0.167	180.7	0.330	6.25
0.77	0.206	135.8	0.509	7.25
1.10	0.276	90.9	0.685	6.52
1.25	0.299	52.5	0.953	5.24
1.57	0.369	37.5	1.039	4.08
2.00	0.487	22.5	1.217	2.00

TABLE(71) Power characteristics of rotor augmented with tip-fin 6 and rotating fairing.

Mass (m) (kg)	Balance Reading (M) (kg)	Average Rotor Speed (N) (rpm)	Torque (T) (Nm)	Power (P) (Watt)
0.00	0.000	259.4	0.000	0.00
0.32	0.088	245.6	0.116	2.99
0.45	0.110	227.4	0.231	5.51
0.65	0.136	187.5	0.388	7.62
0.77	0.178	124.7	0.668	8.72
1.10	0.198	84.6	0.922	8.17
1.25	0.235	50.1	1.191	6.25
1.57	0.389	28.9	1.404	4.25
2.00	0.499	14.4	1.419	2.14

TABLE(72) Power characteristics of rotor augmented with tip-fin 6 and after-body.

Mass(m) (kg)	Balance Reading(M) (kg)	Average Rotor Speed(N) (rpm)	Torque(T) (Nm)	Power(P) (Watt)
0.00	0.000	260.4	0.000	0.00
0.32	0.107	245.6	0.121	3.12
0.45	0.136	217.5	0.242	5.51
0.65	0.175	195.6	0.373	7.63
0.77	0.197	148.4	0.594	9.23
1.10	0.238	96.5	0.839	8.48
1.25	0.289	65.4	0.948	6.49
1.57	0.388	37.3	1.155	4.51
2.00	0.511	12.5	1.719	2.25

TABLE(73) Power characteristics of rotor augmented with tip-fin 6, rotating fairing and after-body.

Mass(m) (kg)	Balance Reading(M) (kg)	Average Rotor Speed(N) (rpm)	Torque(T) (Nm)	Power(P) (Watt)
0.00	0.000	260.6	0.000	0.00
0.32	0.110	240.5	0.127	3.19
0.45	0.148	228.7	0.231	5.52
0.65	0.196	189.1	0.404	8.00
0.77	0.217	133.4	0.662	9.25
1.10	0.278	85.2	0.931	8.31
1.25	0.321	56.5	1.095	6.48
1.57	0.399	37.8	1.173	4.25
2.00	0.528	19.9	1.189	2.31

TABLE(74) Power characteristics of rotor augmented with tip-fin 6 and stationary fairing.

Mass (m) (kg)	Balance Reading (M) (kg)	Average Rotor Speed (N) (rpm)	Torque (T) (Nm)	Power (P) (Watt)
0.00	0.000	261.5	0.000	0.00
0.32	0.121	245.6	0.098	2.52
0.45	0.167	227.6	0.253	6.04
0.65	0.218	196.2	0.413	8.49
0.77	0.266	132.7	0.692	9.61
1.10	0.295	92.3	0.908	8.78
1.25	0.359	55.4	1.158	6.72
1.57	0.426	35.6	1.204	4.49
2.00	0.530	22.5	1.237	2.61

TABLE(75) Power characteristics of rotor augmented with tip-fin 6, stationary fairing and after-body.

Mass (m) (kg)	Balance Reading (M) (kg)	Average Rotor Speed (N) (rpm)	Torque (T) (Nm)	Power (P) (Watt)
0.00	0.000	264.6	0.000	0.00
0.32	0.153	249.7	0.152	3.98
0.45	0.198	226.6	0.316	7.49
0.65	0.247	169.8	0.592	10.52
0.77	0.289	112.5	0.901	10.61
1.10	0.325	78.9	1.152	9.52
1.25	0.398	48.6	1.393	7.09
1.57	0.467	32.9	1.506	5.19
2.00	0.544	14.3	1.943	2.91

TABLE(76) Power characteristics of rotor augmented with tip-fin 7.

Mass(m) (kg)	Balance Reading(M) (kg)	Average Rotor Speed(N) (rpm)	Torque(T) (Nm)	Power(P) (Watt)
0.00	0.000	256.8	0.000	0.00
0.32	0.087	248.7	0.080	2.08
0.45	0.112	222.8	0.192	4.49
0.65	0.168	202.5	0.295	6.25
0.77	0.199	180.8	0.376	7.12
1.10	0.225	128.6	0.600	8.08
1.25	0.289	88.7	0.769	7.14
1.57	0.367	44.8	1.006	4.72
2.00	0.449	20.6	1.198	2.12

TABLE(77) Power characteristics of rotor augmented with tip-fin 7 and rotating fairing.

Mass (m) (kg)	Balance Reading (M) (kg)	Average Rotor Speed (N) (rpm)	Torque (T) (Nm)	Power (P) (Watt)
0.00	0.000	261.2	0.000	0.00
0.32	0.098	249.4	0.095	2.48
0.45	0.128	228.3	0.210	5.02
0.65	0.180	195.6	0.395	8.10
0.77	0.219	120.3	0.722	9.09
1.10	0.268	97.5	0.857	8.75
1.25	0.291	60.3	1.117	7.05
1.57	0.389	24.5	1.438	3.69
2.00	0.493	10.3	1.501	1.32

TABLE(78) Power characteristics of rotor augmented with tip-fin 7 and after-body.

Mass(m) (kg)	Balance Reading(M) (kg)	Average Rotor Speed(N) (rpm)	Torque(T) (Nm)	Power(P) (Watt)
0.00	0.000	261.9	0.000	0.00
0.32	0.101	245.8	0.096	2.48
0.45	0.131	235.1	0.208	5.13
0.65	0.192	187.4	0.411	8.06
0.77	0.228	150.6	0.604	9.52
1.10	0.277	85.2	0.984	8.78
1.25	0.310	67.2	1.130	7.25
1.57	0.390	33.5	1.372	3.76
2.00	0.498	8.3	1.703	1.48

TABLE(79) Power characteristics of rotor augmented with tip-fin 7, rotating fairing and after-body.

Mass(m) (kg)	Balance Reading(M) (kg)	Average Rotor Speed(N) (rpm)	Torque(T) (Nm)	Power(P) (Watt)
0.00	0.000	260.7	0.000	0.00
0.32	0.108	247.5	0.101	2.63
0.45	0.139	229.9	0.229	5.51
0.65	0.199	192.3	0.414	8.34
0.77	0.237	130.9	0.695	9.52
1.10	0.284	94.5	0.873	8.64
1.25	0.321	66.6	0.914	6.98
1.57	0.398	35.2	1.153	4.25
2.00	0.509	12.3	1.172	1.51

TABLE(80) Power characteristics of rotor augmented with tip-fin 7 and stationary fairing.

Mass(m) (kg)	Balance Reading(M) (kg)	Average Rotor Speed(N) (rpm)	Torque(T) (Nm)	Power(P) (Watt)
0.00	0.000	262.5	0.000	0.00
0.32	0.118	247.7	0.123	3.19
0.45	0.176	232.5	0.253	6.15
0.65	0.212	199.6	0.417	8.72
0.77	0.264	140.8	0.688	10.14
1.10	0.294	97.6	0.914	9.34
1.25	0.331	56.7	1.221	7.25
1.57	0.478	30.8	1.296	4.18
2.00	0.521	14.1	1.348	1.56

TABLE(81) Power characteristics of rotor augmented with tip-fin 7, stationary fairing and after-body.

Mass(m) (kg)	Balance Reading(M) (kg)	Average Rotor Speed(N) (rpm)	Torque(T) (Nm)	Power(P) (Watt)
0.00	0.000	263.2	0.000	0.00
0.32	0.138	249.3	0.325	3.72
0.45	0.197	234.8	0.405	7.49
0.65	0.246	202.5	0.480	10.19
0.77	0.294	150.9	0.727	11.49
1.10	0.350	96.7	1.035	10.48
1.25	0.391	46.8	1.557	7.63
1.57	0.487	27.5	1.589	4.25
2.00	0.562	8.34	2.164	1.89

TABLE(82) Power characteristics of rotor augmented with tip-fin 8.

Mass(m) (kg)	Balance Reading(M) (kg)	Average Rotor Speed(N) (rpm)	Torque(T) (Nm)	Power(P) (Watt)
0.00	0.000	253.4	0.000	0.00
0.32	0.098	239.2	0.104	2.61
0.45	0.121	210.3	0.249	5.49
0.65	0.165	175.7	0.398	7.34
0.77	0.199	135.6	0.563	8.00
1.10	0.285	82.5	0.866	7.48
1.25	0.382	47.6	1.105	5.51
1.57	0.442	35.2	1.213	4.47
2.00	0.498	18.6	1.456	2.25

TABLE(83) Power characteristics of rotor augmented with tip-fin 8 and rotating fairing.

Mass (m) (kg)	Balance Reading (M) (kg)	Average Rotor Speed (N) (rpm)	Torque (T) (Nm)	Power (P) (Watt)
0.00	0.000	258.5	0.000	0.00
0.32	0.102	245.7	0.098	2.51
0.45	0.133	236.2	0.182	4.49
0.65	0.167	187.5	0.432	8.49
0.77	0.210	132.6	0.668	9.27
1.10	0.291	80.9	1.005	8.51
1.25	0.390	56.8	1.099	6.54
1.57	0.455	35.2	1.180	4.35
2.00	0.505	17.3	1.433	1.89

TABLE(84) Power characteristics of rotor augmented with tip-fin 8 and after-body.

Mass(m) (kg)	Balance Reading(M) (kg)	Average Rotor Speed(N) (rpm)	Torque(T) (Nm)	Power(P) (Watt)
0.00	0.000	258.9	0.000	0.00
0.32	0.114	246.7	0.087	2.25
0.45	0.156	232.5	0.175	4.26
0.65	0.197	194.5	0.396	8.06
0.77	0.238	150.7	0.595	9.39
1.10	0.291	88.6	0.883	8.19
1.25	0.396	52.5	1.137	6.25
1.57	0.459	35.4	1.144	4.04
2.00	0.510	18.6	1.176	1.49

TABLE(85) Power characteristics of rotor augmented with tip-fin 8, rotating fairing and after-body.

Mass(m) (kg)	Balance Reading(M) (kg)	Average Rotor Speed(N) (rpm)	Torque(T) (Nm)	Power(P) (Watt)
0.00	0.000	259.7	0.000	0.00
0.32	0.120	247.8	0.097	2.52
0.45	0.169	232.5	0.186	4.53
0.65	0.216	195.2	0.415	8.48
0.77	0.276	127.5	0.709	9.47
1.10	0.328	88.3	0.920	8.51
1.25	0.399	47.9	1.299	6.52
1.57	0.468	30.1	1.329	4.19
2.00	0.526	15.0	1.435	1.99

TABLE(86) Power characteristics of rotor augmented with tip-fin 8 and stationary fairing.

Mass(m) (kg)	Balance Reading(M) (kg)	Average Rotor Speed(N) (rpm)	Torque(T) (Nm)	Power(P) (Watt)
0.00	0.000	260.2	0.000	0.00
0.32	0.129	249.7	0.115	3.01
0.45	0.178	232.5	0.207	5.03
0.65	0.228	196.2	0.437	8.98
0.77	0.296	127.5	0.752	10.04
1.10	0.340	80.6	1.088	9.18
1.25	0.418	54.6	1.258	7.19
1.57	0.487	32.6	1.309	4.47
2.00	0.531	15.8	1.360	2.25

TABLE(87) Power characteristics of rotor augmented with tip-fin 8, stationary fairing and after-body.

Mass(m) (kg)	Balance Reading(M) (kg)	Average Rotor Speed(N) (rpm)	Torque(T) (Nm)	Power(P) (Watt)
0.00	0.000	265.4	0.000	0.00
0.32	0.141	253.2	0.113	2.99
0.45	0.188	244.8	0.219	5.61
0.65	0.221	202.5	0.455	9.65
0.77	0.287	135.6	0.792	11.25
1.10	0.378	82.5	1.163	10.05
1.25	0.428	48.7	1.475	7.52
1.57	0.491	27.2	1.759	5.01
2.00	0.562	14.8	1.803	2.64

TABLE(88) Power characteristics of rotor augmented with tip-fin 9.

Mass (m) (kg)	Balance Reading (M) (kg)	Average Rotor Speed (N) (rpm)	Torque (T) (Nm)	Power (P) (Watt)
0.00	0.000	253.4	0.000	0.00
0.32	0.097	240.6	0.088	2.23
0.45	0.121	216.8	0.199	4.51
0.65	0.187	174.9	0.387	7.08
0.77	0.220	127.5	0.591	7.89
1.10	0.278	79.6	0.810	6.75
1.25	0.361	48.2	0.989	4.99
1.57	0.419	25.3	1.227	3.25
2.00	0.487	15.1	1.343	1.65

TABLE(89) Power characteristics of rotor augmented with tip-fin 9 and rotating fairing.

Mass(m) (kg)	Balance Reading(M) (kg)	Average Rotor Speed(N) (rpm)	Torque(T) (Nm)	Power(P) (Watt)
0.00	0.000	261.6	0.000	0.00
0.32	0.123	250.8	0.088	2.31
0.45	0.156	228.1	0.217	5.19
0.65	0.190	194.8	0.396	8.08
0.77	0.241	136.2	0.632	9.01
1.10	0.298	79.6	0.968	8.07
1.25	0.370	39.8	1.372	5.72
1.57	0.452	24.3	1.383	3.52
2.00	0.533	10.6	1.784	1.98

TABLE(90) Power characteristics of rotor augmented with tip-fin 9 and after-body.

Mass (m) (kg)	Balance Reading (M) (kg)	Average Rotor Speed (N) (rpm)	Torque (T) (Nm)	Power (P) (Watt)
0.00	0.000	261.3	0.000	0.00
0.32	0.139	245.2	0.088	2.26
0.45	0.178	220.6	0.233	5.38
0.65	0.218	187.5	0.395	7.76
0.77	0.279	125.2	0.705	9.24
1.10	0.325	71.3	1.007	7.52
1.25	0.397	44.9	1.168	5.49
1.57	0.479	27.6	1.204	3.48
2.00	0.549	19.7	1.315	1.95

TABLE(91) Power characteristics of rotor augmented with tip-fin 9, rotating fairing and after-body.

Mass (m) (kg)	Balance Reading (M) (kg)	Average Rotor Speed (N) (rpm)	Torque (T) (Nm)	Power (P) (Watt)
0.00	0.000	262.8	0.000	0.00
0.32	0.117	247.5	0.097	2.51
0.45	0.153	217.5	0.253	5.76
0.65	0.199	187.5	0.293	8.19
0.77	0.239	127.7	0.677	9.05
1.10	0.287	86.7	0.935	8.49
1.25	0.312	48.9	1.168	5.98
1.57	0.391	27.2	1.366	3.89
2.00	0.498	10.3	1.827	1.97

TABLE(92) Power characteristics of rotor augmented with tip-fin 9 and stationary fairing.

Mass(m) (kg)	Balance Reading(M) (kg)	Average Rotor Speed(N) (rpm)	Torque(T) (Nm)	Power(P) (Watt)
0.00	0.000	262.7	0.000	0.00
0.32	0.137	248.3	0.122	3.18
0.45	0.187	223.6	0.264	6.17
0.65	0.226	191.2	0.449	8.98
0.77	0.278	127.7	0.747	9.99
1.10	0.327	90.9	0.961	9.15
1.25	0.389	52.5	1.217	6.69
1.57	0.448	28.4	1.506	4.48
2.00	0.535	14.2	1.580	2.35

TABLE(93) Power characteristics of rotor augmented with tip-fin 9, stationary fairing and after-body.

Mass(m) (kg)	Balance Reading(M) (kg)	Average Rotor Speed(N) (rpm)	Torque(T) (Nm)	Power(P) (Watt)
0.00	0.000	263.8	0.000	0.00
0.32	0.168	248.8	0.139	3.62
0.45	0.198	227.8	0.273	6.51
0.65	0.259	203.5	0.445	9.49
0.77	0.299	128.6	0.816	10.99
1.10	0.364	79.8	1.163	9.72
1.25	0.392	49.9	1.387	7.25
1.57	0.487	28.6	1.666	4.99
2.00	0.551	11.3	2.426	2.87

TABLE(94) Power characteristics of rotor augmented with tip-fin 10.

Mass (m) (kg)	Balance Reading (M) (kg)	Average Rotor Speed (N) (rpm)	Torque (T) (Nm)	Power (P) (Watt)
0.00	0.000	257.6	0.000	0.00
0.32	0.170	245.8	0.097	2.49
0.45	0.232	220.2	0.225	5.19
0.65	0.297	195.6	0.390	7.99
0.77	0.345	135.8	0.646	9.18
1.10	0.389	82.5	0.935	8.08
1.25	0.432	45.6	1.252	5.98
1.57	0.487	34.8	1.414	4.06
2.00	0.568	10.2	1.666	1.78

TABLE(95) Power characteristics of rotor augmented with tip-fin 10 and rotating fairing.

Mass(m) (kg)	Balance Reading(M) (kg)	Average Rotor Speed(N) (rpm)	Torque(T) (Nm)	Power(P) (Watt)
0.00	0.000	260.6	0.000	0.00
0.32	0.191	248.1	0.122	3.18
0.45	0.256	227.2	0.297	7.06
0.65	0.297	197.4	0.446	9.21
0.77	0.387	136.6	0.737	10.54
1.10	0.478	81.9	1.105	9.48
1.25	0.453	48.2	1.380	7.47
1.57	0.512	30.4	1.420	4.52
2.00	0.589	10.2	1.561	1.24

TABLE(96) Power characteristics of rotor augmented with tip-fin 10 and after-body.

Mass(m) (kg)	Balance Reading(M) (kg)	Average Rotor Speed(N) (rpm)	Torque(T) (Nm)	Power(P) (Watt)
0.00	0.000	260.8	0.000	0.00
0.32	0.180	247.4	0.106	2.75
0.45	0.241	224.8	0.278	6.55
0.65	0.288	188.7	0.468	9.25
0.77	0.371	124.8	0.802	10.48
1.10	0.467	70.2	1.235	9.08
1.25	0.445	46.7	1.366	6.68
1.57	0.501	28.6	1.499	4.49
2.00	0.567	11.3	1.567	1.38

TABLE(97) Power characteristics of rotor augmented with tip-fin 10, rotating fairing and after-body.

Mass(m) (kg)	Balance Reading(M) (kg)	Average Rotor Speed(N) (rpm)	Torque(T) (Nm)	Power(P) (Watt)
0.00	0.000	261.6	0.000	0.00
0.32	0.201	246.8	0.122	3.15
0.45	0.268	223.6	0.309	7.25
0.65	0.299	196.6	0.464	9.55
0.77	0.387	129.6	0.781	10.61
1.10	0.498	76.2	1.161	9.26
1.25	0.538	50.7	1.352	7.18
1.57	0.589	28.5	1.582	4.72
2.00	0.687	9.3	1.597	1.24

TABLE(98) Power characteristics of rotor augmented with tip-fin 10 and stationary fairing.

Mass(m) (kg)	Balance Reading(M) (kg)	Average Rotor Speed(N) (rpm)	Torque(T) (Nm)	Power(P) (Watt)
0.00	0.000	262.5	0.000	0.00
0.32	0.238	245.2	0.142	3.65
0.45	0.289	223.4	0.331	7.75
0.65	0.342	200.8	0.485	10.19
0.77	0.387	136.2	0.805	11.48
1.10	0.496	75.8	1.254	9.95
1.25	0.587	45.4	1.637	7.78
1.57	0.678	29.6	1.671	5.18
2.00	0.729	13.3	1.689	1.99

TABLE(99) Power characteristics of rotor augmented with tip-fin 10, stationary fairing and after-body.

Mass (m) (kg)	Balance Reading (M) (kg)	Average Rotor Speed (N) (rpm)	Torque (T) (Nm)	Power (P) (Watt)
0.00	0.000	264.8	0.000	0.00
0.32	0.268	256.7	0.162	4.34
0.45	0.317	232.5	0.360	8.75
0.65	0.391	202.5	0.543	11.52
0.77	0.438	137.8	0.899	12.97
1.10	0.499	67.5	1.553	10.98
1.25	0.598	45.6	1.784	8.52
1.57	0.689	25.6	2.048	5.49
2.00	0.757	10.4	2.085	2.27

TABLE(100) Wind-turbine / Pump combination characteristics with angle of attack α set at 15°.

Wind Speed V (m/s)	Rotor Speed N (rpm)	Water Flowrate q (x 1000 cc/min)
3.70	42.5	5.0
4.10	50.0	5.5
5.00	198.0	18.0
6.10	253.5	24.0
7.50	232.5	25.0
8.61	269.3	26.0
11.00	356.8	32.0

TABLE(101) Power characteristics and error analysis of Pump/Wind-turbine combination, $\alpha = 15^{\circ}$.

Wind Speed (m/s)	Flow Rate (x1000 cc/min)	Rotor Speed (rpm)	P(mech) (watts)	P(hyd) (watts)	Mech (%)	$d\eta$	Error in η (%)
4.1	5.5	50.0	3.0	0.13	5.6	$\pm$ 0.25	0.4
5.0	18.8	198.0	7.8	0.40	7.7	$\pm$ 0.60	0.8
7.5	20.0	232.5	9.8	0.45	4.5	$\pm$ 1.12	2.5

TABLE(102) Overall Efficiency of the Pump/wind-turbine combination, $\alpha = 15^{\circ}$.

Wind Speed (m/s)	Rotor Speed (rpm)	P (watts)	P(mech) (watts)	Torque (Nm)	Overall Efficiency (%)
4.1	50.0	13.2	3.0	0.56	22
5.0	198.0	23.9	7.8	0.36	30
7.5	232.5	80.8	9.8	0.42	14

TABLE(103) Error analysis of maximum power of fully augmented Wind-turbine.

Wind Speed (m/s)	m (kg)	M (kg)	Rotor Speed (rpm)	Torque (Nm)	Maximum Power (watts)	Error in Max.Power (%)
4.1	0.85	0.170	61	0.53	3.40	0.17
5.0	1.45	0.149	134	1.05	14.50	3.20
7.5	1.97	0.624	130	1.35	18.32	0.95

TABLE(104) Error analysis of power coefficient (Cp).

Wind Speed (m/s)	m (kg)	M (kg)	Rotor Speed (rpm)	Torque (Nm)	P(mech) (watts)	P (watts)	Cp	% erro in Cp
4.1	0.85	0.17	61	0.53	3.40	13.20	0.26	35
5.0	1.20	0.30	141	0.70	10.34	23.93	0.43	33
7.5	1.97	0.62	128	1.05	14.10	80.75	0.18	17